



UNIVERSITY OF
BIRMINGHAM

REINFORCED CONCRETE BEAM-COLUMN JOINTS STRENGTHENED IN SHEAR WITH EMBEDDED BARS

Ridwan

A Thesis submitted in partial fulfillment for the degree of

Doctor of Philosophy

School of Engineering

College of Engineering and Physical Sciences

The University of Birmingham

2016

UNIVERSITY OF
BIRMINGHAM

University of Birmingham Research Archive

e-theses repository

This unpublished thesis/dissertation is copyright of the author and/or third parties. The intellectual property rights of the author or third parties in respect of this work are as defined by The Copyright Designs and Patents Act 1988 or as modified by any successor legislation.

Any use made of information contained in this thesis/dissertation must be in accordance with that legislation and must be properly acknowledged. Further distribution or reproduction in any format is prohibited without the permission of the copyright holder.

ABSTRACT

Beam-column (BC) joints play an important role in the seismic performance of moment-resisting reinforced concrete (RC) frame structures. Without adequate joint shear reinforcement, as is the case with existing RC frame structures designed according to the pre-1970s' building codes, BC joints can be the most vulnerable elements during an earthquake. Several techniques for improving the seismic performance of BC joints have been proposed, but these techniques have been criticised for being labour-intensive and/or susceptible to premature de-bonding. To overcome these shortcomings, a novel technique utilising embedded reinforcement bars was developed in this study for strengthening shear-deficient RC BC joints.

Seven exterior BC joints were constructed and tested under displacement-controlled cyclic loading. All specimens had the same dimensions and reinforcement configurations. One of the specimens was adequately designed according to the ACI 352R-02 code; whilst the rest were designed in accordance to the pre-1970 code provisions to represent joints' shear strength deficiency. Two of the six shear deficient joints were the control specimens and the rest were strengthened with deep embedment bars. To study the effect of the embedded bar type, steel or carbon FRP bars were used as additional joints' shear reinforcement. The number of embedded bars was also varied in order to examine the effect of the joints' shear reinforcement ratio.

The results showed that the unstrengthened specimens experienced joint shear damage in the form of cross-diagonal cracks; while the strengthened specimens exhibited a more enhanced

behaviour where damage occurred in the beam region at the early stages of loading, suggesting the outset of a beam hinge (BH) mechanism, and then the stiffness and strength of the strengthened specimens degraded after reaching peak load at 3% drift ratio. Compared to the duplicate control specimen, all strengthened specimens gave a better performance. For example, the enhancement of the normalized principal tensile stress was improved by 16 - 25%.

Three-dimensional finite element (FE) models were developed using ABAQUS to study the behaviour of the tested exterior RC BC joints. The models were calibrated to the results obtained from the experimental programme conducted in this study. The models were used for numerical parametric study on different parameters known to affect the joints' shear strength, including the column's axial load level, the concrete's compressive strength and the additional joints' shear reinforcement ratio.

Based on the FE study, the first joint crack can be defined by the function of a constant and the normalized principal tensile strength, $k_a \sqrt{f_c}$. The value of the normalized joint's shear ratio at the first joint crack ranged from 0.27 to 0.31. Moreover, the maximum joint shear strength also changes linearly with the variation of the concrete strength, column axial load and embedded bar size.

In addition to the experimental and FE study, an analytical method to evaluate shear capacity in the joint for BC joints strengthened with embedded bars was developed. The accuracy of the proposed method was checked against the test results from unstrengthened exterior RC BC joint tests available from the literature and also the results of the controlled specimens

obtained in the experiments of this thesis. A good agreement between the analytical prediction and the experiments, were found within 38 unstrengthened BC joints reported by other researchers in addition to the control specimens in this study. The joints' shear capacity prediction using the proposed analytical model also showed good agreement with the experimentally DE strengthened BC joints.

ACKNOWLEDGEMENTS

I would like to express my profound gratitude to my main supervisor Dr Samir Dirar. This thesis would not have been possible without his wisdom, inspiration, never ending patience and invaluable advice. I am also grateful to my co-supervisors Dr Marios Theofanous and Dr Jian Yang for kind advice and encouragement. I have benefited a lot from their important ideas and original concepts. I would like to extend my thanks to Dr Yaser Jemaa for his invaluable contribution and help during my experimental programme.

I would like to gratefully acknowledge the full funding for this study provided by Indonesian Directorate General of Higher Education (DGHE) through the grant number 323/E4.4/K/2012. Without the financial aid from this institution, my PhD research and experience would not have been possible.

I would like to thank the technicians at the Concrete Laboratory, Department of Civil Engineering University of Birmingham. In particular, without the assistance of Dave Cope and Mike Vanderstam, the laborious experimental programme of this thesis would not have been completed. Their assistance in making the experimental research a smooth experience has also been much appreciated. Thanks are also due to Janet's Proofreading Service who helped checking the spelling and grammar of this thesis.

Finally, I would like to express my sincere love and gratitude to my beloved family, especially my late father and mother. Their endless love, support and prayers helped me get through the difficult time during my PhD years.

TABLE OF CONTENTS

ABSTRACT	i
ACKNOWLEDGEMENTS	iv
Table of Contents.....	v
List of Tables	xi
List of Figures	xiii
Notation	xxi
CHAPTER 1.....	1
INTRODUCTION	1
1.1. GENERAL	1
1.2. RESEARCH SIGNIFICANCE	2
1.3. PROBLEM DEFINITION	3
1.4. ORIGINALITY, AIMS AND OBJECTIVES	4
1.5. RESEARCH METHODOLOGY	5
1.6. THESIS LAYOUT	6
CHAPTER 2.....	8
LITERATURE REVIEW	8
2.1. GENERAL	8
2.2. SEISMIC PERFORMANCE OF EXISTING EXTERIOR REINFORCED CONCRETE BEAM-COLUMN JOINTS.....	13
2.3. PARAMETERS AFFECTING SHEAR STRENGTH OF REINFORCED CONCRETE JOINTS.....	24
2.3.1. Effect of column axial load	24

2.3.2. Effect of concrete compressive strength	27
2.3.3. Effect of joint reinforcement confinement.....	29
2.4. FIBRE REINFORCED POLYMER	30
2.4.1. Mechanical Properties.....	33
2.4.2. Physical properties	35
2.4.3. Manufacturing of Carbon Fibres.....	35
2.5. STRENGTHENING OF EXTERIOR REINFORCED CONCRETE BEAM- COLUMN JOINTS USING FIBRE REINFORCED POLYMER MATERIAL	37
2.5.1. Ghobarah et al.	39
2.5.2. Antonopoulos and Triantafillou (2003)	40
2.5.3. Tsonos (2008)	43
2.5.4. Karayannis and Sirkelis (2008).....	45
2.5.5. Alsayed et al. (2010)	47
2.5.6. Ilki et al. (2011).....	49
2.5.7. Sezen (2012)	51
2.6. STRENGTHENING OF REINFORCED CONCRETE STRUCTURES UTILISING DEEP EMBEDMENT TECHNIQUE	52
2.6.1. Valerio et al. (2009)	53
2.6.2. Chaallal et al. (2011).....	55
2.7. PREDICTION MODELS	57
2.7.1. Analytical Modeling	57
2.7.2. Finite Element Modeling	63
2.8. CURRENT CODE OF PRACTICES IN DESIGNING REINFORCED CONCRETE BEAM-COLUMN JOINTS.....	68

2.8.1. ACI 318-14: Building Code Requirements for Structural Concrete and Commentary (2014).....	68
2.8.2. ACI-ASCE Committee 352R-02	70
2.9. SUMMARY	72
CHAPTER 3.....	74
EXPERIMENTAL PROGRAMME	74
3.1. GENERAL	74
3.2. MATERIAL PROPERTIES	74
3.2.1. Concrete	74
3.2.2. Steel.....	75
3.2.3. Carbon Fibre Reinforced Polymer	76
3.2.4. Epoxy Resin	76
3.3. DESCRIPTION OF TEST UNITS	77
3.4. MANUFACTURE OF THE SPECIMENS	81
3.5. STRENGTHENING APPLICATION	84
3.6. TEST SET-UP.....	86
3.7. LOADING PROTOCOL	89
3.8. DATA ACQUISITION SYSTEM.....	91
CHAPTER 4.....	94
EXPERIMENTAL RESULTS	94
4.1. GENERAL	94
4.2. TEST RESULTS AND OBESERVATIONS	94
4.2.1. Control specimen, BCJ-CS-A Test #1	94
4.2.2. Control specimen, BCJ-CS-A Test #2	98

4.2.3. Strengthened specimen, BCJ-SS-S4	103
4.2.4. Strengthened specimen, BCJ-SS-F4	107
4.2.5. Strengthened specimen, BCJ-SS-S8	111
4.2.6. Strengthened specimen, BCJ-SS-F8	116
4.2.7. Specimen with Adequately Designed Joint, BCJ-CS-B	120
4.3. ANALYSIS OF TEST RESULTS	126
4.3.1. Strength and Failure Modes	127
4.3.2. Key Observation Points of the Joints' Shear Behaviour	134
4.3.3. Stiffness and Energy Dissipation Characteristic	138
4.3.4. Beam Fixed-end Rotation	141
4.3.5. Strain Measurements	142
4.4. EFFECT OF TEST PARAMETERS	149
4.4.1. Effect of Shear Reinforcement Ratio	150
4.4.2. Effect of Strengthening Material	152
4.5. SUMMARY	155
CHAPTER 5.....	159
FINITE ELEMENT MODELLING OF EXTERIOR REINFORCED CONCRETE	
BEAM-COLUMN JOINTS	159
5.1. GENERAL	159
5.2. GEOMETRIC MODELLING, ELEMENT TYPE AND MESH	159
5.2.1. Concrete Joint and Loading Plates	160
5.2.2. Reinforcement Bars	161
5.2.3. Mesh	163
5.3. MATERIAL BEHAVIOUR	164

5.3.1. Concrete	164
5.3.2. Steel Reinforcing Bars	173
5.4. BOUNDARY CONDITIONS, CONSTRAINTS, ANALYSIS TYPE AND LOADING	174
5.5. VALIDATION	177
5.5.1. Control Specimen, BCJ-CS-A Test #2	177
5.5.2. Strengthened Specimen, BCJ-SS-S4.....	184
5.5.3. Strengthened Specimen, BCJ-SS-F4.....	191
5.6. PARAMETRIC STUDY	198
5.6.1. Effect of concrete compressive strength	198
5.6.2. Effect of column axial load	202
5.6.3. Effect of embedded bar sizes	205
5.7. SUMMARY	207
CHAPTER 6.....	210
SHEAR CAPACITY EVALUATION OF BEAM-COLUMN JOINTS STRENGTHENED WITH EMBEDDED BARS.....	210
6.1. GENERAL	210
6.2. MECHANICS OF REINFORCED CONCRETE JOINTS STRENGTHENED WITH EMBEDDED FRP BARS	210
6.2.1. Equilibrium Considerations	213
6.2.2. Analytical Evaluation of Joint Shear Capacity Strengthened with Deep Embedment Method	215
6.3. NUMERICAL SOLUTION AND VALIDATION	219
6.4. EXAMPLE FOR A JOINT	230

6.5. SUMMARY	234
CHAPTER 7.....	236
CONCLUSIONS AND RECOMMENDATIONS	236
7.1. GENERAL	236
7.2. CONCLUSIONS.....	237
7.2.1. Conclusions from the Literature Review	237
7.2.2. Conclusions from the Experiments	239
7.2.3. Conclusions from the Finite Element Analysis.....	242
7.2.4. Conclusions from the Analytical Model	244
7.3. RECOMMENDATIONS FOR FUTURE WORK	245
REFERENCES	247
APPENDICES	255

LIST OF TABLES

Table 2.1 Usual tensile properties of reinforcing bars (Reproduced from ACI 440, 2006).....	34
Table 2.2. Densities of reinforcing bars (gram/cm ³) (Reproduced from ACI 440, 2006).....	35
Table 2.3. Typical coefficients of thermal expansion reinforcing bars (Reproduced from ACI 440, 2006)	35
Table 2.4. Classification of manufacturing processes for FRP composites (Hollaway and Leeming, 1999).....	37
Table 3.1. Concrete material properties.....	75
Table 3.2. Steel reinforcement properties.....	76
Table 3.3. Details of tested beam-column joint specimens	79
Table 3.4. Details of beam-column joint specimens, dimensions and reinforcement	81
Table 4.1. Summary of test results for BCJ-CS-A test #1	94
Table 4.2. Summary of test results for BCJ-CS-A test #2	99
Table 4.3. Summary of test results for BCJ-SS-S4	103
Table 4.4. Summary of test results for BCJ-SS-F4	107
Table 4.5. Summary of test results for BCJ-SS-S8	112
Table 4.6. Summary of test results for BCJ-SS-F8	116
Table 4.7. Summary of test results for BCJ-CS-B	121
Table 4.8. Summary of test results	129
Table 4.9. Key response points for tested specimens	138
Table 5.1. Comparison of numerical and experimental key results for BCJ-CS-A Test #2 ..	179
Table 5.2. Experiment and FE peak load comparison for BCJ-CS-A Test #2	184
Table 5.3. Comparison of numerical and experimental key results for BCJ-SS-S4	186

Table 5.4. Experiment and FE peak load at specific drift ratio	190
Table 5.5. Comparison of numerical and experimental key results for BCJ-SS-F4	191
Table 5.6. Experiment and FE peak load at specific drift ratio	195
Table 6.1. Comparison of analytical model predictions with the experimental results from several researchers	227
Table 6.2. Comparison of analytical model predictions with the experimental results from Kaku and Asakusa (1991).....	228
Table 6.3. Comparison of analytical model predictions with experimental results from this experiment	229

LIST OF FIGURES

Figure 2.1. Damage to reinforced concrete moment framed building after Kocaeli earthquake, 1999 (Sezen et al. 2003)	9
Figure 2.2. Mechanisms of post-elastic deformation of moment resisting frames subjected to lateral load, after Hakuto et al. (2000)	11
Figure 2.3. Categories of beam column joint, after Priestley (1997)	13
Figure 2.4. Reinforcement details of Hakuto et al. (2000): (a) Details of specimens O6 and O7; (b) Observed cracking of specimen O6 towards the end of testing; (c) Observed cracking of specimen O7 towards the end of testing	15
Figure 2.5. Main mechanism of joint shear resistance of testing specimens by Hakuto et al. (2000).....	16
Figure 2.6. Experimental study by Clyde et al. (2000): (a) Reinforcement details of test specimen; (b) Damage to test specimen under $0.10f_c/A_g$ axial load level; (c) Damage to test specimen under $0.25f_c/A_g$ axial load level.	17
Figure 2.7. Experimental test by Pampanin et al. (2002): (a) Reinforcing detail of specimen T1; (b) Hysteretic curve and observed damage mechanism.	19
Figure 2.8. Development of concrete wedge mechanism.....	19
Figure 2.9. Experimental test by Parvin et al. (2010): (a) Reinforcing details and dimensions; (b) Crack pattern due to shear failure in the joint; (c) Crack pattern due to the slippage of the main beam bottom reinforcement.....	21
Figure 2.10. Internal forces and crack patterns after Parvin et al. (2010): (a) Pull direction of loading; (b) Push direction of loading.	22
Figure 2.11. (a) Geometry of tested specimens; and (b) Test setup by Genesio (2012)	23

Figure 2.12. Experimental study by Genesio (2012).....	24
Figure 2.13. Effect of axial load on joint shear strength, Hassan (2011)	26
Figure 2.14. Effect of axial load on principal tensile stress at peak shear strength of the joint, Hassan (2011)	26
Figure 2.15. Influence of concrete strength on joint shear stress observed at Point B and Point C, Kim and LaFave (2007)	28
Figure 2.16. Role of confinement to joint shear strength, Kim and LaFave (2007).....	29
Figure 2.17. Tensile properties for steel and FRP reinforcement (Guadagnini et al., 2003)....	34
Figure 2.18. Schematic of pultrusion process after GangaRao et al. (2007).....	36
Figure 2.19. Failure mode of strengthened specimens tested by Ghobarah and Said (2002) : (a) Shear failure mode of specimen rehabilitated using FRP without anchorage; (b) Ductile failure mode of specimen rehabilitated using FRP with cover plate and anchors through the joint	39
Figure 2.20. Specimen tested by Antonopoulos and Triantafillou (2003) : (a) Geometry of specimen with the presence of a transverse beam on joints T-C, T-F33 and T-F22S2; (b) Details of reinforcement.....	41
Figure 2.21. Proposed strengthening scheme by Antonopoulos and Triantafillou (2003) : (a) Description of specimens and strengthening alternatives; (b) Layout of FRP layers...	42
Figure 2.22. Dimensions and cross-sectional details of tested specimens, Tsonos (2008)	44
Figure 2.23. FRP jacketing strengthening schemes.....	45
Figure 2.24. Specimen tested by Karayannis and Sirkelis (2008) : (a) Reinforcement details; (b) Strengthening scheme using CFRP sheets	46
Figure 2.25. Reinforcement details of Alsayed et al. (2010) test specimens	48

Figure 2.26. CFRP application of strengthened specimen (Alsayed et al., 2010) : (a) Representation of scheme #1; (b) Representation of scheme #2.....	48
Figure 2.27. Failure mode of strengthened specimen after test (Alsayed et al., 2010): (a) Tearing and debonding of sheet of repaired joint ER1; (b) Beam failure of repaired joint ER2.....	49
Figure 2.28. Specimen details (Ilki et al., 2011): (a) Geometry of specimen; (b) Reinforcement details	50
Figure 2.29. Strengthening application (Ilki et al., 2011).....	51
Figure 2.30. (a) Cross section of test beams; (b) Test layout for the strengthened specimen (Valerio et al., 2009).....	53
Figure 2.31. Deep embedment strengthening procedure proposed by Valerio et al. (2009): (a) Schematic showing hole positions; (b) Epoxy adhesive was injected into the holes; (c) Embedded bars were inserted into the holes; (d) Layout of embedded bars on beam's cross section.....	54
Figure 2.32. Details of tested beams (Chaallal et al., 2011): (a) Elevation; (b) Cross section with no stirrups; (c) Cross section with stirrups	55
Figure 2.33. Load-displacement response of tested beams (Chaallal et al., 2011): (a) Series S0; (b) Series S1; (c) Series S3	56
Figure 2.34. Analytical model proposed by Pantazopoulou and Bonacci (1992): (a) Actions at the boundaries of the joint; (b) Stress equilibrium at vertical direction; (c) Stress equilibrium at horizontal direction	58
Figure 2.35. Analytical model proposed by Antonopoulos and Triantafillou (2002): (a) Moment and shear acting at joint; (b) Stress equilibrium at horizontal direction; (c) Stress equilibrium at vertical direction	59

Figure 2.36. Joint shear resistance mechanisms, Hwang and Lee (1999)	60
Figure 2.37. Comparison of damage propagation in the joint between the experiment and the FE model: (a) Experiment conducted by T. El-Amoury and Ghobarah (2002); (b) FE model by Danesh et al. (2008)	64
Figure 2.38. Geometry and reinforcement details of exterior beam-column joint tested by Bayasi and Gebman (2002)	65
Figure 2.39. FE analysis of Abbas et al. (2014): (a) Conventional steel reinforcement bars model; (b) Load-displacement hysteresis for the FE and experiment results	66
Figure 2.40. Contact pairs at the joint (Kam, 2014)	67
Figure 2.41. γ values for: (a) Type 1; and (b) Type 2 connections, ACI-ASCE 352R-02	71
Figure 3.1. Stress-strain curves	76
Figure 3.2. The dimensions of a typical specimen, unit in mm	78
Figure 3.3. (a) Reinforcement details of the test specimens; (b) Shear reinforcement in the joint for BCJ-CS-A and BCJ-CS-B; unit in (mm)	80
Figure 3.4. Construction details of beam-column joint specimens	83
Figure 3.5. Strengthening configuration	85
Figure 3.6. Experimental set-up – schematic drawing	87
Figure 3.7. 3D view of setup	88
Figure 3.8. Hydraulic jack used to apply axial load on the column	88
Figure 3.9. Column support	89
Figure 3.10. Loading history	90
Figure 3.11. Strain gauge locations	91
Figure 3.12. Shear deformation measurement on joint area	93
Figure 3.13. LVDT location	93

Figure 4.1. Damage propagation – BCJ-CS-A test#1	97
Figure 4.2. Load-displacement response of the control specimen BCJ-CS-A test #1.....	98
Figure 4.3. Damage propagation – BCJ-CS-A test #2	101
Figure 4.4. Load-displacement response of the duplicate control specimen, BCJ-CS-A test #2	102
Figure 4.5. Damage propagation – BCJ-SS-S4	105
Figure 4.6. Load-displacement response of the strengthened specimen BCJ-SS-S4	106
Figure 4.7. Damage propagation – BCJ-SS-F4	109
Figure 4.8. Load-displacement response of the strengthened specimen BCJ-SS-F4	111
Figure 4.9. Damage propagation – BCJ-SS-S8	114
Figure 4.10. Load-displacement response of the strengthened specimen, BCJ-SS-S8	115
Figure 4.11. Damage propagation – BCJ-SS-F8	118
Figure 4.12. Load-displacement response of the strengthened specimen, BCJ-SS-F8	120
Figure 4.13. Damage propagation – BCJ-CS-B	124
Figure 4.14. Load-displacement response of BCJ-CS-B.....	125
Figure 4.15. Forces acting on beam-column joint.....	126
Figure 4.16. Normalized principal tensile stress versus joint shear deformation for control specimens, BCJ-SS-S4 and BCJ-SS-F4	131
Figure 4.17. Normalized principal tensile stress versus joint shear deformation for specimen BCJ-SS-S8, BCJ-SS-F8 and BCJ-CS-B	132
Figure 4.18. Back bone curves of normalized principal tensile stress versus joint shear deformation for tested specimens	133
Figure 4.19. Load versus joint shear deformation for control specimens, BCJ-SS-S4 and BCJ-SS-F4	135

Figure 4.20. Load versus joint shear deformation for specimen BCJ-SS-S8, BCJ-SS-F8 and BCJ-CS-B	136
Figure 4.21. Back bone curves of load versus joint shear deformation for tested specimens	137
Figure 4.22. Comparison of normalized peak-to-peak stiffness.....	139
Figure 4.23. Comparison of energy dissipation.....	141
Figure 4.24. Envelope curves of normalized load-beam fixed-end rotation	142
Figure 4.25. Envelope curves of load-strain for column reinforcement.....	143
Figure 4.26. Envelope curves of load-strain: (a) Top beam reinforcement; (b) Bottom beam reinforcement.....	146
Figure 4.27. Envelope curves of load-strain for existing joints' shear reinforcement	147
Figure 4.28. Envelope curves of load-strain for embedded bars for: (a) Group B specimen; (b) Group C specimen	149
Figure 4.29. Enveloped curves of the normalized load-drift ratio of Group B and Group C: (a) Using steel bars; (b) Using CFRP bars	151
Figure 4.30. Envelope curves of the normalized principal tensile stress-drift ratio of Group B and Group C: (a) Using steel bars; (b) Using CFRP bars.....	152
Figure 4.31. Envelope curves of the normalized load-drift ratio of the strengthened specimens: (a) Using 4 embedded bars; (b) Using 8 embedded bars.....	153
Figure 4.32. Envelope curves of the normalized principal tensile stress-drift ratio of the strengthened specimens: (a) Using 4 embedded bars; (b) Using 8 embedded bars....	154
Figure 5.1. Geometric model of test specimen.....	160
Figure 5.2. Eight-node brick element.....	161
Figure 5.3. Elements to model reinforcement	162
Figure 5.4. Finite element mesh for all models	163

Figure 5.5. Assumed uniaxial stress-strain relation for concrete under compressive loading	166
Figure 5.6. Compression concrete model plotted using Equations (5-1) to (5-9)	169
Figure 5.7. Uniaxial stress-strain response of concrete in tension	170
Figure 5.8. Concrete material model under cyclic loading, Abaqus and Inc (2008).....	172
Figure 5.9. Material model for steel reinforcement bar.....	173
Figure 5.10. Symmetry boundary condition applied at mid-width of specimen	176
Figure 5.11. Load-displacement response for BCJ-CS-A Test #2: (a) 100 mm element size; (b) 50 mm element size; (c) 30 mm element size; (d) Envelope curves of FE analysis and experiment.....	178
Figure 5.12. Load-displacement response of the experiment and ABAQUS for BCJ-CS-A Test #2: (a) Hysteresis curves; (b) Envelope curves.....	180
Figure 5.13. Cumulative energy comparison.....	181
Figure 5.14. Comparison of crack propagation of BCJ-CS-A Test #2.....	182
Figure 5.15. (a) Principal compressive stress in concrete; (b) Tensile stress in reinforcement for BCJ-CS-A Test #2	183
Figure 5.16. Load-displacement response for BCCJ-SS-S4: (a) 100 mm element size; (b) 50 mm element size; (c) 30 mm element size; (d) Envelope curves FE analysis and experiment	185
Figure 5.17. Load-displacement response of experiment and ABAQUS for BCJ-SS-S4; (a) hysteresis curves; (b) Envelope curves.....	187
Figure 5.18. Cumulative energy comparison.....	188
Figure 5.19. Comparison of crack propagation of BCJ-SS-S4.....	189
Figure 5.20. (a) Principal compressive stress in concrete; (b) Tensile stress in reinforcement at 3% drift ratio of the strengthened specimen BCJ-SS-S4.....	190

Figure 5.21. Load-displacement response for BCCJ-SS-F4: (a) 100 mm element size; (b) 50 mm element size; (c) 30 mm element size; (d) Envelope curves FE analysis and experiment	192
Figure 5.22. Load-displacement comparison between experiment and ABAQUS for control specimen: BCJ-SS-F4 (a) Hysteresis loops; (b) Peak-to-peak	194
Figure 5.23. Cumulative energy comparison.....	194
Figure 5.24. Comparison of crack propagation of BCJ-SS-F4.....	196
Figure 5.25. (a) Principal compressive stress in concrete; (b) Tensile stress in reinforcement at 3% drift ratio of the strengthened specimen BCJ-SS-F4.....	197
Figure 5.26. Effect of concrete compressive strength on the normalized joint principal tensile stress at Points A and C for: (a) Duplicate control specimen, BCJ-CS-A; (b) BCJ-SS-S4; (c) BCJ-SS-F4	201
Figure 5.27. Effect of axial load on the normalized joint principal tensile stress at Points A and C.....	204
Figure 5.28. Effect of embedded bar sizes on the normalized joint principal tensile stress at Points A and C	206
Figure 6.1. Idealisation of external beam-column joint, modified after Akguzel (2011): (a) Moments and shear forces acting on the boundaries of the plane frame element; (b) Kinematics and compatibility condition in joint region; (c) Mohr's circle for average stresses	212
Figure 6.2. Joint stress equilibrium on joint with embedded bars, modified after Antonopoulos and Triantafillou (2002).....	213
Figure 6.3. Reinforcement detail for beam-column joint specimen, Tsonos et al. (1992).....	222
Figure 6.4. Joint dimensions and details used in the design example, unit in mm.....	231

NOTATION

Chapter 2

h_b	=	The distance between the extreme longitudinal reinforcement in the beam
h_c	=	The distance measured from the centroid of extreme longitudinal reinforcement in the column to the centroid of bar extension at the free end of the 90-degree hooked bar
A_{str}	=	The diagonal strut effective area
a_s	=	The depth of the diagonal strut
b_s	=	the width of the diagonal strut
a_b	=	the depth of the compression zone in the beam
a_c	=	the depth of the compression zone in the column
D	=	Diagonal shear force mechanism
F_h	=	Horizontal shear force mechanism
F_v	=	Vertical shear force mechanism
f_c	=	Concrete cylinder compressive strength
A_{sh}	=	Total cross-sectional area of rectangular hoop reinforcement
A_g	=	Gross area of concrete section
A_{ch}	=	Cross-sectional area of a member measured to the outside edges of transverse reinforcement
s	=	Centre-to-centre spacing of transverse reinforcement
b_c	=	Cross-sectional dimension of member core measured to the outside edges of the transverse reinforcement
V_n	=	Nominal joint shear strength
A_j	=	The effective joint area

Chapter 3

f_c	=	Concrete cylinder compressive strength
f_t	=	Concrete tensile strength
f_y	=	Yield strength of the steel reinforcement
f_u	=	Ultimate strength of the steel reinforcement
E_s	=	Elastic modulus of the steel reinforcement
A_g	=	Column cross-sectional area
L	=	The distance from the reversal cyclic loading point to the column face
l	=	The initial distance between the mounting rods of the LVDT
h_b	=	The beam depth

Chapter 4

p_t	=	Principal tensile stress
p_c	=	Principal compressive stress
f_a	=	Column axial compressive stress
N_c	=	Column axial compressive load
h_c	=	Column depth
w_c	=	Column width
V_{jh}	=	Horizontal shear force acting across joint region
v_{jh}	=	Joint horizontal shear stress
T_b	=	Tensile force at beam bars
V_b	=	Beam shear force
L_b	=	Beam length

Chapter 5

E_{ci}	=	The concrete secant modulus from the origin to the peak compressive stress
f_{cm}	=	The mean compressive strength
G_{cl}	=	The localized crushing energy
l_{eq}	=	The characteristic length of the respective FE integration point

b	=	A material parameter with a value range of $0 < b \leq 1$
f_{ct}	=	Concrete tensile strength
G_f	=	Fracture energy
d_t	=	Concrete tension damage parameter
d_c	=	Concrete compression damage parameter

Chapter 6

N_v	=	The concrete secant modulus from the origin to the peak compressive stress
V_b	=	Beam shear force
M_j	=	Equivalent joint moment
M_c	=	
M_b	=	
w_c	=	Column width
h_c	=	Column depth
w_b	=	Beam width
h_b	=	Beam height
f_t	=	Average stress in the horizontal direction at midwidth of the joint
f_{Ft}	=	Average normal stress in embedded bar at midwidth of joint
N_h	=	Compressive axial stress of the beam, usually $N_h = 0$
f_l	=	Average stress in the longitudinal reinforcement (at midwidth of the joint)

Chapter 2

θ	=	Angle of inclination of diagonal compression strut
ζ	=	Softening coefficient at concrete softened-compressive strength
ε_r	=	Average strain of cracked concrete

Chapter 3

δ	=	Vertical displacement of the beam-end
γ	=	Joint shear deformation
α	=	The initial inclination of the LVDTs to the horizontal or vertical
θ	=	The angle of beam rotation
δ_l	=	Displacement measured on the bottom beam side
δ_2	=	Displacement measured on the top beam side

Chapter 4

μ	=	Displacement ductility
Δ_u	=	Beam tip displacement at the load step corresponding to 20% reduction in ultimate load
Δ_y	=	The displacement of the reduced stiffness equivalent elasto-plastic yield

Chapter 5

σ_{bo}	=	Initial equibiaxial compressive yield stress of concrete
σ_{co}	=	Initial uniaxial compressive stress
$\sigma_{c(1)}$	=	The concrete stress in elastic region
ε_c	=	The concrete strain
$\sigma_{c(2)}$	=	The concrete stress in hardening region
ε_{ci}	=	The concrete strain at the peak stress
$\sigma_{c(3)}$	=	The concrete stress in softening region
ε_{cr}	=	The concrete cracking strain

Chapter 6

θ	=	Angle of the first principal stress direction from the longitudinal t -axis
ε_1	=	Maximum principal strain in the joint panel
ε_2	=	Minimum principal strain in the joint panel
ε_t	=	Average strain along the direction t of the joint panel
ε_l	=	Average strain along the direction l of the joint panel
σ_t	=	Average normal concrete stress the t -direction
σ_l	=	Average normal concrete stress the l -direction
v	=	Average joint shear stress
σ_1	=	Maximum principal stress in the concrete
σ_2	=	Minimum principal stress in the concrete
ρ_s	=	Stirrup reinforcement ratio
ρ_b	=	Total main beam reinforcement ratio
β_t	=	Factor with values between 0 and 1, relating the magnitude of stresses in the main beam reinforcement ratio
ρ_{Ft}	=	Embedded reinforcement ratio in the transverse direction
ρ_c	=	Total main column reinforcement ratio at the boundaries of the joint core
$\rho_{c,in}$	=	Total main column reinforcement ratio inside the joint core
β_l	=	Factor that relates the magnitude of stress (or strains) in the column reinforcement outside the core to the average stresses of the reinforcement inside the core at the beam centerline
ρ_t	=	Effective horizontal reinforcement ratio
ρ_l	=	Effective vertical reinforcement ratio

CHAPTER 1

INTRODUCTION

1.1. GENERAL

The recent spate of large earthquakes in Indonesia (Aceh 2004, Nias 2005, Padang and Tasikmalaya 2009) and in many parts of the world had devastating consequences. In Padang earthquake (2009), for instance, with the nature of its buildings and large population, there were an estimated 250,000 families affected through the loss of their homes or businesses (Griffith et al., 2010). Situated on the west coast of Sumatra, Padang is one of the most seismically active regions of the world. An investigation conducted into the collapsed buildings showed that poorly designed concrete members and the lack of shear reinforcement in the joint were observed, even in the buildings that were constructed since the introduction of the Indonesia Reinforced Concrete Building Code (SNI 2002).

There are several techniques have been developed to enhance the performance of under-designed reinforced concrete (RC) buildings. The use of RC jackets as a technique in strengthening RC structures has been practiced for two decades. The strengthened elements, e.g. beams, columns or beams along with the joint regions, were encased using high-strength concrete and reinforced with transverse reinforcement and, where possible, the longitudinal reinforcement bars were extended around the joint to strengthen the column joint (Dritsos, 2005). It has been experimentally demonstrated that the RC jacketing technique increases strength, stiffness and energy dissipation capacity, as well as shifting the failure to the beam (Tsonos, 1999). Even though this strengthening method became the most favourable choice of

engineers, it is obvious that this technique involves labour-intensive work; such as drilling through the beams and cutting through the floor slab, as well as the in-plane bending of the added transverse reinforcement. Also by altering the dynamic characteristic of the building, careful re-analysis of the entire structure should be encouraged in applying this technique (Karayannis and Sirkelis, 2008). Another technique for upgrading the performance of RC members is the application of fibre reinforced polymers (FRPs). They have higher strength-to-weight ratios when compared to conventional construction materials. Numerous research projects on upgrading existing RC beam-column joints have focused on the use of FRP composites. This strengthening technique eliminates many of the previously mentioned important limitations that concrete jacketing induces.

1.2. RESEARCH SIGNIFICANCE

Beam-column joints play an important role in the seismic performance of moment-resisting RC frame structures. Without proper design and detailing of the joint shear reinforcement, as is the case with RC buildings designed according to the pre-1970s' building codes, RC connections can be the most vulnerable elements during an earthquake and can undergo shear failure in the joint. Practical and effective techniques are therefore required for strengthening shear-deficient RC beam-column joints.

When un-anchored externally bonded (EB) or near-surface mounted (NSM) FRP reinforcement is used, de-bonding, which is attributable to the low tensile strength of the concrete cover, takes place at a stress level of 20 to 30% of the ultimate tensile strength of the FRPs (Dirar et al., 2012). Furthermore, the application of EB or NSM FRP strengthening

systems requires surface preparation and protection against vandalism and fire. To overcome these shortcomings, the deep embedment (DE) FRP strengthening technique was developed for shear strengthening of concrete beams (Valerio et al., 2009). The DE technique provides higher strengthening effectiveness because it relies on direct transfer of stresses from the FRP to the core of concrete; unlike the EB and NSM FRP techniques. Moreover, surface preparation and protection against fire and vandalism are not required.

The use of FRP as a strengthening material is favourable because of many advantages such as: its high strength-to-weight ratio, high corrosion resistance, no significant increase in member size, easy applicability and limited disruption to building occupancy (Engindeniz et al., 2005). In addition, the wide use of this material to strengthen the elements of the structure of buildings and bridges, has addressed its efficiency and its convenience (Bakis et al., 2002). However, experimental results have shown that FRP de-bonding remains the main drawback and prevents the utilisation of the high tensile strength of the FRPs. This failure is related to the relatively low tensile strength of the concrete cover and so it does not constrain the bonding force between the FRP and the concrete (Mofidi and Chaallal, 2011).

1.3. PROBLEM DEFINITION

On a typical moment-resisting frame, three types of beam-column joint can be identified: interior, exterior and corner. The exterior beam-column joints are considered the most critical elements during an earthquake due to the following reasons:

- a) They are more crucial than the other types of joints due to the confinement provided by transverse beams or slabs is limited compared to the interior joint.

- b) The anchorage length of the beam bars inside the exterior joint is limited, compared to the interior joints where the bars will continue through the joint.
- c) Any damage occurring in the interior or exterior joints will affect the integrity of the whole frame, compared to the local influence of the corner joints.

A poorly designed joint with a lack of adequate transverse reinforcement, will experience concrete shear failure in the form of diagonal tension and bond failure of the rebar (especially for interior joints); where the steel reinforcement was not properly anchored with standard hooks (Paulay and Priestley, 1992). If the frame of the building has remained intact, many of the beam-column joints are distressed due to the lack of joint reinforcement and this threatens the integrity of building (Akguzel, 2011).

On the other hand, strengthening of RC joints is a challenging task and poses major practical difficulties. RC jackets and steel jackets are among the strengthening methods that have been widely used for decades. However, these techniques have been criticized for being labour intensive and complicated details. Moreover, the use of concrete jackets increases the dimensions and self-weight of structural elements. These strengthening techniques have been revised and developed to meet the new seismic code requirements; while some others have been developed based on new materials, such as FRP (Thermou and Elnashai, 2006).

1.4. ORIGINALITY, AIMS AND OBJECTIVES

For the first time, this research explores the application of the DE technique for strengthening a shear-deficient RC beam-column joint. In this study, two materials: carbon FRP (CFRP) bar and steel bar were considered for an embedded strengthening system.

This research aims to provide a fundamental understanding of the seismic response of shear critical exterior RC beam-column joints strengthened using the deep embedment (DE) method. The objectives of this research can be summarised as follows:

- (i) To find out the main mechanisms of failure of deficient exterior RC beam-column joint and assess the efficiency of existing strengthening methods utilising FRP material.
- (ii) To propose a deep embedment strengthening technique for the shear deficient exterior RC beam-column joints.
- (iii) To study the effect of embedded bar type, steel and CFRP bars as additional joint shear reinforcement.
- (iv) To enrich the general understanding and develop a test database of RC beam-column joints strengthened with the deep embedment system.
- (v) To identify the effect of axial column load level, concrete strength and additional joint reinforcement ratio on the seismic response of RC beam-column joints.
- (vi) To develop and validate an analytical joint shear strength evaluation of RC beam-column joints strengthened with deep embedding bars.

1.5. RESEARCH METHODOLOGY

The behaviour of deficient joints and the effectiveness of strengthening methods were studied through a review of the published literature. In order to meet the objectives outlined above, two approaches: experimental and finite element studies were conducted. Experimental work was used to evaluate the effects of the type of embedded bars; steel and CFRP bars were investigated on an experiment. The study contains the fabrication and testing of seven exterior RC beam-column joints. Two types of load were applied during the tests. The first one is constant axial load acting on the upper part of the column and the second one is a reversal

quasi-static load applied at the beam end. Variables considered during this experimental study are: the type of material used for the embedded joint reinforcement (steel and CFRP bar) and the ratio of the embedded joint reinforcement.

The effects of axial load, concrete strength and embedded bar size were assessed in a finite element study. It includes the construction of a finite element model for beam-column joints using ABAQUS software to simulate the behaviour of the tested specimens. The result from this model was validated against the result from the experimental study. Then the validated model was used to conduct a parametric study on the parameters that affect joint strength; including column axial load level, concrete compressive strength and embedded bar size.

Finally, an analytical model was developed to determine the joint shear strength of unstrengthened and strengthened beam-column joints.

1.6. THESIS LAYOUT

This thesis is divided into seven chapters. The contents of each chapter are as follows:

- a. Chapter 1 provides an introduction to the role of the existing RC frames under subjected reversed cyclic load and the drawbacks of the existing FRP retrofitting technique. This chapter also contains the aims and objectives of this research as well as the research methodology.
- b. Chapter 2 contains literature reviews for substandard RC beam-column joints. Attention is given to the failure mechanism of exterior joints extracted from recent earthquakes and experimental results from previous researchers. Research studies conducted on the

strengthening of exterior RC joints using various FRPs' products, along with different kinds of techniques are also presented.

- c. Chapter 3 provides the details of the experimental program followed; e.g. material properties, test specimens, instrumentation, test set-up and loading procedures. In addition to this, the proposed strengthening method using a deep embedment technique is also introduced in this chapter.
- d. Chapter 4 gives the experimental results from the work conducted on unstrengthened and strengthened specimens. This is followed by analysis and discussion of the test results in terms of cracking pattern, failure modes, joint shear deformation, cumulative energy dissipation and strain measurements under reversed cyclic loading.
- e. Chapter 5 presents the details of the finite element modelling using ABAQUS software; including element types, material constitutive models and the geometry and boundary conditions. These results were verified against the experimental results from Chapter 4. The FE models are then used for parametric study on parameters that affect joint strength. In this study, three parameters are considered: column axial load level, concrete compressive strength and embedded bar size.
- f. Chapter 6 contains an analytical evaluation for determining the joint shear strength of unstrengthened and strengthened RC joints using the deep embedment method. The accuracy of the analytical formulation developed in this chapter is checked against the test results from the unstrengthened exterior RC joint tests available from the literature and also tests conducted in this study. The same formula is also employed to determine the joint shear capacity of the strengthened joints used in this study.
- g. Chapter 7 compiles the conclusions obtained from this research. Recommendations for future research are also included in this chapter.

CHAPTER 2

LITERATURE REVIEW

2.1. GENERAL

Post-earthquake inspections of collapsed buildings (i.e., Kocaeli, Turkey, 1999 and Padang, Indonesia, 2009) revealed that damage was attributed to the poor quality of the construction practices employed. In some cases, residential and commercial buildings were constructed using substandard seismic details. The use of short columns; non-symmetric unreinforced masonry infill walls, which led some slender columns to behave as short columns or created a soft storey on the ground floor; absence of or inadequate capacity design that promoted a column sway mechanism, particularly on lower floors, and lack of shear reinforcement in the joint were some of the causes for the collapse of buildings in the region affected by the earthquake (Sezen et al., 2003). The collapse of or severe damage to buildings within the earthquake region due to inadequate joint resistance highlighted the pronounced adverse effect of inadequate beam-column joints on the seismic response of RC framed buildings.

An example of structural damage of beam-column joints in typical RC framed buildings affected by the Kocaeli earthquake in 1999 is seen in Figure 2.1 which shows that both the beam and the column elements were still intact but the joints were heavily damaged. A closer look at the beam-column joint depicted in Figure 2.1.(b) reveals insufficient anchorage length of the beam reinforcement in the joint area and the absence of transverse reinforcement in the joint. As shown in Figure 2.1.(c), where a building under construction is depicted, transverse

reinforcement in the joint region is beneficial, as horizontal ties have maintained the integrity of the joint.



(a) Failure of beam-column joint

(b) Close-up of beam-column joint failure

(Image source: <http://nisee.berkeley.edu/elibrary/Image/IZT-673>)



(c) Damage to beam-column joint of building under construction in Adapazari, Turkey

(Image source: <http://nisee.berkeley.edu/elibrary/Image/IZT-749>)

Figure 2.1. Damage to reinforced concrete moment framed building after Kocaeli earthquake, 1999 (Sezen et al. 2003)

Major drawbacks of pre-1970s RC structures exposed by recent earthquakes can be classified as column deficiencies, beam deficiencies and overall frame deficiencies. They are summarised by Faison et al. (2004) as follows:

- Column deficiencies comprise (a) shear links with 90 degree hooks; (b) shear link spacing too large to provide enough confinement; (c) lap splices positioned above floor slab within high moment regions and with insufficient length to provide adequate force transfer; and (d) large shear link spacing at lap splice locations.
- Beam deficiencies comprise (a) transverse shear ties with open-loop stirrup and 90 degree hooks; (b) large transverse shear tie spacing; (c) small diameter transverse reinforcement not designed to accommodate earthquake effects; (d) absence of stirrups at the mid-span of beams; (e) top longitudinal reinforcement discontinued at the beam mid-span and hence unable to accommodate cyclic loading; (f) insufficient anchorage length of bottom longitudinal reinforcement, i.e. discontinued at the column face or positioned only slightly within the beam-column joint; and (g) longitudinal steel reinforcement at end frames terminating without hooks or with hooks that are bent out of the joint core, so it does not provide adequate development length and continuity.
- Frame deficiencies comprise (a) weak column/strong beam behaviour leading to soft storey collapse; (b) shear capacity less than that required to form both beam and column plastic hinges; (c) beam-column joints with inadequate shear capacity; (d) beam-column joints with inadequate confinement; (e) beams eccentrically framing to the columns; (f) insufficient anchorage length of bottom slab reinforcement which does not pass through the column reinforcement in interior flat slab/column frames; and (g) overly stiff vertical load resisting systems that have inadequate deformation compatibility with lateral force resisting systems.

Understanding post-elastic behaviour of non-linear RC structures has brought a significant development to their design and detailing of RC structures. In order to ensure proper balance of flexural strength between appointed plastic hinge regions and other failure modes, the capacity design principle was developed (Park and Paulay, 1975).

According to capacity design principles, the earthquake resistance of moment resisting frames in critical regions is designed in such a way that energy is dissipated in a controlled and predictable fashion. The required displacement ductility factor in the post-elastic range during a major earthquake is designed to suit the most desirable structural mechanism so that flexural yielding occurs at appointed plastic hinge positions. All other regions in the structure are designed to not fail in shear and/or due to loss of reinforcement anchorage prior to the formation of the plastic hinges at the desired locations.

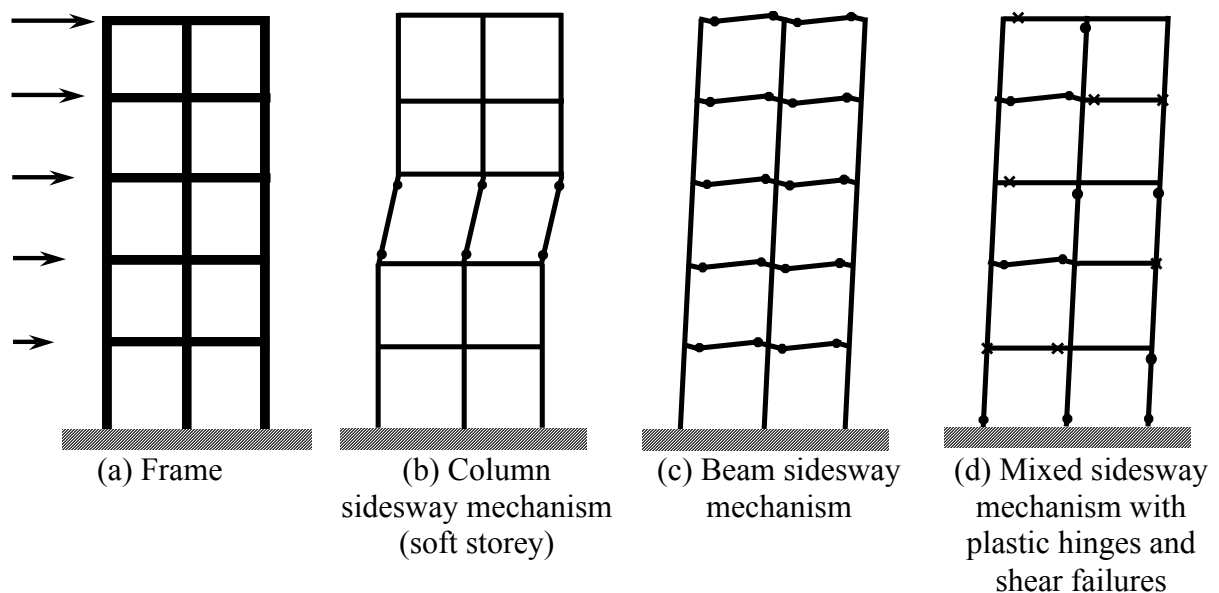


Figure 2.2. Mechanisms of post-elastic deformation of moment resisting frames subjected to lateral load, after Hakuto et al. (2000)

In order to accommodate the inelastic deformation demand at plastic hinge regions, sufficient ductility has to be provided through appropriate detailing. Ductility is defined as the ability to undergo large inelastic deformations without significant reduction in strength. All other potentially brittle regions are protected against premature failure, such as shear and anchorage failure under seismic loading, by designing not according to the applied loads but according to the moment and shear consistent with the formation of plastic hinges. In RC frame structures, ductility leads to stable hysteresis loops developed at the plastic hinges which are designed to be located in the beams. In this way, stable and large hysteretic energy can be dissipated in the plastic hinges without significant loss of resistance while the rest of the structure remains undamaged (Park and Paulay, 1975).

The formation of the plastic hinges in the beams is considered preferable to the formation of the plastic hinges in the column because:

- i) Columns have inherently lower ductility capacity than beams because they are subjected to high compressive stresses;
- ii) The ductility demand for a column mechanism is higher than for a beam mechanism for the same level of dissipated energy, since a column mechanism is confined in one storey only, whereas a beam mechanism spreads throughout the entire frame;
- iii) The formation of a column mechanism leads to pronounced $p-\delta$ effects which compromise the overall integrity of the building.

In typical pre-1970s design practice the column might be designed for a seismic load combination, without taking into account the moment capacity of adjacent beams, thus resulting in columns weaker than the beam and promoting the formation of a column sway

mechanism in the structure (Figure 2.2.(b)). The capacity design principle has been incorporated into current seismic design codes (i.e. ACI 318, Eurocode 8, and Australian/New Zealand Standard AS-NZS 1170-2) and dictates that a beam sway mechanism (Figure 2.2.(c)) is implemented rather than a column sway mechanism. In order to achieve this, beams are designed to be weaker than columns, which is generally referred to as strong column-weak beam design.

2.2. SEISMIC PERFORMANCE OF EXISTING EXTERIOR REINFORCED CONCRETE BEAM-COLUMN JOINTS

Joints can be classified into several types based on the kinematic constraints of surrounding members and their response to seismic actions. Figure 2.3 shows the difference between interior and exterior joints. Figure 2.3.(a) depicts a typical frame, in which two perimeter beams and one interior beam are converging. The joint is considered as an interior joint for loading in the plane of the frame, but it can be considered as an exterior joint in the orthogonal direction as suggested by the dashed line. Figure 2.3.(b) shows an internal joint in which four beams are converging and which may be subjected to seismic response as interior joints in either or both of the two orthogonal directions, and Figure 2.3.(c) shows a corner joint in which two perimeter beams orthogonal to each other are converging (Priestley, 1997).

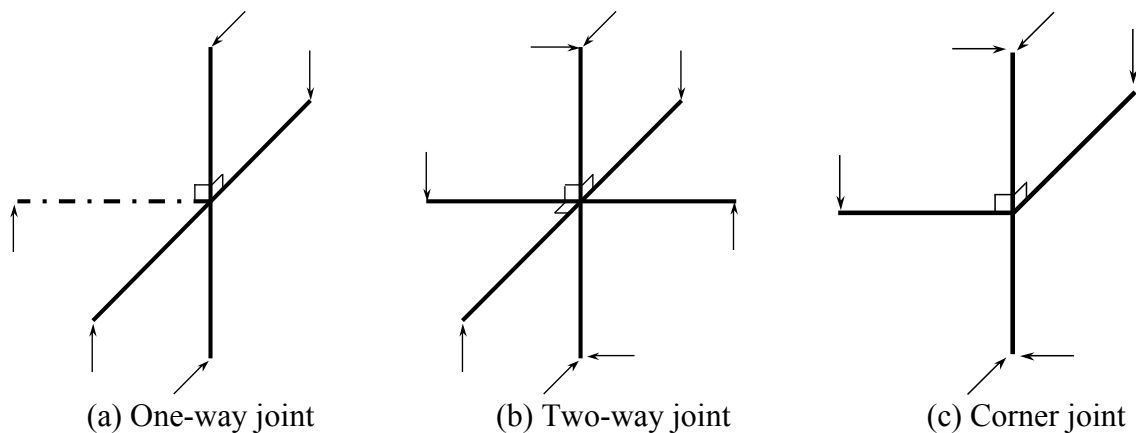


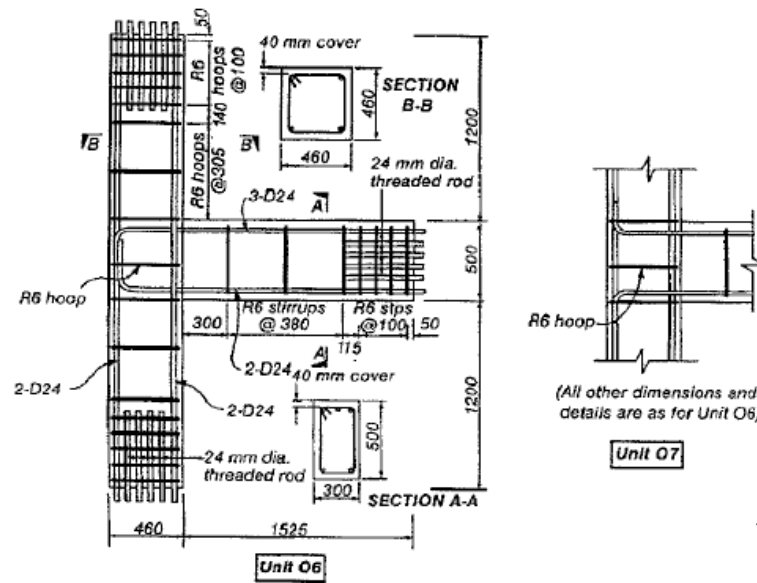
Figure 2.3. Categories of beam column joint, after Priestley (1997)

RC frame structures designed before the 1970s are considered to have substandard detailing compared to structures designed according to current seismic design criteria. Field reports also indicate that beam-column joints are one of the most critical structural elements, often vulnerable to shear and/or bond (anchorage) failures that can cause partial or total collapse of the structure. It is also well recognised that beam-column joints play an important role in maintaining the structural integrity of the frame under seismic action.

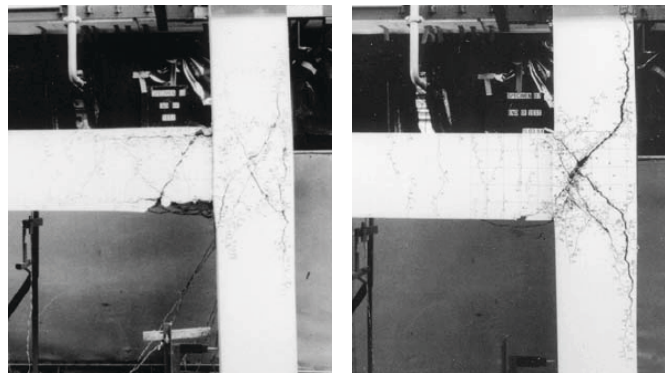
Exterior RC beam-column joints with little or no transverse reinforcement in the joint region have been extensively studied with the focus being on their seismic performance and failure mechanism. In this section, a review of relevant experimental studies on the structural response of exterior beam-column joints subjected to cyclic lateral load is given.

Hakuto et al. (2000) conducted tests on two full-scale exterior beam-column joints, designated as O6 and O7, emulating the RC frames with substandard details constructed in New Zealand in the 1950s (Figure 2.4.(a)). The longitudinal reinforcement bars of the beam of specimen O6 were bent into the joint core and extended to a distance of $12d_b$ (d_b =diameter of longitudinal bar in beam) as required by the NZS 3101:1995, while the reinforcement bars of specimen O7 were bent out of the joint core and the hook tails extended to a distance of $4d_b$ as required by the New Zealand standard in the 1950s. The beam-column joint transverse reinforcement comprised one 6 mm diameter closed stirrup. Both specimens were tested under a cyclic point load applied to the beam end simulating seismic actions; there was no axial load applied to the column during these tests. Test results showed that the performance of specimen O6 was significantly improved compared to that of specimen O7 where the hooks of the beam bars were bent out of the joint core. Specimen O7 failed in shear at a maximum nominal joint

horizontal shear stress of $0.045f_c'$ while specimen O6 was capable of withstanding nominal joint horizontal shear stresses up to $0.053f_c'$ which corresponded to the formation of a plastic hinge at the beam end (Figure 2.4.c), thus exhibiting an increased capacity of 18% compared to that of specimen O7, the failure of which occurred in the joint region with little signs of damage to the beam.



(a)



(b)

(c)

Figure 2.4. Reinforcement details of Hakuto et al. (2000): (a) Details of specimens O6 and O7; (b) Observed cracking of specimen O6 towards the end of testing; (c) Observed cracking of specimen O7 towards the end of testing.

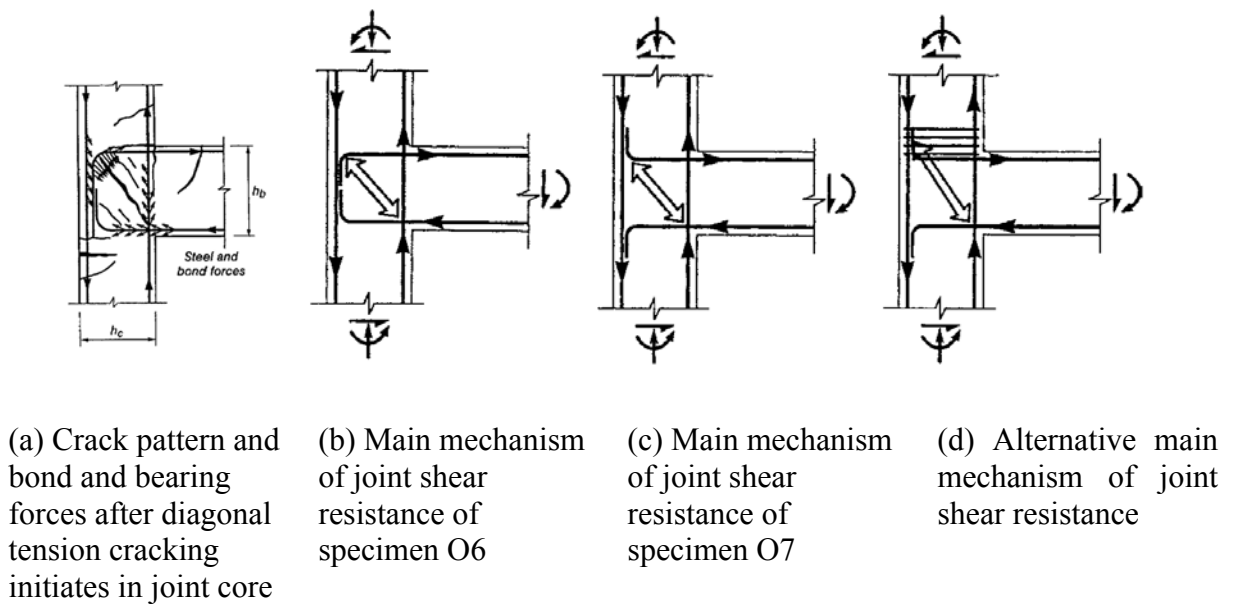


Figure 2.5. Main mechanism of joint shear resistance of testing specimens by Hakuto et al. (2000)

Figure 2.5.(a) shows internal forces acting on exterior RC beam-column joints under cyclic loading. The beam and column forces are transferred across the joint core through a diagonal compression strut after the joint diagonal tension cracking is initiated. In the case of pre-1970s construction practice, as depicted in Figure 2.5.(c), the effective node point at the top of the diagonal compression strut is not developed unless a considerable number of column hoops was placed above the joint core to resist the horizontal component of the compression strut (Figure 2.5.(d)).

The authors also discussed an assessment method based on limiting the shear strength of a joint to that corresponding to the onset of initial cracking in the joint panel. Although this approach seems to be valid for the assessment, this criterion may be overly conservative due to the fact that the joint core may be capable of transferring significantly higher shear forces after diagonal tension cracking occurs, by means of a diagonal compression strut. The joint, however, does not necessarily reach its maximum lateral load-carrying capacity when

diagonal cracking first occurs. Nonetheless, diagonal tension is important because the tensile strains perpendicular to the concrete diagonal compression strut will weaken the compressive strength of the strut. In this case, $k_1 f_c'$ can be used as a diagonal tension criterion, since the tensile strength of the concrete is a function of f_c' where the k factor is obtained from experimental testing and f_c' is the concrete compression strength. Diagonal compression failure is assumed to occur when a limiting joint shear stress $k_2 f_c'$ is reached. This would appear to be a more appropriate failure criterion for the joint than a failure criterion based solely on the nominal level of the applied shear stress, since the effect of column axial load on the joint strength would be explicitly accounted for.

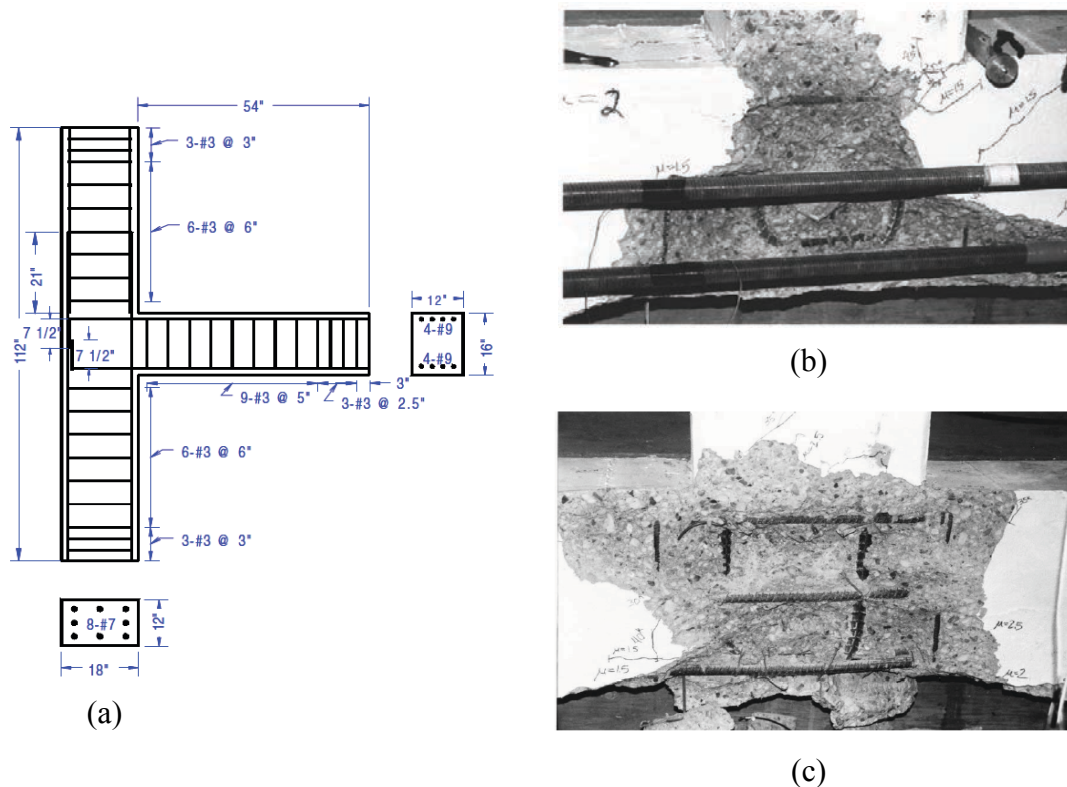


Figure 2.6. Experimental study by Clyde et al. (2000): (a) Reinforcement details of test specimen; (b) Damage to test specimen under $0.10f'_c A_g$ axial load level; (c) Damage to test specimen under $0.25f'_c A_g$ axial load level.

Four half-scale RC exterior joints were tested by Clyde et al. (2000) to study their behaviour in shear-critical mode. The specimens were designed in accordance with buildings constructed in the 1960s and hence they did not comply with the current seismic design specifications. No joint stirrup was provided within the joint core and the beam longitudinal reinforcement bars were not adequately anchored in the connection. The beam-column joint specimens were subjected to quasi-static cyclic loading applied at the beam end. A constant axial compressive force, equal to $0.1f_c A_g$ for the first two specimens and $0.25f_c A_g$ for the remaining ones, was applied at the top of the columns. Details of the specimens and the damage to the joints at the end of the tests are given in Figure 2.6. It was observed from the test results that the beam-column joints subjected to a lower axial load were over one and a half times more ductile than the beam-column joints subjected to higher column compression. On the other hand, higher axial load levels also improved the shear capacity of the joint. There was an increase of 8% in joint shear capacity as a result of increasing confinement due to axial compressive load.

Pampanin et al. (2002) presented results from a series of tests conducted on 2/3 scaled beam-column subassemblies subjected to a combination of reversed cyclic lateral loading and constant axial load acting on the column. The test specimens were designed for gravity loads only to comply with the Italian construction practice during the 1950s and 1970s. The reinforcing details of the specimens were characterised by the use of smooth bars; the absence of transverse reinforcement in the joint region; poor anchorage of the beam longitudinal bars; and the lack of any capacity design principles (Figure 2.7.(a)). The tested specimens exhibited a brittle hybrid failure mechanism in the form of shear damage in the joint area, combined with slippage of the beam longitudinal reinforcing bars within the joint region and high

compressive stresses concentrated in the vicinity of the anchorage. This resulted in the expulsion of a concrete wedge; spalling of the concrete cover on the outer face of the column; localised failure of the column in the joint region; and a significant loss of the column load-bearing capacity (Figure 2.7.(b)). The development of the concrete wedge mechanism is illustrated in Figure 2.8.

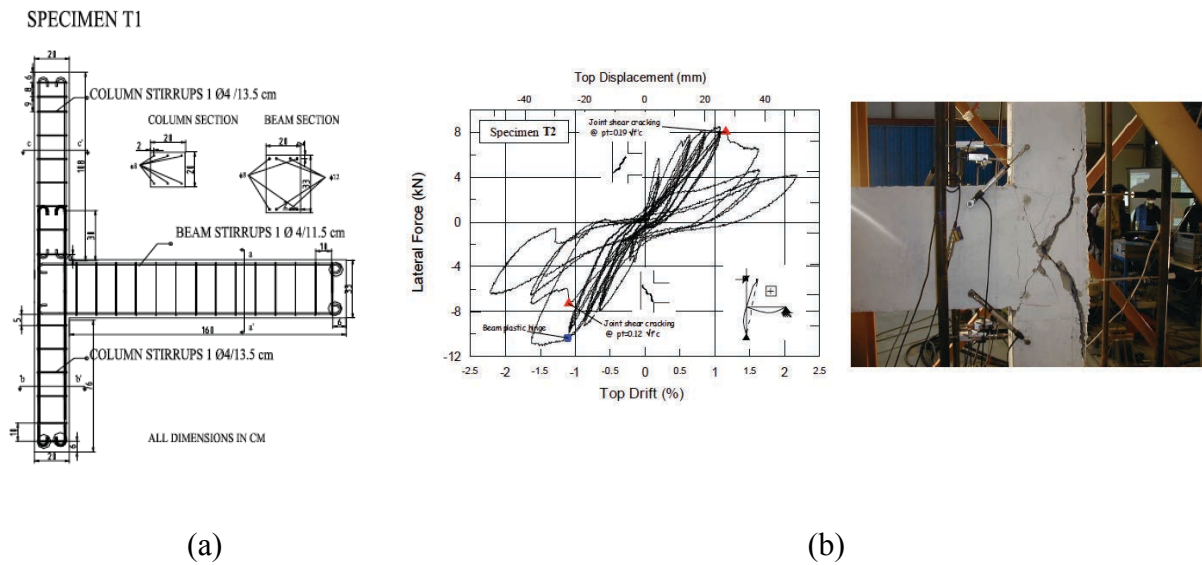


Figure 2.7. Experimental test by Pampanin et al. (2002): (a) Reinforcing detail of specimen T1; (b) Hysteretic curve and observed damage mechanism.

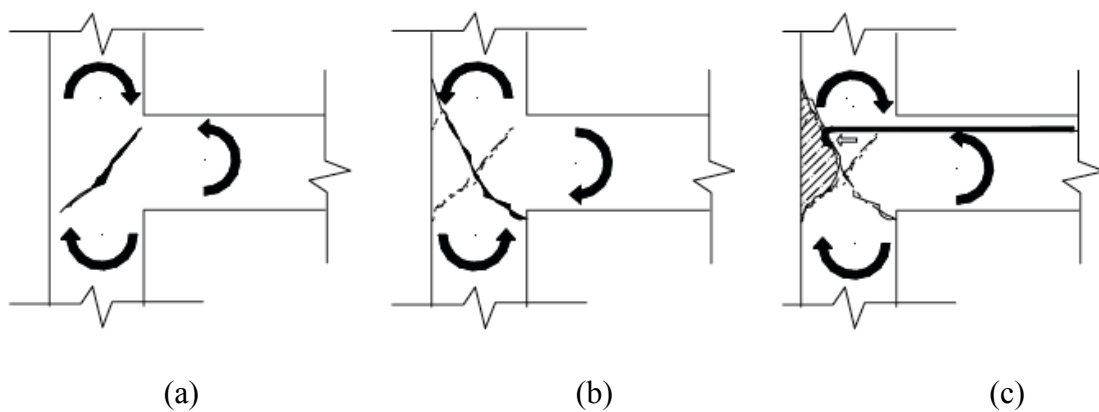


Figure 2.8. Development of concrete wedge mechanism

Parvin et al. (2010) conducted an experimental study on non-seismically designed RC beam-column joints subjected to cyclic loading. Three full-scale beam-column joints were fabricated to represent typical pre-1970s RC structures that were built without considering any seismic design provisions. The first specimen, designated as US2, had continuous longitudinal reinforcement bars in the column and was tested under cyclic loading, whilst subjecting the column to 24% of its axial capacity. The remaining specimens, namely US3 and US4, had a column lap splice just above the joint and were subjected to 24% and 12% of the column axial capacity respectively, prior to the application of the cyclic load. No ties were installed in the joint core and the main beam bottom reinforcements bars had a short embedment length of 150 mm in the joint region, a configuration commonly encountered in buildings constructed prior to the application of seismic design specifications. Two modes of failure were observed, namely shear failure in the joint (Figure 2.9.(b)) and slippage of the reinforcement bars at the bottom of the main beam (Figure 2.9.(c)). It was concluded from the test results that the slippage of the main beam bottom reinforcement was more critical than the shear failure in the joint, resulting in a lower lateral load carrying capacity and lower stiffness, and leading to a sudden loss of stiffness in all specimens.

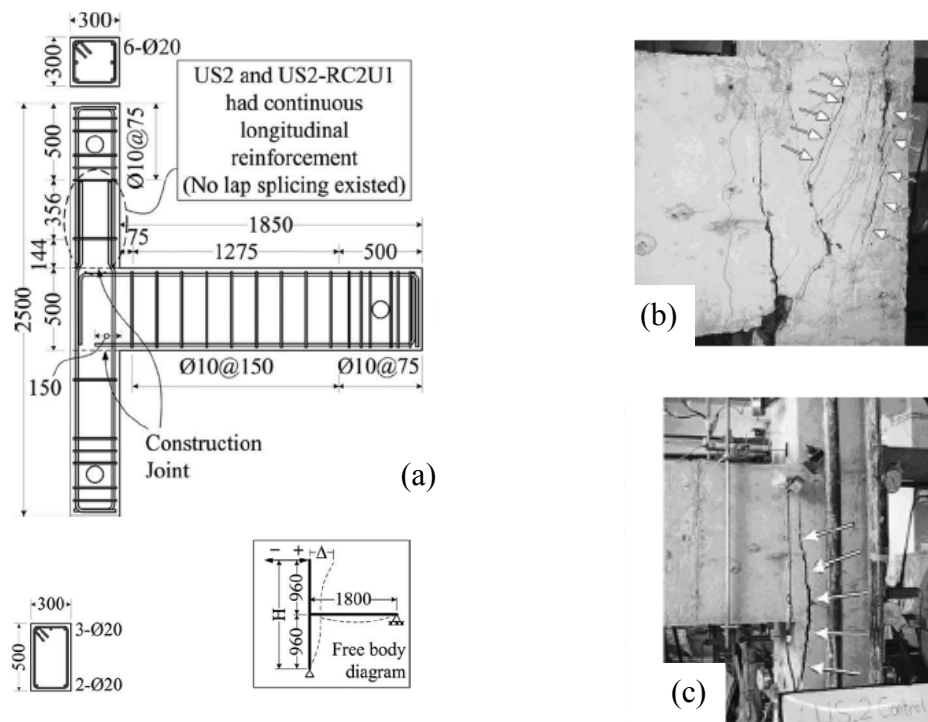


Figure 2.9. Experimental test by Parvin et al. (2010): (a) Reinforcing details and dimensions; (b) Crack pattern due to shear failure in the joint; (c) Crack pattern due to the slippage of the main beam bottom reinforcement.

It was observed that in the pull direction of loading, due to the adequate anchorage of the longitudinal reinforcement bars at the top of the beam, the tensile force from the top fibre of the beam cross section was transferred to the joint core. Since no stirrup was provided in the joint, only the concrete resisted the joint shear force and hence no yielding of the beam reinforcement was observed. To sum up, the lack of transverse reinforcement in the joint region governed the deficiency in the pull direction of loading.

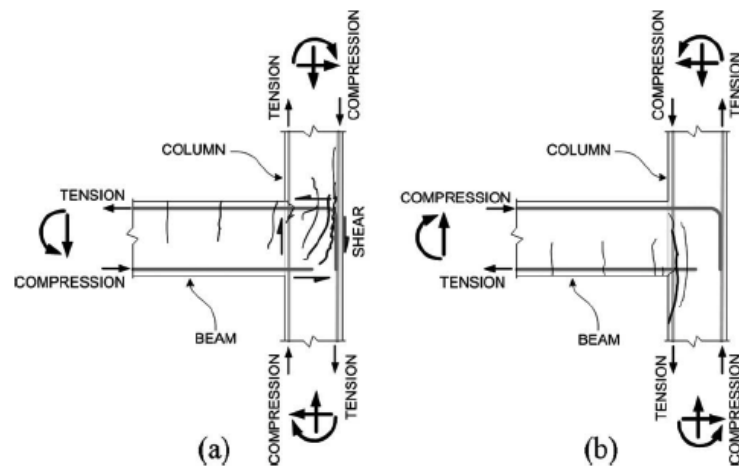


Figure 2.10. Internal forces and crack patterns after Parvin et al. (2010): (a) Pull direction of loading; (b) Push direction of loading.

In the push direction of loading, the tension force at the bottom fibre of the beam cross section caused slippage of the bottom beam reinforcements inside the joint due to their short embedment length in the column, leading to an abrupt reduction in the lateral load carrying capacity. Moreover, no shear damage was observed in the joint area (Figure 2.9.(c)). The slippage of bottom beam bars during the push direction of loading caused the separation of the beam from the column at the beam-column interface so that shear deformation at the joint region became insignificant. Figure 2.10 helps to explain this mechanism by describing internal forces in the longitudinal reinforcements that created shearing forces at the joint region and resulted in shear diagonal cracks.

Another experimental study on the exterior beam-column connection was carried out by Genesio (2012) at the Bhabha Atomic Research Centre (BARC) research facility. Five full-scaled as built beam-column joints were constructed according to the pre-1970s construction practice, with different anchorage schemes as shown in Figure 2.11.(a). Specimens JT1-1, JT2-1, JT3-1 and JT4-1 were expected to fail in shear before the yielding of the beam or

column main reinforcement, while specimen JT5-1 was designed to have a beam yielding failure mechanism after initial diagonal cracking in the joint existed.

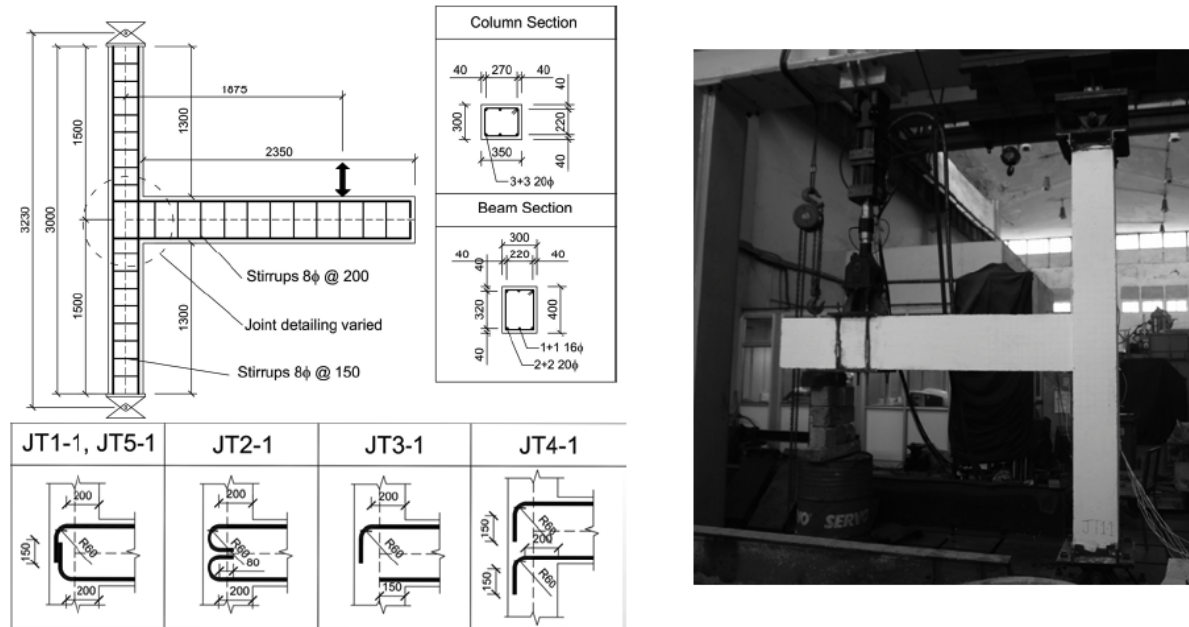


Figure 2.11. (a) Geometry of tested specimens; and (b) Test setup by Genesio (2012)

Tests JT1-1 to JT4-1 were designed to highlight the influence of the anchorage of the beam bars on the shear strength of joints without transverse reinforcement in the core. The anchorage of the beam bars with 90-degree hooks bent in was confirmed to be much more efficient than 90-degree hooks bent out, straight anchorage and plain round bars with 180-degree hooks. For joint JT5-1, the flexural failure of the beam occurred after the first diagonal cracking of the joint. This failure mode was shown to not provide any improvement in the ductility of the beam-column connection in comparison to the shear behaviour without the yielding of the beam bars.

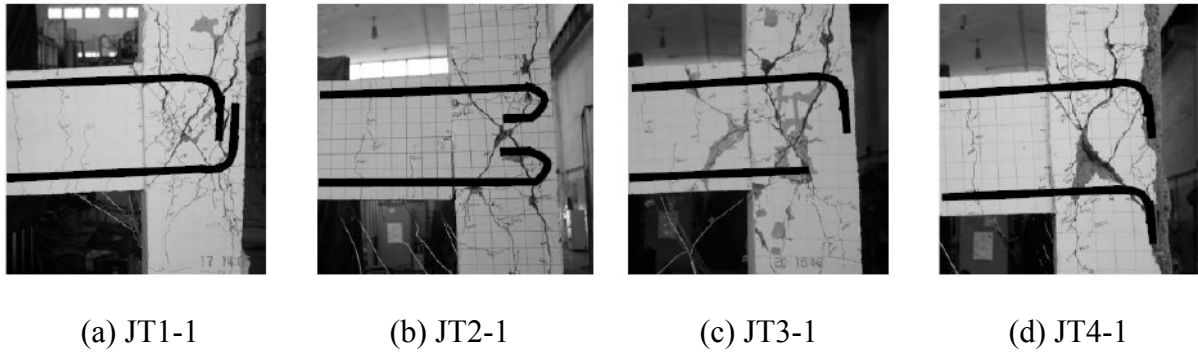


Figure 2.12. Experimental study by Genesio (2012)

2.3. PARAMETERS AFFECTING SHEAR STRENGTH OF REINFORCED CONCRETE JOINTS

The parameters affecting the shear behaviour of beam-column joints depend on the joint type and the failure mode sequence. Evidence gathered from experimental studies has identified a number of key parameters affecting, directly and indirectly, the behaviour of unconfined exterior beam-column joints. Studies conducted by Kim and LaFave (2007) and Hassan (2011) examined the influence of parameters, such as the ratio of the column axial load to the column capacity; the concrete compressive strength; the confinement of the concrete in the joint by the reinforcements; the beam reinforcement ratio; and the joint aspect ratio on the joint response under cyclic loading. The effect of three of those parameters, namely the column axial load, the concrete compressive strength and the confinement provided by the joint reinforcements, is discussed in detail hereafter.

2.3.1. Effect of column axial load

The effect of the axial load level to which the column is subjected on the shear strength of RC beam-column joints is inherently complex due to the various mechanisms governing the shear

resistance of joints. Experimental studies conducted by Clyde et al. (2000) and Pantelides et al. (2002) revealed that the joint shear strength increases with increasing axial load. On the other hand, an analytical study conducted by Pantazopoulou and Bonacci (1992) found that the joint shear strength is not affected by the existence of axial load. Figure 2.13.a shows the relationship between the axial load ratio and the joint shear strength coefficient (γ_j), where the joint shear strength coefficient, is defined as the joint shear stress normalized with the concrete strength. This figure was produced by Hassan (2011) from a database comprising 100 unconfined beam-column joint tests available in the literature. In this study, three modes of failure were defined; J, BJ and BCJ. In failure mode J, the joint fails prior to the yielding of the beam and column longitudinal reinforcement. Failure mode BJ occurs when the beam longitudinal reinforcement yields prior to the joint failure, whilst failure mode BCJ corresponds to both beam and column longitudinal reinforcement yielding prior to the failure of the joint.

It was found that the beneficial effect of the column axial load on the joint strength was more pronounced when the column was subjected to loads higher than $0.2f_c A_g$. The joint shear strength enhancement due to the existence of column axial loads smaller than $0.2f_c A_g$ was deemed less significant. Figure 2.13.(b) demonstrates the positive effect of the column axial load on the joint shear strength. Joints exhibiting BJ failure were observed to reach high strength with increasing axial loads, presumably because a higher axial load enhances the bond strength of the beam longitudinal reinforcement in the joint, thus increasing the beam flexural strength and the joint strength at failure (Pantelides et al, 2002). It was observed that for the same joint aspect ratio, there was an increase of 10-20% in joint shear strength due to the increase in axial load.

Hassan (2011) also discussed the relationship between the column axial load and the principal tensile stress as presented in Figure 2.14. For failure mode J, it was clearly shown that the principal tensile stress at failure decreased with increasing axial load, thus explaining the positive effect of the column axial load on the strength of the joint.

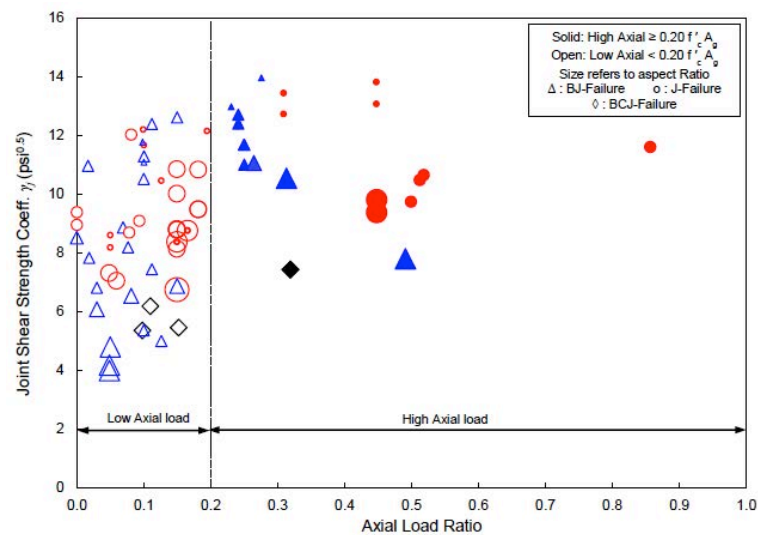


Figure 2.13. Effect of axial load on joint shear strength, Hassan (2011)

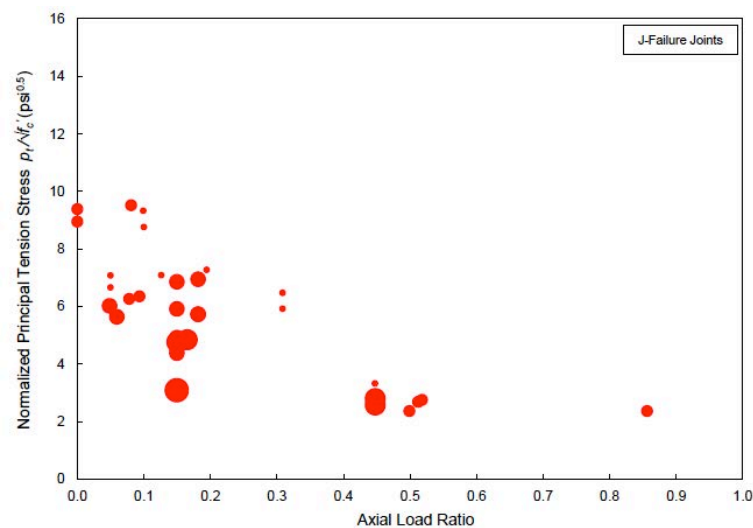
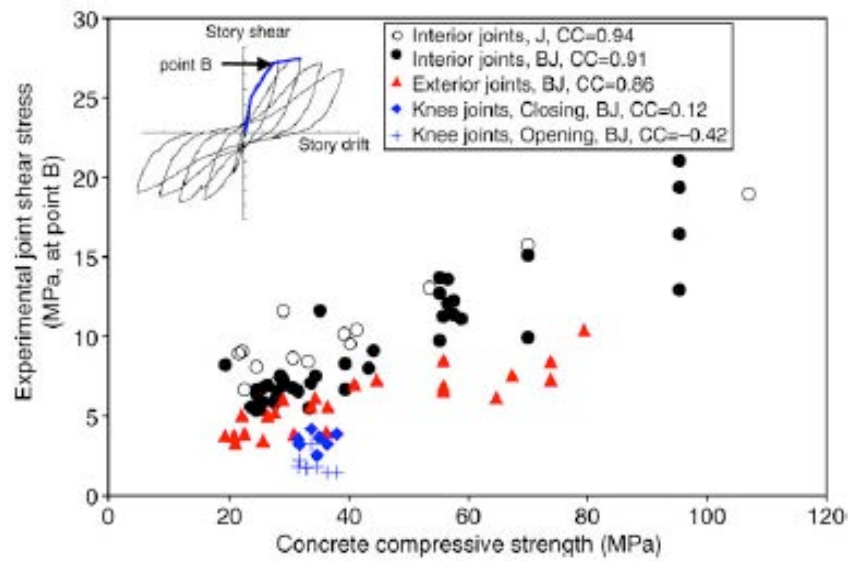


Figure 2.14. Effect of axial load on principal tensile stress at peak shear strength of the joint, Hassan (2011)

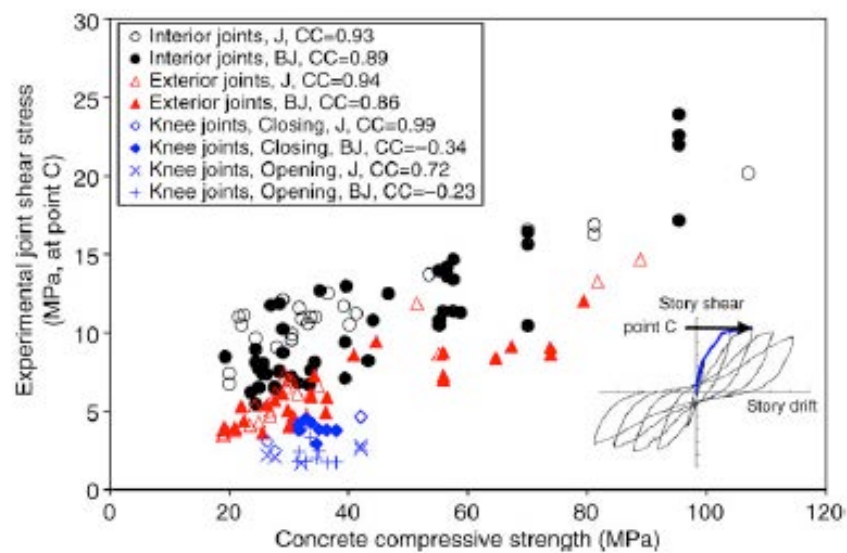
2.3.2. Effect of concrete compressive strength

A database of experimental studies on RC joints was collated by Kim and LaFave (2007) who studied the effect of concrete compressive strength on the joint response. In their study, they considered a broad range of concrete compressive strengths varying from 19 to 89 MPa. Three key points, A, B and C, were defined with respect to the joint response. In general, Point A corresponds to the initiation of the joint diagonal cracking, whilst Points B and C correspond to the yielding of the longitudinal reinforcement bars and the concrete crushing respectively.

Figure 2.15 demonstrates that the concrete compressive strength affects the joint shear stress positively at both Point B and Point C. A similar level of correlation between the joint shear stress and the concrete compressive strength is observed for both Point B and Point C for all joint types and failure modes considered. In addition, increasing the concrete strength improves the joint resistance by improving the load bearing capacity of both the column and the beam compression zone, as well as the bond strength of the beam bars within the joint region.



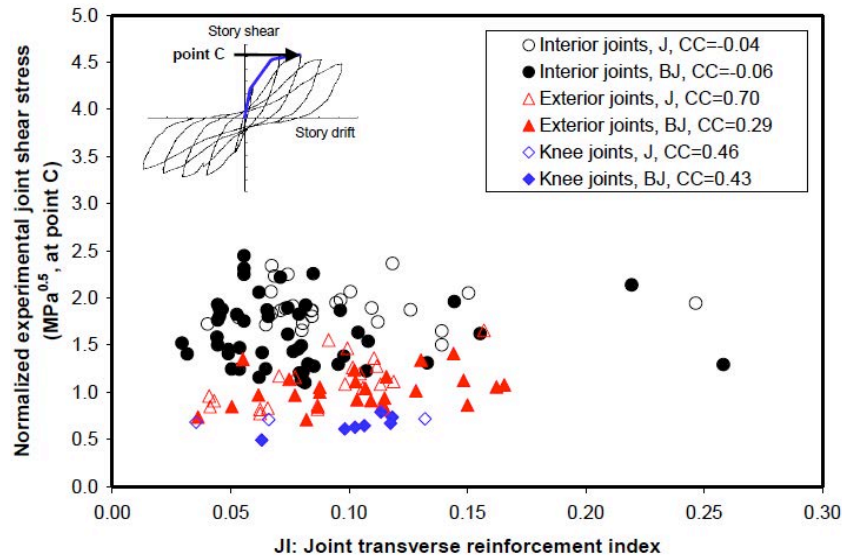
(a) Point B, yielding of the longitudinal reinforcement



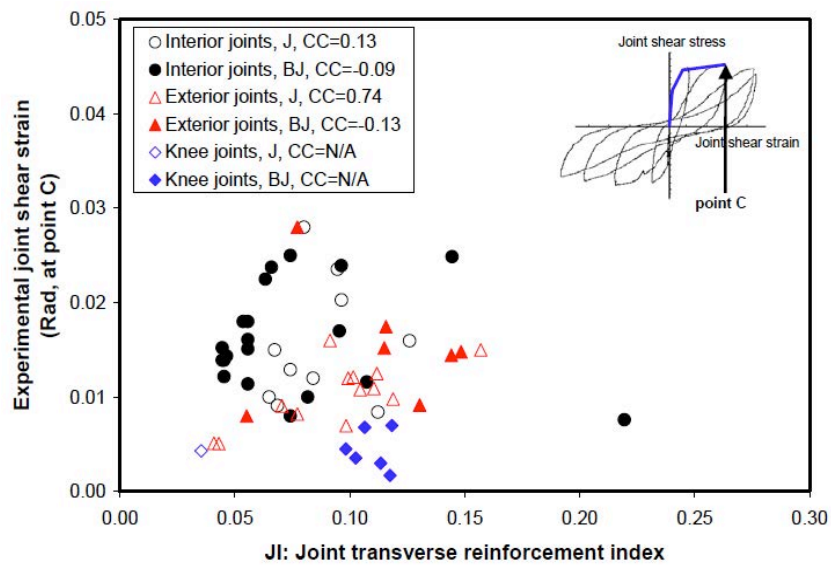
(b) Point C, crushing of the concrete

Figure 2.15. Influence of concrete strength on joint shear stress observed at Point B and Point C, Kim and LaFave (2007)

2.3.3. Effect of joint reinforcement confinement



(a) Normalised joint shear stress



(b) Joint shear strain

Figure 2.16. Role of confinement to joint shear strength, Kim and LaFave (2007)

The effect of the joint reinforcement on the joint shear strength can be defined as the joint confinement index, $\rho_{sv}f_{yh}/f_c$ where ρ_{sv} is the volumetric joint hoop ratio, f_{yh} is the yield stress

of transverse joint reinforcement and f_c is the concrete compressive strength. Figure 2.16 depicts that, for the case of exterior joints with J-type failure, the correlation coefficients for the contribution of joint transverse reinforcement to the joint shear stress and strain at Point C were 0.70 and 0.74 respectively. This result indicates that the amount of joint transverse reinforcement is associated with the joint shear strength of exterior joints of J-failure type, where the joint and beam longitudinal reinforcement remains in the elastic range (Kim and LaFave, 2007). For all other cases, the joint transverse reinforcement index and the joint shear stress seem uncorrelated.

2.4. FIBRE REINFORCED POLYMER

FRP composites consist of three essential constituents: fibres, polymers, and additives. Several kinds of additives are used to enhance the properties of FRP materials such as plasticisers, impact modifiers, heat stabilisers, antioxidants, light stabilisers, flame-retardants, blowing agents, and couplings agents (GangaRao et al., 2007). These FRP composites have a range of favourable properties that make them well-suited for a range of applications in several industries, such as structural/construction, automotive, aerospace and sporting goods.

For structural applications, FRPs can be manufactured in a number of forms, such as structural shapes, reinforcing bars and deformation systems (e.g. exterior wound fibres and sand coating) as well as fabric wraps for structural and non-structural components (GangaRao et al., 2007). FRP composites are produced by building up several layers of fibre with polymers, through wetting and curing polymer layers together or bonding a number of prefabricated laminates. With respect to the fibre material, there are three types of FRPs that

are commercially available for reinforcement products; aramid FRP (AFRP), carbon FRP (CFRP) and glass FRP (GFRP).

AFRP are classified as highly crystalline aromatic polyamide fibres. They offer good mechanical properties; high tensile strength-to-weight ratio compared with the other types of fibres; and high resistance to organic solvents, fuels and lubricants. In addition, AFRP have a negative coefficient of thermal expansion in the longitudinal direction. The major disadvantage of AFRP is their low compressive strength. Moreover, these fibres are also defined as hygroscopic materials because they can absorb moisture up to 10% of fibre weight. The presence of high moisture content in the fibre will precipitate the formation of internal cracks at pre-existing microvoids and promote longitudinal splitting (GangaRao et al., 2007).

Carbon fibres contain at least 90% of carbon by weight and are produced by a controlled pyrolysis of appropriate fibres. This type of fibre is manufactured from one of the three types of precursor (starting material), namely, polyacrylonitrile (PAN) fibres, cellulosic fibres and phenolic fibres (GangaRao et al., 2007). During fabrication, the fibres are consecutively treated in three different schemes, namely:

- (a) Thermosetting: The fibres are stretched and heated at a temperature of 400°C and during this procedure, carbon chains are cross-linked so that fibres will not melt in consecutive treatments.
- (b) Carbonizing: During this process, impurities are removed by heating the fibres to a temperature of 800°C in an oxygen free environment.
- (c) Graphitization: During this process, the fibres are stretched between 50% and 100% elongation and heated at temperatures ranging between 1100°C and 3000°C.

To improve the carbon fibre/epoxy bonding strength, surface treatment and epoxy sizing are performed. The favourable mechanical properties of carbon fibres include: (a) high tensile strength-to-weight ratio; (b) high tensile Young's modulus-to-weight ratio; (c) very low coefficient of linear thermal expansion; and (d) high fatigue strength, where by the fatigue strength of CFRP is 60%-70% of the static ultimate strength after 1 million cycles (Rasheed, 2015). However, their main disadvantages are: (a) high brittleness and electrical conductivity and (b) low impact resistance coupled with their high material cost which limits their use in more widespread commercial applications (GangaRao et al., 2007).

Glass fibres are the most common of all reinforcing fibres for polymeric matrix composites and are drawn from an organic product of fusion that has cooled without crystallizing. Molten glass spun from electrically heated platinum-rhodium is used to make these fibres. After that, a protective coat (called sizing) is applied individually on filaments before they are bundled into a strand and wound on a drum at speeds of up to 2 miles/minute (GangaRao et al., 2007). Sizing added during the production process is aimed to (a) reduce the abrasive effect of filaments rubbing against one another; (b) reduce the static friction of filaments; (c) reduce the damage of fibres during mechanical handling; (d) pack filaments into a strand; and (e) facilitate the moulding process. Among the advantages of glass fibres are their low cost, high tensile strength, high chemical resistance and excellent insulating properties. On the other hand, the disadvantages include their relatively low tensile modulus, high specific weight, sensitivity to abrasion during handling and relatively low fatigue resistance. The types of glass fibres commonly used are E-glass, S-glass or R-glass (applicable for extra-high strength and high-modulus purposes) and C-glass (with greater resistance to acid corrosion). E-glass is

the most common type of glass fibre in use because it has the lowest cost of all commercially available reinforcing fibres, low susceptibility to moisture and high mechanical properties.

2.4.1. Mechanical Properties

The mechanical properties of the FRP product are significantly affected by the selection of the proper matrix (resin). Two types of polymeric matrices are commonly used for FRP composites; thermosetting and thermoplastic. Thermosetting polymers form a rigid three-dimensional structure by joining the low molecular-weight liquid through a chemical cross-link process. Once set, this structure cannot be reshaped by either heat or pressure. On the contrary, thermoplastic polymers are constructed by linking the molecules together using weak secondary bonds in a linear structural form; hence their structure can be destroyed by heat or pressure. Thermosetting polymers are more favourable than thermoplastic polymers in the FRP industry (GangaRao et al., 2007).

Polyesters, vinyl esters and epoxies are the most commonly used types of thermosetting polymers. These materials have good chemical resistance and thermal stability, and exhibit low creep and stress relaxation. On the other hand, the disadvantages are their short shelf-life, low strain at fracture, low impact strength and long manufacturing time.

Fillers and additives are used not only to reduce the cost of the composites but also to improve their performance that might not be achieved by the fibres and resins alone. Fillers enhance the mechanical properties by reducing the fibre and resin ingredients as well as the organic content in composite laminates. In addition, filled resins have less shrinkage and are

hence more dimensionally stable and promote improved transfer of stresses between fibres. Furthermore, the use of additives can facilitate a number of critical functions: fire resistance, emission control, viscosity control and coloration.

The unidirectional behaviour of the FRP bars is linear up to failure as shown in Figure 2.17. They do not exhibit a yielding plateau as conventional steels do. Generally, FRP bars have a higher tensile strength than conventional steels. On the other hand, FRP bars have a lower compressive strength than steel due to the buckling of constituent fibres.

Table 2.1 Usual tensile properties of reinforcing bars (Reproduced from ACI 440, 2006)

	Steel	GFRP	CFRP	AFRP
Nominal yield stress (MPa)	276 to 517	N/A	N/A	N/A
Tensile strength (MPa)	483 to 690	483 to 1600	600 to 3690	1720 to 2540
Elastic modulus (GPa)	200	35 to 51	120 to 580	41 to 125
Yield strain, %	0.14 to 0.25	N/A	N/A	N/A
Rupture strain, %	6 to 12	1.2 to 3.1	0.5 to 1.7	1.9 to 4.4

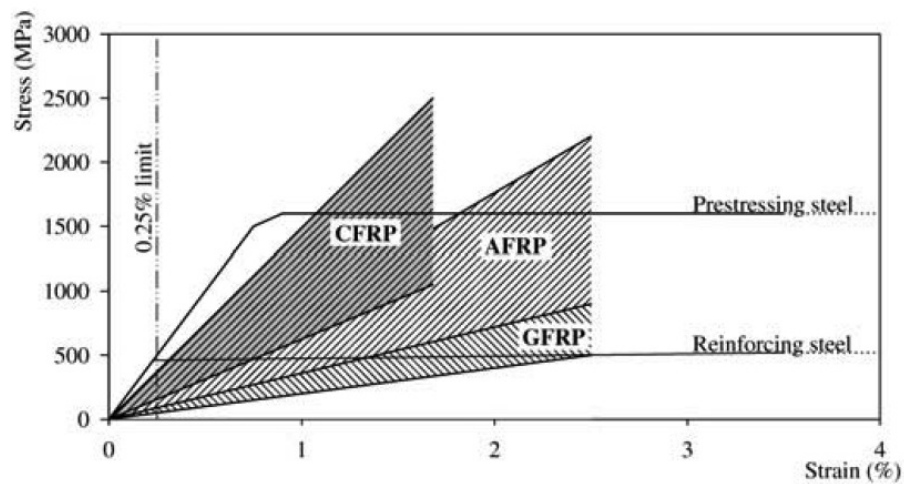


Figure 2.17. Tensile properties for steel and FRP reinforcement (Guadagnini et al., 2003)

2.4.2. Physical properties

The main parameters defining the physical properties of any material are the coefficients of thermal expansion and the density. FRP bars have differential thermal expansion coefficients in the longitudinal and transverse directions. The type of fibre governs the longitudinal coefficient of thermal expansion, whilst the type of resin dictates the transverse coefficient of thermal expansion (ACI 440, 2006). Furthermore, the density of FRP bars is considerably less than that of steel bars. Typical values for the coefficient of thermal expansion and density of different types of FRP bars compared to that of common steel bars are presented in Tables 2.1 and 2.2.

Table 2.2. Densities of reinforcing bars (gram/cm³) (Reproduced from ACI 440, 2006)

Steel	GFRP	CFRP	AFRP
7.9	1.25 to 2.10	1.50 to 1.60	1.25 to 1.40

Table 2.3. Typical coefficients of thermal expansion reinforcing bars (Reproduced from ACI 440, 2006)

Direction	CTE, ($\times 10^{-6}/^{\circ}\text{C}$)			
	Steel	GFRP	CFRP	AFRP
Longitudinal, α_L	11.7	6.0 to 10.0	-9.0 to 0.0	-6.0 to -2.0
Transverse, α_T	11.7	21.0 to 23.0	74.0 to 104.0	60.0 to 80.0

2.4.3. Manufacturing of Carbon Fibres

FRP products are formed in various ways, such as pultrusion, hand lay-up and filament winding, as listed in Table 2.4. Among these manufacturing processes, straight FRP bars are produced using the pultrusion technique whilst FRP fabrics for bonding or wrapping for external strengthening are commonly produced using the hand lay-up technique.

The pultrusion process derives its name from the processes involved in the making of the FRP product namely (a) “pul”, from the pulling force applied to fibres and (b) “trusion”, from the extrusion that extrudes (pushes) hot molten polymer through a die. So in the pultrusion process, reinforcement in the form of fibres is continuously pulled from creels and pre-shaped with a series of guides to producing FRP bars. During pultrusion, fibres are wetted in a resin bath before feeding them through fibre preformers or a heated die. The resin bath consists of accelerators, filler materials, catalysts and wetting agents. After the curing process, the hardened FRP product is cooled while being gripped and pulled and cut to the required length. Some FRP rebars are processed in two steps: in the first step, the bars are pultruded to a partially cured state and in the second step, additional layers are applied on top of the first stage product to give surface lugs identical to steel bars (GangaRao et al., 2007).

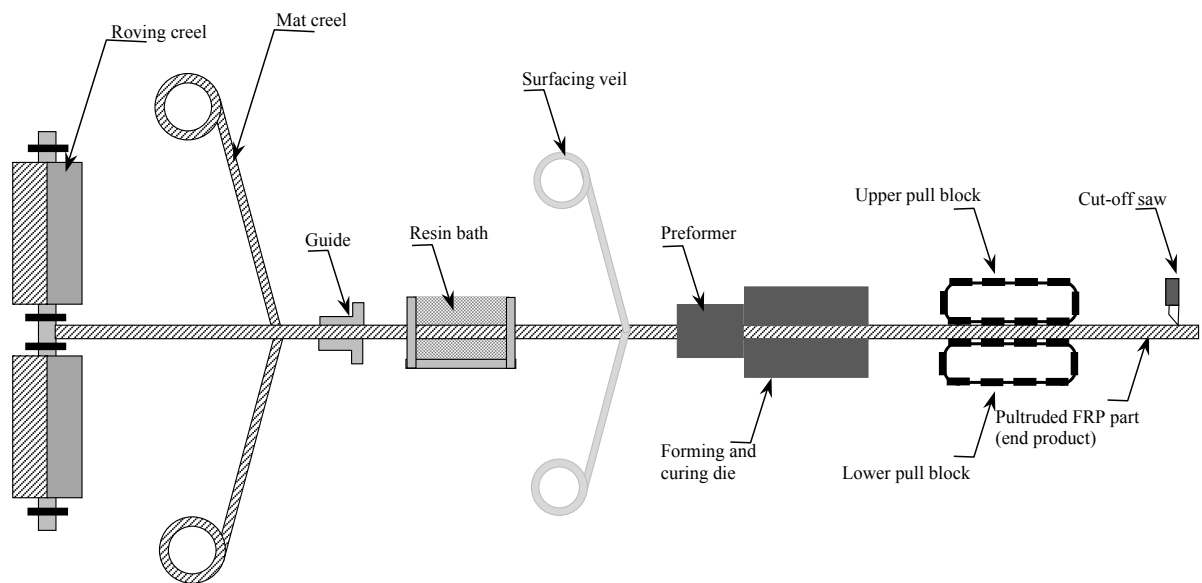


Figure 2.18. Schematic of pultrusion process after GangaRao et al. (2007)

Figure 2.18 shows the pultrusion process followed in manufacturing FRP composite products developed by the Constructed Facilities Centre at West Virginia University. Following this method, the continuous strands of the fibres are pulled from a creel of fibres to be

impregnated in a resin tank. Once they are saturated with resin, they are shaped through a heated die in which they can be cured as shown in Figure 2.18. Before the FRP bars are cut to the required lengths, their surface must be treated in the form of spirals or sand coating to ensure a strong bond with concrete.

Table 2.4. Classification of manufacturing processes for FRP composites (Hollaway and Leeming, 1999)

Class	Process
Open lay-up	Hand lay-up Spray up
Intermediate	Cold press Resin transfer moulding (RTM)/resin injection Autoclave/vacuum bag
Compression	Hot press
Continuous	Pultrusion Continuous sheet
Winding processes	Filament winding

2.5. STRENGTHENING OF EXTERIOR REINFORCED CONCRETE BEAM-COLUMN JOINTS USING FIBRE REINFORCED POLYMER MATERIAL

Several rehabilitation techniques have been investigated and adopted in practical applications to enhance the seismic performance of existing RC beam-column joints. These techniques include epoxy repair, partial removal and replacement of the concrete of damaged elements, RC jacketing and steel jacketing. A comprehensive review of the cutting edge on the use of conventional strengthening techniques can be found in Engindeniz et al. (2005).

The techniques are generally referred to as conventional or traditional techniques and are associated with various difficulties in their practical application. To overcome the difficulties associated with the application of these techniques, researches have aimed their attention at using epoxy-bonded fibre-reinforced polymers (FRP). These reinforcing systems have been widely used in various forms (e.g., epoxy-bonded flexible sheets, ready-made strips, and near-surface-mounted rods) for upgrading existing beam-column joints since 1998. The FRP systems have been shown to provide significant benefits and advantages over the conventional techniques, including: (a) higher strength-to-weight ratio and stiffness-to-weight ratio; (b) higher corrosion resistance; (c) lighter unit weight resulting in less-expensive equipment for economical handling, shipping, and transportation, as well as lighter erection equipment; (d) high durability, leading to lower life-cycle cost; (e) easier-to-control tension crack growth due to effectively confining the concrete; (f) better customization for specific needs; (g) fast field installation, and limited disruption to building occupancy; (h) no significant increase in member size; and (i) simple onsite corrections in the case of installation defects when bonding FRP with the concrete substrate (Engindeniz et al., 2005).

However, some drawbacks exist, especially to FRP wrapping materials for external strengthening applications, for example: (a) uncertainties regarding the durability of FRPs, as their long-term performance data is limited; (b) concerns of fire resistance, adverse effects from smoke and toxicity, and poor resistance of resins to UV rays; (c) limited knowledge of material properties and application procedures; and (d) strong dependency of the performance on the preparation of the substrate and the workmanship during installation and, hence, inherent uncertainty regarding their performance.

In the following section, a review of the state-of-the-art experimental studies on upgrading the seismic performance of deficient exterior RC beam-column joints using FRP materials is presented. Note that the scope of this section is limited to the rehabilitation of exterior RC beam-column joints using FRP materials, hence other cases, such as interior beam-column joints and exterior beam-column joints with slab, are not included due to their limited relevance to the scope of this study.

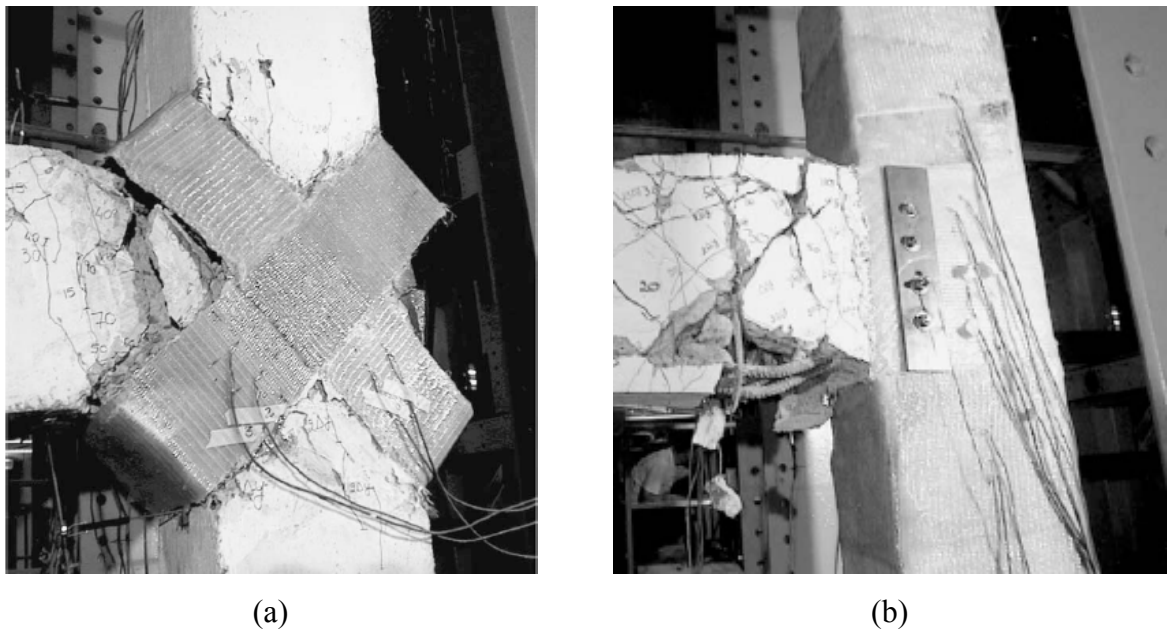


Figure 2.19. Failure mode of strengthened specimens tested by Ghobarah and Said (2002) :
(a) Shear failure mode of specimen rehabilitated using FRP without anchorage; (b) Ductile failure mode of specimen rehabilitated using FRP with cover plate and anchors through the joint

2.5.1. Ghobarah et al.

Several techniques for upgrading pre-1970 RC beam-column joints were proposed by Ghobarah and Said (2002), El-Amoury and Ghobarah (2002) and Ghobarah and El-Amoury (2005). The specimens were strengthened using various fibre-wrap rehabilitation schemes, without and with mechanical anchorage, including steel plates as well as threaded rods core-

drilled through the joint. The beams with no anchorage ruptured by shear failure in the joint whereas those with anchorage failed by flexural hinging of the beam as shown in Figures 2.19.(a) and 2.19.(b), respectively. The result clearly highlighted the importance of FRP anchorage for the performance of FRP joint strengthening techniques and showed that the proposed method eliminated the brittle shear failure in the joint, improved the bond condition and reduced the stiffness degradation of the joint.

2.5.2. Antonopoulos and Triantafillou (2003)

A comprehensive experimental program on RC joints strengthened with FRP subjected to cyclic loading was conducted by Antonopoulos and Triantafillou (2003). The importance of parameters, such as the FRP ratio, the presence of mechanical anchorage and the presence of joint reinforcement on the effectiveness of the studied strengthening techniques, was investigated through 18 tests on 2/3-scale exterior RC shear deficient subassemblages. All specimens had the same dimensions and reinforcement configuration and were designed to fail in shear representing a substandard RC beam-column connection. Two specimens were provided with one shear reinforcement in the joint whilst the rest had no joint shear reinforcement. Moreover, three out of 16 specimens (having no stirrups in the joint) had a transverse beam on one side to mimic the confinement offered from the transverse elements converging at the joint. Details of the tested specimens are shown in Figure 2.20.

The specimens were strengthened using carbon and glass FRP strips and sheets with different areas of fraction of FRP reinforcement applied on the beam and column elements. The area of fraction is defined as the ratio of the cross-sectional area of the FRP over the member's cross-sectional area of the strengthened element. Further details of strengthening schemes are given

in Figure 2.21. The bond characteristics between the concrete and the FRP material was improved by roughening the concrete surface at the locations where the FRP materials were applied, and removing the debris using vacuum. The arrangement of FRP was initially outlined on the specimen and then the FRP was cut to the needed length. Later, FRP strips were cleaned using acetone and they were bonded to the concrete surface through the use of two-part adhesive epoxy. A plastic roller was used to achieve proper bonding and remove the excess adhesive.

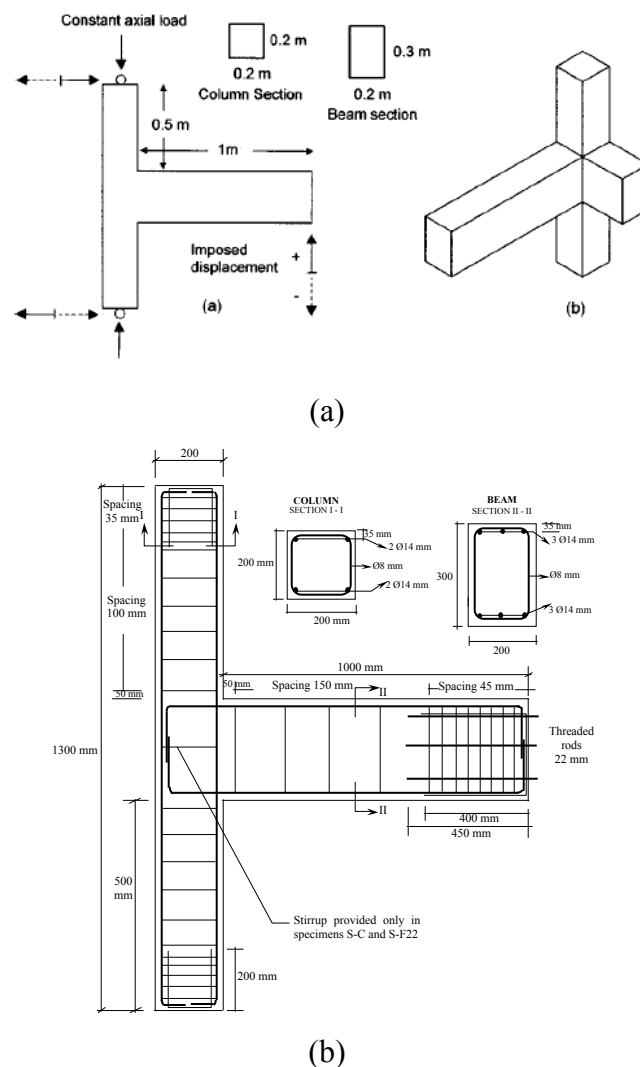


Figure 2.20. Specimen tested by Antonopoulos and Triantafillou (2003) : (a) Geometry of specimen with the presence of a transverse beam on joints T-C, T-F33 and T-F22S2; (b) Details of reinforcement

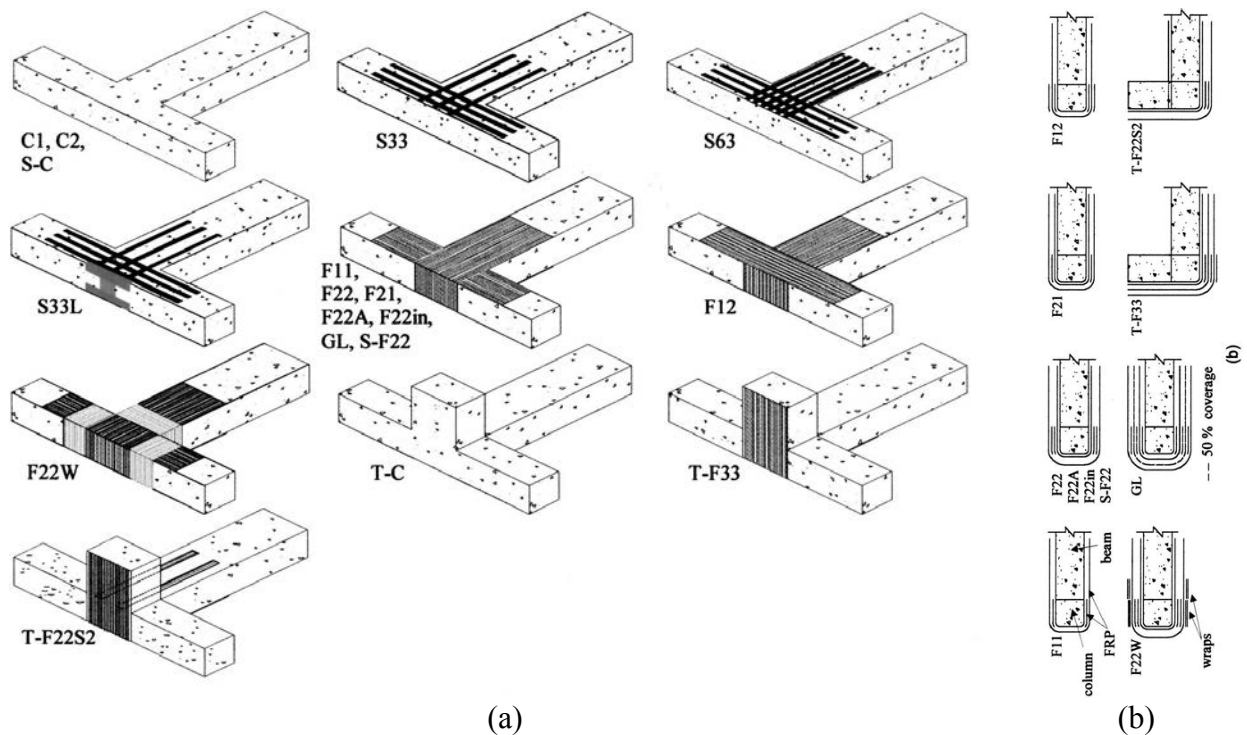


Figure 2.21. Proposed strengthening scheme by Antonopoulos and Triantafillou (2003) : (a) Description of specimens and strengthening alternatives; (b) Layout of FRP layers.

Based on the test results it was concluded that:

- Both the strength and the energy dissipation of the joint increased with the increasing number of FRP layers. However, this increase was not proportional due to premature debonding.
- The presence of mechanical anchorages increased the effectiveness of the FRP rehabilitation technique.
- The effectiveness of the FRP increased with decreasing the ratio of transverse reinforcement in the joint.
- Flexible FRP sheets were more effective than strips.

Debonding adversely affected the response of all specimens except the ones where mechanical anchorage was provided. For example, for specimens S33 and S63, debonding of the FRPs from the beam initiated at the beam face and progressed gradually with increasing loads, subsequently leading to debonding of the column FRP strips.

2.5.3. Tsonos (2008)

Tsonos (2008) conducted an experimental investigation to evaluate the effectiveness of two proposed retrofitting methods, namely CFRP-jackets and RC-jackets. Exterior joint specimens were constructed with non-optimal design parameters, such as having no joint reinforcement and having less column transverse reinforcement than that specified by the new Greek Code for the Design of Reinforced Concrete Structures (C.D.C.S., 2000) or by Eurocode 2-2003 and Eurocode 8-2004 (Figure 2.22).

In the case of the RC-jackets strengthening technique, new collar stirrups were added to the joint region and the column; after that the cement was grouted on each sides of the joint and column. The bond between the existing and new concrete was improved by removing the concrete cover of the original specimen and roughening the surface by sandblasting.

In the case of the FRP strengthening application, the external areas of the concrete surface were prepared by grinding them to achieve a fully smooth surface and a rounded corner with a radius of 30 mm. CFRP sheets were attached in the following sequence: (1) Ten layers of CFRP sheets were applied in the joint area with the fibre orientation parallel to the beam longitudinal axis; (2) Strips of CFRP were added to secure the anchorage length of CFRP joint layers; (3) To prevent premature debonding, the opening was made by drilling the

existing slab close to the joint region, and the beam was enclosed with four layers of CFRP through the opening; (4) Seven layers of CFRP sheets were wrapped to increase column shear strength; and (5) Two opposite column faces were wrapped with nine layers of CFRP sheets to increase column flexural strength (Figure 2.23).

The test results demonstrated that a concrete jacket is more effective for post-earthquake retrofitting, while, in the case of pre-earthquake strengthening, both methods seem to be equally effective. Moreover, the study presented a practical method of predicting the ultimate shear strength in the RC joint retrofitted with FRP, based on the confinement conceptual approach.

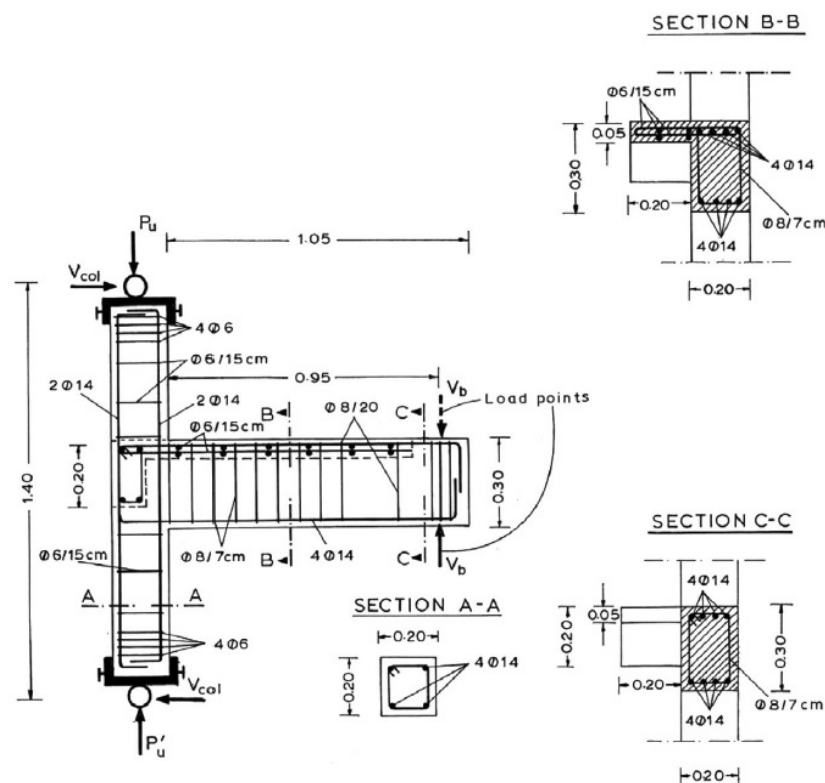


Figure 2.22. Dimensions and cross-sectional details of tested specimens, Tsonos (2008)

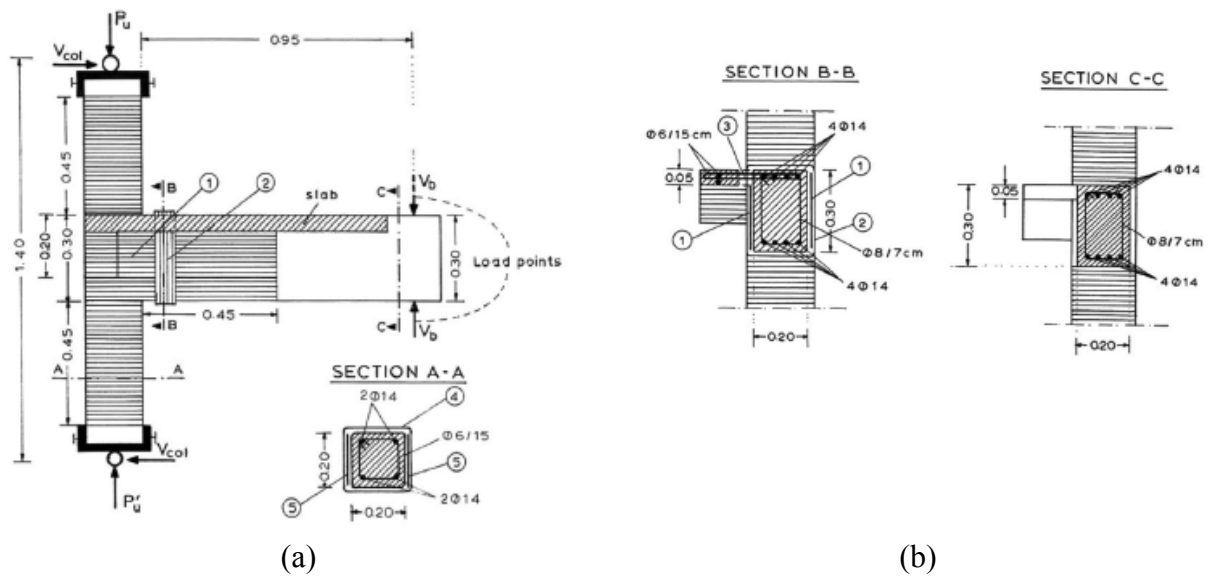


Figure 2.23. FRP jacketing strengthening schemes

- (1) 10 layers of CFRP sheets to increase the shear strength of the joint
- (2) Strips of CFRP sheets to secure anchorage length of the joint layers
- (3) Drilled holes in the slabs of specimens FRPF1 and FRPS1
- (4) 7 layers of CFRP sheets to increase the shear strength of the columns
- (5) 9 layers of CFRP sheets to increase the flexural strength of the columns

2.5.4. Karayannis and Sirkelis (2008)

Karayannis and Sirkelis (2008) reported the results of experimental research conducted on exterior RC joints strengthened with a combination of epoxy resin and CFRP. The unstrengthened specimens were grouped into the specimens without joint transverse reinforcement (Group A) and those with (Group B) joint transverse reinforcement. The reinforcement configuration of the unstrengthened specimens of Group A is presented in Figure 2.24.(a), whilst the specimens of Group B were identical to those of Group A, but were provided with four 8 mm stirrups as transverse reinforcement within the joint region.

Two specimens from each group were initially subjected to moderate cyclic loads and then each was repaired using resin injections and CFRP sheets respectively, whereas the third specimen was strengthened using CFRP sheets prior to the application of any loads. The

CFRP sheets were wrapped to confine both the column and the beam critical regions as well as the joint body, according to the arrangement shown in Figure 2.24.(b).

The proposed strengthening technique led to a significant improvement of the loading capacity, the energy absorption characteristics and the ductility, and shifted the failure mode from joint failure to flexural beam hinging. The test results showed that the seismic response of specimens subjected to large scale damage could be restored by repairing the damaged joint using the epoxy injection method. Moreover, the load carrying capacity and the energy absorption were better than those of the control specimen. The test also concluded that the CFRP contribution to the shear strength depends on the presence of joint reinforcement.

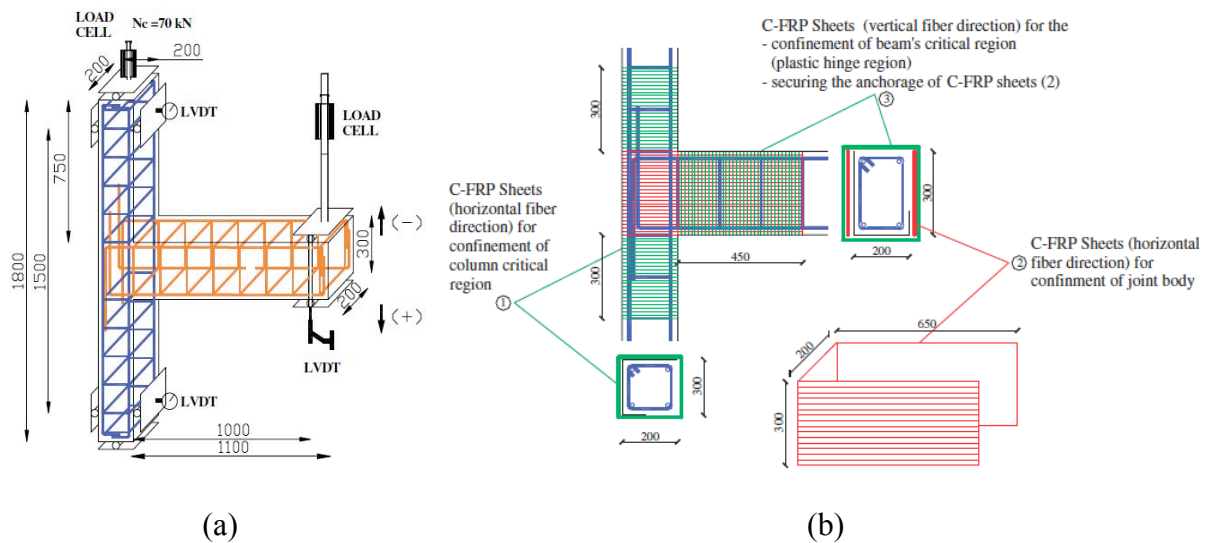


Figure 2.24. Specimen tested by Karayannis and Sirkelis (2008) : (a) Reinforcement details;
(b) Strengthening scheme using CFRP sheets

2.5.5. Alsayed et al. (2010)

The efficiency and effectiveness of CFRP sheets in upgrading the shear strength and ductility of seismically deficient exterior joints was studied by Alsayed et al. (2010). Four specimens were constructed to represent pre-seismic code design construction practice, eg. inadequate joint shear strength with no transverse reinforcement (Figure 2.25). Two of these specimens were the control specimens, whilst the rest were upgraded with CFRP sheets applied under two different methods. In the first method, the beam, joint body and part of the columns were wrapped using CFRP sheets (Figure 2.26.(a)). In the second method, only the joint body was wrapped with CFRP sheets. To mitigate debonding, a mechanical anchorage in the form of steel plates bolted on each side of the beam was provided (Figure 2.26.(b)). All sub-assemblages were subjected to a combination of cyclic lateral load and a constant axial column load equal to 20% of the column axial capacity. The results showed that externally bonded CFRP sheets effectively improved both the shear strength and deformation capacity of beam-column joints. The effectiveness of the applied upgrading technique was shown to be strongly dependent on the way the CFRP sheets were attached and on the presence or absence of a mechanical anchorage.

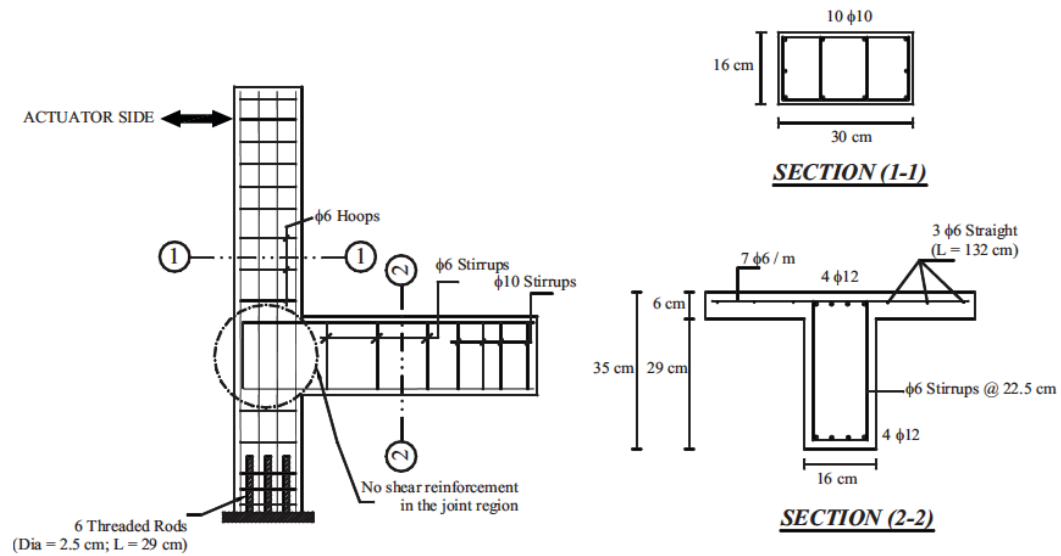


Figure 2.25. Reinforcement details of Alsayed et al. (2010) test specimens

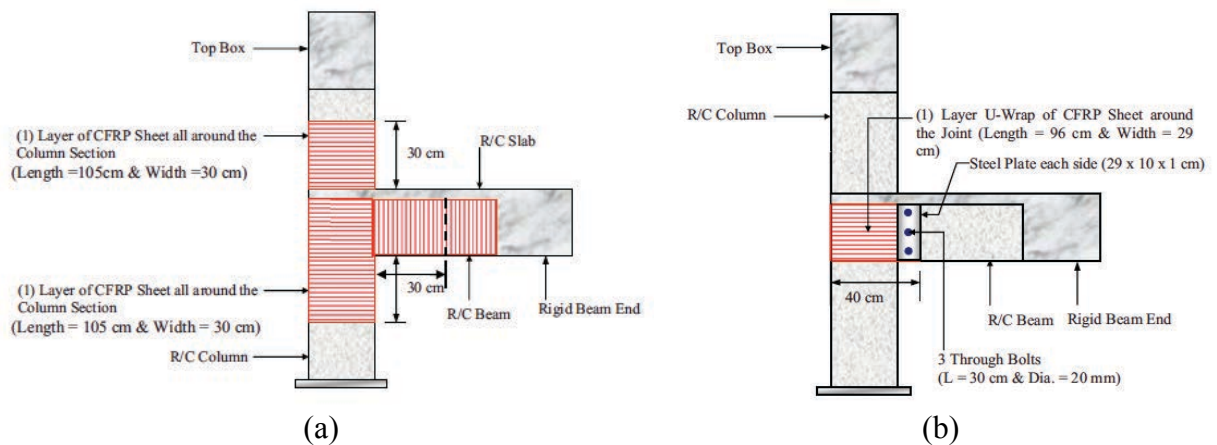


Figure 2.26. CFRP application of strengthened specimen (Alsayed et al., 2010) : (a) Representation of scheme #1; (b) Representation of scheme #2.

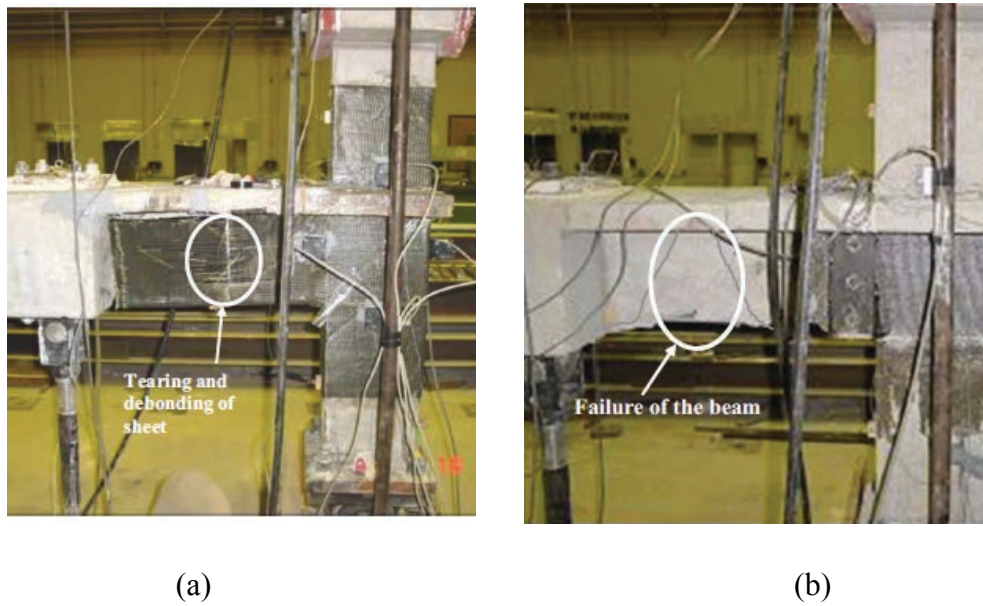


Figure 2.27. Failure mode of strengthened specimen after test (Alsayed et al., 2010): (a) Tearing and debonding of sheet of repaired joint ER1; (b) Beam failure of repaired joint ER2.

Strengthening scheme #1 was proven to be effective because both the joint and the beam strength were improved. However, debonding of the CFRP sheets existed at higher levels of loading due to the absence of mechanical anchorage (Figure 2.27.(a)). On the other hand, strengthening scheme #2 was more efficient since the use of CFRP sheets was kept to a minimum, but their utilisation was higher as debonding was mitigated through the use of mechanical anchorage (Figure 2.27.(b)).

2.5.6. Ilki et al. (2011)

Ilki et al. (2011) studied the behavior of FRP-strengthened joints employing smooth bars and low strength concrete. Dimensions of the specimens and reinforcing details are presented in Figure 2.28. Two series of eight full-scale exterior joints having no transverse reinforcement in the joint region were constructed. The specimens consisted of a column, an in-plane beam, a transverse beam and a slab, and were tested under the combined action of a constant column

axial load and cyclic load applied at the beam end. The strengthening scheme and FRP application are given in Figure 2.29. Two pieces of FRP sheets were applied; the first piece is the square FRP sheet that covers the joint core whilst the second piece is attached on top of piece 1 diagonally to provide sufficient anchorage of piece 1 to the specimen. It was clearly established that the application of the FRP sheets alone was not sufficient to prevent slippage of the beam longitudinal bars. When the joints were retrofitted with FRP sheets after the rehabilitation of anchorage bars through welding, the strength decay was significantly delayed.

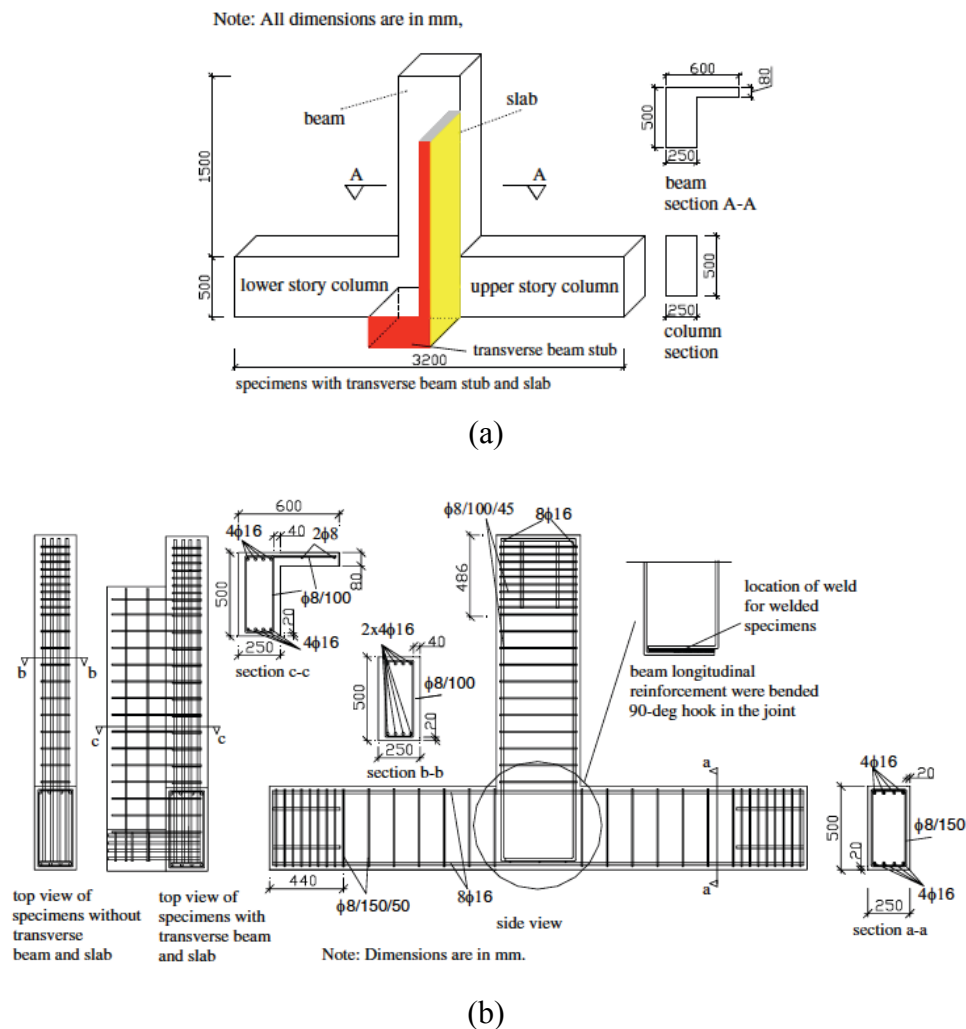


Figure 2.28. Specimen details (Ilki et al., 2011): (a) Geometry of specimen; (b) Reinforcement details

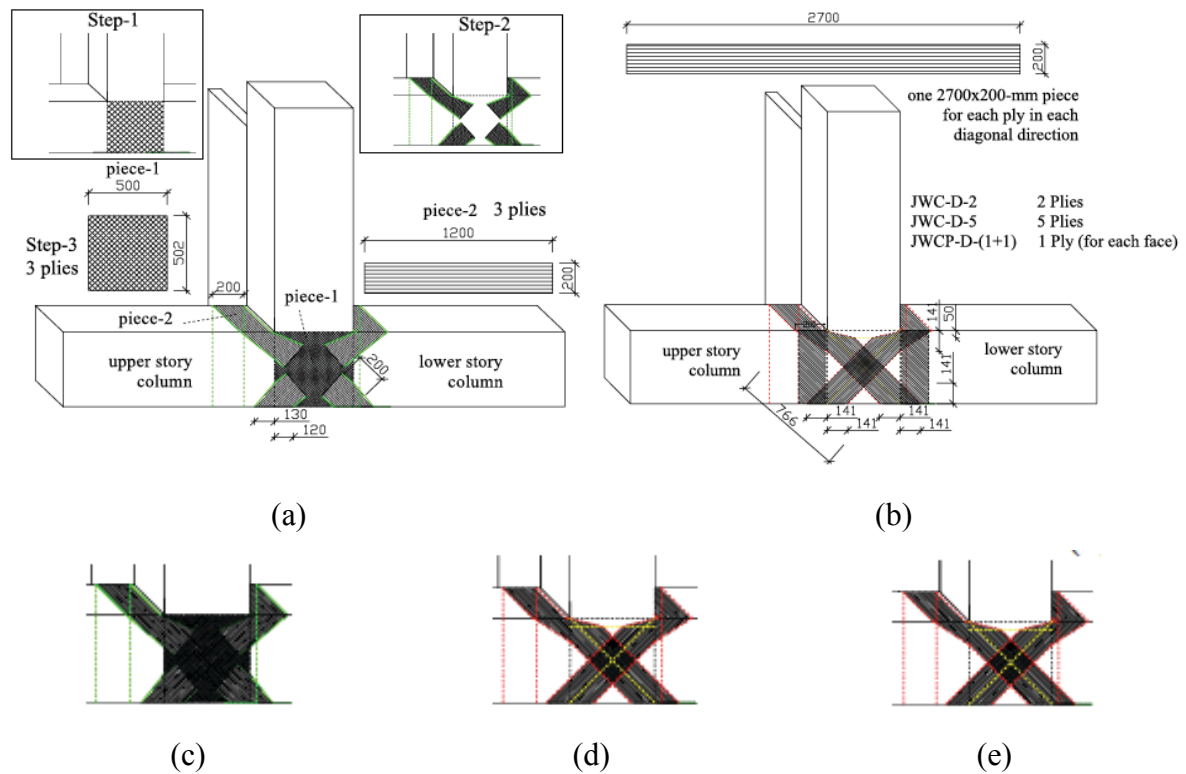


Figure 2.29. Strengthening application (Ilki et al., 2011)

2.5.7. Sezen (2012)

The repair and strengthening of RC joints using FRP composites was also conducted by Sezen (2012). Three exterior joints were tested under cyclic loading. The joint region of the specimens suffered significant damage, whereas limited damage was observed in the beams. The damaged specimens were repaired and strengthened by removing the damaged loose concrete and replacing it with high-strength non-shrink mortar. The FRP strips were diagonally wrapped over the joint region and longitudinal FRP strips were applied and anchored on the beams. As a result, all the specimens failed with the rupture of the beam longitudinal FRP strips either at the beam-column joint interface or within the plastic hinge region of the beam, thus shifting damage and failure away from the joint.

2.6. STRENGTHENING OF REINFORCED CONCRETE STRUCTURES UTILISING DEEP EMBEDMENT TECHNIQUE

Experimental research of various strengthening techniques of beam-column joints involving the use of externally bonded FRPs showed that most of the specimens experienced debonding of the FRPs followed by the rupture or the fracture of FRPs at subsequent loading stages. This is due to the relatively low tensile strength of the concrete surface on which externally bonded FRPs are applied, which limits the bonding strength between the FRP and the concrete (Mofidi and Chaallal, 2011). Experimental studies showed that when non-anchored externally bonded (EB) or near surface mounted (NSM) FRP reinforcement is used, de-bonding takes place at a stress level of about 20% to 30% of the ultimate tensile strength of the FRPs (Dirar et al., 2013), thus significantly compromising their performance and leading to their under-exploitation.

In terms of the practical application of the FRPs, surface preparation of the concrete substrate is required and the adhesive material needs to be applied by skilled workers. Moreover, the exposed FRP also requires protection against vandalism and fire. Debonding failure, inadequate surface preparation, as well as exposed FRPs, are some shortcomings that have to be considered when selecting an appropriate strengthening technique.

To overcome these shortcomings, the deep embedment (DE) technique was developed for the strengthening of shear deficient concrete beams using FRPs (Valerio et al., 2009). The DE technique is more effective compared to the conventional EB and NSM techniques, because it relies on direct transfer of stresses from the FRP to the core of concrete. Moreover, surface preparation and protection against fire and vandalism are not required. In the next section,

relevant research on strengthening RC structures employing the deep embedment method is presented.

2.6.1. Valerio et al. (2009)

When access to the members to be strengthened is limited to one side only, as is commonly the case for contiguous bridge decks or RC frames with brickwork infill panels, the EB technique becomes difficult to apply. For this reason, the deep embedment (DE) FRP strengthening technique was developed by Valerio et al. (2009) for shear strengthening of concrete beams. Tests on small-scale and large-scale beams replicating existing bridge beams in service were carried out. The effective depth (d) to real depth ratio (h), the longitudinal and transverse reinforcement ratio and the applied pre-stressing forces were selected similar to the respective design parameters of real beams. Details on the dimension and reinforcement configuration for the tested beams are presented in Figure 2.30.

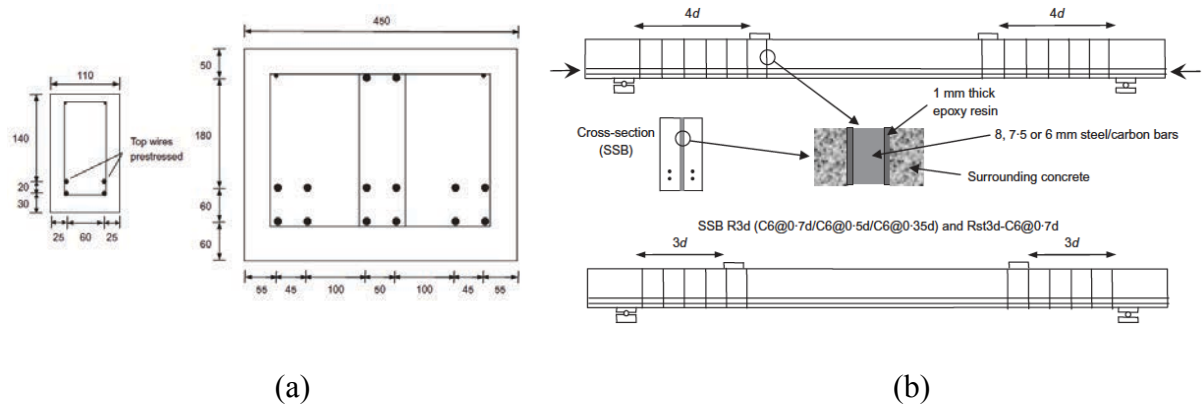


Figure 2.30. (a) Cross section of test beams; (b) Test layout for the strengthened specimen (Valerio et al., 2009)

To install embedded bars, holes with a 2 mm clear distance were drilled at the required position inside the shear span upwards from the beam soffit (Figure 2.31.(a)). After the holes were cleaned using compressed air, the epoxy adhesive was injected and the bars were

inserted manually until excess resin was flowing out of the beam, ensuring the holes were filled properly. The procedure was proven to be quick and easy. After the FRP bars were inserted into the holes, they stayed in position without providing any external support during curing.

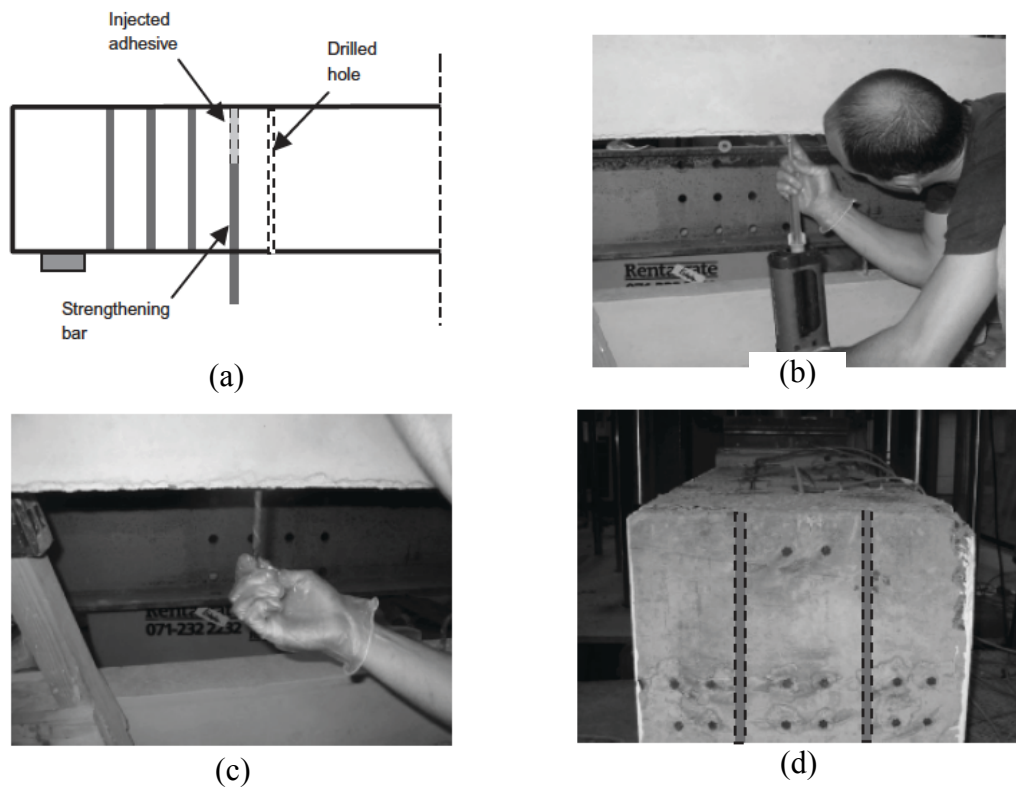


Figure 2.31. Deep embedment strengthening procedure proposed by Valerio et al. (2009): (a) Schematic showing hole positions; (b) Epoxy adhesive was injected into the holes; (c) Embedded bars were inserted into the holes; (d) Layout of embedded bars on beam's cross section

The test results showed that the DE technique was an effective means of strengthening deficient beams in shear. The shear failure of the strengthened beams occurred only when the bars debonded from the surrounding concrete near the embedded bar ends. It was also evident that the method effectively relies on the bond between the embedded bars and the inner side

of the drilled holes, so that the bond between the concrete and embedded bars can be maintained by using appropriate adhesive and roughening the inside of the hole surface.

2.6.2. Chaallal et al. (2011)

Following the success of the DE strengthening technique, Chaallal et al. (2011) conducted an extensive experimental study comparing the effectiveness of the following strengthening methods: a) EB, b) NSM, and c) the newly developed embedded through section (ETS). Twelve tests were carried out on six full-scale RC T-Beams. The beams were classified into three different groups based on the amount of internal transverse reinforcement installed.

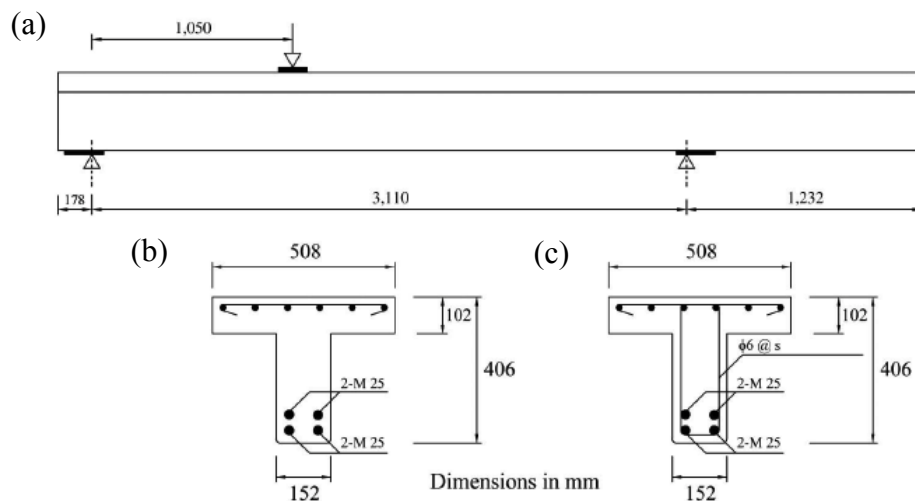


Figure 2.32. Details of tested beams (Chaallal et al., 2011): (a) Elevation; (b) Cross section with no stirrups; (c) Cross section with stirrups

The beams were tested under three-point bending as shown in Figure 2.32. Two tests were carried out on each beam. One beam end was tested leaving the other end overhanging beyond the support and virtually unstressed. After the execution of the first test, the previously unstressed part of the beam was tested using the same loading arrangement.

The ETS bars were installed following the procedure outlined below:

- (a) Holes were made at the required locations at the middle of the width of the beam cross-section;
- (b) The holes were then cleaned using pressurized water to remove any debris and cement residue;
- (c) After blocking the hole end, epoxy was injected until it filled about two third of the hole volume;
- (d) The FRP bars were then covered with a thin layer of epoxy and inserted into the holes;
- (e) Any excess epoxy was removed after the insertion of the bars.

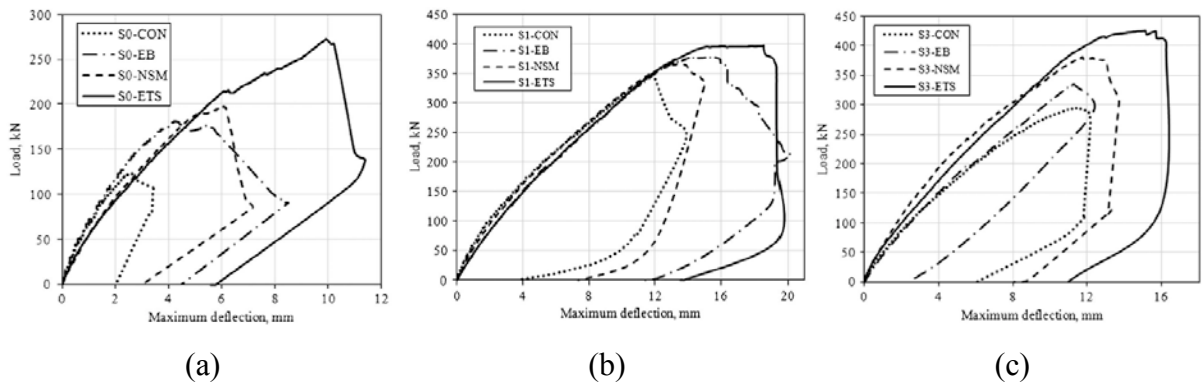


Figure 2.33. Load-displacement response of tested beams (Chaallal et al., 2011): (a) Series S0; (b) Series S1; (c) Series S3

The test results demonstrated the superior efficiency of the ETS method compared to the EB and NSM methods by considering the amount of FRP per unit length used. The efficiency was defined by introducing the parameter ψ_f , which is the ratio of FRP contribution to the shear capacity (V_f) and ultimate tensile capacity per unit length of FRP used. On average, the efficiency value of the ETS method was 110% and 210% higher compared to nominally identical specimens strengthened using the EB and NSM methods respectively. It was again confirmed that the beams strengthened using the EB method failed due to debonding of the FRPs, whilst beams strengthened using the NSM method failed due to the separation of the

side concrete cover. Beams strengthened using the ETS method displayed a very high shear resistance (about 60% higher compared to the control specimens) and their failure mode changed from shear failure to flexural failure, thus highlighting the effectiveness of the method. The corresponding increase in shear resistance using the EB and NSM methods was 23% and 31% respectively.

2.7. PREDICTION MODELS

Structural models are divided into two categories: analytical and finite element (FE) models. The analytical model depends on the application of the equilibrium and compatibility equations on a free-body diagram in order to develop a closed form solution. On the other hand, the FE model depends on the use of finite element software to predict the stresses and strains in the elements. The basic concept in the physical interpretation in the FE method is the subdivision of the mathematical model into disjoint components of simple geometry called finite elements. The response of the FE model is then considered to be approximated by that of the discrete model obtained by assembling the connection of all elements.

2.7.1. Analytical Modeling

Pantazopoulou and Bonacci (1992) proposed a joint assessment procedure based on the mechanics of interior beam-column joints in laterally loaded frames. Their formulation established the compatibility of the strain and stress equilibrium states at the centre of the joint region throughout the range of responses up to failure and assumes good bond condition of the beam and column reinforcement. It was shown that the joint capacity could be restricted by the crushing of the principal diagonal strut or by the yielding of the vertical reinforcement after hoop reinforcement yielding in the joint panel.

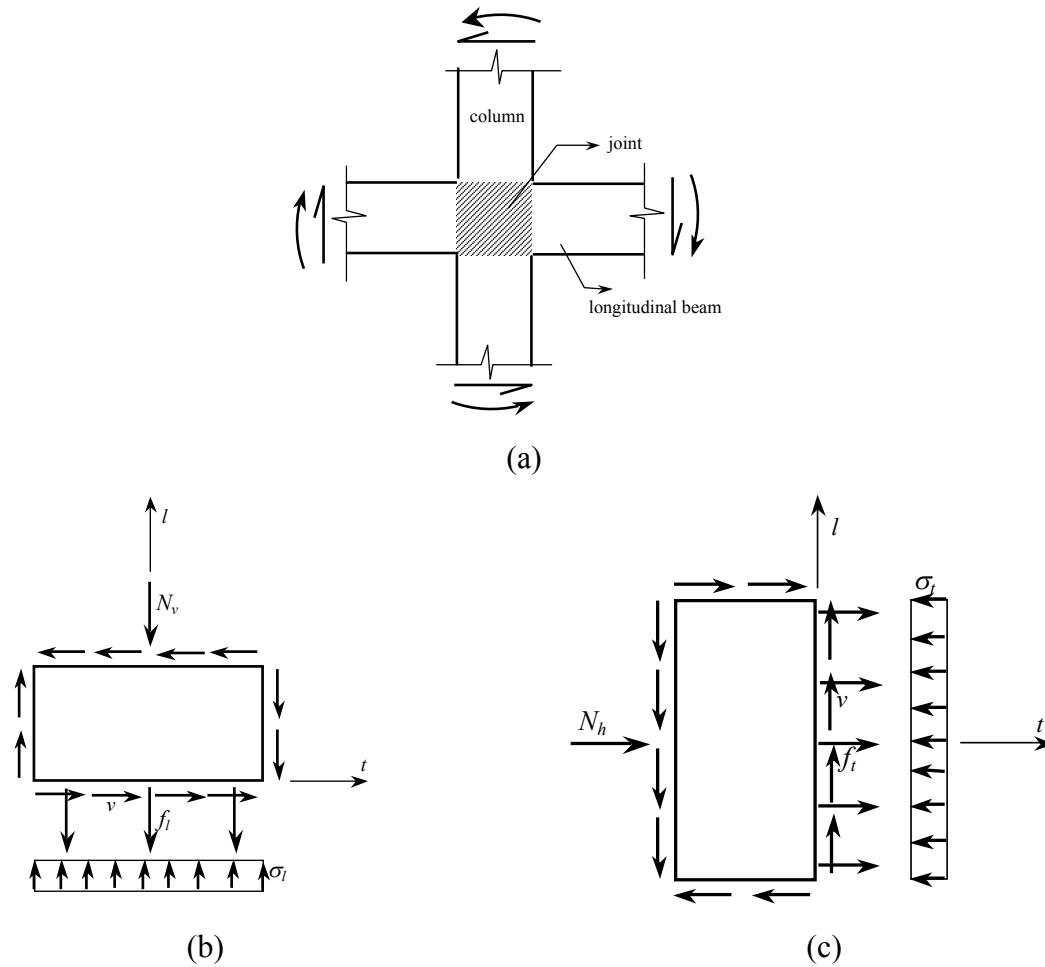


Figure 2.34. Analytical model proposed by Pantazopoulou and Bonacci (1992): (a) Actions at the boundaries of the joint; (b) Stress equilibrium at vertical direction; (c) Stress equilibrium at horizontal direction

Antonopoulos and Triantafillou (2002) proposed an extended version of the aforementioned model to evaluate the shear capacity of beam-column joints retrofitted with externally bonded FRP. The analytical model provided solutions to determine stresses and strains at ultimate capacity defined by the presence of concrete crushing or FRP failure due to fracture or debonding. For ease in tracing several possible stages of the response, such as: (a) yielding of the transverse or longitudinal reinforcement; (b) crushing of the concrete along the principal compressive direction; and (c) debonding failure of FRP sheets, a computer program was also developed.

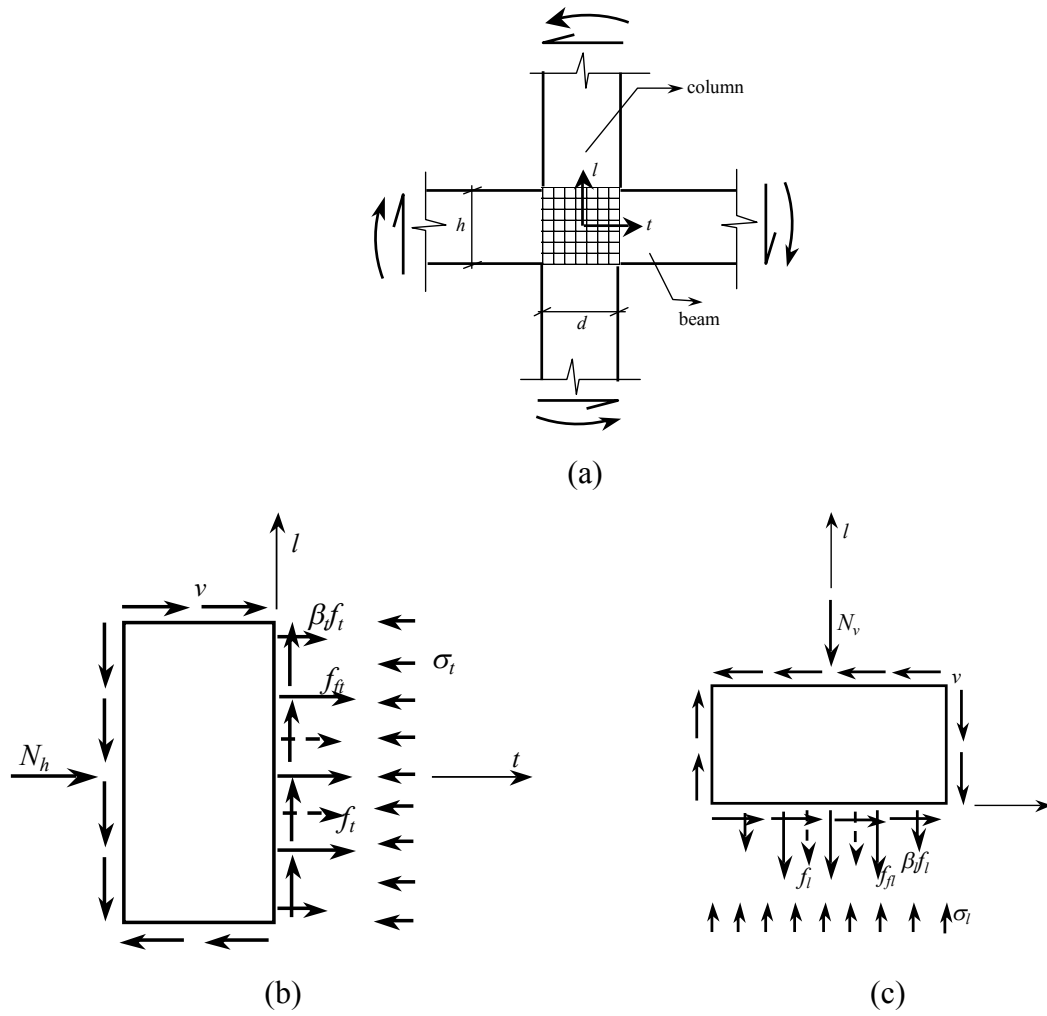


Figure 2.35. Analytical model proposed by Antonopoulos and Triantafillou (2002): (a) Moment and shear acting at joint; (b) Stress equilibrium at horizontal direction; (c) Stress equilibrium at vertical direction

A different approach called the softened strut-and-tie model (SST) was proposed by Hwang and Lee (1999) to predict the shear strength of the exterior RC beam-column joint under seismic loading. The SST model was developed based on the same concept proposed by Paulay et al. (1978).

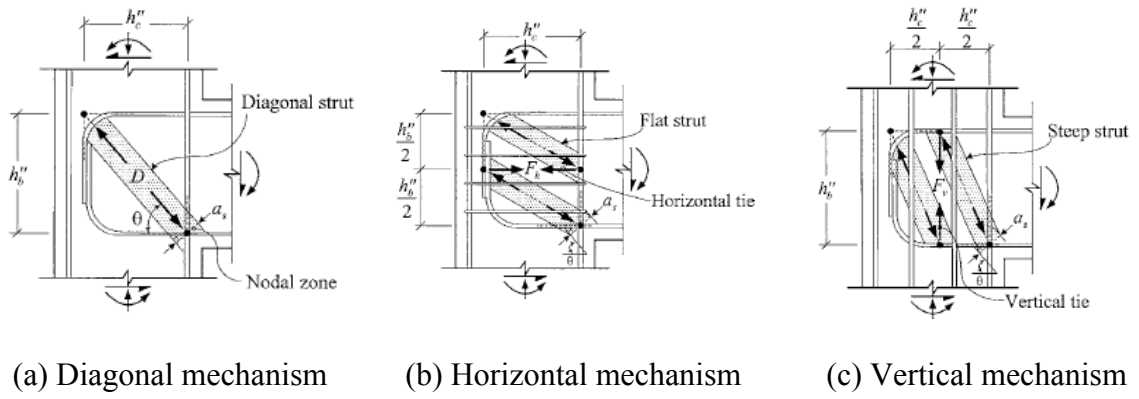


Figure 2.36. Joint shear resistance mechanisms, Hwang and Lee (1999)

Three joint shear mechanisms proposed in the SST method, as depicted in Figure 2.36, are namely: the diagonal mechanism, the horizontal mechanism and the vertical mechanism. The diagonal mechanism (See Figure 2.36.(a)) is treated as a single diagonal compression strut with the angle of inclination θ :

$$\theta = \tan^{-1} \left(\frac{h_b''}{h_c''} \right) \quad (2-1)$$

where h_b'' is the distance between the extreme longitudinal reinforcement in the beam and h_c'' is the distance measured from the centroid of extreme longitudinal reinforcement in the column to the centroid of bar extension at the free end of the 90-degree hooked bar.

The diagonal strut effective area is defined as:

$$A_{str} = a_s \times b_s \quad (2-2)$$

where a_s and b_s are the depth and the width of the diagonal strut, respectively. The depth of strut is subjected to the formation of the beam hinging at the column face. In the case of a beam hinge occurring at the column face, then a_s is equal to a_c . On the other hand, the depth of a strut without a beam hinge at the column face is defined as:

$$a_s = \sqrt{a_b^2 + a_c^2} \quad (2-3)$$

where a_b and a_c are the depths of the compression zones in the beam and column respectively.

The horizontal mechanism contains one horizontal tie and two flat struts as depicted in Figure 2.36.(b). The horizontal tie represents the joint hoops. A 50% reduction in the hoops area located outside the middle half of the joint should be considered.

The vertical mechanism (See Figure 2.36.(c)) consists of one vertical tie and two steep struts. The vertical tie represents the intermediate column bars and is estimated in the same way as the horizontal tie.

The contribution of the three joint shear mechanism to the horizontal joint shear forces is determined using Equation (2-4):

$$V_{jh} = D \cos \theta + F_h + F_v \cot \theta \quad (2-4)$$

where D , F_h and F_v are the diagonal, horizontal and vertical shear force mechanisms, respectively. The ratios of the joint shear mechanisms can be defined as:

$$D \cos \theta : F_h : F_v \cot \theta = R_d : R_h : R_v \quad (2-5)$$

Equation (2-5) can be rearranged as:

$$D = \frac{1}{\cos \theta} \times \frac{R_d}{(R_d + R_h + R_v)} \times V_{jh} \quad (2-6)$$

$$F_h = \frac{R_h}{(R_d + R_h + R_v)} \times V_{jh} \quad (2-7)$$

$$F_v = \frac{1}{\cot \theta} \times \frac{R_v}{(R_d + R_h + R_v)} \times V_{jh} \quad (2-8)$$

where R_d , R_h , and R_v are the ratios of the shear forces resisted by the three shear mechanisms.

The values of these ratios are defines as:

$$R_d = \frac{(1-\gamma_h)(1-\gamma_v)}{1-\gamma_h\gamma_v} \quad (2-9)$$

$$R_h = \frac{\gamma_h(1-\gamma_v)}{1-\gamma_h\gamma_v} \quad (2-10)$$

$$R_v = \frac{\gamma_v(1-\gamma_h)}{1-\gamma_h\gamma_v} \quad (2-11)$$

where:

$$\gamma_h = \frac{2 \tan \theta - 1}{3} \text{ and } \gamma_v = \frac{2 \cot \theta - 1}{3} \text{ for } 0 \leq \gamma_h \text{ and } \gamma_v \leq 1$$

The maximum compressive stress acting on the nodal zone that is perpendicular to the d -direction is given by:

$$\sigma_{d,\max} = \frac{1}{A_{str}} \left[D + \frac{\cos\left(\theta - \tan^{-1}\left(\frac{h_b''}{2h_c''}\right)\right)}{\cos\left(\theta - \tan^{-1}\left(\frac{h_b''}{2h_c''}\right)\right)} F_h + \frac{\cos\left(\tan^{-1}\left(\frac{2h_b''}{2h_c''}\right) - \theta\right)}{\sin\left(\tan^{-1}\left(\frac{2h_b''}{2h_c''}\right)\right)} F_v \right] \quad (2-12)$$

The maximum compressive stress of cracked concrete at the nodal zone should not exceed the maximum concrete softened-compressive strength ($\zeta f_c'$). The softening coefficient is ζ and can be determined as:

$$\zeta = \frac{5.8}{\sqrt{f_c'}} \frac{1}{\sqrt{1 + 400\varepsilon_r}} \quad (2-13)$$

where ε_r is the average transversal strain of cracked concrete subjected to compressive stresses equal to f_c' .

2.7.2. Finite Element Modeling

The finite element method is a powerful tool to assess a wide range of engineering problems numerically in determining the deformation and stress analysis of building and bridge structures. With the development in computer technology and CAD systems, complex problems can now be modelled easily and, hence, several alternative configurations can be tested on a computer. Several FE packages are available to facilitate the process of constructing and solving a model, such as Vector2, DIANA and ABAQUS. In this section, a summary of research conducted on RC beam-column joints using FE software ABAQUS is described.

Danesh et al. (2008)

Danesh et al. (2008) carried out a finite element investigation using ABAQUS to study the effectiveness of GFRP layers for strengthening shear deficient of exterior RC beam-column joint tests conducted by El-Amoury and Ghobarah (2002). The FE study covered the unstrengthened and strengthened beam-column joint specimens.

The concrete damage plasticity (CDP) was employed to model the concrete behaviour in the plastic range where the failure of concrete was characterized with the tensile cracking and compressive crushing mechanism. Inelastic concrete stress-strain response under uniaxial compression was defined in forms of stress-inelastic strain response, while the concrete under uniaxial tension was assumed to be linear until the initial macroscopic cracks at failure was formed. Longitudinal and transverse steel reinforcement behaviour was modelled as an elastic-plastic material using bilinear curve. In addition, the GFRP was assumed to be an orthotropic material, where the failure criterion was generally defined in the stresses space

based on the shear strength and the maximum compressive and tensile strength in orthogonal directions. The concrete elements were discretised using an 8-node solid element (C3D8R) while T3D2 and four-node shell elements (S4R) were used to model the reinforcement and GFRP elements, respectively.

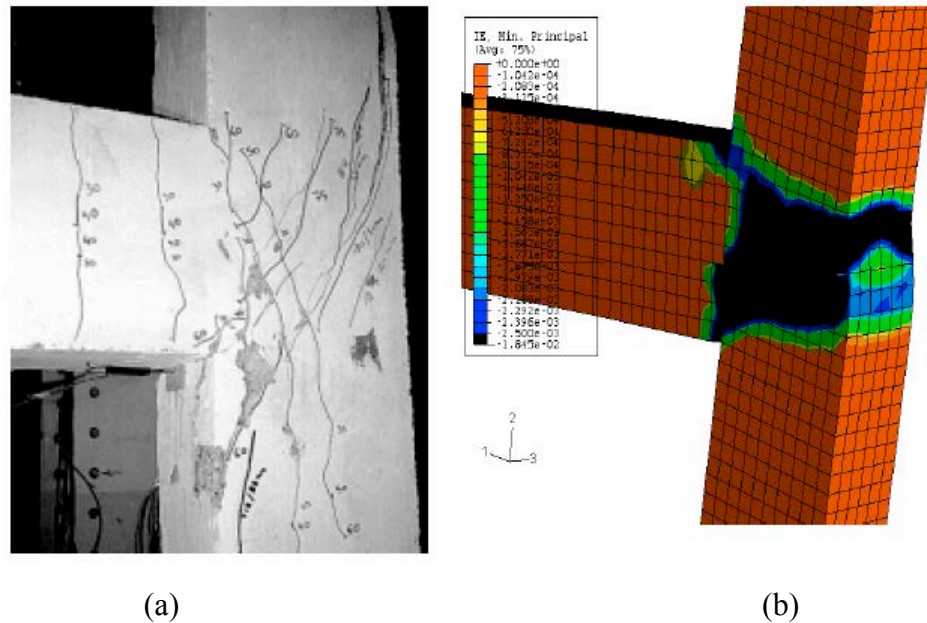


Figure 2.37. Comparison of damage propagation in the joint between the experiment and the FE model: (a) Experiment conducted by T. El-Amoury and Ghobarah (2002); (b) FE model by Danesh et al. (2008)

The crack propagations in the experiment were compared to those of the FE analysis in Figure 2.37. In the experiment, the joint failure was observed before the yielding of the main beam longitudinal bars. To recognize the crushed element in the FE study, the minimum strain at the crushing concrete was assumed at a value of 0.0025. The comparison of the crack pattern between the experiment and the FE study showed a good accuracy; both results showed cracks initiated at the upper side of the beam-column interface and the diagonal crack propagated towards the joint and reached the back of the column face at failure.

Abbas et al. (2014)

Abbas et al. (2014) conducted FE simulations to investigate the behaviour of steel-fibre RC (SFRC) beam-column joints tested by Bayasi and Gebman (2002) subjected to combination of reversed cyclic and constant column axial load. The 8-node brick elements were used to discretize the concrete element. Sensitivity analysis was conducted to determine the optimum mesh element size. Based on the validation to the experiment, the 50 mm element size was chosen, as it showed the best results to reproduce the experiment data. The reinforcement bars were modelled using the two-node truss element and were precisely located to match the reinforcement details in the experiment. In addition, the pre-mature localized cracking at the loading point and supports was avoided by utilizing a rigid element to distribute the stresses developed during the analysis.

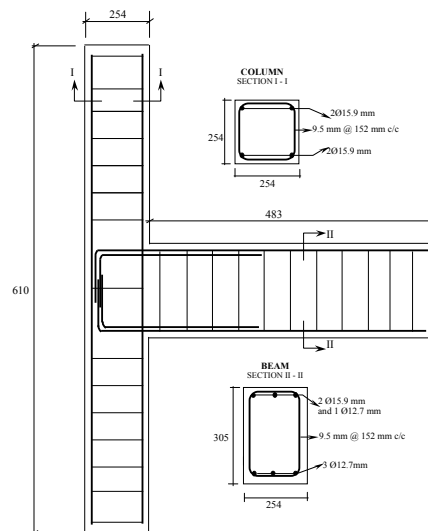


Figure 2.38. Geometry and reinforcement details of exterior beam-column joint tested by Bayasi and Gebman (2002)

From the experiment, steel-fibres enhanced the tensile post-cracking and exhibited concrete more ductile compared to the plain concrete (Kotsovos and Pavlović, 1995). However, the improvement was not observed in the case of uniaxial compression. This concluded that the

introduction of steel-fibres improved concrete in tension, preventing the formation of crack, whilst in compression their effect on concrete in compression could be neglected. Hence, the brittle cracking model in ABAQUS was used to model the concrete. This model was used for concrete in which the material behaviour is dictated by tensile cracking. Elastic-plastic material using bilinear curve (See Figure 2.39.(a)) was adopted to model the conventional steel reinforcement bars.

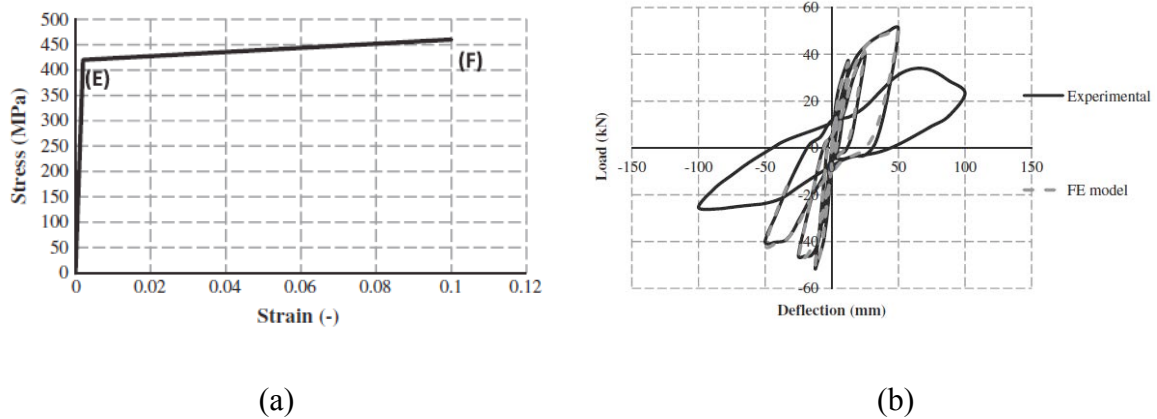


Figure 2.39. FE analysis of Abbas et al. (2014): (a) Conventional steel reinforcement bars model; (b) Load-displacement hysteresis for the FE and experiment results

The analysis was carried out using explicit dynamic procedure available in ABAQUS/Explicit with a low rate of loading. The results comparison between the experiment and FE analysis showed a good agreement as depicted in Figure 2.39.(b). The failure in the FE analysis was associated with the increase in the kinetic energy, indicating the extensive cracks propagated within the joint region. However, the maximum ductility achieved in the FE was 50% lower than that of in the experiment.

Kam (2014)

Kam (2014) developed FE models using ABAQUS to study the effects of beam widths and beam depths on the performance of RC wide beam-column joints subjected to cyclic load. A

linear 8-node solid element (C3D8R) was used to model the concrete elements. The first order fully integrated element will experience locking behaviour under bending and resulted in false shear strain; hence the stiffness under bending will be over predicted. This issue can be solved by using reduced integration method, but this will bring another problem, “hourglassing” (Kam, 2014). C3D8R element has one integration point; all the developed strains will be evaluated as zero and cause an uncontrolled distortion. In order to achieve accurate results, enhanced hourglass control should be implemented. The beam and column longitudinal reinforcements were modelled using 2-node 3D truss element (T3D2) and were perfectly bonded to the concrete element. The CDP model was employed to model the concrete behaviour under cyclic load in which the compressive crushing and the tensile cracking are the main failure mechanisms. Two constitutive models were used to model the steel reinforcement bar: the fixed angle softened truss to model the behaviour of mild steel and elastic perfectly plastic relationship to model the behaviour of high yield steel.

In order to capture the pinching effect, cohesive crack was employed to model the diagonal cracks at the joint and cracks at the beam. In cohesive crack, the cracks are defined as surface-to-surface contact that is applied by a small sliding formulation. In his study, Kam (2014) utilized five contact pairs as depicted in Figure 2.40.

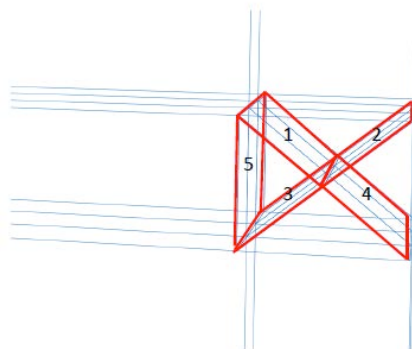


Figure 2.40. Contact pairs at the joint (Kam, 2014)

The results showed that the beam width had significant contribution in controlling the seismic performance at a joint by affecting the load transfer path in wide beams and the corresponding joint core. On the other hand, the beam depth was found insignificant effect in altering the load path, but it affected the seismic performance of the joint. The result also showed that joint shear stress in wide beam-column joint is higher than that of conventional joint.

2.8. CURRENT CODE OF PRACTICES IN DESIGNING REINFORCED CONCRETE BEAM-COLUMN JOINTS

2.8.1. ACI 318-14: Building Code Requirements for Structural Concrete and Commentary (2014)

The ACI 318-14 mentions that joint shear strength is not sensitive to the amount of shear reinforcement and is only set as a function of concrete compressive strength, provided that the required minimum amount of transverse reinforcement is installed for confinement.

The total cross-sectional area of rectangular hoop reinforcement shall not be less than that required by both:

$$A_{sh} = 0.3sb_c \left(\frac{A_g}{\#A_{ch}} - 1 \right) \left[\frac{f'_c}{f_{yt}} \right] \quad (2-14)$$

$$A_{sh} = 0.09sb_c \frac{f'_c}{f_{yt}} \quad (2-15)$$

where:

A_g = gross area of concrete section, mm²

A_{ch} = cross-sectional area of a member measured to the outside edges of transverse reinforcement, mm²

s = centre-to-centre spacing of transverse reinforcement, mm

b_c = cross-sectional dimension of member core measured to the outside edges of the transverse reinforcement, mm

f_c = concrete compressive strength, MPa

f_{yt} = yield strength of transverse reinforcement, MPa

Transverse reinforcement shall be spaced at a distance not exceeding: (a) one-fourth of the minimum dimension; (b) six times the diameter of the smallest longitudinal bar; and (c) s_o , as calculated by:

$$s_o = 100 + \left(\frac{350 - h_x}{3} \right) \quad (2-16)$$

where h_x is the maximum centre-to-centre spacing of longitudinal bars laterally supported by corners of crossties around the perimeter of the column.

The nominal joint shear strength is determined according to different joint geometry, as follows:

For joints confined by beams on all four faces:

$$V_n = 1.7\lambda\sqrt{f'_c A_j} \quad (2-17)$$

For joints confined by beams on three faces or on two opposite faces:

$$V_n = 1.2\lambda\sqrt{f'_c A_j} \quad (2-18)$$

For other cases:

$$V_n = 1.0\lambda\sqrt{f'_c A_j} \quad (2-19)$$

where f'_c is the concrete compressive strength and A_j is the effective joint area.

2.8.2. ACI-ASCE Committee 352R-02

The ACI-ASCE Committee 352R-02 code provides recommendations for determining proportions, design and details of monolithic beam-column connections in cast-in-place concrete frame construction. The recommendations are prepared to comply with the strength and ductility requirements related to the function of the connection within a structural frame. The structural connections are classified into two categories:

- Type 1 is composed of members designed to satisfy ACI 318 strength requirements without significant inelastic deformation.
- Type 2 is designed to have sustained strength under deformation reversals into the inelastic range.

The nominal joint shear strength is computed using equation:

$$V_n = 0.083\gamma\sqrt{f'_c} b_j h_c \quad (2-20)$$

where h_c and f'_c are the column depth in the direction of joint shear being considered and the concrete compressive strength, respectively. The effective joint width b_j should not exceed the smallest of the three values in Equation (2-21):

$$\left\{ \begin{array}{l} \frac{b_b + b_c}{2} \\ \# \quad b_b + \sum \frac{mh_c}{2} \\ \% \\ b_c \end{array} \right. \quad (2-21)$$

The constant γ depends on the connection classification and type as shown in Figure 2.41.

The stirrup reinforcements required to confine the column should be at least equal to:

$$A_{sh} = 0.3 \frac{s_h b_c'' f_c'}{f_{yh}} \left(\frac{A_g}{A_c} - 1 \right) \quad (2-22)$$

but should not be less than:

$$A_{sh} = 0.09 \frac{s_h b_c'' f_c'}{f_{yh}} \quad (2-23)$$

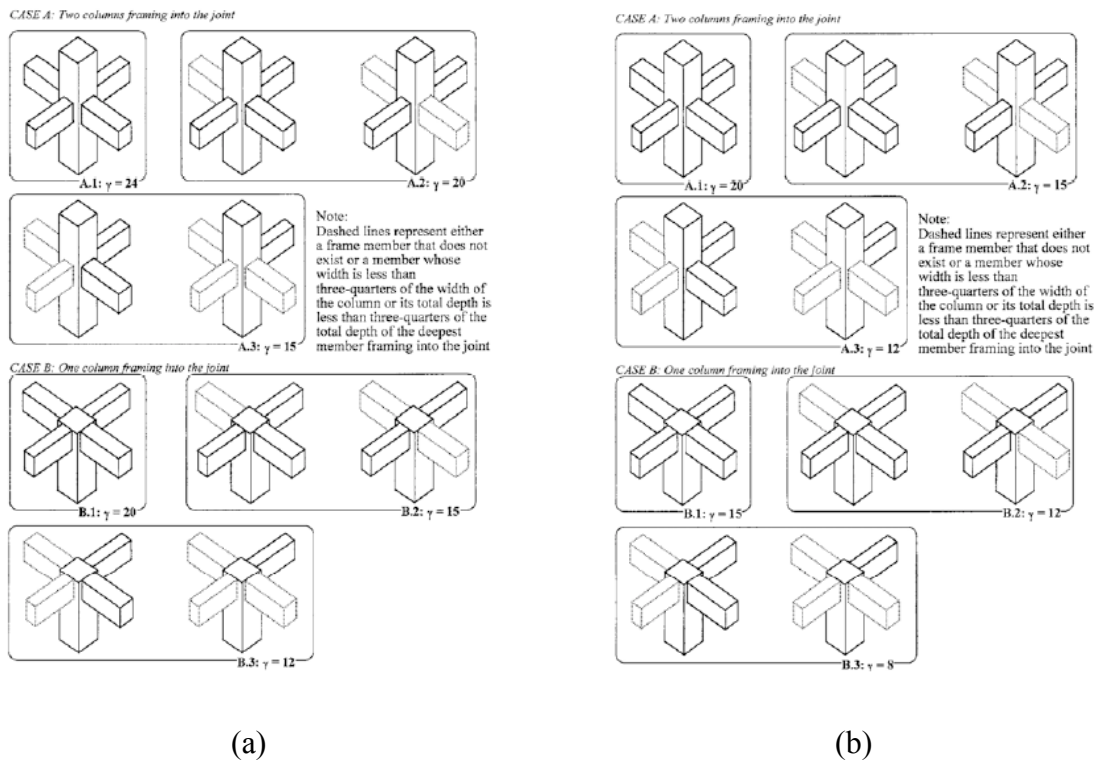


Figure 2.41. γ values for: (a) Type 1; and (b) Type 2 connections, ACI-ASCE 352R-02

2.9. SUMMARY

Based on the literature review and current understanding of the seismic behaviour of shear deficient exterior RC beam-column joints, the following conclusions can be summarised:

1. RC beam-column joints of buildings constructed prior to the 1970s are prone to sustain shear failure in the joint under seismic excitations. This is based on findings from beam-column joint tests and post-earthquake reports.
2. The major drawbacks of pre-1970s RC structures have been classified as column, beam, and frame deficiencies. In addition, the most common type of deficiency is the lack of confinement due to the absence of transverse reinforcement in the joint area.
3. A number of key parameters affect the behaviour of exterior RC beam-column joints, such as the ratio of the column axial load, the concrete compressive strength, and the confinement provided by the shear reinforcement in the joint.
4. Numerous rehabilitation techniques have been investigated and adopted to enhance the seismic performance of exterior RC beam-column joints, such as epoxy repair, partial removal and replacement of the concrete of damaged elements, RC and steel jacketing. Those techniques are referred to as conventional techniques and are associated with various difficulties in practical applications.
5. Recent efforts have focused on the use of FRPs for upgrading the existing beam-column joints in various ways, such as epoxy-bonded, and near surface mounted rods.
6. The FRP strengthening techniques were shown to provide significant benefits and advantages over the conventional techniques, e.g. high strength-to-weight ratio, high corrosion resistance, light unit weight and high durability.
7. Experimental research into beam-column joints strengthened using externally bonded FRPs also showed that debonding of the FRPs was followed by the rupture of the

fracture of FRPs at subsequent loading stages. In terms of practical applications of the FRPs, surface preparation of the concrete substrate is required and the adhesive material needs to be applied by skilled workers.

8. The DE technique was developed for the strengthening of shear deficient concrete beams by Valerio et al. (2009) and Chaallal et al. (2011). Their test results showed that the DE technique is more effective compared to the conventional EB and NSM techniques, because this technique relies on the direct transfer of stresses from the FRP to the core of concrete. Moreover, surface preparation and protection against fire and vandalism are not required.

CHAPTER 3

EXPERIMENTAL PROGRAMME

3.1. GENERAL

This chapter describes the experimental study performed on exterior RC beam-column joints subjected to reversed cyclic loading. Details on manufacturing the beam-column joint specimens, properties of the materials used in the construction and strengthening scheme, the test setup and loading procedure are provided. The instrumentation used for load, global and local deformation and strain measurement together with the equations used for analyzing the experimental data are also discussed in this chapter.

3.2. MATERIAL PROPERTIES

3.2.1. Concrete

Beam-column joint specimens were designed and constructed using normal weight concrete with a target concrete cylinder compressive strength of 30 MPa and a maximum aggregate size of 20 mm. This compressive strength value was chosen to represent concrete strength in existing buildings with inadequate shear reinforcement in the joint constructed before the introduction of modern seismic design codes. The mix proportion of coarse aggregate/sand/cement for all batches was 1:2.5:3. The water cement ratio (w/c) for each specimen was 0.42. The specimens were cast in a horizontal position (on the side) and were mechanically vibrated to eliminate voids and then they were wet-cured in the laboratory for seven days. Polyethylene sheets were used to cover the wet burlap to retain moisture. To determine concrete properties, cubes (100 mm × 100 mm × 100 mm) and cylinders (100 mm

diameter \times 200 mm length) were also prepared and cured under the same conditions as the beam-column joint specimens. Table 3.1 shows the concrete cylinder compressive and tensile strengths on the day of testing.

Table 3.1. Concrete material properties

Specimen	At day of testing	
	f_c (MPa)	f_t (MPa)
BCJ-CS test #1	33.71	3.17
BCJ-CS test #2	31.31	3.12
BCJ-SS-S4	45.52	3.65
BCJ-SS-F4	31.80	3.29
BCJ-SS-S8	24.88	2.22
BCJ-SS-F8	32.29	3.35
BCJ-CS-B	28.68	2.57

The actual concrete compressive and tensile strengths were obtained from the average value of compressive and tensile splitting tests carried out on the cube and cylinder specimens respectively.

3.2.2. Steel

Two sizes of grade B500B deformed steel bars were used as longitudinal and transverse reinforcement. The longitudinal reinforcement bars were 16 mm in diameter while 8 mm bars were used as stirrups. The average values of yield strength (f_y), ultimate strength (f_u) and elastic modulus (E_s) of the steel reinforcement obtained from three samples are shown in Table 3.2 and stress-strain curve for 8 mm steel reinforcement is provided in Figure 3.1

Table 3.2. Steel reinforcement properties

Bar size (mm)	f_y (MPa)	f_u (MPa)	E_s (MPa)	Remarks
8	581	672	198672	Stirrups
16	512	671	200000	Beam and column longitudinal reinforcement

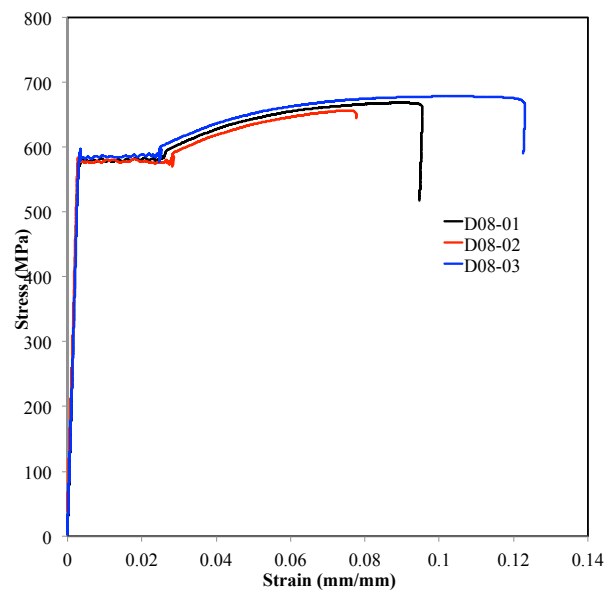


Figure 3.1. Stress-strain curves

3.2.3. Carbon Fibre Reinforced Polymer

High strength carbon FRP (CFRP) bars (Carbopree& HS7.5) were used for retrofitting. The properties provided by the manufacturer, Sireg SpA (Italy), are as follows: diameter=7.5 mm, tensile strength=2300 kN and modulus of elasticity=130 GPa. Further information can be found in Appendix A.1.

3.2.4. Epoxy Resin

The epoxy resin used for the bonding of CFRP bars was HIT-RE 500 from Hilti Inc. HIT-RE 500 is an ultimate-performance epoxy based adhesive that consists of two components, resin

and hardener. This type of resin is specifically designed for fastening into solid base material in a wide range of material temperatures ranging from -5°C to 49°C . The specifications of this adhesive, as provided by manufacturer, are as follows: compressive strength=82.7 MPa, tensile strength=43.5 MPa, modulus of elasticity=1493 MPa, bond strength=12.4 MPa and absorption=0.06 %.

3.3. DESCRIPTION OF TEST UNITS

Seven exterior RC beam-column joint specimens were constructed. One of the specimens was adequately designed according to the ACI 352R-02 code whilst the rest were designed in accordance to the pre-1970 code provisions to represent joint shear strength deficiency. All specimens had the same dimensions and reinforcement configurations. To study the effect of embedded bar type, steel or CFRP bars were used as additional joint shear reinforcement. The number of embedded bars was also varied in order to examine the effect of joint shear reinforcement ratio.

The specimen design originated from the full-scale beam-column joint tests of El-Amoury (2004). The joint represented a component of a residential RC building structure with floor-to-floor height of 3.00m and 3.74m bays. The structure was constructed in accordance to the pre 1970s specification (ACI 318-63). The original joint dimensions were scaled-down to account for the available space and the testing frame in the laboratory and the reinforcement configurations were designed to expose target failure mode.

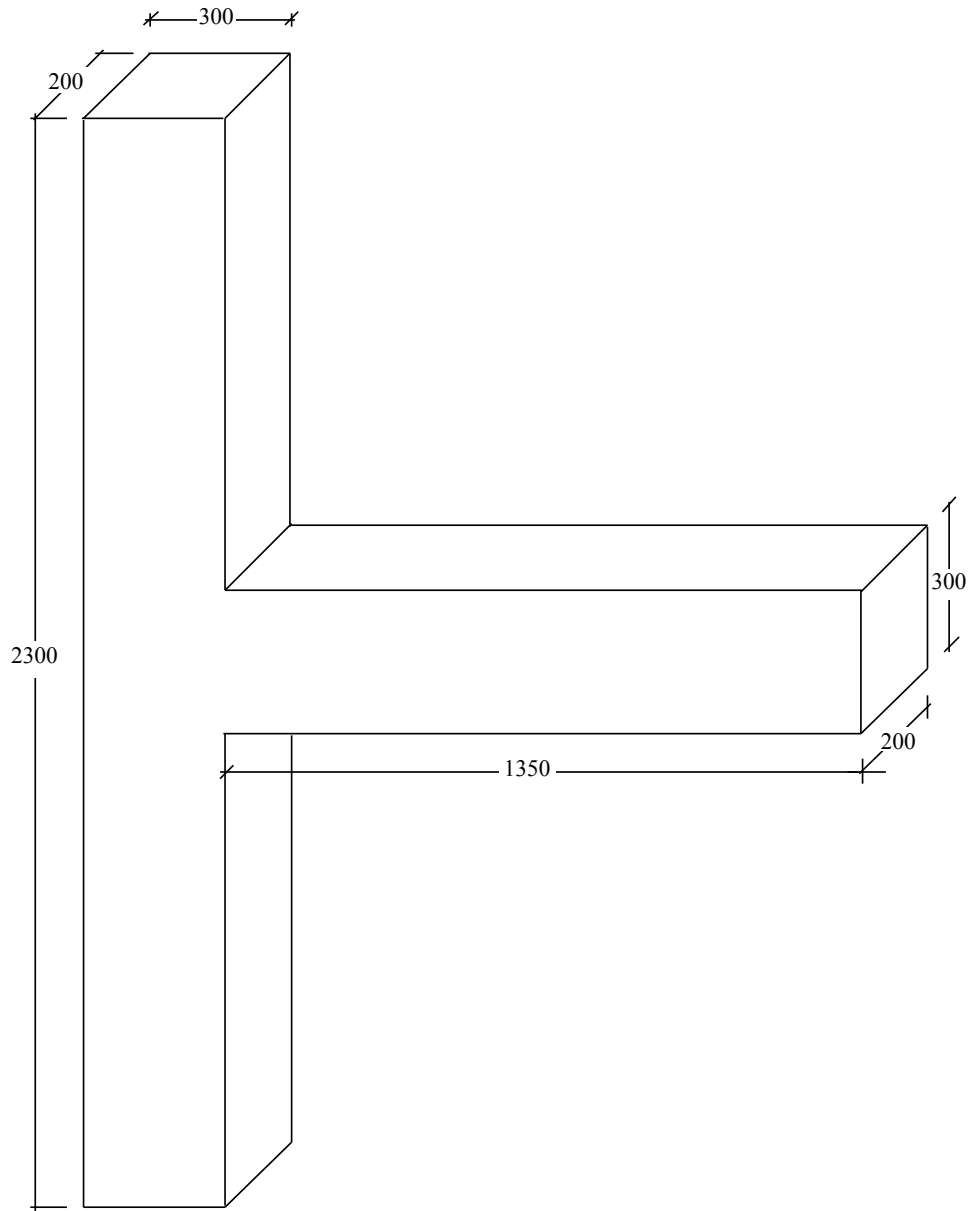


Figure 3.2. The dimensions of a typical specimen, unit in mm.

The beam was reinforced with 3 no. 16 mm deformed steel bars as top and bottom longitudinal reinforcement. These bars were bent into the joint core and extended for a distance of 195 mm ($\sim 12 \times d_b$) to form bars anchorage and eliminate bond failure. For resisting shear force, the beam was reinforced using 8 mm stirrups. The first stirrup was located at a distance of 50 mm from the column face; then the stirrups were spaced at 125 mm centre-to-centre for the following 1000 mm of the beam length. Finally end stirrups were spaced at 50

mm centre-to-centre to prevent bearing failure under applied load (see Figure 3.3). Four corner and four internal 16 mm steel bars were used as longitudinal reinforcement whereas 8 mm bars were used as shear reinforcement for the column. Again, the first stirrup was placed at 50 mm from the beam face and consecutive stirrups were spaced at 125 mm centre-to-centre for the following 750 mm of the column length (see Figure 3.3). Finally end stirrups were spaced at 50 mm centre-to-centre at both column ends. Only one horizontal closed stirrup was installed inside the joint core.

The tested specimen had a three-part designation. The first part, BCJ, stands for beam-column joints. The second part explains whether the specimen was a control (CS) or strengthened (SS) specimen. The last part clarifies whether the specimen was deficient in shear (A), adequately designed (B), strengthened with steel bars (S#) or strengthened with CFRP bars (F#), where # refers to the number of embedded bars in joint core.

Table 3.3. Details of tested beam-column joint specimens

No	Specimen	Axial load ($\% \times f_c \times A_g$)	Number of stirrups in joint core	Number of embedded bars in joint core	Strengthened	Number of test	Description
1	BCJ-CS-A (Group A)	8	1	0	No	2	Controlled specimen-shear deficient
2	BCJ-SS-S4			4	Yes-Steel bar	1	Shear deficient
3	BCJ-SS-F4 (Group B)				Yes-CFRP bar		Shear deficient
4	BCJ-SS-S8		5	8	Yes-Steel bar	1	Shear deficient
5	BCJ-SS-F8 (Group C)				Yes-CFRP bar		Shear deficient
6	BCJ-CS-B (Group D)		5	0	No	1	Adequately designed control specimen

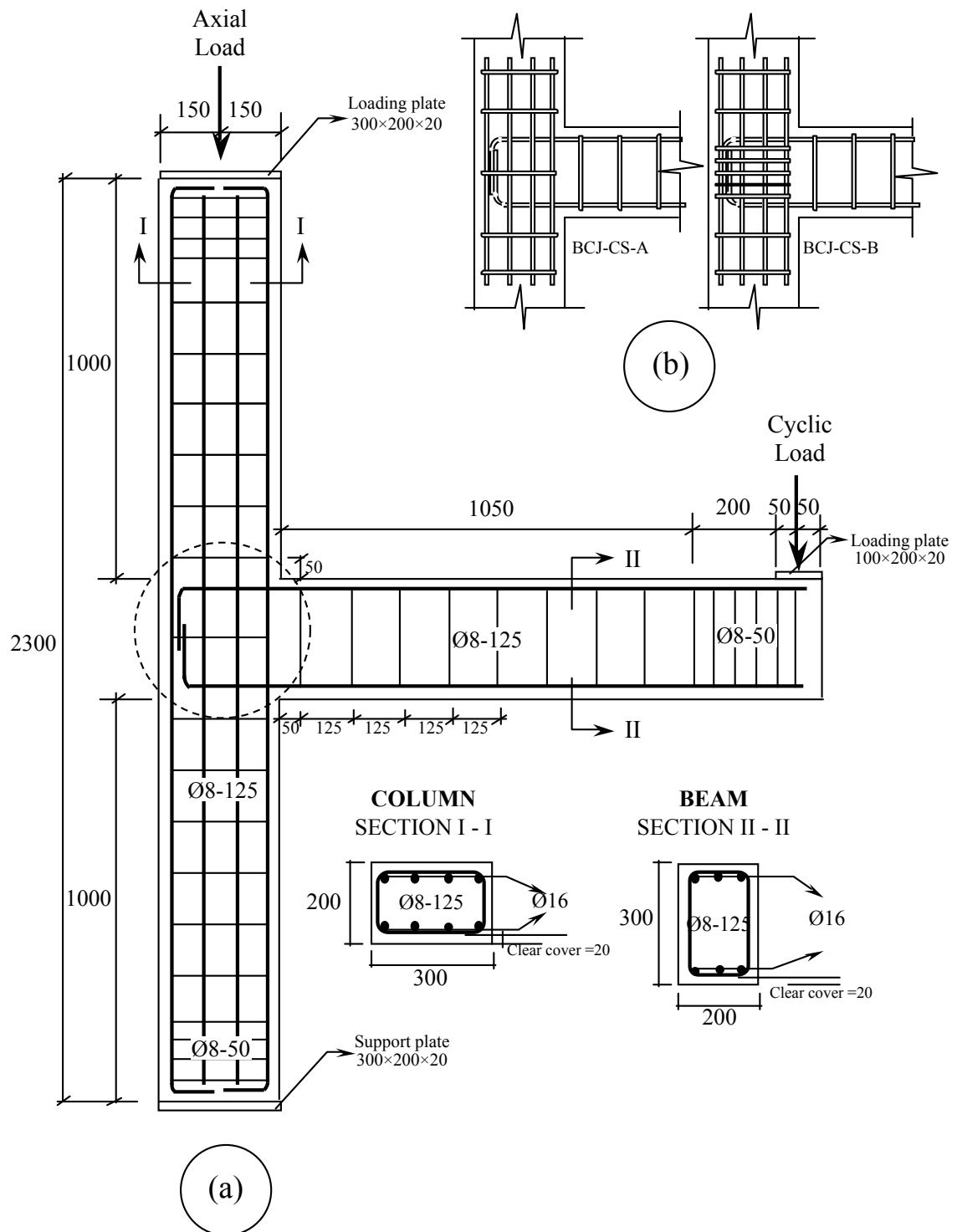


Figure 3.3. (a) Reinforcement details of the test specimens; (b) Shear reinforcement in the joint for BCJ-CS-A and BCJ-CS-B; unit in (mm)

The estimated flexural capacity of the beam based on ACI 318-14 code for a concrete strength of 30 MPa was 72 kN-m for both positive (upward) and negative (downward) loading, whereas the column flexural capacity was 88.6 kN-m under an axial load of 150 kN. This gives a column-to-beam flexural capacity ratio ($M_{n,c}/M_{n,b}$) of 1.23 and thereby avoid the strong beam-weak column condition (refer to section 18.7.3.2 ACI 318-14). The joint shear stress at flexural failure of the specimen is 820 psi (5.6 MPa) which is higher than the allowable joint stress, $12\sqrt{f'_c}$ (f'_c in psi), making the beam-column joint subassembly deficient in shear (Ehsani and Wight, 1985).

Table 3.4. Details of beam-column joint specimens, dimensions and reinforcement

Specimen code	Column characteristics			Beam characteristics			Joint area	
	Sections (mm)	Bars (mm)	Stirrups (mm)	Sections (mm)	Bars (mm) (Top and Bottom)	Stirrups (mm)	Stirrups	Embedded bars
Group A BCJ-CS-A	200 × 300	8Ø16	Ø8-125	200 × 300	3Ø16 3Ø16	Ø8-125	1Ø8	0
Group B BCJ-SS-S4								4Ø8Steel
BCJ-SS-F4								4Ø8CFRP
Group C BCJ-SS-S8							5Ø8	8Ø8Steel
BCJ-SS-F8								8Ø8CFRP
Group D BCJ-CS-B								0

3.4. MANUFACTURE OF THE SPECIMENS

The test specimens were cast in a horizontal position. A reusable wooden mould was designed for easy assembly and disassembly after casting. The bottom and sides of the mould consisted of 20 mm plywood with the sides stiffened with 50 mm square wooden blocks. The gaps between the plywood sheets were sealed to prevent bleeding of concrete that may occur

during casting. The sides of the mould were tied together using threaded steel rods to prevent bulging of the mould under lateral pressure of wet concrete.

The cage construction was divided into two separate parts: column and beam. To build each reinforcement cage, longitudinal bars were tied to the two end stirrups after sliding all the stirrups needed inbetween. The intermediate stirrups were then tied to the longitudinal bars. Prior to joining the column and beam cages into one BCJ reinforcement cage, the steel bars were instrumented with strain gauges. The beam cage was then positioned and tied perpendicular to the column cage in the joint area. Finally, one stirrup was placed right in the middle of the joint core. Commercially available spacers were used to maintain the proper cover distance between the mould and the reinforcement bars.

After the BCJ reinforcement cage were placed into the mould, four threaded steel rods were installed at the upper and lower end of column cage (Figure 3.4.(b) and 3.4.(c)). These threaded rods were needed to attach the loading plate and the support plate to the upper and lower end column, respectively. The threaded rods were placed at the required position inside on each end of column reinforcement cage and bolted to the upper and lower end of column mould.



(a) Reinforcement cage



(b) Column upper end detail



(c) Column lower end detail



(d) Joint reinforcement detail



(e) Specimen after casting



(f) Specimen during curing

Figure 3.4. Construction details of beam-column joint specimens

Care was taken during strain gauge installation. Strain gauges were placed on both column and beam flexural reinforcement at selected locations within the joint area (see section 3.8). Ribs of the bars at strain gauge location were removed and the surface was smoothened using fine sand paper until any scratches disappeared. The bar surface was cleaned and the strain gauge was glued to the bar surface and coated to avoid damage during concrete casting. At any location, two strain gauges were installed to provide redundancy. The wires were gathered into bundles and run along the centre of reinforcing cage to the nearest end in order to hinder the loss of concrete-rebar bond.

3.5. STRENGTHENING APPLICATION

In order to install the embedded bars, holes were made within the joint core by installing 10 mm acrylic rods at the required positions within the joint reinforcement cage before casting the concrete. The acrylic rods were removed from the concrete one day after casting. Prior to installing the embedded bars, the holes were enlarged by drilling them using 12 mm driller bit and then cleaned by a wire brush and compressed air to remove any cement or aggregate residues. This procedure was also to ensure that the holes had higher surface roughness and consequently allowing better bond performance between the concrete and embedded bars. A high viscosity epoxy adhesive was used to fill two third of the holes. The bars were then covered with a thin layer of the adhesive and inserted into the holes. Any excess epoxy was removed. It should be noted that Valerio et al. (2009) demonstrated that it was possible to install embedded bars by drilling holes. The procedure explained above was used for simplicity, as it did not require drilling holes.

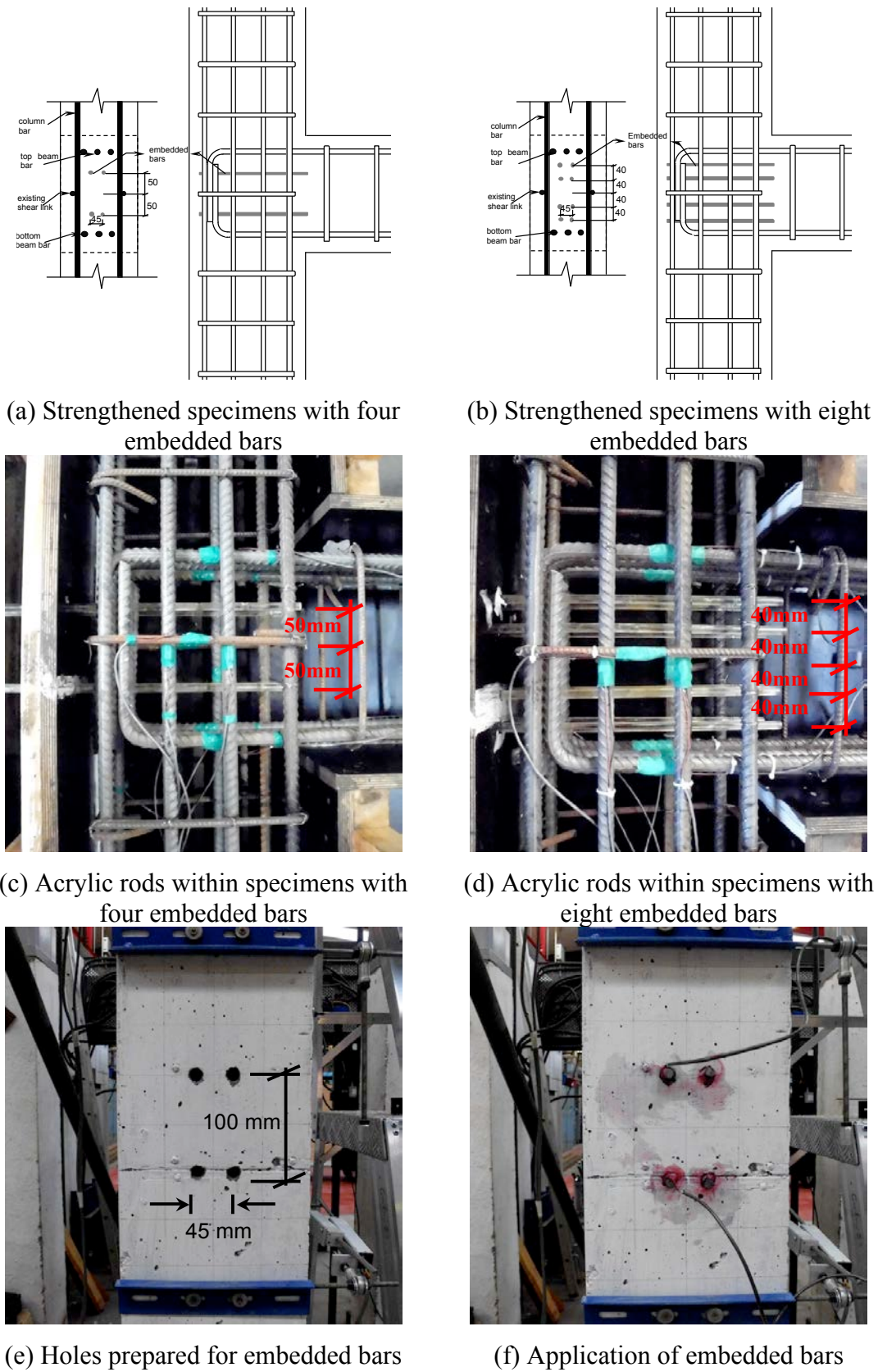


Figure 3.5. Strengthening configuration

3.6. TEST SET-UP

The test rig comprised two separate frames; one reaction frame was used to resist the axial load applied on the column whereas the other reaction frame was used to resist the cyclic load applied on the beam. The specimens were tested with the column in the vertical position, hinged at the top and bottom column ends and subjected to a cyclic load applied at the beam tip using a hydraulic actuator of ± 100 mm stroke. A 30 mm thick steel plate was connected to a channel section using 4 20 mm threaded rods to form a collar. The bottom column hinge consisted of two 30 mm thick steel plates with semi-spherical grooves separated by a steel roller. The top and bottom column ends were supported laterally against a reaction frame. Figures 3.6 and 3.7 show schematic diagrams of the test setup.

A constant axial load of 150 kN was applied on the column using a hydraulic jack (see Figure 3.8). This load represents the gravity load that acts on the column from upper floors and was approximately equal to $0.08f_c A_g$, where f_c is concrete cylinder compressive strength and A_g is column cross-sectional area. This column load was continuously adjusted in such a way that the axial load acting on the column remained constant. However, an insignificant variation (± 25 kN) was unavoidable due to the vertical reaction to the cyclic load applied at the beam tip.

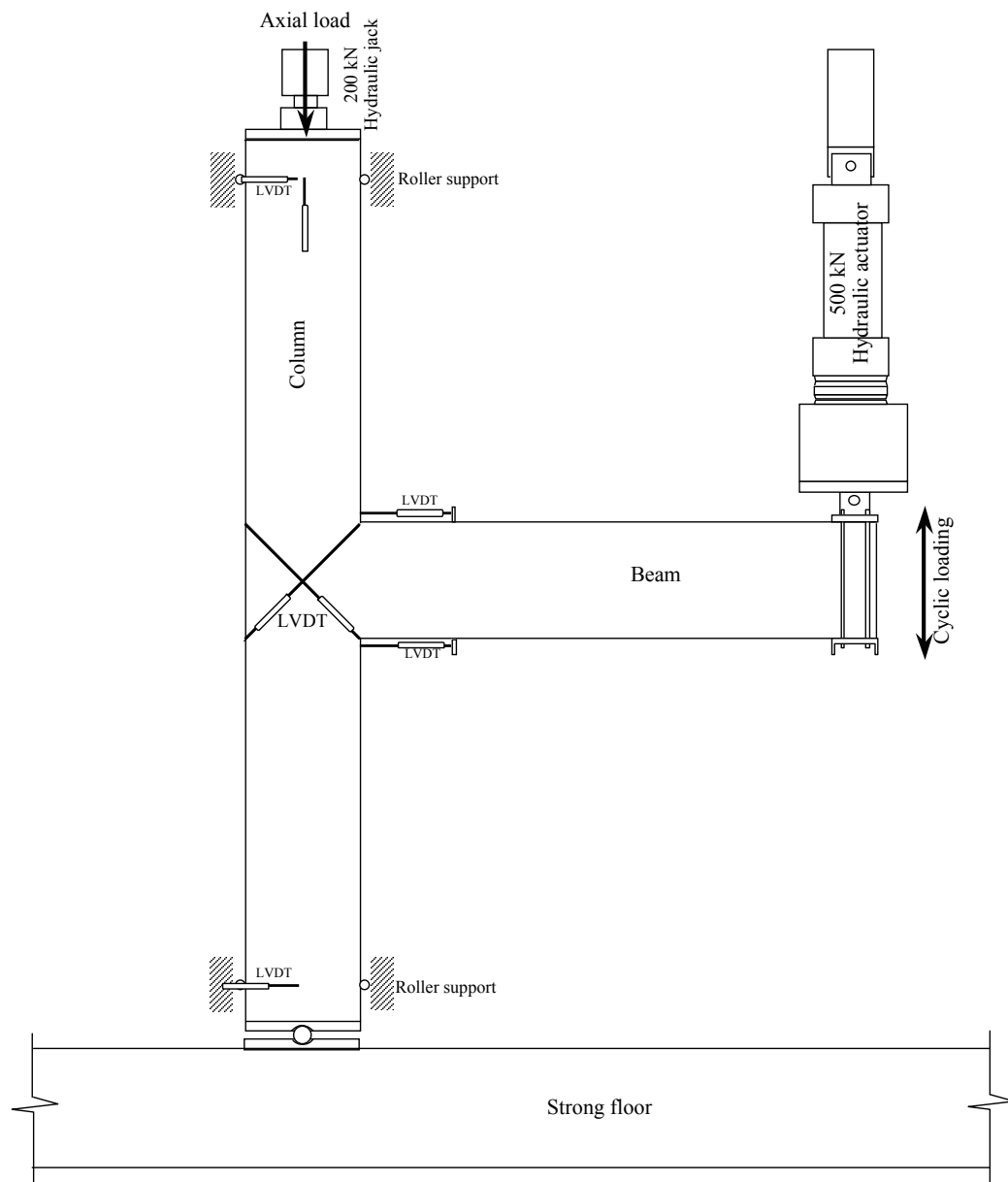


Figure 3.6. Experimental set-up – schematic drawing

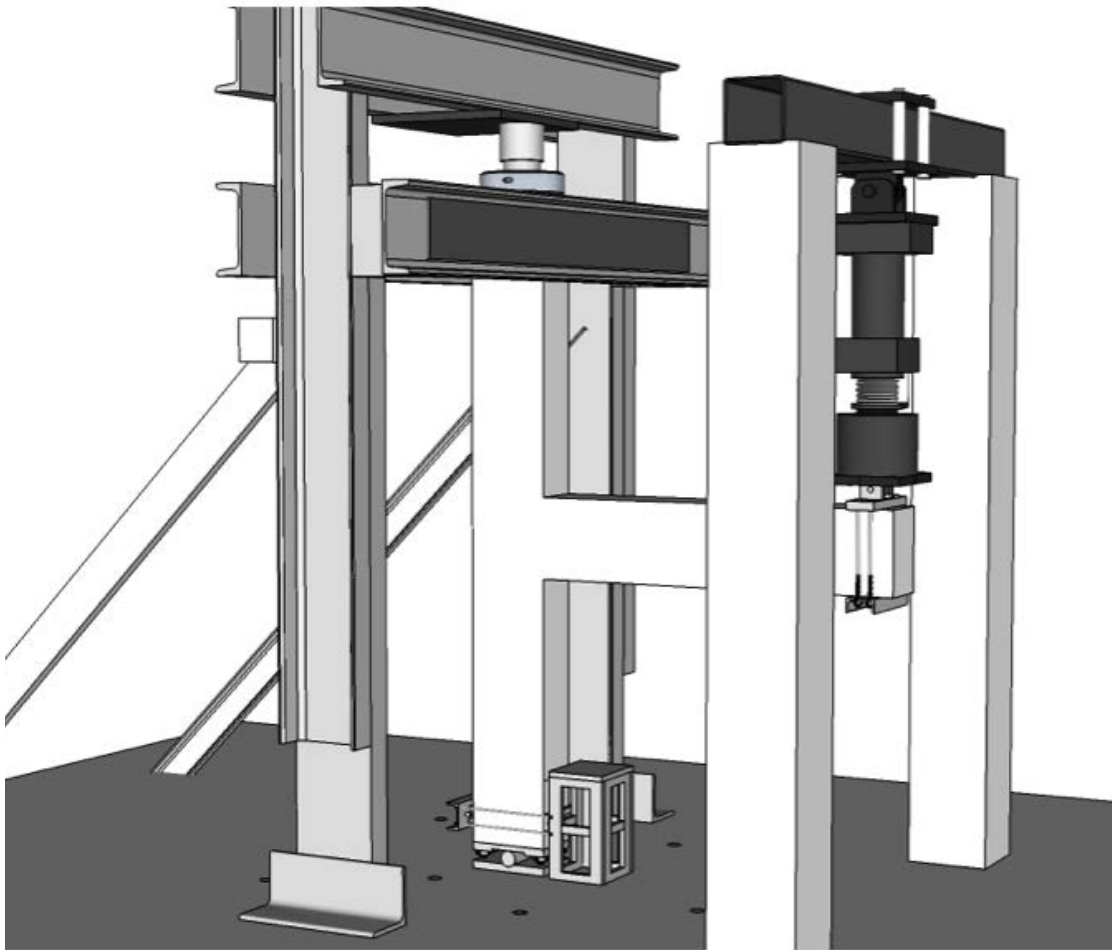


Figure 3.7. 3D view of setup

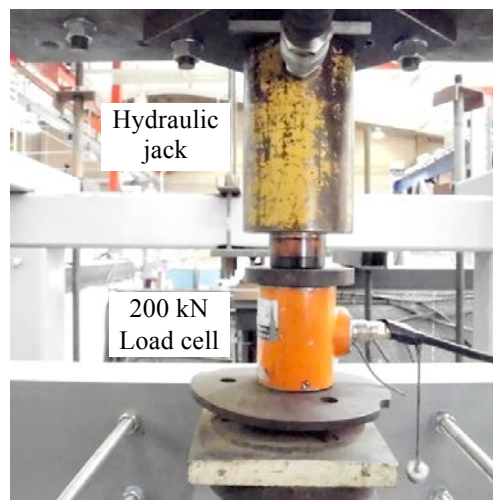
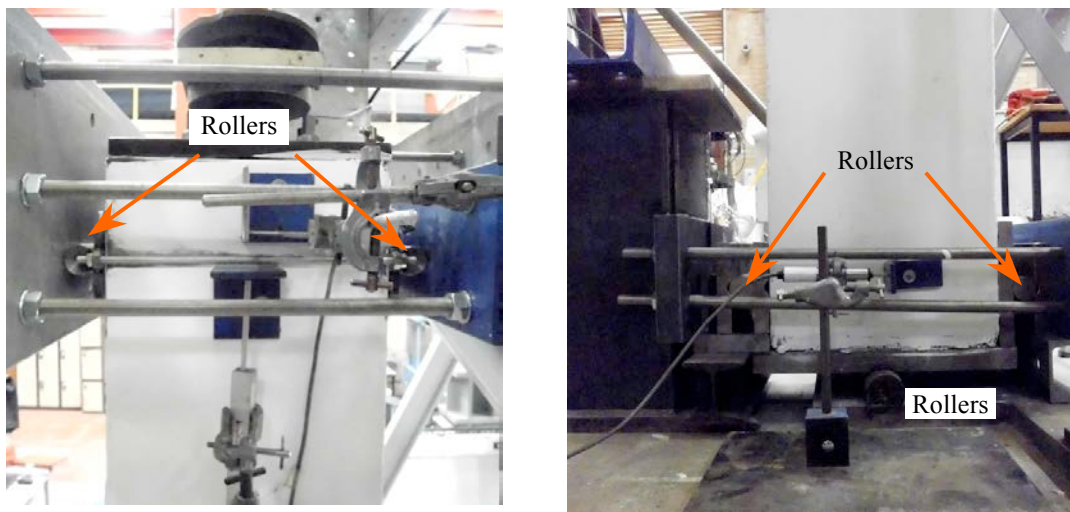


Figure 3.8. Hydraulic jack used to apply axial load on the column

The two ends of the column were restrained against both vertical and horizontal displacements whereas their rotations were allowed (hinged boundary conditions). These boundary conditions were achieved by supporting the column in the horizontal direction using roller supports as depicted in Figure 3.6. Also, each end was tied down to the strong floor to prevent vertical displacements, as shown in Figure 3.9.



(a) Column upper end support

(b) Column lower end support

Figure 3.9. Column support

3.7. LOADING PROTOCOL

The specimens were designed to experience shear failure at the joint without development of the full flexural capacity of the beam section. The hierarchy of strength and sequence of events proved that the unstrengthened specimens experience joint shear cracking at the load of 20.9 kN while first yield of the beam reinforcement occurs at the load of 46.6 kN (refer to Appendix A.2 Section E). Wong (2005) suggested that displacement control, which is based on inter-story drift ratio, should be used for testing shear deficient beam-column joint. The advantage of drift ratio-based displacement control is that it enables examination of the joint shear capacity well after the development of joint shear cracks in both diagonal directions, but

without significant deterioration of the joint strength due to severe cyclic loading. As suggested in ACI 374, a minimum of two cycles at each of deformation level is sufficient to incur damage associated with the number of cycles at a given drift level. In this research, the displacement was gradually increased to achieve the specific inter-story drift ratios of 0.04%, 0.10%, 0.25%, 0.35%, 0.50%, 0.75%, 1.00%, 1.50%, 2.00%, 3.00%, 4.00%, 5.00% and 6.00% (see Figure 3.9). Inter-story drift ratio is defined as:

$$\text{Inter-story drift ratio} = \frac{\delta}{L} \quad (3-1)$$

where δ is the vertical displacement of the beam-end and L is the distance from the loading point to the column face ($L = 1300$ mm).

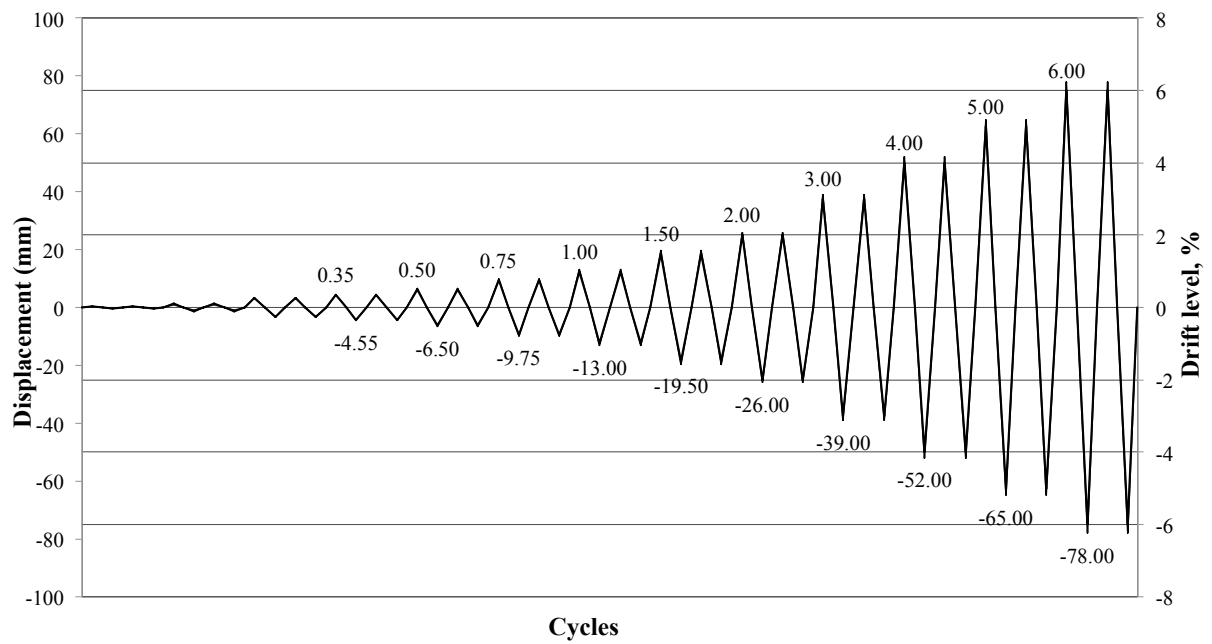


Figure 3.10. Loading history

3.8. DATA ACQUISITION SYSTEM

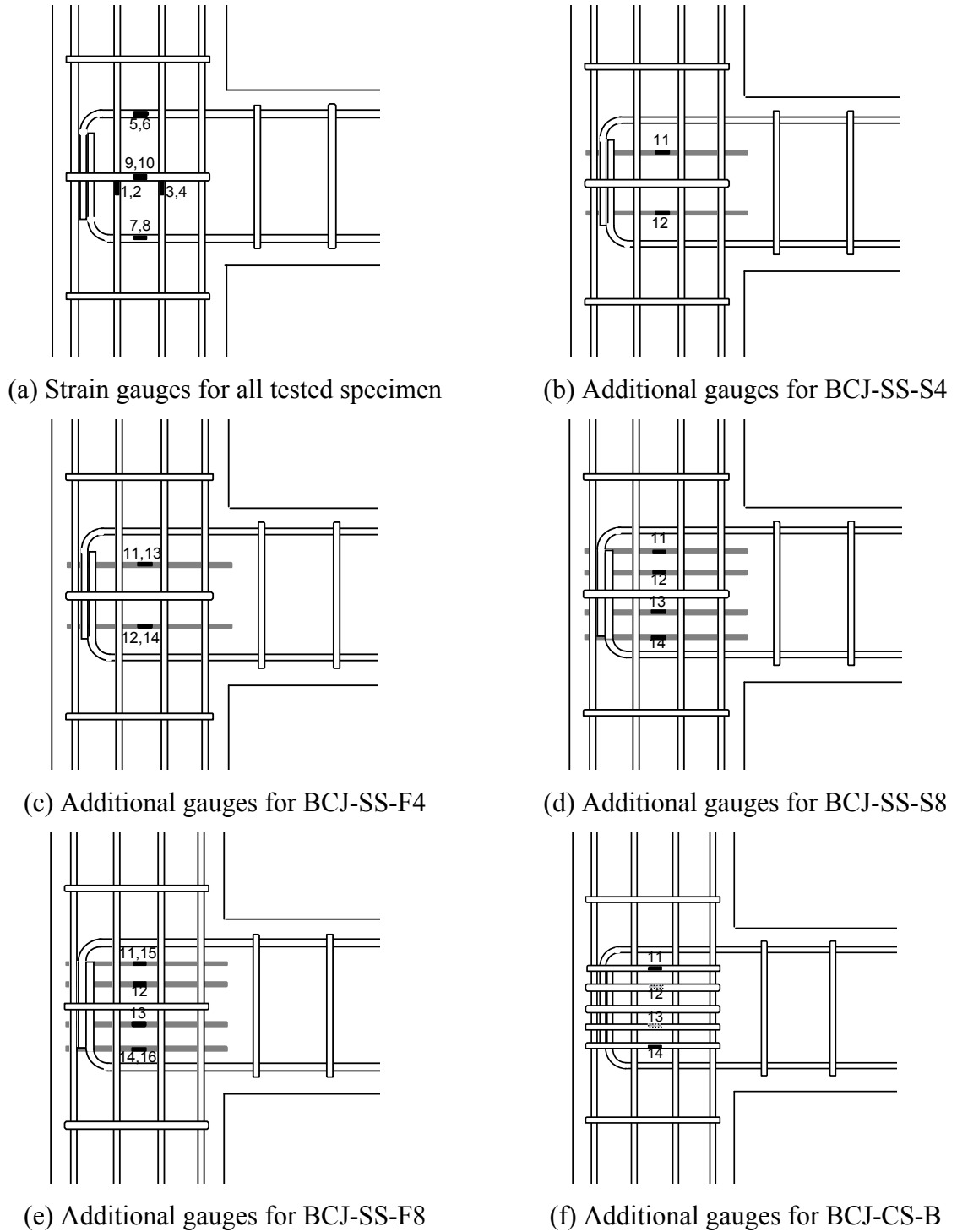


Figure 3.11. Strain gauge locations

A data acquisition system was used to record the readings of all strain gauges, LVDTs and load cells continuously throughout the test. The instrumentations were installed in order to measure the developed strain and displacements. Two longitudinal bars at each side of the beam were instrumented with strain gauges to measure the variation of strain at the maximum moment region. Additionally two opposite intermediate column bars were instrumented with strain gauges to measure the developed strain. Furthermore, the stirrup inside the joint core was instrumented with one strain gauge on each side. Figure 3.11 shows the location of strain gauges.

Each specimen was instrumented with LVDTs at several locations (see Figure 3.6 and 3.13) to measure beam rotations and joint deformation. Two LVDTs were installed diagonally on the joint area to measure joint deformation while one LVDT was placed on each beam and column to quantify rigid body movements. At any given locations, the difference between the LVDT readings divided by their spacing would give the rotation value in radians. The joint deformation value (γ) can be calculated from LVDTs readings by substituting into the following equation:

$$\gamma = \frac{\delta - \delta'}{2l} \times (\tan \alpha + \cot \alpha) \quad (3-2)$$

where δ and δ' are the LVDT reading with elongations taken as positive, l is the initial distance between the mounting rods, and α is the initial inclination of the LVDTs to the horizontal or vertical (see Figure 3.11).

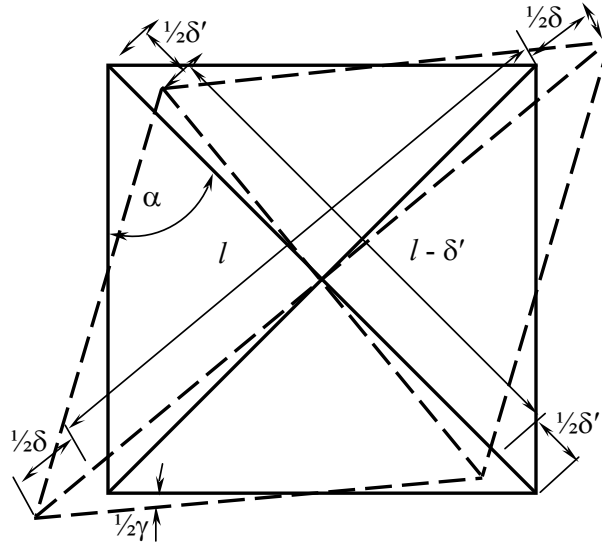
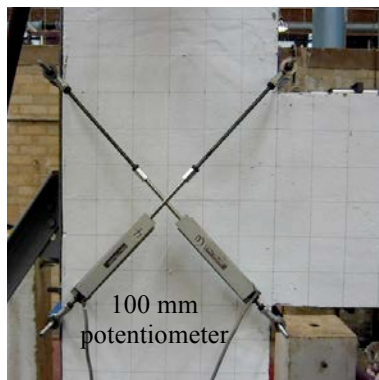


Figure 3.12. Shear deformation measurement on joint area

Two LVDTs were attached to the beam bottom and top surfaces at 150 mm from the column face to measure beam rotations. The angle of beam rotation was calculated as

$$\theta = \frac{\delta_1 - \delta_2}{h_b} \quad (3-3)$$

where h_b is the beam depth while δ_1 and δ_2 are the bottom and top displacements measured on the tension and compression beam faces, respectively.



(a) LVDTs for joint distortion
measurement



(b) LVDT for beam rotation
measurement

Figure 3.13. LVDT location

CHAPTER 4

EXPERIMENTAL RESULTS

4.1. GENERAL

The experimental findings of the unstrengthened and strengthened RC beam-column joints as well as those of an adequately designed RC beam-column joint are presented in this chapter. The failure modes and damage propagation observed during testing are reported. The strength, stiffness, energy dissipation characteristics and strain readings on critical locations within the joint area are also evaluated to compare the performance of the specimens and identify the effect of the proposed strengthening system.

4.2. TEST RESULTS AND OBSERVATIONS

4.2.1. Control specimen, BCJ-CS-A Test #1

The control specimen, BCJ-CS-A, was designed to fail in shear in order to create a baseline reading for the remaining specimens. The test results in terms of the maximum recorded/calculated values for each loading direction are summarised in Table 4.1 whilst curves for story column shear and horizontal shear stress at joint are presented in Appendix 5.

Table 4.1. Summary of test results for BCJ-CS-A test #1

Drift Level (%)	Loading		Applied Load/Stress			Joint Panel Results		
	Cycle	Direction	^a V_c	^b V_{jh}	^c v_{jh}	^d p_t	^e p_c	^f γ
			(kN)	(kN)	(MPa)	(MPa)	(MPa)	*10 ⁻³ (radian)
0.04	1 st	Upward	0.925	6.993	0.117	0.006	-2.090	-0.0022
		Downward	-1.319	-9.968	-0.166	0.013	-2.096	-0.0044
	2 nd	Upward	1.063	8.037	0.134	0.009	-2.092	-0.0087
		Downward	-1.340	-10.124	-0.169	0.014	-2.097	-0.0087

Drift Level (%)	Loading		Applied load/stress			Joint Panel Results		
	Cycle	Direction	^a V_c	^b V_{jh}	^c v_{jh}	^d p_t	^e p_c	^f γ
			(kN)	(kN)	(MPa)	(MPa)	(MPa)	*10 ⁻³ (radian)
0.10	1 st	Upward	2.009	15.186	0.253	0.030	-2.114	-0.0109
		Downward	-3.404	-25.728	-0.429	0.085	-2.168	-0.0065
	2 nd	Upward	2.009	15.186	0.253	0.030	-2.114	-0.0131
		Downward	-3.515	-26.563	-0.443	0.090	-2.174	-0.0175
0.25	1 st	Upward	4.364	32.982	0.550	0.136	-2.219	-0.0087
		Downward	-7.499	-56.674	-0.945	0.364	-2.448	-0.0284
	2 nd	Upward	4.101	30.999	0.517	0.121	-2.204	-0.0153
		Downward	-7.588	-57.353	-0.956	0.372	-2.455	-0.0327
0.35	1 st	Upward	6.118	46.237	0.771	0.254	-2.337	0.0131
		Downward	-9.929	-75.044	-1.251	0.586	-2.669	-0.0546
	2 nd	Upward	5.924	44.776	0.746	0.240	-2.323	0.0153
		Downward	-10.461	-79.062	-1.318	0.638	-2.721	-0.0677
0.50	1 st	Upward	9.266	70.034	1.167	0.523	-2.606	0.0568
		Downward	-13.209	-99.832	-1.664	0.921	-3.005	-0.0830
	2 nd	Upward	9.335	70.556	1.176	0.529	-2.613	0.0677
		Downward	-13.098	-98.997	-1.650	0.910	-2.993	-0.0720
0.75	1 st	Upward	14.293	108.025	1.800	1.038	-3.122	0.1856
		Downward	-17.821	-134.692	-2.245	1.433	-3.516	-0.0939
	2 nd	Upward	13.685	103.433	1.724	0.972	-3.056	0.2009
		Downward	-17.994	-135.997	-2.267	1.453	-3.536	-0.6222
1.00	1 st	Upward	17.255	130.413	2.174	1.369	-3.452	0.5982
		Downward	-20.265	-153.166	-2.553	1.715	-3.799	-0.0044
	2 nd	Upward	16.074	121.489	2.025	1.235	-3.319	0.6091
		Downward	-20.321	-153.584	-2.560	1.722	-3.805	-0.0633
1.50	1 st	Upward	21.992	166.213	2.770	1.918	-4.001	0.9934
		Downward	-26.024	-196.690	-3.278	2.398	-4.481	-0.4716
	2 nd	Upward	21.322	161.151	2.686	1.839	-3.922	1.0239
		Downward	-25.948	-196.116	-3.269	2.389	-4.472	-0.5742
2.00	1 st	Upward	25.513	192.828	3.214	2.337	-4.420	1.3077
		Downward	-31.700	-239.587	-3.993	3.085	-5.168	-1.0239
	2 nd	Upward	24.146	182.495	3.042	2.173	-4.257	1.3907
		Downward	-30.795	-232.750	-3.879	2.975	-5.058	-1.2597
3.00	1 st	Upward	33.854	255.869	4.264	3.348	-5.432	2.3928
		Downward	-42.354	-320.110	-5.335	4.394	-6.478	-2.6504
	2 nd	Upward	32.660	246.840	4.114	3.202	-5.286	2.7792
		Downward	-40.075	-302.888	-5.048	4.113	-6.196	-2.7727

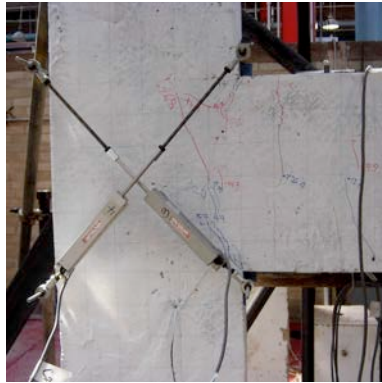
Drift Level (%)	Loading		Applied load/stress			Joint Panel Results		
	Cycle	Direction	^a V_c	^b V_{jh}	^c v_{jh}	^d p_t	^e p_c	^f γ
			(kN)	(kN)	(MPa)	(MPa)	(MPa)	*10 ⁻³ (radian)
4.00	1 st	Upward	41.270	311.917	5.199	4.260	-6.344	4.4908
		Downward	-43.479	-328.616	-5.477	4.533	-6.617	-4.2681
	2 nd	Upward	37.382	282.536	4.709	3.781	-5.864	5.6676
		Downward	-39.820	-300.958	-5.016	4.081	-6.165	-5.0890
5.00	1 st	Upward	37.272	281.701	4.695	3.768	-5.851	7.4032
		Downward	-37.320	-282.066	-4.701	3.773	-5.857	-11.1801
	2 nd	Upward	29.511	223.044	3.717	2.819	-4.902	7.1281
		Downward	-30.402	-229.776	-3.830	2.927	-5.010	-14.3196
6.00	1 st	Upward	28.130	212.606	3.543	2.652	-4.735	9.6301
		Downward	-27.723	-209.527	-3.492	2.603	-4.686	-21.1049
	2 nd	Upward	21.660	163.708	2.728	1.879	-3.962	10.8854
		Downward	-21.930	-165.743	-2.762	1.911	-3.994	10.8941

^a Story column shear; ^b Horizontal shear force at joint; ^c Horizontal shear stress at joint

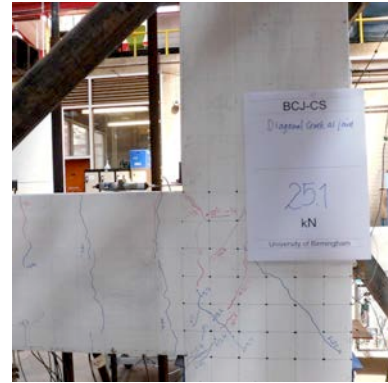
^d Normalized principal tensile stress at joint; ^e Normalized principal compressive stress at joint

^f Joint shear deformation

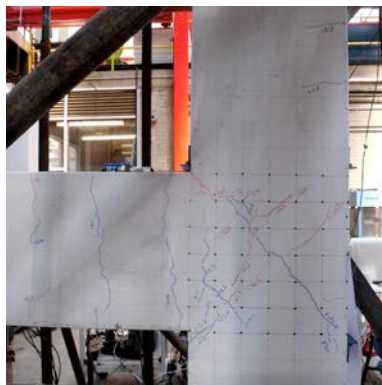
The damage propagation is shown in Figure 4.1. The first hairline cracks appeared at the top and bottom of the beam-column interface at drift ratios of $\pm 0.10\%$ (± 4 kN). With increased loading, these cracks extended into the beam. Diagonal cracks in the joint started to form at the upward direction load of 25.1 kN (1.00% drift ratio) at a calculated stress level of 2.174 MPa. At this point, the normalized principal tensile stress, $p_t/\sqrt{f'_c}$ was approximately 0.236. Reversing the load direction at the same drift ratio resulted in diagonal cracks forming an X-pattern and spreading to the perimeter of the joint. At 2.00% drift ratio (36.7 kN), new diagonal cracks appeared and existing cracks started to propagate towards the column back face, about 100 mm above the joint-column level. Beyond a drift ratio of 3.00%, severe damage of the concrete core resulted in a shear hinge mechanism. A brittle failure in the form of a concrete wedge mechanism was also observed beyond a 3.00% drift ratio.



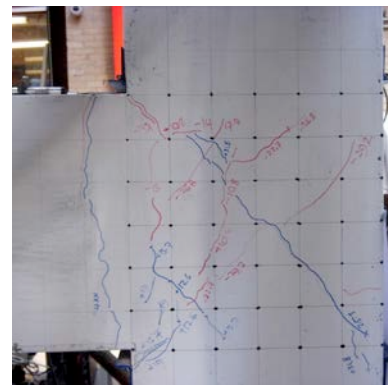
(a) 1% drift, 1st cycle-upward loading
26.8 kN



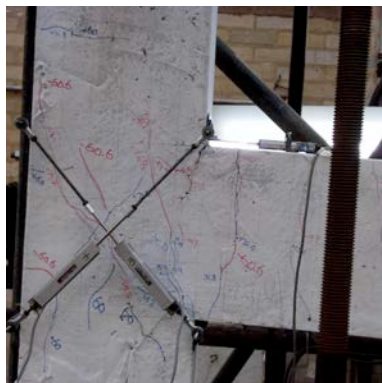
(b) 1% drift, 1st cycle-downward loading
25.1 kN



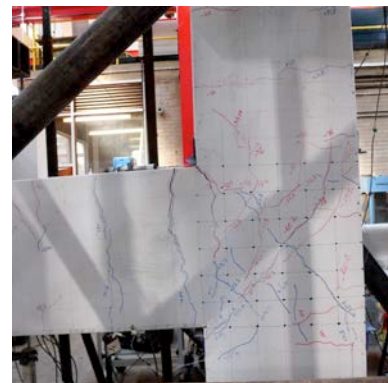
(c) 2% drift, 1st cycle-upward loading
36.7 kN



(d) 2% drift, 1st cycle-downward loading
45.0 kN



(e) 3% drift, 1st cycle-downward loading
60.6 kN



(f) 3% drift, 1st cycle-downward loading
60.6 kN

Figure 4.1. Damage propagation – BCJ-CS-A test#1

Figure 4.2 presents the load-displacement response of the control specimen. As indicated by the envelope curve, the specimen had an initial linear load displacement response up to a drift ratio of 0.75% (± 9.75 mm). Upon further loading, cracking led to a gradual reduction in

stiffness and the envelope curve turned nonlinear. The maximum load carrying capacity (63 kN) was achieved at the first cycle of the 4.00% drift ratio (52 mm), and the load started to decrease rapidly due to shear failure in the joint.

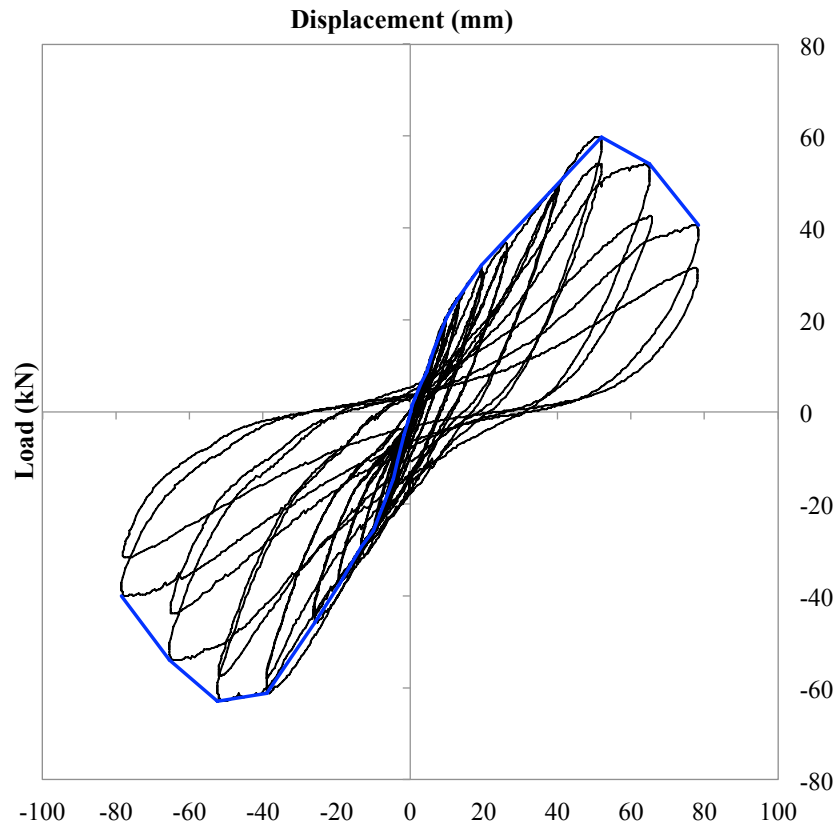


Figure 4.2. Load-displacement response of the control specimen BCJ-CS-A test #1

4.2.2. Control specimen, BCJ-CS-A Test #2

During testing of the first control specimen, it was observed that the lateral steel beam that supported the upper column end deflected undesirably and the test was paused to rectify this issue. It was therefore decided to fabricate and test a duplicate control specimen in order to eliminate the effect of the deflection of the steel beam and to confirm the failure mode and load carrying capacity of the control specimen. The test results in terms of the maximum recorded/calculated values for each loading direction are summarised in Table 4.2 whilst curves for story column shear and horizontal shear stress at joint are presented in Appendix 5.

Table 4.2. Summary of test results for BCJ-CS-A test #2

Drift Level (%)	Loading		Applied Load/Stress			Joint Panel Results		
	Cycle	Direction	^a V_c	^b V_{jh}	^c v_{jh}	^d p_t	^e p_c	^f γ
			(kN)	(kN)	(MPa)	(MPa)	(MPa)	*10 ⁻³ (radian)
0.04	1 st	Upward	2.665	20.144	0.336	0.044	-2.544	0.0028
		Downward	-3.024	-22.858	-0.381	0.057	-2.557	0.0009
	2 nd	Upward	2.541	19.205	0.320	0.040	-2.540	0.0022
		Downward	-2.886	-21.814	-0.364	0.052	-2.552	0.0002
0.10	1 st	Upward	5.510	41.645	0.694	0.180	-2.680	0.0013
		Downward	-6.463	-48.846	-0.814	0.242	-2.742	-0.0024
	2 nd	Upward	5.759	43.523	0.725	0.195	-2.695	0.0002
		Downward	-6.988	-52.812	-0.880	0.279	-2.779	-0.0007
0.25	1 st	Upward	11.061	83.602	1.393	0.622	-3.122	-0.0002
		Downward	-10.854	-82.037	-1.367	0.603	-3.103	-0.0275
	2 nd	Upward	10.454	79.010	1.317	0.566	-3.066	-0.0281
		Downward	-10.882	-82.245	-1.371	0.605	-3.105	-0.0288
0.35	1 st	Upward	13.658	103.224	1.720	0.877	-3.377	-0.0286
		Downward	-13.285	-100.406	-1.673	0.839	-3.339	-0.0646
	2 nd	Upward	13.520	102.180	1.703	0.863	-3.363	-0.0617
		Downward	-12.511	-94.561	-1.576	0.762	-3.262	-0.0698
0.50	1 st	Upward	17.193	129.944	2.166	1.251	-3.751	0.0041
		Downward	-15.536	-117.419	-1.957	1.072	-3.572	-0.1054
	2 nd	Upward	17.000	128.482	2.141	1.230	-3.730	0.0240
		Downward	-15.605	-117.941	-1.966	1.079	-3.579	-0.1178
0.75	1 st	Upward	22.827	172.527	2.875	1.885	-4.385	0.2607
		Downward	-19.375	-146.434	-2.441	1.492	-3.992	-0.1540
	2 nd	Upward	22.330	168.770	2.813	1.828	-4.328	0.2911
		Downward	-18.864	-142.573	-2.376	1.435	-3.935	-0.1654
1.00	1 st	Upward	27.080	204.674	3.411	2.383	-4.883	0.6531
		Downward	-23.228	-175.554	-2.926	1.932	-4.432	-0.2450
	2 nd	Upward	25.934	196.011	3.267	2.248	-4.748	0.6539
		Downward	-22.855	-172.736	-2.879	1.889	-4.389	-0.3079

Drift Level (%)	Loading		Applied Load/Stress			Joint Panel Results		
	Cycle	Direction	^a V_c	^b V_{jh}	^c v_{jh}	^d p_t	^e p_c	^f γ
			(kN)	(kN)	(MPa)	(MPa)	(MPa)	*10 ⁻³ (radian)
1.50	1 st	Upward	34.123	257.904	4.298	3.226	-5.726	1.3604
		Downward	-27.923	-211.041	-3.517	2.483	-4.983	-0.7569
	2 nd	Upward	32.618	246.527	4.109	3.045	-5.545	1.3495
		Downward	-27.150	-205.196	-3.420	2.391	-4.891	-0.8466
2.00	1 st	Upward	38.584	291.616	4.860	3.768	-6.268	2.2164
		Downward	-33.640	-254.251	-4.238	3.168	-5.668	-1.4748
	2 nd	Upward	36.057	-5.961	4.542	3.461	-5.961	2.5215
		Downward	-31.859	-240.787	-4.013	2.953	-5.453	-1.6153
3.00	1 st	Upward	40.835	308.629	5.144	4.044	-6.544	4.2057
		Downward	-37.189	-281.075	-4.685	3.598	-6.098	-3.9930
	2 nd	Upward	33.115	250.285	4.171	3.105	-5.605	5.4018
		Downward	-32.729	-247.362	-4.123	3.058	-5.558	-4.9351
4.00	1 st	Upward	34.496	260.722	4.345	3.272	-5.772	7.4206
		Downward	-31.265	-236.299	-3.938	2.882	-5.382	-9.4286
	2 nd	Upward	26.500	200.290	3.338	2.315	-4.815	9.9855
		Downward	-25.120	-189.853	-3.164	2.152	-4.652	-14.3923

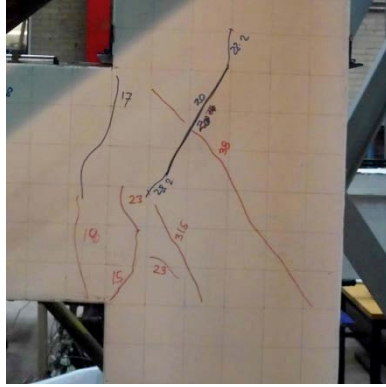
^a Story column shear; ^b Horizontal shear force at joint; ^c Horizontal shear stress at joint

^d Normalized principal tensile stress at joint; ^e Normalized principal compressive stress at joint

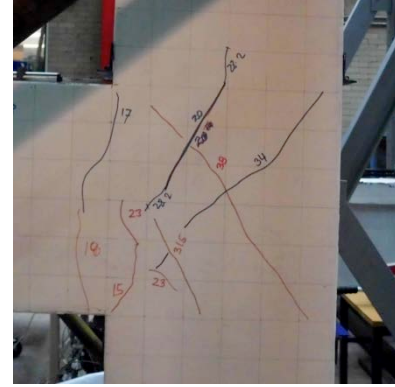
^f Joint shear deformation

The damage propagation for the duplicate control specimen is shown in Figure 4.3. The first crack was observed at the beam-column interface at drift ratios of $\pm 0.25\%$ (± 15 kN). With increased loading, the cracks extended into the beam. Diagonal cracks in the joint started to form at the upward direction load of 31.5 kN (0.75% drift ratio) at a calculated stress level of 2.875 MPa. At this point, the normalized principal tensile stress, p_t/f_{ct} was approximately 0.337. At 2.00% drift ratio (54.0 kN), new diagonal cracks appeared and the existing cracks started to propagate towards the column back face, about 100 mm above the joint-column level. Beyond a drift ratio of 3.00%, severe damage of the concrete core resulted in a shear hinge mechanism. A brittle failure in the form of a concrete wedge mechanism was also observed beyond a 3.00% drift ratio. Of note is that both the damage propagation and failure

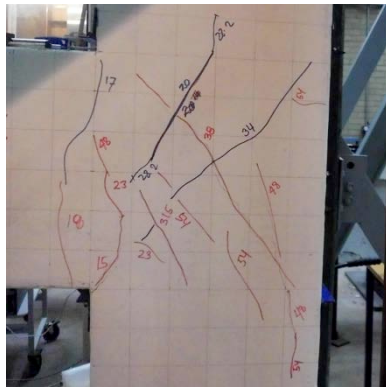
mode of the two control specimens are quite comparable.



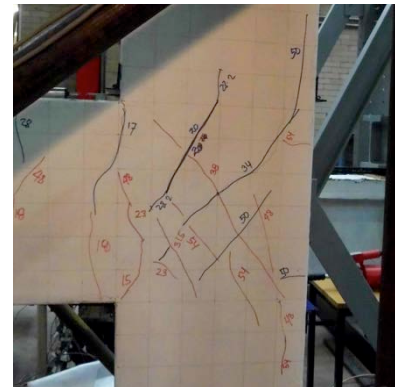
(a) 1% drift, 1st cycle-upward loading
38.0 kN



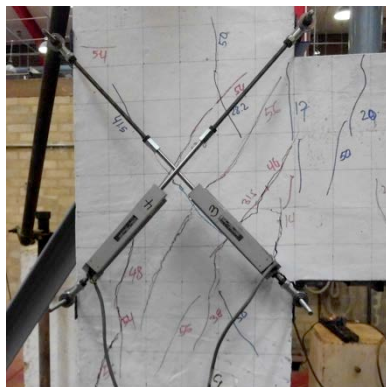
(b) 1% drift, 1st cycle-downward loading
34.0 kN



(c) 2% drift, 1st cycle-upward loading
54.0 kN



(d) 2% drift, 1st cycle-downward loading
50.0 kN



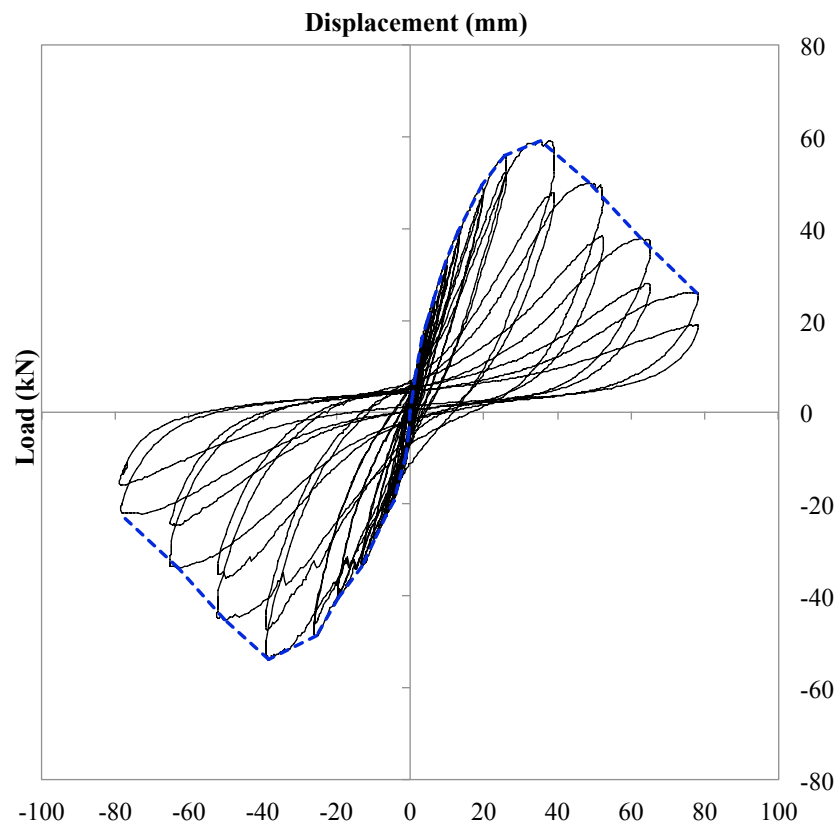


Figure 4.4. Load-displacement response of the duplicate control specimen, BCJ-CS-A test #2

The load-displacement response for the duplicate control specimen is presented in Figure 4.4. There was no significant stiffness degradation up to 1.00% drift ratio (± 13 mm). Due to cracking, the specimen stiffness started to deteriorate gradually from 1.50% (19.5 mm) to 4.00% (52 mm) drift ratio, with rapid degradation taking place after 5.00% (65 mm) drift ratio. The specimen reached its maximum load carrying capacity (59 kN) at the first cycle of the 3.00% drift ratio loading step and then the load decreased rapidly. This maximum load level is quite comparable to that (63 kN) of the first control specimen. However, the first control specimen achieved its maximum load at a drift ratio of 4.00% which suggests that the overall response of the duplicate control specimen is stiffer than that of the first control specimen. This was to be expected and can be explained by the undesirable deflection of the

lateral steel beam in the case of the first control specimen. It can therefore be concluded that the deflection of the lateral steel beam affected the specimen stiffness but had an insignificant effect on damage propagation, failure mode and load carrying capacity.

4.2.3. Strengthened specimen, BCJ-SS-S4

This specimen was strengthened with four 8 mm steel bars embedded inside the joint core (see Figure 3.11.b). The test results in terms of the maximum recorded/calculated values for each loading direction are summarised in Table 4.3 whilst curves for story column shear and horizontal shear stress at joint are presented in Appendix 5.

Table 4.3. Summary of test results for BCJ-SS-S4

Drift Level (%)	Loading		Applied Load/Stress			Joint Panel Results		
	Cycle	Direction	^a V_c	^b V_{jh}	^c v_{jh}	^d p_t	^e p_c	^f γ
			(kN)	(kN)	(MPa)	(MPa)	(MPa)	*10 ⁻³ (radian)
0.04	1 st	Upward	2.720	20.561	0.343	0.046	-2.546	-0.0007
		Downward	-5.427	-41.018	-0.684	0.175	-2.675	-0.0002
	2 nd	Upward	2.444	18.474	0.308	0.037	-2.537	0.0017
		Downward	-4.240	-32.042	-0.534	0.109	-2.609	0.0004
0.10	1 st	Upward	5.648	42.688	0.711	0.188	-2.688	0.0024
		Downward	-11.379	-86.003	-1.433	0.652	-3.152	-0.0009
	2 nd	Upward	5.897	44.567	0.743	0.204	-2.704	0.0033
		Downward	-9.957	-75.252	-1.254	0.521	-3.021	0.0022
0.25	1 st	Upward	10.385	78.488	1.308	0.559	-3.059	0.0068
		Downward	-17.704	-133.805	-2.230	1.307	-3.807	0.0011
	2 nd	Upward	9.280	70.138	1.169	0.461	-2.961	0.0103
		Downward	-19.112	-144.451	-2.408	1.463	-3.963	0.0055
0.35	1 st	Upward	11.628	87.881	1.465	0.676	-3.176	0.0138
		Downward	-20.728	-156.663	-2.611	1.645	-4.145	0.0103
	2 nd	Upward	9.832	74.313	1.239	0.510	-3.010	0.0151
		Downward	-20.521	-155.097	-2.585	1.621	-4.121	0.0081
0.50	1 st	Upward	14.113	106.668	1.778	0.923	-3.423	0.0214
		Downward	-25.189	-190.375	-3.173	2.160	-4.660	-0.0866
	2 nd	Upward	13.423	101.450	1.691	0.853	-3.353	0.0140
		Downward	-24.678	-186.513	-3.109	2.100	-4.600	-0.1377
0.75	1 st	Upward	19.830	149.879	2.498	1.543	-4.043	0.2237
		Downward	-30.119	-227.636	-3.794	2.745	-5.245	-0.2907
	2 nd	Upward	17.966	135.788	2.263	1.335	-3.835	0.0895
		Downward	-28.931	-218.660	-3.644	2.603	-5.103	-0.3276

Drift Level (%)	Loading		Applied Load/Stress			Joint Panel Results		
	Cycle	Direction	^a V_c	^b V_{jh}	^c v_{jh}	^d p_t	^e p_c	^f γ
			(kN)	(kN)	(MPa)	(MPa)	(MPa)	*10 ⁻³ (radian)
1.00	1 st	Upward	24.042	181.712	3.029	2.026	-4.526	0.4546
		Downward	-32.038	-242.144	-4.036	2.975	-5.475	-0.4830
	2 nd	Upward	22.786	172.214	2.870	1.881	-4.381	0.5072
		Downward	-32.397	-244.857	-4.081	3.018	-5.518	-0.5758
1.50	1 st	Upward	32.632	246.632	4.111	3.046	-5.546	1.3606
		Downward	-40.282	-304.454	-5.074	3.976	-6.476	-1.1247
	2 nd	Upward	31.210	235.881	3.931	2.875	-5.375	1.4117
		Downward	-39.371	-297.565	-4.959	3.865	-6.365	-1.1502
2.00	1 st	Upward	38.957	294.434	4.907	3.814	-6.314	2.0710
		Downward	-47.601	-359.771	-5.996	4.875	-7.375	-1.6806
	2 nd	Upward	38.059	287.650	4.794	3.704	-6.204	2.3489
		Downward	-45.060	-340.567	-5.676	4.562	-7.062	-1.7729
3.00	1 st	Upward	43.086	325.642	5.427	4.319	-6.819	2.8382
		Downward	-48.844	-369.165	-6.153	5.028	-7.528	-2.3017
	2 nd	Upward	39.509	298.609	4.977	3.881	-6.381	3.1472
		Downward	-46.731	-353.196	-5.887	4.768	-7.268	-2.6156
4.00	1 st	Upward	40.448	305.706	5.095	3.996	-6.496	3.7169
		Downward	-47.864	-361.754	-6.029	4.907	-7.407	-3.3731
	2 nd	Upward	39.288	296.939	4.949	3.854	-6.354	4.6953
		Downward	-46.510	-351.526	-5.859	4.741	-7.241	-4.1982
5.00	1 st	Upward	37.838	285.980	4.766	3.678	-6.178	5.5943
		Downward	-45.212	-341.715	-5.695	4.581	-7.081	-6.4898
	2 nd	Upward	29.442	222.522	3.709	2.664	-5.164	4.8418
		Downward	-37.921	-286.606	-4.777	3.688	-6.188	-7.0889
6.00	1 st	Upward	27.343	206.657	3.444	2.414	-4.914	5.2135
		Downward	-32.660	-246.840	-4.114	3.050	-5.550	-11.6202
	2 nd	Upward						
		Downward						

^a Story column shear; ^b Horizontal shear force at joint; ^c Horizontal shear stress at joint

^d Normalized principal tensile stress at joint; ^e Normalized principal compressive stress at joint

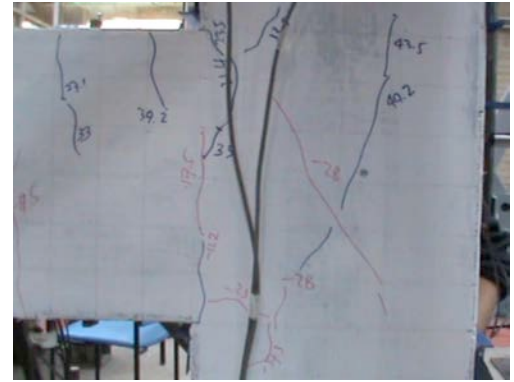
^f Joint shear deformation

The damage propagation for BCJ-SS-S4 is shown in Figure 4.5. A flexural crack appeared at the bottom of the beam-column interface at a drift ratio of 0.10% (11.2 kN). With increased loading at the same direction, this flexural crack extended and reached two-thirds of the beam depth. Diagonal cracks in the joint started to form at the upward direction load of 28.72 kN

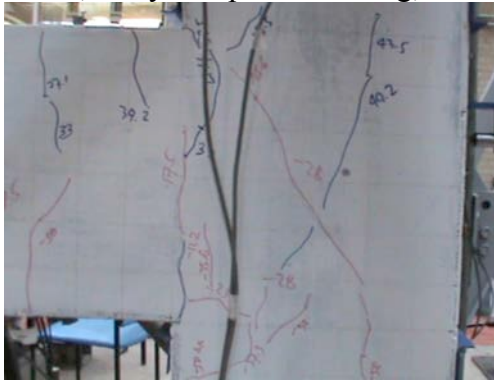
(0.75% drift ratio). The corresponding calculated stress level was 2.498 MPa and the normalized principal tensile stress, $p_t/\sqrt{f_c}$ was 0.229. Reversing the load direction at the same drift ratio resulted in diagonal cracks forming an X-pattern and spreading to the perimeter of the joint at a load of 40.2 kN. At 2.00% drift ratio (58 kN), existing diagonal cracks opened.



(a) 1% drift, 1st cycle-upward loading, 37.3 kN



(b) 1% drift, 1st cycle-downward loading, 43.5 kN



Further diagonal cracks formed at mid-depth of the joint area and at the upper corner of the beam-column interface at a downward loading direction of 2.00% drift ratio (65.8 kN). Beyond a drift ratio of 3.00%, additional cracks continued to develop and severe damage was observed; e.g. diagonal cracks propagated towards the upper and lower column faces, diagonal cracks formed in the beam within a distance of 200 mm from the column face, and concrete spalls occurred at several locations within the joint area.

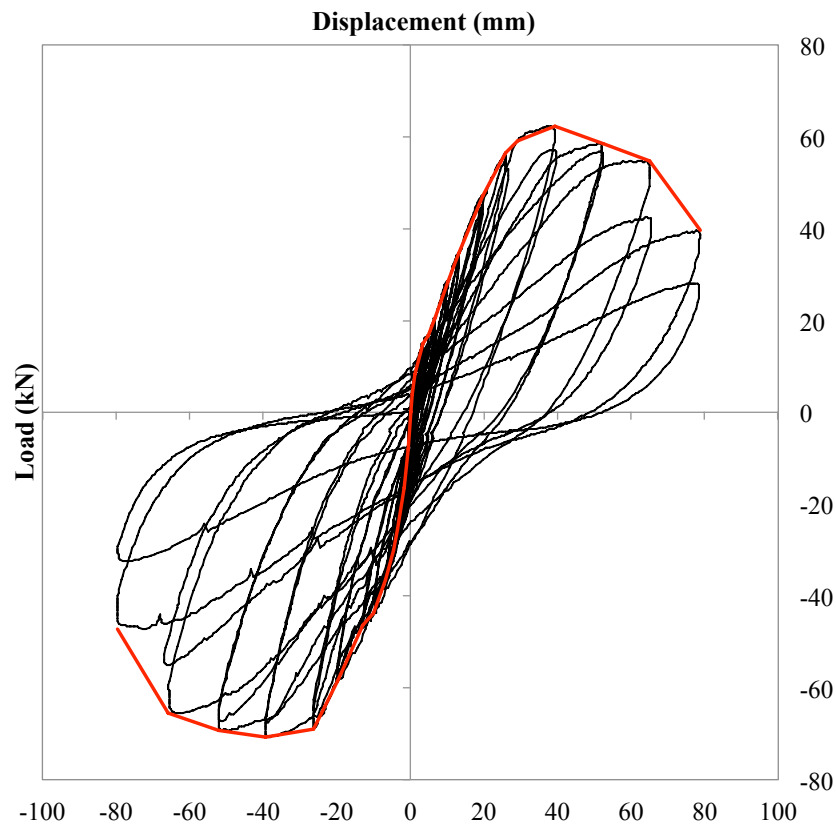


Figure 4.6. Load-displacement response of the strengthened specimen BCJ-SS-S4

For specimen BCJ-SS-S4, the load-displacement response in Figure 4.6 indicates that the behaviour of the specimen remained elastic without significant loss of stiffness up to 2.00% drift ratio (26 mm). The specimen gained its maximum load carrying capacity (70.8 kN) at a 3.00% drift ratio (39 mm). Up to 3.00% drift ratio, pinching length was increasing gradually, indicating that the specimen was capable of dissipating energy. In addition, the stiffness

degradation was limited up to 4.00% drift ratio (52 mm) when it started to deteriorate rapidly. Strength degradation was also observed after the specimen reached its maximum load carrying capacity.

4.2.4. Strengthened specimen, BCJ-SS-F4

This specimen was strengthened with four 7.5 mm CFRP bars (see Figure 3.11.(c)). The test results in terms of the maximum recorded/calculated values for each loading direction are summarised in Table 4.4 whilst curves for story column shear and horizontal shear stress at joint are presented in Appendix 5.

Table 4.4. Summary of test results for BCJ-SS-F4

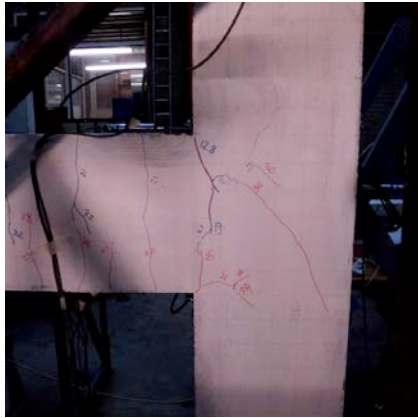
Drift Level (%)	Loading		Applied Load/Stress			Joint Panel Results		
	Cycle	Direction	^a V_c	^b V_{jh}	^c v_{jh}	^d p_t	^e p_c	^f γ
			(kN)	(kN)	(MPa)	(MPa)	(MPa)	*10 ⁻³ (radian)
0.04	1 st	Upward	2.486	18.787	0.313	0.039	-2.539	0.0062
		Downward	-3.259	-24.632	-0.411	0.066	-2.566	0.0088
	2 nd	Upward	2.458	18.578	0.310	0.038	-2.538	0.0086
		Downward	-3.867	-29.224	-0.487	0.092	-2.592	0.0088
0.10	1 st	Upward	5.261	39.766	0.663	0.165	-2.665	0.0271
		Downward	-6.642	-50.203	-0.837	0.254	-2.754	0.0194
	2 nd	Upward	5.924	44.776	0.746	0.206	-2.706	0.0200
		Downward	-6.297	-47.594	-0.793	0.230	-2.730	0.0266
0.25	1 st	Upward	10.578	79.949	1.332	0.577	-3.077	0.0323
		Downward	-10.730	-81.097	-1.352	0.591	-3.091	-0.0187
	2 nd	Upward	10.095	76.296	1.272	0.533	-3.033	-0.0029
		Downward	-10.385	-78.488	-1.308	0.559	-3.059	-0.0154
0.35	1 st	Upward	13.257	100.197	1.670	0.836	-3.336	0.0119
		Downward	-11.890	-89.865	-1.498	0.701	-3.201	-0.0183
	2 nd	Upward	13.865	104.790	1.746	0.898	-3.398	0.0183
		Downward	-12.166	-91.952	-1.533	0.728	-3.228	-0.0220
0.50	1 st	Upward	17.621	133.179	2.220	1.297	-3.797	0.0664
		Downward	-14.970	-113.140	-1.886	1.012	-3.512	-0.0581
	2 nd	Upward	17.234	130.257	2.171	1.255	-3.755	0.0651
		Downward	-14.528	-109.800	-1.830	0.966	-3.466	-0.0638

Drift Level (%)	Loading		Applied Load/Stress			Joint Panel Results		
	Cycle	Direction	^a V_c	^b V_{jh}	^c v_{jh}	^d p_t	^e p_c	^f γ
			(kN)	(kN)	(MPa)	(MPa)	(MPa)	*10 ⁻³ (radian)
0.75	1 st	Upward	22.951	173.467	2.891	1.900	-4.400	0.1791
		Downward	-19.554	-147.791	-2.463	1.512	-4.012	-0.2666
	2 nd	Upward	21.943	165.848	2.764	1.784	-4.284	0.1203
		Downward	-19.430	-146.852	-2.448	1.498	-3.998	-0.3076
1.00	1 st	Upward	27.343	206.657	3.444	2.414	-4.914	0.4508
		Downward	-20.079	-151.757	-2.529	1.571	-4.071	-0.3537
	2 nd	Upward	27.191	205.509	3.425	2.396	-4.896	0.5099
		Downward	-20.148	-152.279	-2.538	1.579	-4.079	-0.3947
1.50	1 st	Upward	36.098	272.829	4.547	3.466	-5.966	1.2397
		Downward	-26.431	-199.769	-3.329	2.306	-4.806	-0.8996
	2 nd	Upward	34.524	260.931	4.349	3.275	-5.775	1.3145
		Downward	-18.339	-138.606	-2.310	1.377	-3.877	-0.6936
2.00	1 st	Upward	42.644	322.302	5.372	4.265	-6.765	2.1427
		Downward	-32.328	-244.336	-4.072	3.010	-5.510	-1.5807
	2 nd	Upward	40.628	307.063	5.118	4.018	-6.518	2.3460
		Downward	-30.602	-231.289	-3.855	2.802	-5.302	-1.6664
3.00	1 st	Upward	49.272	372.400	6.207	5.081	-7.581	4.2351
		Downward	-36.291	-274.290	-4.572	3.489	-5.989	-4.8577
	2 nd	Upward	40.766	308.107	5.135	4.035	-6.535	4.5668
		Downward	-31.500	-238.073	-3.968	2.910	-5.410	-5.4970
4.00	1 st	Upward	41.249	311.760	5.196	4.094	-6.594	5.5284
		Downward	-30.188	-228.158	-3.803	2.753	-5.253	-11.8594
	2 nd	Upward	30.933	233.794	3.897	2.842	-5.342	7.5475
		Downward	-23.283	-175.972	-2.933	1.938	-4.438	-15.0506
5.00	1 st	Upward	29.290	221.374	3.690	2.646	-5.146	11.6401
		Downward	-21.170	-160.003	-2.667	1.695	-4.195	-24.1467
	2 nd	Upward	22.054	166.683	2.778	1.796	-4.296	11.1988
		Downward	-14.983	-113.244	-1.887	1.014	-3.514	-28.9469
6.00	1 st	Upward	21.115	159.585	2.660	1.689	-4.189	8.8288
		Downward	-12.732	-96.231	-1.604	0.783	-3.283	-40.2143
	2 nd	Upward	16.958	128.169	2.136	1.225	-3.725	2.0002
		Downward	-7.844	-59.283	-0.988	0.343	-2.843	-50.7676

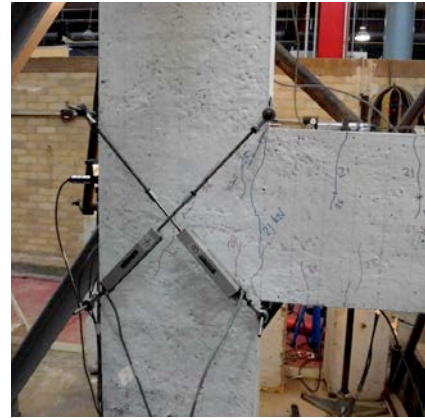
^a Story column shear; ^b Horizontal shear force at joint; ^c Horizontal shear stress at joint

^d Normalized principal tensile stress at joint; ^e Normalized principal compressive stress at joint

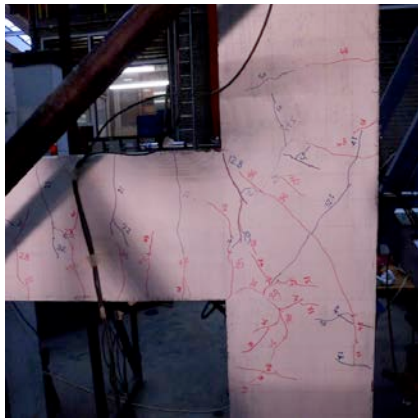
^f Joint shear deformation



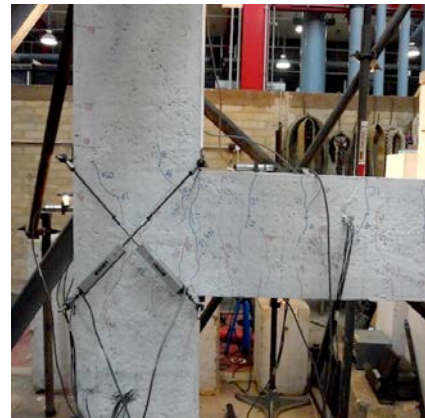
(a) 1% drift, 1st cycle-upward loading
36 kN



(b) 1% drift, 1st cycle-downward loading
32.5 kN



(c) 2% drift, 1st cycle-upward loading
58 kN



(d) 2% drift, 1st cycle-downward loading
50 kN



(e) 3% drift, 1st cycle-upward loading
66 kN



(f) 3% drift, 1st cycle-downward loading
54 kN

Figure 4.7. Damage propagation – BCJ-SS-F4

The damage propagation for BCJ-SS-F4 is shown in Figure 4.7. The first hairline crack appeared in the joint at 0.10% drift ratio (12.8 kN), forming a diagonal line starting at the beam corner. A flexural crack appeared at the beam-column interface at 0.35% drift ratio (21 kN). Between 0.35 and 0.75% drift ratios, new flexural cracks developed in the beam and at the column face, at loads ranging from 21 to 29 kN. An additional diagonal crack appeared in the joint at 1.00% drift ratio (36 kN). At 1.50% drift ratio (48.1 kN), two further diagonal cracks developed within the joint area in an X-pattern and spread to the perimeter of the joint. At the upward load corresponding to 3.00% drift ratio (39 mm), vertical hairline cracks formed in the column followed by diagonal cracks in the beam close to the position of the applied cyclic load. Beyond a drift ratio of 3.00%, additional cracks continued to develop and severe damage was observed; e.g. diagonal cracks in the joint and at the beam-column interface opened wider, concrete spalls occurred within the joint area, and the cracks started to propagate towards the column back face, about 150 mm below and above the joint-column level.

Figure 4.8 shows the load-displacement response for BCJ-SS-F4. The specimen had an initial linear load-displacement response up to a drift ratio of 0.25% (± 3.25 mm). Upon further loading, cracking led to a gradual reduction in stiffness and the response turned nonlinear. The maximum load carrying capacity (71.3 kN) was achieved at the first cycle of 3.00% drift ratio (± 39 mm). The embedded CFRP bars seem to have controlled crack propagation because there was limited stiffness degradation up to the maximum load carrying capacity. From the second cycle of the 3% drift ratio (± 39 mm) until the end of the test, both the load carrying capacity and stiffness significantly deteriorated.

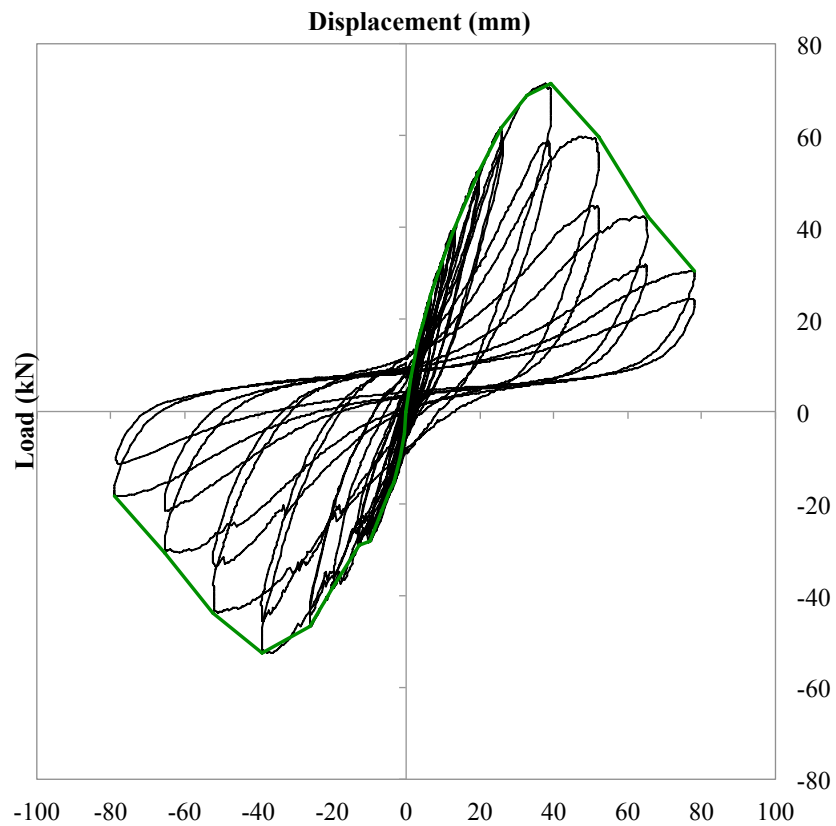


Figure 4.8. Load-displacement response of the strengthened specimen BCJ-SS-F4

4.2.5. Strengthened specimen, BCJ-SS-S8

This specimen is part of Group C and was strengthened with eight 8 mm steel bars embedded inside the joint core (see Figure 3.11.(d)). The test results in terms of the maximum recorded/calculated values for each loading direction are summarised in Table 4.5 whilst curves for story column shear and horizontal shear stress at joint are presented in Appendix 5.

Table 4.5. Summary of test results for BCJ-SS-S8

Drift Level (%)	Loading		Applied Load/Stress			Joint Panel Results		
	Cycle	Direction	^a V_c	^b V_{jh}	^c v_{jh}	^d p_t	^e p_c	^f γ
			(kN)	(kN)	(MPa)	(MPa)	(MPa)	*10 ⁻³ (radian)
0.04	1 st	Upward	3.121	23.588	0.393	0.060	-2.560	0.0015
		Downward	-2.707	-20.457	-0.341	0.046	-2.546	0.0006
	2 nd	Upward	1.657	12.525	0.209	0.017	-2.517	0.0024
		Downward	-2.651	-20.039	-0.334	0.044	-2.544	0.0000
0.10	1 st	Upward	3.300	24.945	0.416	0.067	-2.567	0.0009
		Downward	-5.482	-41.436	-0.691	0.178	-2.678	-0.0009
	2 nd	Upward	-4.668	-35.278	-0.588	0.131	-2.631	0.0035
		Downward	-4.668	-35.278	-0.588	0.131	-2.631	0.0015
0.25	1 st	Upward	6.270	47.385	0.790	0.229	-2.729	0.0024
		Downward	-9.363	-70.764	-1.179	0.469	-2.969	-0.0013
	2 nd	Upward	-9.432	-71.286	-1.188	0.475	-2.975	0.0024
		Downward	-9.432	-71.286	-1.188	0.475	-2.975	-0.0002
0.35	1 st	Upward	-11.545	-87.255	-1.454	0.668	-3.168	0.0011
		Downward	-11.545	-87.255	-1.454	0.668	-3.168	-0.0041
	2 nd	Upward	8.797	66.485	1.108	0.420	-2.920	0.0009
		Downward	-11.324	-85.585	-1.426	0.647	-3.147	-0.0030
0.50	1 st	Upward	12.277	92.787	1.546	0.738	-3.238	0.0035
		Downward	-14.569	-110.113	-1.835	0.970	-3.470	0.0013
	2 nd	Upward	11.545	87.255	1.454	0.668	-3.168	0.0009
		Downward	-14.859	-112.305	-1.872	1.001	-3.501	-0.0052
0.75	1 st	Upward	15.991	120.863	2.014	1.121	-3.621	0.0082
		Downward	-19.278	-145.704	-2.428	1.481	-3.981	-0.0209
	2 nd	Upward	16.696	126.186	2.103	1.197	-3.697	-0.0095
		Downward	-19.527	-147.582	-2.460	1.509	-4.009	-0.0259
1.00	1 st	Upward	21.267	160.733	2.679	1.706	-4.206	0.0134
		Downward	-21.488	-162.403	-2.707	1.731	-4.231	-0.0751
	2 nd	Upward	21.101	159.481	2.658	1.687	-4.187	-0.0360
		Downward	-21.432	-161.986	-2.700	1.725	-4.225	-0.0859
1.50	1 st	Upward	29.166	220.434	3.674	2.631	-5.131	0.3215
		Downward	-28.862	-218.138	-3.636	2.595	-5.095	-0.7038
	2 nd	Upward	28.144	212.711	3.545	2.509	-5.009	0.4965
		Downward	-28.420	-214.798	-3.580	2.542	-5.042	-1.0931

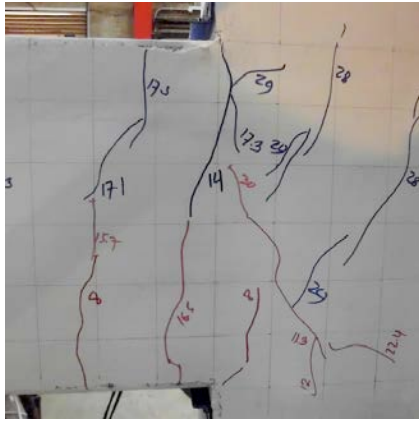
Drift Level (%)	Loading		Applied Load/Stress			Joint Panel Results		
	Cycle	Direction	^a V_c	^b V_{jh}	^c v_{jh}	^d p_t	^e p_c	^f γ
			(kN)	(kN)	(MPa)	(MPa)	(MPa)	*10 ⁻³ (radian)
2.00	1 st	Upward	36.443	275.438	4.591	3.508	-6.008	1.5645
		Downward	-33.737	-254.982	-4.250	3.180	-5.680	-1.6636
	2 nd	Upward	35.656	269.489	4.491	3.412	-5.912	1.8588
		Downward	-33.654	-254.355	-4.239	3.170	-5.670	-2.0246
3.00	1 st	Upward	43.735	330.547	5.509	4.399	-6.899	3.4894
		Downward	-40.338	-304.871	-5.081	3.983	-6.483	-5.5565
	2 nd	Upward	38.211	288.798	4.813	3.723	-6.223	3.7246
		Downward	-34.275	-259.052	-4.318	3.245	-5.745	-6.2905
4.00	1 st	Upward	39.702	300.070	5.001	3.905	-6.405	5.5970
		Downward	-33.488	-253.103	-4.218	3.150	-5.650	-11.7294
	2 nd	Upward	29.677	224.296	3.738	2.692	-5.192	6.5887
		Downward	-26.514	-200.395	-3.340	2.316	-4.816	-13.9533
5.00	1 st	Upward	27.730	209.580	3.493	2.460	-4.960	13.8894
		Downward	-23.600	-178.372	-2.973	1.975	-4.475	-18.4279
	2 nd	Upward						
		Downward						

^a Story column shear; ^b Horizontal shear force at joint; ^c Horizontal shear stress at joint

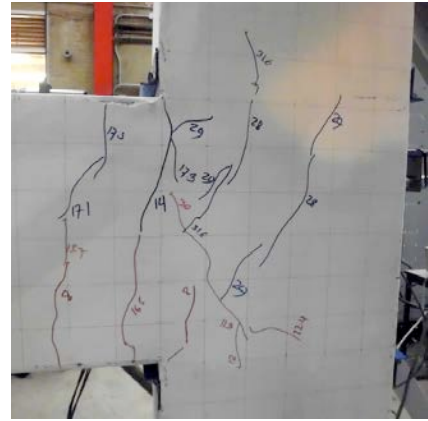
^d Normalized principal tensile stress at joint; ^e Normalized principal compressive stress at joint

^f Joint shear deformation

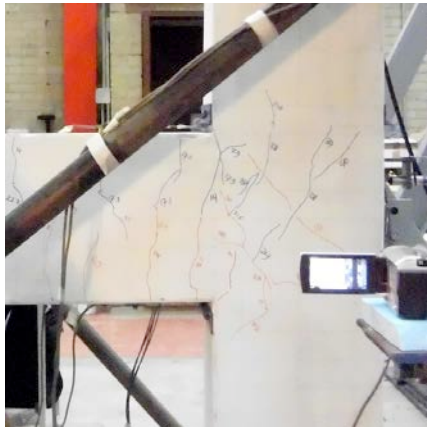
The damage propagation for BCJ-SS-S8 is shown in Figure 4.9. The first flexural crack formed at the bottom of the beam hinge area at a distance of 11 mm from the column face at a load of 8 kN (0.25% drift ratio). Upon further loading to $\pm 0.5\%$ drift ratio (± 16.5 kN), several hairline flexural cracks appeared within the beam at a distance of 400 mm from the column face. These cracks developed from the bottom and the top sides of the beam to its mid-height. The first diagonal joint crack developed at the lower side of the joint area at 0.75% drift ratio (23.16 kN) and reversing the load direction at the same drift level resulted in another joint crack at the centre of the joint body (28 kN). The corresponding joint stress level was 2.014 MPa and the normalized principal tensile stress, $p_t/\sqrt{f_c}$ was approximately 0.225.



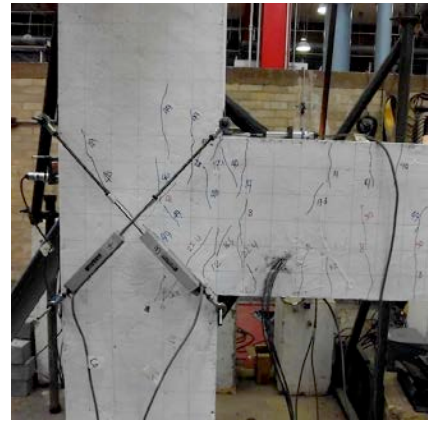
(a) 1% drift, 1st cycle-upward loading
30 kN



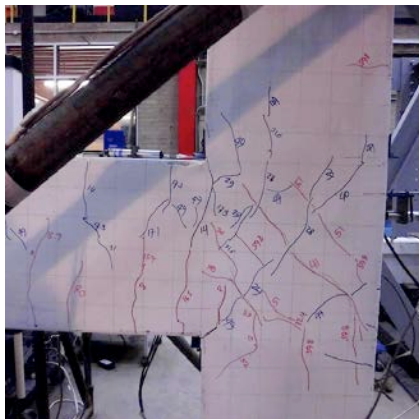
(b) 1% drift, 1st cycle-downward loading
31.6 kN



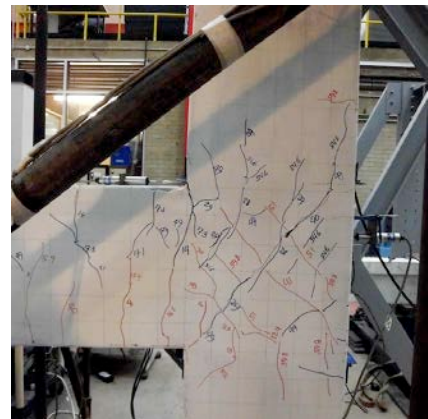
(c) 2% drift, 1st cycle-upward loading
52 kN



(d) 2% drift, 1st cycle-downward loading
49 kN



(e) 3% drift, 1st cycle-upward loading
59.8 kN



(f) 3% drift, 1st cycle-downward loading
54.6 kN

Figure 4.9. Damage propagation – BCJ-SS-S8

Between 1.00 and 2.00% drift ratios, additional diagonal cracks continued to develop within the joint area and a diagonal crack also formed in the beam at the load of 52 kN (2.00% drift ratio). At 3.00% drift level (59.8 kN), several diagonal cracks still continued to appear at the joint area forming 3 parallel diagonal lines and several hairline diagonal cracks also appeared in the beam at a distance of 800 mm from the column face. Beyond a drift ratio of 3.00%, severe damage was observed; e.g. diagonal cracks extended to upper part of column at a distance of 250 mm from the joint-column level and concrete spalls occurred within the joint area.

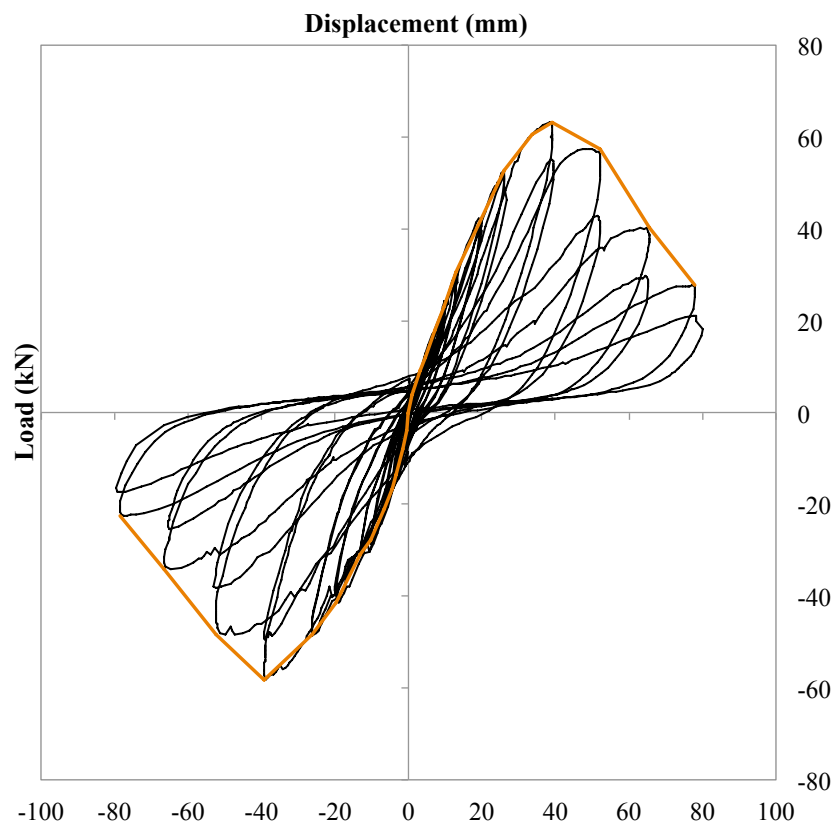


Figure 4.10. Load-displacement response of the strengthened specimen, BCJ-SS-S8

For BCJ-SS-S8, the load-displacement response (see Figure 4.10) shows that there was no significant stiffness degradation up to 2.00% drift ratio (± 26 mm). The specimen attained its

maximum load carrying capacity (63.3 kN) at 3.00% drift ratio (± 39 mm). Further loading beyond 4.00% drift ratio (± 52 mm) resulted in significant reduction in both the load carrying capacity and stiffness.

4.2.6. Strengthened specimen, BCJ-SS-F8

This specimen comprised eight 7.5 mm CFRP bars embedded at the same bar positions as those of BCJ-SS-S8 (see Figure 3.11.e). The test results in terms of the maximum recorded/calculated values for each loading direction are summarised in Table 4.6 whilst curves for story column shear and horizontal shear stress at joint are presented in Appendix 5.

Table 4.6. Summary of test results for BCJ-SS-F8

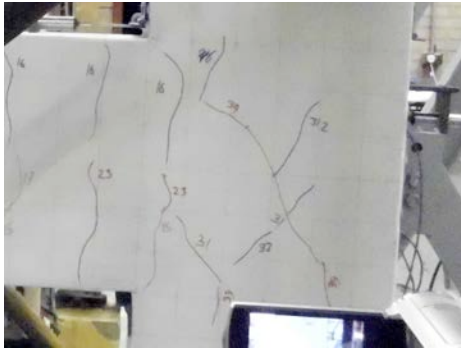
Drift Level (%)	Loading		Applied Load/Stress			Joint Panel Results		
	Cycle	Direction	^a V_c	^b V_{jh}	^c v_{jh}	^d p_t	^e p_c	^f γ
			(kN)	(kN)	(MPa)	(MPa)	(MPa)	*10 ⁻³ (radian)
0.04	1 st	Upward	5.413	40.914	0.682	0.174	-2.674	0.0000
		Downward	-2.983	-22.544	-0.376	0.055	-2.555	-0.0015
	2 nd	Upward	2.928	22.127	0.369	0.053	-2.553	0.0004
		Downward	-3.162	-23.901	-0.398	0.062	-2.562	-0.0009
0.10	1 st	Upward	6.794	51.351	0.856	0.265	-2.765	0.0194
		Downward	-5.165	-39.035	-0.651	0.159	-2.659	-0.0103
	2 nd	Upward	6.062	45.819	0.764	0.215	-2.715	0.0048
		Downward	-5.717	-43.210	-0.720	0.193	-2.693	-0.0129
0.25	1 st	Upward	11.752	88.821	1.480	0.688	-3.188	0.0103
		Downward	-10.564	-79.845	-1.331	0.576	-3.076	-0.0452
	2 nd	Upward	11.807	89.238	1.487	0.693	-3.193	-0.0065
		Downward	-9.059	-68.468	-1.141	0.443	-2.943	-0.0417
0.35	1 st	Upward	13.699	103.537	1.726	0.881	-3.381	0.0002
		Downward	-12.014	-90.804	-1.513	0.713	-3.213	-0.0655
	2 nd	Upward	13.547	102.389	1.706	0.865	-3.365	0.0079
		Downward	-11.545	-87.255	-1.454	0.668	-3.168	-0.0663
0.50	1 st	Upward	17.994	135.997	2.267	1.338	-3.838	0.0668
		Downward	-14.196	-107.295	-1.788	0.932	-3.432	-0.0860
	2 nd	Upward	17.662	133.492	2.225	1.302	-3.802	0.0757
		Downward	-14.003	-105.834	-1.764	0.912	-3.412	-0.0901

Drift Level (%)	Loading		Applied Load/Stress			Joint Panel Results		
	Cycle	Direction	^a V_c	^b V_{jh}	^c v_{jh}	^d p_t	^e p_c	^f γ
			(kN)	(kN)	(MPa)	(MPa)	(MPa)	*10 ⁻³ (radian)
0.75	1 st	Upward	23.808	179.938	2.999	1.999	-4.499	0.2289
		Downward	-19.154	-144.764	-2.413	1.467	-3.967	-0.1283
	2 nd	Upward	22.648	171.171	2.853	1.865	-4.365	0.3218
		Downward	-18.864	-142.573	-2.376	1.435	-3.935	-0.1379
1.00	1 st	Upward	28.696	216.886	3.615	2.575	-5.075	0.5804
		Downward	-20.866	-157.707	-2.628	1.661	-4.161	-0.1560
	2 nd	Upward	27.550	208.223	3.470	2.439	-4.939	0.6068
		Downward	-20.176	-152.488	-2.541	1.582	-4.082	-0.1732
1.50	1 st	Upward	37.838	285.980	4.766	3.678	-6.178	1.2841
		Downward	-27.467	-207.596	-3.460	2.429	-4.929	-0.4486
	2 nd	Upward	36.830	278.361	4.639	3.555	-6.055	1.3844
		Downward	-27.122	-204.987	-3.416	2.388	-4.888	-0.5350
2.00	1 st	Upward	44.508	336.392	5.607	4.494	-6.994	2.1069
		Downward	-33.157	-250.598	-4.177	3.110	-5.610	-1.1364
	2 nd	Upward	41.995	317.396	5.290	4.186	-6.686	2.2343
		Downward	-32.370	-244.649	-4.077	3.015	-5.515	-1.2954
3.00	1 st	Upward	47.450	358.623	5.977	4.856	-7.356	3.0438
		Downward	-40.089	-302.993	-5.050	3.952	-6.452	-4.1913
	2 nd	Upward	42.354	320.110	5.335	4.230	-6.730	3.3039
		Downward	-36.305	-274.395	-4.573	3.491	-5.991	-5.0065
4.00	1 st	Upward	42.782	323.345	5.389	4.282	-6.782	4.0015
		Downward	-34.855	-263.436	-4.391	3.315	-5.815	-8.8408
	2 nd	Upward	34.192	258.426	4.307	3.235	-5.735	3.6266
		Downward	-28.738	-217.199	-3.620	2.580	-5.080	-9.6675
5.00	1 st	Upward	33.861	255.921	4.265	3.195	-5.695	5.5847
		Downward	-26.832	-202.795	-3.380	2.354	-4.854	-13.1312
	2 nd	Upward	26.597	201.021	3.350	2.326	-4.826	9.1360
		Downward	-21.198	-160.211	-2.670	1.698	-4.198	-13.3169
6.00	1 st	Upward	24.899	188.183	3.136	2.126	-4.626	14.5296
		Downward	-18.726	-141.529	-2.359	1.420	-3.920	-16.5322
	2 nd	Upward	19.154	144.764	2.413	1.467	-3.967	19.0183
		Downward	-13.671	-103.329	-1.722	0.878	-3.378	-19.6836

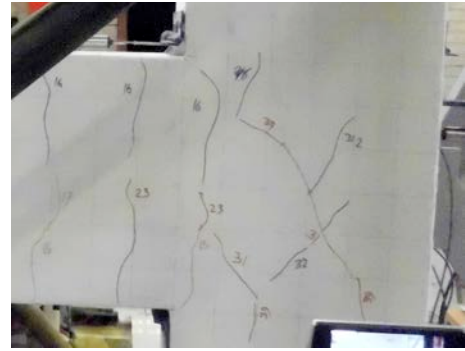
^a Story column shear; ^b Horizontal shear force at joint; ^c Horizontal shear stress at joint

^d Normalized principal tensile stress at joint; ^e Normalized principal compressive stress at joint

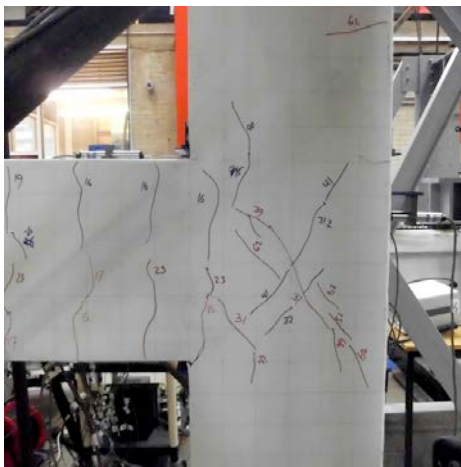
^f Joint shear deformation



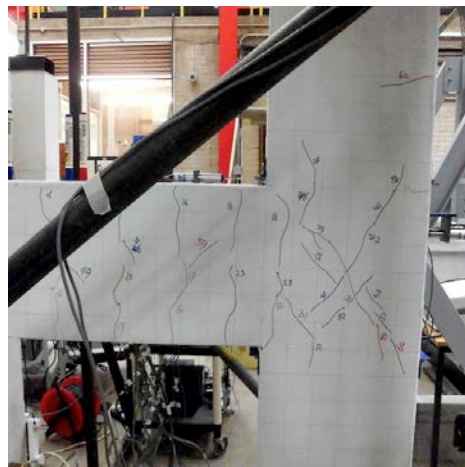
(a) 1% drift, 1st cycle-upward loading
39 kN



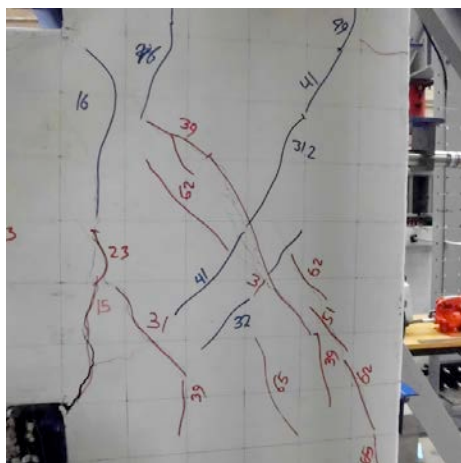
(b) 1% drift, 1st cycle-downward loading
32 kN



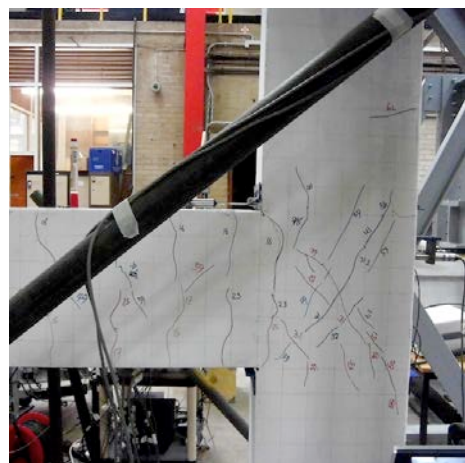
(c) 2% drift, 1st cycle-upward loading
62 kN



(d) 2% drift, 1st cycle-downward loading
kN



(e) 3% drift, 1st cycle-upward loading
65 kN



(f) 3% drift, 1st cycle-downward loading
59 kN

Figure 4.11. Damage propagation – BCJ-SS-F8

The damage propagation for BCJ-SS-F8 is shown in Figure 4.11. For this specimen, the first hairline crack appeared in the beam at 0.25% drift ratio (15.0 kN) at a distance of 16 mm from the column face. Between 0.35 and 0.5% drift ratios (17 to 23 kN), new flexural cracks continued to develop in the beam. The first diagonal cracks appeared at both sides of the joint at 0.75% drift ratio (31 kN), corresponding to a stress level of 2.999 MPa. At this point, the normalized principal tensile stress, p_t/f_c was approximately 0.352. At 1.0% drift ratio (39 kN), these cracks extended to the joint corner. At the upward load corresponding to 1.50% drift ratio (51 kN), a horizontal hairline crack formed in the back of the column. In the following cycles, between 2.00 and 3.00% drift level (62 to 65 kN), damage concentrated on the beam region. Shear cracks appeared at several locations at a load of 62 kN and these cracks developed within a distance of 100 mm to 900 mm from the column face. At the upward drift ratio of 3.00% (65 kN), opening of the beam-column interface started at the bottom side. At the same time, the joint diagonal cracks also propagated towards the joint perimeter. Reversing the load direction at the same drift level resulted in another opening of the upper side of the beam-column interface at the load of (59 kN).

Figure 4.12 presents the load-displacement response for BCJ-SS-F8. The specimen had an initial linear load-displacement response up to a drift ratio of 0.1% (± 1.3 mm). Subsequently, the load-displacement response was quasi-linear, without significant stiffness degradation, up to a drift ratio of 1.50% (± 19.5 mm). The specimen reached its maximum load capacity (68.7 kN) at the first cycle of the 3% drift ratio. Upon further loading, both the overall stiffness and load carrying capacity deteriorated with the increase in drift ratio (displacement).

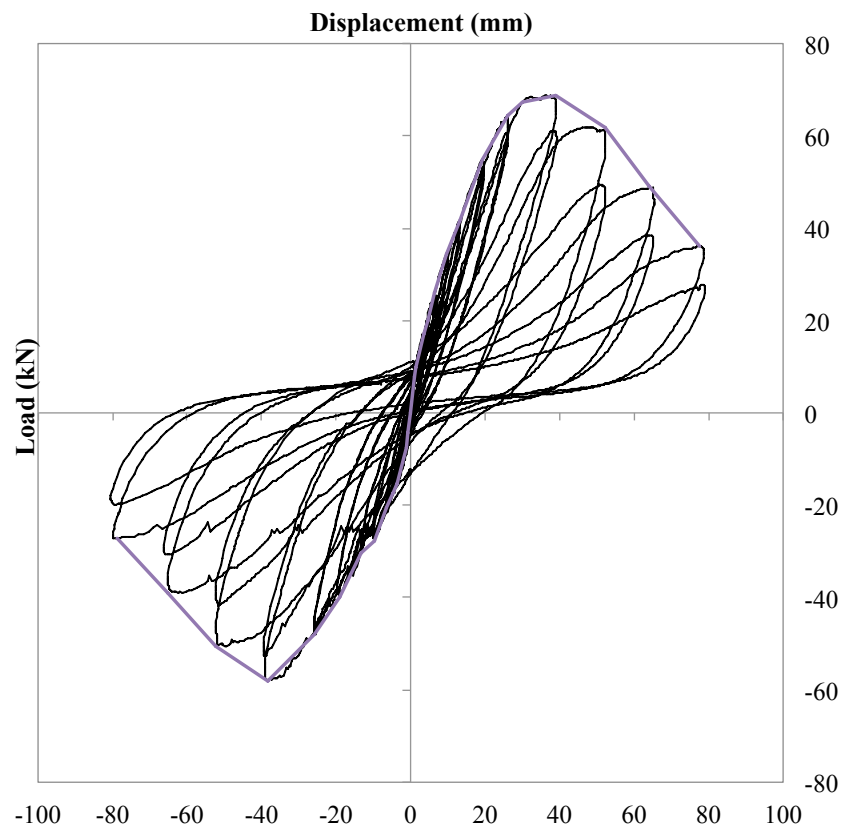


Figure 4.12. Load-displacement response of the strengthened specimen, BCJ-SS-F8

4.2.7. Specimen with Adequately Designed Joint, BCJ-CS-B

This is a specimen with the joint adequately designed according to ACI 352R-02 code to withstand earthquake action. The joint area was reinforced with 8 mm diameter closed steel stirrups spaced at 50 mm centre-to-centre. The test results in terms of the maximum recorded/calculated values for each loading direction are summarised in Table 4.7 whilst curves for story column shear and horizontal shear stress at joint are presented in Appendix 5.

Table 4.7. Summary of test results for BCJ-CS-B

Drift Level (%)	Loading		Applied Load/Stress			Joint Panel Results		
	Cycle	Direction	^a V_c	^b V_{jh}	^c v_{jh}	^d p_t	^e p_c	^f γ
			(kN)	(kN)	(MPa)	(MPa)	(MPa)	*10 ⁻³ (radian)
0.04	1 st	Upward	2.430	18.370	0.306	0.037	-2.537	-0.0009
		Downward	-2.845	-21.501	-0.358	0.050	-2.550	-0.0026
	2 nd	Upward	2.610	19.726	0.329	0.043	-2.543	-0.0050
		Downward	-3.204	-24.214	-0.404	0.064	-2.564	-0.0085
0.10	1 st	Upward	5.717	43.210	0.720	0.193	-2.693	-0.0090
		Downward	-6.104	-46.133	-0.769	0.218	-2.718	-0.0175
	2 nd	Upward	6.145	46.446	0.774	0.220	-2.720	-0.0234
		Downward	-6.007	-45.402	-0.757	0.211	-2.711	-0.0238
0.25	1 st	Upward	11.545	87.255	1.454	0.668	-3.168	-0.0249
		Downward	-10.012	-75.670	-1.261	0.526	-3.026	-0.0662
	2 nd	Upward	11.462	86.629	1.444	0.660	-3.160	-0.0694
		Downward	-9.556	-72.226	-1.204	0.485	-2.985	-0.0633
0.35	1 st	Upward	16.682	126.082	2.101	1.195	-3.695	0.0011
		Downward	-11.752	-88.821	-1.480	0.688	-3.188	-0.0242
	2 nd	Upward	12.608	95.292	1.588	0.771	-3.271	-0.0199
		Downward	-11.462	-86.629	-1.444	0.660	-3.160	-0.0205
0.50	1 st	Upward	17.524	132.448	2.207	1.287	-3.787	0.0555
		Downward	-14.100	-106.564	-1.776	0.922	-3.422	-0.0231
	2 nd	Upward	17.290	130.674	2.178	1.261	-3.761	0.0223
		Downward	-13.782	-104.164	-1.736	0.889	-3.389	-0.0821
0.75	1 st	Upward	23.090	174.510	2.909	1.916	-4.416	0.3022
		Downward	-18.960	-143.303	-2.388	1.446	-3.946	-0.1159
	2 nd	Upward	22.068	166.787	2.780	1.798	-4.298	0.3521
		Downward	-17.400	-131.509	-2.192	1.273	-3.773	-0.1035
1.00	1 st	Upward	27.467	207.596	3.460	2.429	-4.929	0.7890
		Downward	-21.405	-161.777	-2.696	1.722	-4.222	-0.2578
	2 nd	Upward	27.039	204.361	3.406	2.378	-4.878	0.9080
		Downward	-20.963	-158.437	-2.641	1.672	-4.172	-0.2722

Drift Level (%)	Loading		Applied Load/Stress			Joint Panel Results		
	Cycle	Direction	^a V_c	^b V_{jh}	^c v_{jh}	^d p_t	^e p_c	^f γ
			(kN)	(kN)	(MPa)	(MPa)	(MPa)	*10 ⁻³ (radian)
1.50	1 st	Upward	35.974	271.890	4.531	3.451	-5.951	1.8586
		Downward	-27.122	-204.987	-3.416	2.388	-4.888	-0.6168
	2 nd	Upward	34.248	258.843	4.314	3.241	-5.741	1.9714
		Downward	-26.086	-197.159	-3.286	2.266	-4.766	-0.6523
2.00	1 st	Upward	41.719	315.309	5.255	4.152	-6.652	2.9700
		Downward	-33.378	-252.268	-4.204	3.136	-5.636	-1.1374
	2 nd	Upward	40.282	304.454	5.074	3.976	-6.476	3.3743
		Downward	-31.223	-235.986	-3.933	2.877	-5.377	-1.2503
3.00	1 st	Upward	44.563	336.809	5.613	4.501	-7.001	4.5362
		Downward	-38.722	-292.660	-4.878	3.785	-6.285	-3.5221
	2 nd	Upward	40.572	306.646	5.111	4.011	-6.511	5.1242
		Downward	-34.869	-263.540	-4.392	3.317	-5.817	-3.4562
4.00	1 st	Upward	43.983	332.426	5.540	4.430	-6.930	6.7707
		Downward	-38.377	-290.051	-4.834	3.743	-6.243	-6.9821
	2 nd	Upward	37.852	286.084	4.768	3.679	-6.179	7.3700
		Downward	-32.245	-243.709	-4.062	3.000	-5.500	-7.6628
5.00	1 st	Upward	39.965	302.053	5.034	3.937	-6.437	8.9070
		Downward	-34.220	-258.635	-4.311	3.238	-5.738	-10.4935
	2 nd	Upward	33.792	255.399	4.257	3.186	-5.686	10.4828
		Downward	-28.351	-214.276	-3.571	2.534	-5.034	-10.9131
6.00	1 st	Upward	34.980	264.375	4.406	3.330	-5.830	12.9236
		Downward	-28.254	-213.546	-3.559	2.522	-5.022	-14.7887
	2 nd	Upward	29.414	222.313	3.705	2.660	-5.160	15.6426
		Downward	-22.965	-173.571	-2.893	1.901	-4.401	-17.6391

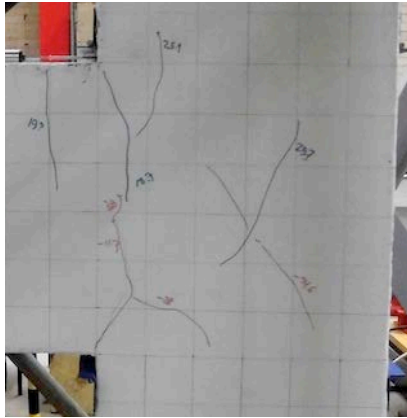
^a Story column shear; ^b Horizontal shear force at joint; ^c Horizontal shear stress at joint

^d Normalized principal tensile stress at joint; ^e Normalized principal compressive stress at joint

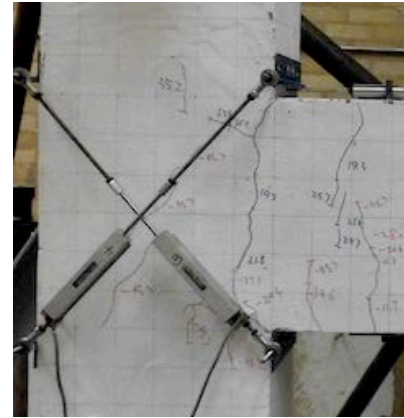
^f Joint shear deformation

The damage propagation is shown in Figure 4.13. The first flexural crack formed in the beam at the downward direction drift ratio of 0.25% drift ratio (19.3 kN). Reversing the load at the second cycle of the same drift ratio resulted in cracks in both the beam and beam-column interface. With the load applied between 0.35 and 0.5% drift ratios (11.7 to 25.1 kN), flexural cracks continued to form in the beam region. Diagonal cracks in the joint started to develop at 0.75% drift ratio (33.4 kN) and continued to propagate at 1.0% drift ratio (34.6 kN) and 1.5%

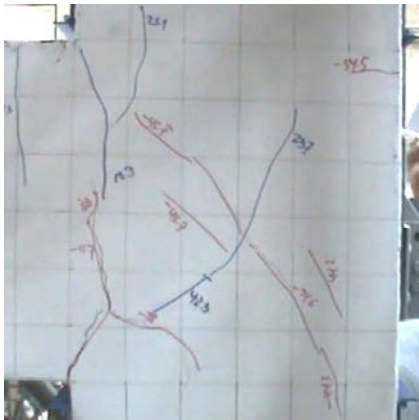
drift ratio (45.7 kN). At the same time cracks were also observed in the beam region and the beam-column interface. The stress level at the moment of joint cracking was 2.909 MPa and the normalized principal tensile stress, $p_t/\sqrt{f_c}$ was approximately 0.358. A diagonal shear crack formed in the beam region at the upward drift ratio of 2.00% drift ratio (54.5 kN) and reversing the load direction at the same drift ratio resulted in a new diagonal crack forming within the joint area and at the back of the lower part of the column. At the upward drift ratio of 3.00% (56.7 kN), several new shear cracks formed in the beam region followed by two parallel diagonal cracks within the joint region. The cracks that formed previously at the lower side of the beam-column interface started to open further. Reversing the load at the same drift ratio also caused cracks at the upper side of the beam-column interface to become wider.



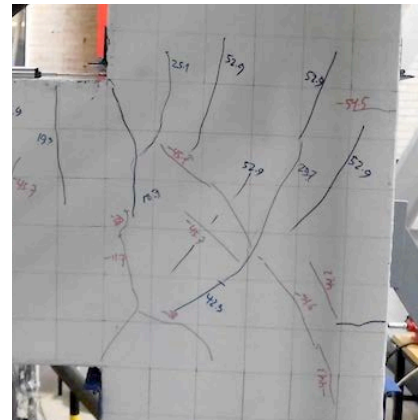
(a) 1% drift, 1st cycle-upward loading
34.6 kN



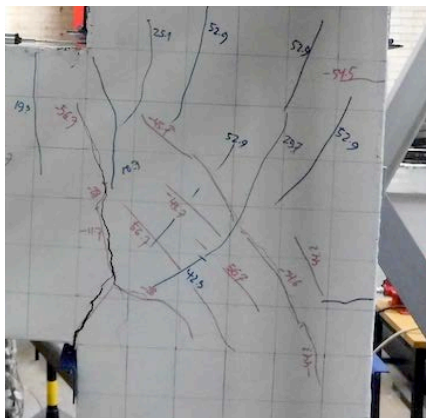
(b) 1% drift, 1st cycle-downward loading
35.2 kN



(c) 2% drift, 1st cycle-upward loading
54.5 kN



(d) 2% drift, 1st cycle-downward loading
52.9 kN



(e) 3% drift, 1st cycle-upward loading
56.7 kN



(f) 3% drift, 1st cycle-downward loading
58.4 kN

Figure 4.13. Damage propagation – BCJ-CS-B

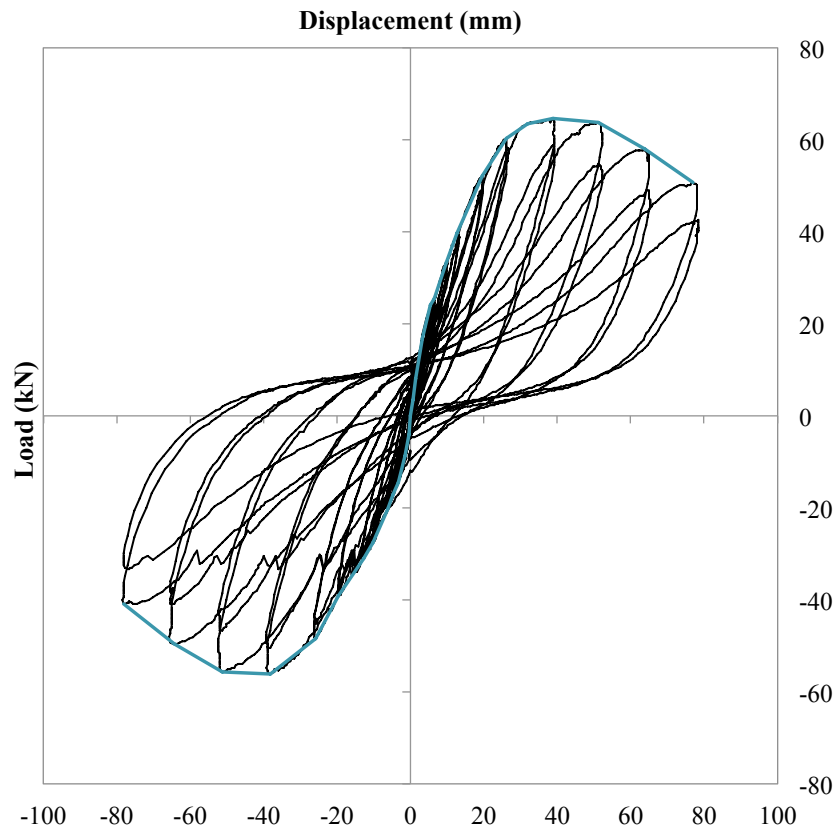


Figure 4.14. Load-displacement response of BCJ-CS-B

Figure 4.14 depicts the load-displacement response for BCJ-CS-B. This specimen had an initial linear load-displacement response up to a drift ratio of 0.25% (± 3.25 mm). Similar to the strengthened specimen, the subsequent load-displacement response was quasi-linear, without significant stiffness degradation, up to a drift ratio of 1.50% (± 19.5 mm). The specimen reached its maximum load carrying capacity (64.5 kN) at the first cycle of the 3.00% drift ratio. A limited yield plateau can be seen in the envelope curve at this load level. Starting at 4.00% (52 mm) drift ratio until the end of the test, pinching length increased gradually, indicating the capability of the specimen to dissipate energy. Moreover, stiffness and strength degradation increased gradually as depicted in Figure 4.14.

4.3. ANALYSIS OF TEST RESULTS

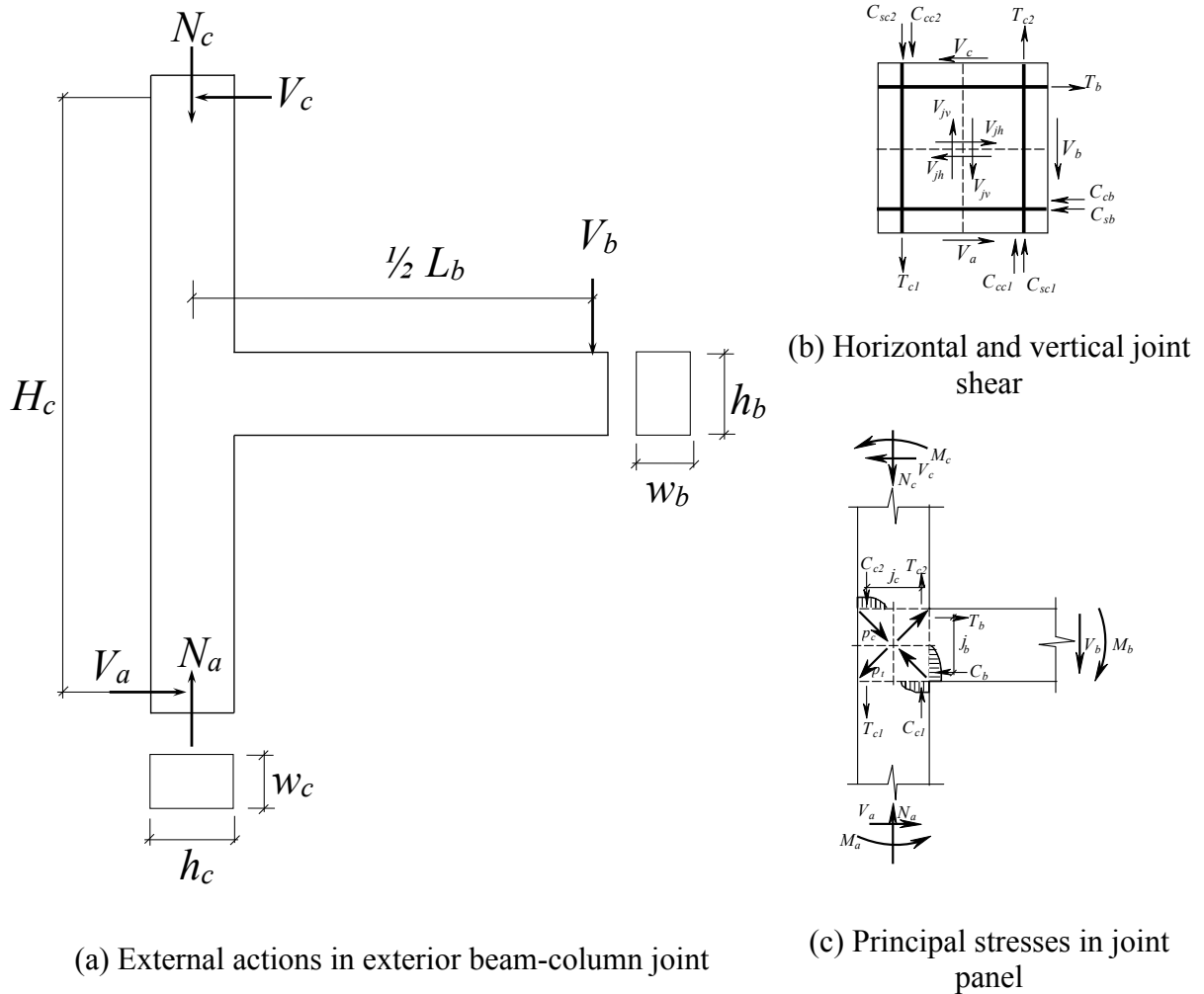


Figure 4.15. Forces acting on beam-column joint

Evaluation of the joints' shear strength in this study is based on the evaluation of the nominal value of the horizontal shear stress (v_{jh}) as calculated in Equation (4.1). The contribution of the column axial compressive stress to the joints' shear stress is considered. The method adopted in this study involves calculating the principal compressive and tensile stresses, p_c and p_t , at mid-depth of the joint's core (see Figure 4.15), as proposed by Hakuto et al. (2000):

$$p_{c,t} = -\frac{f_a}{2} \pm \sqrt{\left(\frac{f_a}{2}\right)^2 + v_{jh}^2}, \quad f_a = \frac{N_c}{h_c w_c}, \quad V_{jh} = T_b - V_c, \quad v_{jh} = \frac{V_{jh}}{w_j h_c}, \quad T_b = V_b \frac{1}{j_b} \left(\frac{L_b}{2} - \frac{h_c}{2} \right),$$

$$V_c = \frac{V_b L_b}{2H_c} \quad (4-1)$$

where $p_{c,t}$ = joints' principal stresses; f_a = column axial compressive stress; V_{jh} = horizontal shear force acting across the joint region; T_b = tensile force in beam bars; V_b = beam shear force and v_{jh} = horizontal shear stress.

4.3.1. Strength and Failure Modes

As mentioned in section 4.2.2, during testing of specimen BCJ-CS-A Test #1, the lateral steel beam that supported the upper end of the column was not rigid enough to resist the load. This caused the measured load and the displacement during upward loading to be less and delayed the cracking of the specimen, as compared to that of the second control specimen (BCJ-CS-A test #2). For that reason, the results of the strengthened specimens will be compared to those of specimen BCJ-CS-A Test #2. Overall, both control specimens (BCJ-CS-A Test #1 and BCJ-CS-A Test #2) experienced hybrid local damage and a failure mechanism. This mechanism was characterised by shear damage in the form of cross-diagonal cracks. As a result, a wide concrete wedge developed; leading to the spalling of the outer face of the concrete column after a drift ratio of 3.00%, which is typical of joint shear (JS) failure. This can be attributable to the inadequate shear reinforcement in the joint region.

Compared to the control specimens, all the strengthened specimens exhibited more enhanced behaviour where damage occurred in the beam region at the early stages of loading, suggesting the outset of a beam hinge (BH) mechanism and then diagonal cracks propagated

in the joint after 1.00% drift ratio. Stable hysteresis behaviour with high energy dissipation capacity was also maintained until the end of the test (see Figures 4.6, 4.8, 4.10 and 4.12).

The significant contribution of the embedded bars can be seen in Table 4.8. The displacement ductility μ is defined as Δ_u/Δ_y , where Δ_u is the beam tip displacement at the load step corresponding to 20% reduction in ultimate load and Δ_y is the displacement of the reduced stiffness equivalent to elasto-plastic yield (Park, 1989).

All the strengthened specimens performed better, in terms of the joints' shear strength and dissipated energy, compared to BCJ-CS-A Test #2. This result demonstrates the potential of the strengthening technique. A substantial improvement in the global performance of BCJ-SS-S4 and BCJ-SS-F4 can be seen in the joints' shear stress, which for both specimens increased by 6% and 21% for the case of upward loading; while both specimens BCJ-SS-S8 and BCJ-SS-F8 had an increase of 7% and 16% in the joints' shear stress compared to that of the duplicate control specimen (BCJ-CS-A Test #2). At the local level, a 25% enhancement in the normalized principal tensile stress demand in the joint panel of BCJ-SS-F4 was recorded, when compared to that of the duplicate control specimen; whilst the corresponding increase for BCJ-SS-S8 and BCJ-SS-F8 were 22% and 18%, respectively. In terms of materials, joints strengthened by CFRP bars had higher capacities compared to those of specimens strengthened by steel bars. The strengthened specimens also showed higher joints' shear strength than BCJ-CS-B. For example, BCJ-SS-F4 and BCJ-SS-F8 had significant enhancement in the joints' shear stress at the upward loading compared to that of BCJ-CS-B. The corresponding increases at the upward loading for specimens BCJ-SS-F4 and BCJ-SS-F8 were 11% and 7%, respectively.

Table 4.8. Summary of test results

Specimen	Load Direction	V_c^a (kN)	v_{jh}^b (MPa)	p_c/f_c^c	$p_t/\sqrt{f_c}^d$	μ^e	$p_{t,1}/\sqrt{f_c}^f$	$p_{t,2}/\sqrt{f_c}^g$	$p_{t,3}/\sqrt{f_c}^h$	Energy ⁱ (kN-mm)	Failure Mode
BCJ-CS-A Test #1	Upward	41.27	5.20	-0.19	0.73	1.4	0.24	0.40	0.58	11930.35	JS
	Downward	-43.48	-5.48	-0.20	0.78	1.8	0.30	0.53	0.76		
BCJ-CS-A Test #2	Upward	40.84	5.14	-0.21	0.72	1.8	0.43	0.67	0.72	11534.14	JS
	Downward	-37.19	-4.69	-0.19	0.64	1.5	0.35	0.57	0.64		
BCJ-SS-S4	Upward	43.09	5.43	-0.15	0.64	2.5	0.30	0.57	0.64	19541.75	BH JS
	Downward	-48.84	-6.15	-0.17	0.75	2.9	0.44	0.72	0.75		
BCJ-SS-F4	Upward	49.27	6.21	-0.24	0.90	1.9	0.43	0.76	0.90	13623.23	BH JS
	Downward	-36.29	-4.57	-0.19	0.62	1.9	0.28	0.53	0.62		
BCJ-SS-S8	Upward	43.74	5.51	-0.28	0.88	1.7	0.34	0.70	0.88	14056.42	BH JS
	Downward	-40.34	-5.08	-0.26	0.80	1.8	0.35	0.64	0.78		
BCJ-SS-F8	Upward	47.45	5.98	-0.23	0.85	2.2	0.45	0.79	0.85	16447.84	BH JS
	Downward	-40.09	-5.05	-0.20	0.70	1.7	0.29	0.55	0.70		
BCJ-CS-B	Upward	44.56	5.61	-0.24	0.84	3.3	0.45	0.78	0.84	20233.18	BH
	Downward	-38.72	-4.88	-0.22	0.71	2.2	0.32	0.59	0.71		

^a Story column shear at peak load; ^b Horizontal shear stress in the joint at peak load;

^c Normalized principal compressive stress in the joint at peak load; ^d Normalized principal tensile stress in the joint at peak load;

^e Ductility;

^{e, i} Calculated at the loading step corresponding to 20% reduction in ultimate load;

^{f, g, h} Normalized principal tensile stress at 1.00, 2.00, and 3.00% drift ratios, respectively.

Table 4.8 shows a significant increase in displacement ductility for the case of the BCJ-SS-S4 specimen. A 39% (upward direction) and 93% (downward direction) increase in the displacement ductility of the BCJ-SS-S4 specimen was observed compared to that of BCJ-CS-A Test #2. The corresponding increases at the upward loading for specimens BCJ-SS-F4 and BCJ-SS-F8 were 6% and 22%, respectively. While the increases at the downward loading for specimens BCJ-SS-F4, BCJ-SS-S8 and BCJ-SS-F8 were 27%, 20% and 13%, respectively.

On the other hand, there was no displacement ductility enhancement observed for the case of upward loading of BCJ-SS-S8. During the upward loading of the BCJ-SS-S8, the displacement yield, Δ_y , was observed somewhere at a point between 2.00% (26 mm) and 3.00% (39 mm) drift ratio, and the ultimate displacement, Δ_u , (the load step where the 20% reduction in ultimate load) was reached at the second cycle of 4.00% drift ratio. As can be seen in Figure 4.10, after the specimen reached its peak load at 3.00% drift ratio, the load dropped significantly at the second cycle of 4.00% drift ratio. Damage accumulation in the joint during the peak load caused significant strength degradation, hence prevented the increase in the displacement ductility of BCJ-SS-S8.

The specimen BCJ-CS-B, as expected, had superior displacement ductility compared to that of the strengthened specimens. The joints' shear reinforcement of BCJ-CS-B was designed according to ACI 352R-02 and aimed to satisfy strength and ductility requirements relating to the function of the connection within a structural frame. Test results showed that the displacement ductility for specimens BCJ-SS-S4, BCJ-SS-F4, BCJ-SS-S8 and BCJ-SS-F8 were 24%, 42%, 48% and 33% less than that of BCJ-CS-B.

The variation of normalized principal tensile stress with joint shear deformation (see Figures 4.16) shows that the strengthened specimens had higher joint stiffness at upward loading, except for specimen BCJ-SS-S4. For this specimen, the first joint cracking and maximum load were reached during the downward loading direction. In most cases, beyond a downward drift ratio of about 1.00%, the stiffness of the strengthened joints deteriorated due to excessive cracking. Post-test observation showed splitting cracks surrounding the embedded bars. This suggests loss of bond between the concrete and embedded bars/epoxy.

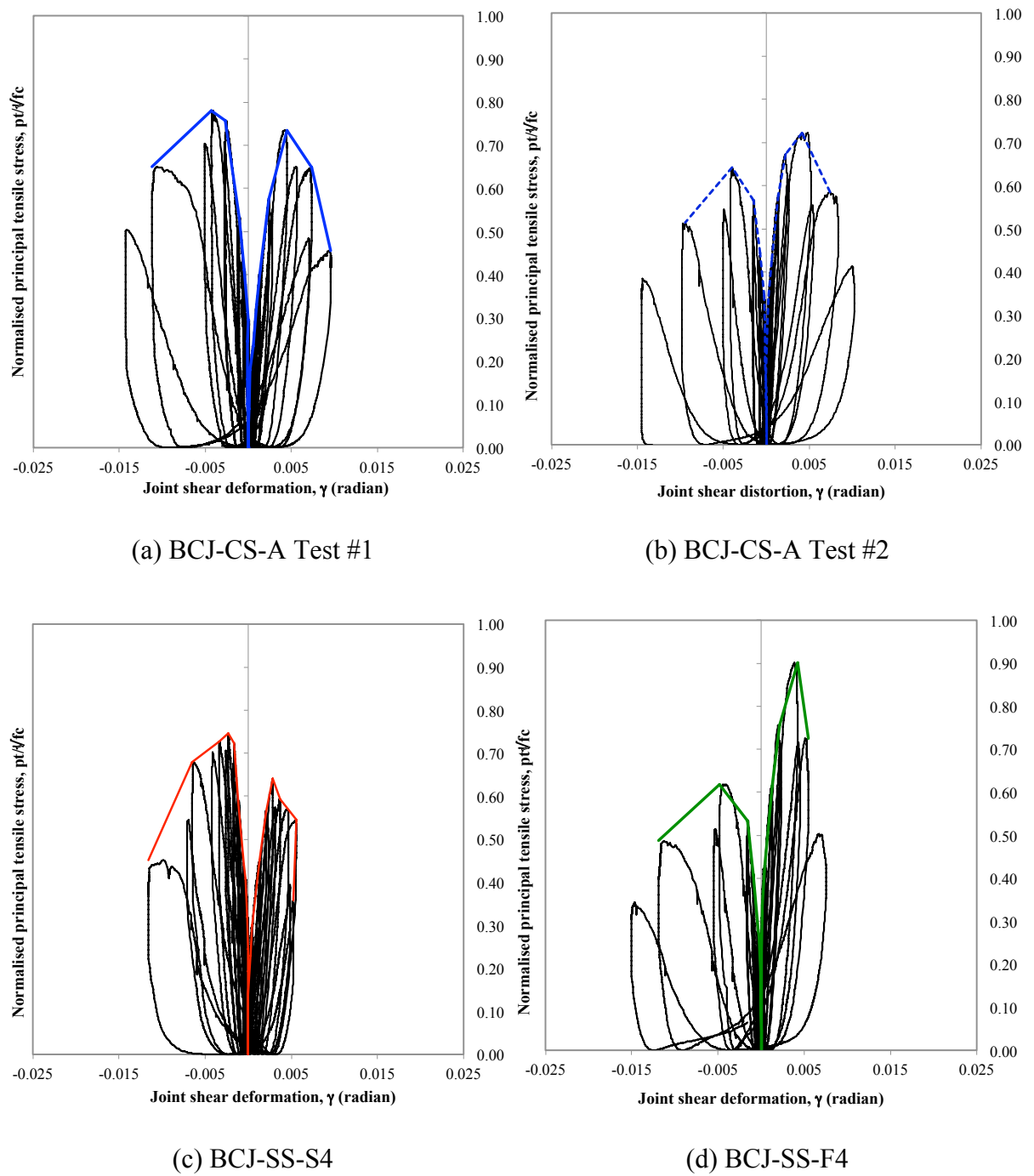
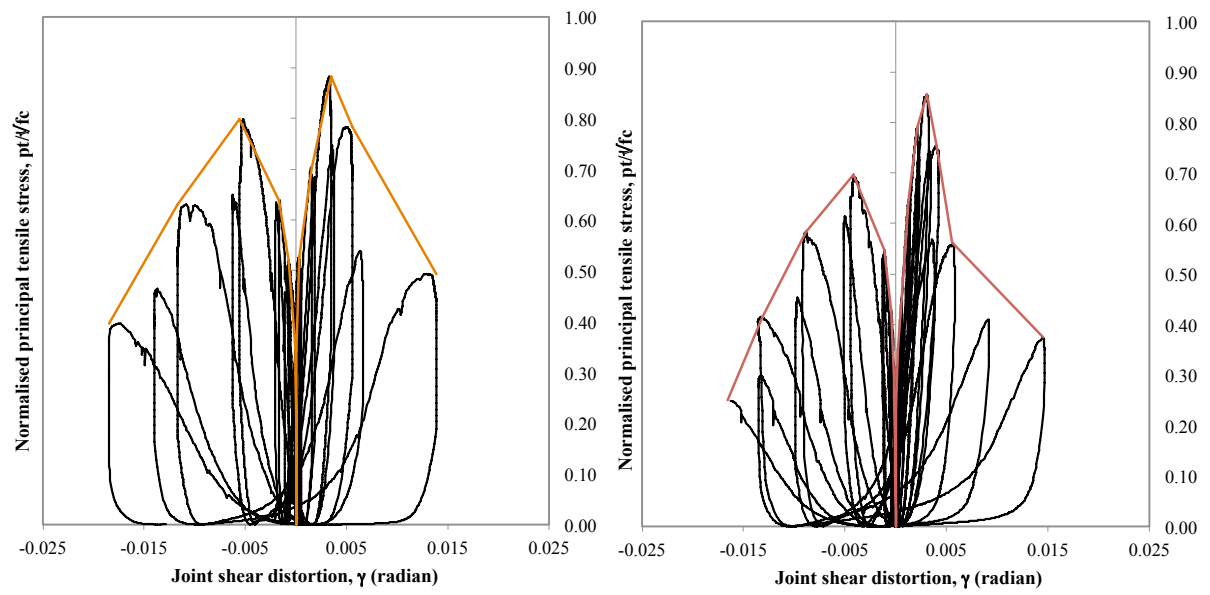
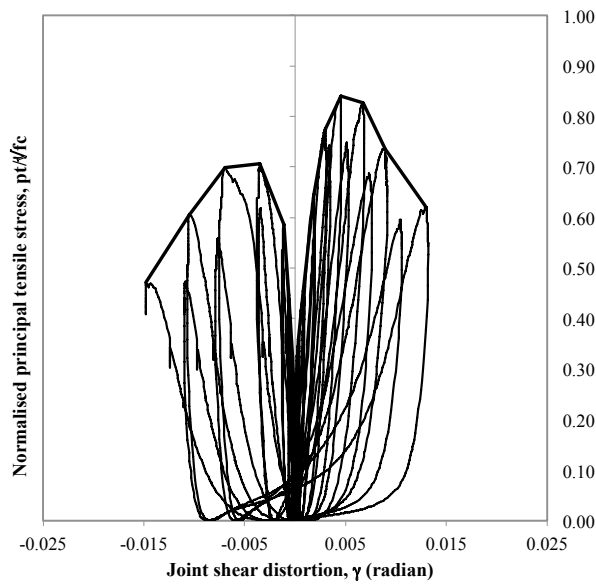


Figure 4.16. Normalized principal tensile stress versus joint shear deformation for control specimens, BCJ-SS-S4 and BCJ-SS-F4



(a) BCJ-SS-S8

(b) BCJ-SS-F8



(c) BCJ-CS-B

Figure 4.17. Normalized principal tensile stress versus joint shear deformation for specimen BCJ-SS-S8, BCJ-SS-F8 and BCJ-CS-B

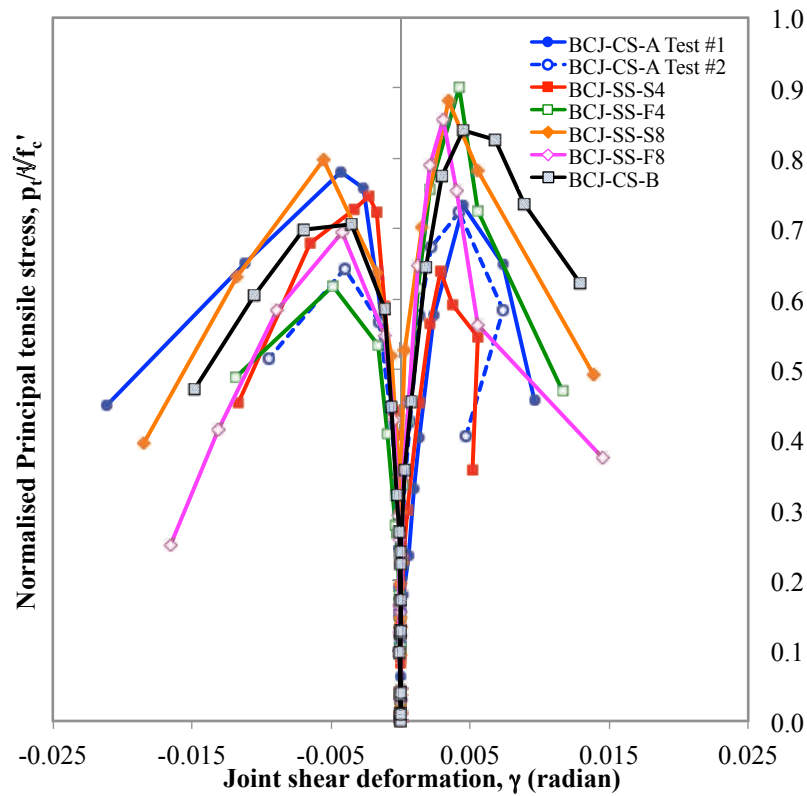


Figure 4.18. Back bone curves of normalized principal tensile stress versus joint shear deformation for tested specimens

The normalized principal tensile stresses of the strengthened specimens at the peak loads in the upward loading direction were comparable to those of specimen BCJ-CS-B, except for BCJ-CS-S4. This demonstrates that the use of embedded bar as a joints' shear reinforcement has the potential for the retrofitting of existing buildings with deficient beam-column joints. In addition, the results also showed that the normalized principal tensile stress of specimen BCJ-SS-F4 was 7% higher than that of specimen BCJ-CS-B.

4.3.2. Key Observation Points of the Joints' Shear Behaviour

The overall and local behaviour of a BCJ subjected to reverse cyclic loading can be represented by the envelope of the hysteresis curve that linearly connects three points showing the most distinct stiffness changes. Studies conducted by Kim and LaFave (2007) revealed that distinct stiffness changes produced from load-displacement relationships were similar to those of load-joint shear deformation relationships. In other words, the development of new damage in and around a joint panel also generates distinct stiffness changes in overall behaviour. For that reason, load-joint shear deformation curves (see Figure 4.17) are used to produce the envelope curves of all tested specimens in this study. The envelope curves are characterized by three distinct points (A, B, and C). After drawing an initial tangent line from the origin, the point that corresponds to the development of diagonal cracks in the joint panel was considered to be the first point (A). Point A triggers a significantly different tangent line compared to the initial line. A second tangent line joins point A and the point that corresponds to the yielding of the longitudinal beam reinforcement. This second point (B) triggers a significantly different tangent line compared to the second tangent line due to stiffness change. In the case of joints' shear failure, where beam reinforcement does not usually yield, the stiffness change can be marked by the yielding of the joints' transverse reinforcement. Finally, a third line joins B and the point (C) corresponding to the peak load. Beyond point C, the applied load decreases due to concrete crushing.

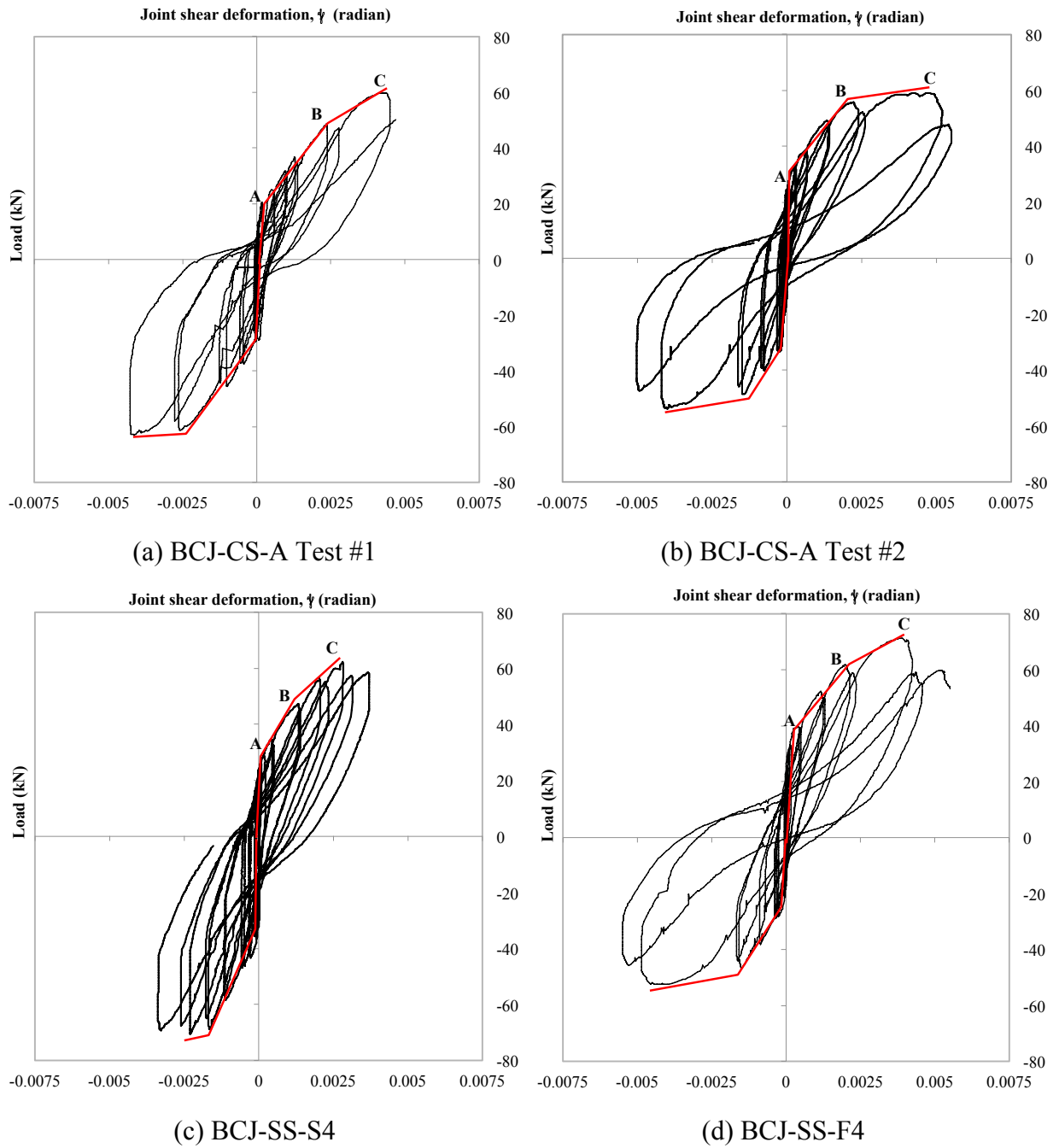


Figure 4.19. Load versus joint shear deformation for control specimens, BCJ-SS-S4 and BCJ-SS-F4

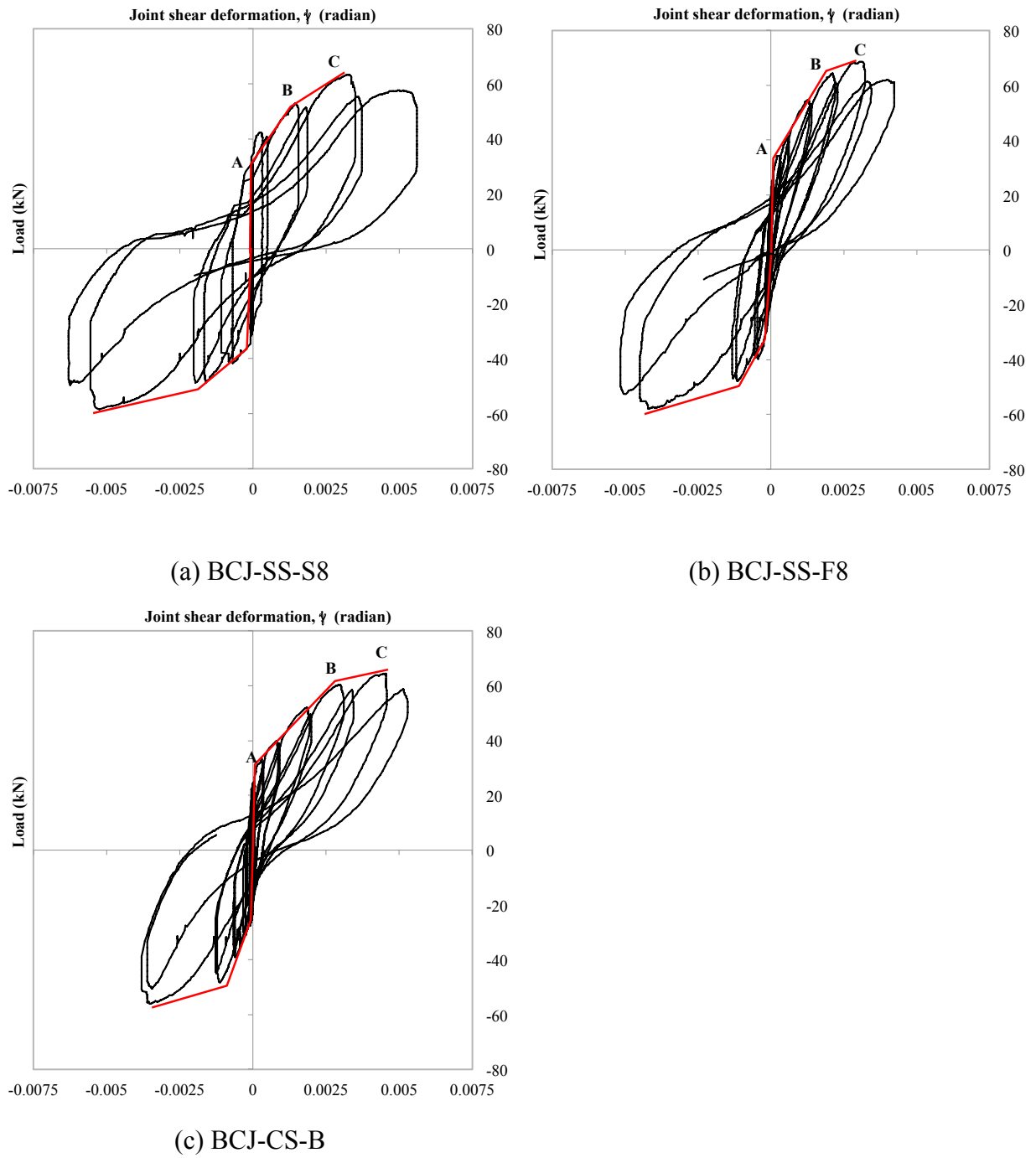


Figure 4.20. Load versus joint shear deformation for specimen BCJ-SS-S8, BCJ-SS-F8 and BCJ-CS-B

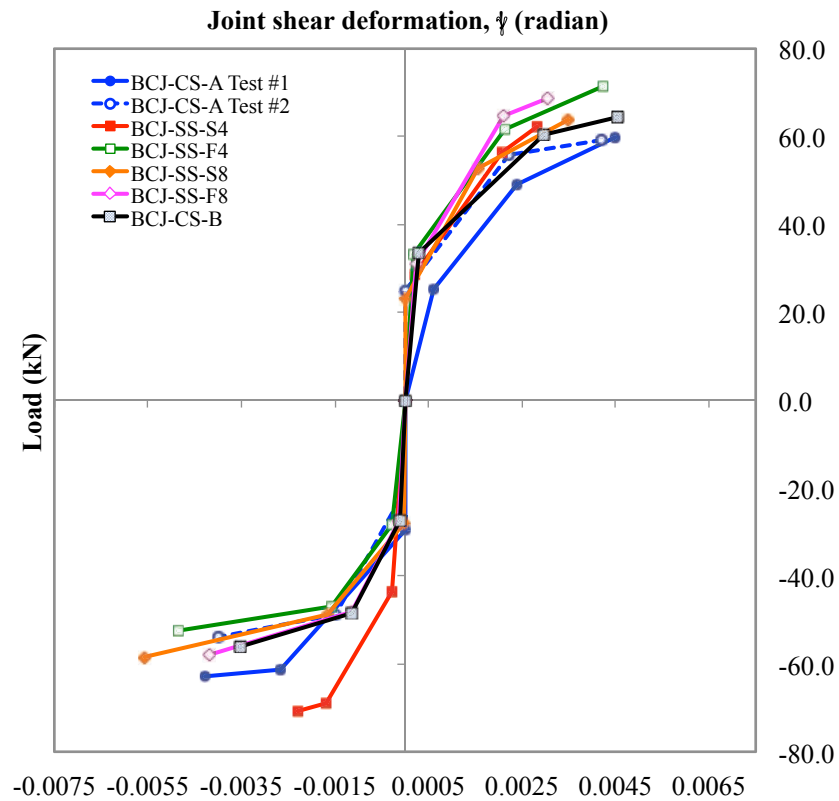


Figure 4.21. Back bone curves of load versus joint shear deformation for tested specimens

Figure 4.21 shows that the joints' stiffness of the strengthened specimens was higher compared to that of the control specimen for both upward and downward loading. For example, the joints' stiffness of the specimens BCJ-SS-S4, BCJ-SS-F4, BCJ-SS-S8 and BCJ-SS-F8 at point C was enhanced by about 53, 20, 30 and 60.5%, respectively. The significant contribution of the strengthening method to the global and local behaviour of the joints is explained in details in section 4.4.

Table 4.9 presents the load and joint deformation of the corresponding key points for the tested specimens.

Table 4.9. Key response points for tested specimens

Specimen ID	Key points	Upward load direction		Upward load direction	
		Load (kN)	Joint deformation $\times(10^{-3}$ radian)	Load (kN)	Joint deformation $\times(10^{-3}$ radian)
BCJ-CS-A Test #1	A	25.10	0.5982	-29.35	-0.0044
	B	49.03	2.3928	-61.34	-2.6504
	C	59.77	4.4908	-62.97	-4.2681
BCJ-CS-A Test #2	A	24.90	0.0041	-22.50	-0.1054
	B	55.88	2.2164	-48.72	-1.4748
	C	59.14	4.2057	-53.86	-3.9930
BCJ-SS-S4	A	28.72	0.2237	-43.62	-0.2907
	B	56.42	2.0710	-68.94	-1.6806
	C	62.40	2.8382	-70.74	-2.3017
BCJ-SS-F4	A	33.24	0.1791	-28.32	-0.2666
	B	61.76	2.1427	-46.82	-1.5807
	C	71.36	4.2351	-52.56	-4.8577
BCJ-SS-S8	A	23.16	0.0082	-27.92	-0.0209
	B	52.78	1.5645	-48.86	-1.6636
	C	63.34	3.4894	-58.42	-5.5565
BCJ-SS-F8	A	31.00	0.2289	-27.74	-0.1283
	B	64.60	2.1069	-48.02	-1.1364
	C	68.72	3.0438	-58.06	-4.1913
BCJ-CS-B	A	33.40	0.3022	-27.46	-0.1159
	B	60.42	2.9700	-48.34	-1.1374
	C	64.54	4.5362	-56.08	-3.5221

4.3.3. Stiffness and Energy Dissipation Characteristic

The variations of the peak-to-peak stiffness, as well as the cumulative energy dissipation with the drift ratio are presented in Figures 4.22 and Figure 4.23, respectively. The peak-to-peak

stiffness is defined as the slope of the line connecting the peak load points in the load-displacement curve reached at each displacement level. The cumulative energy dissipated is computed by summing up the area under the load-displacement curve.

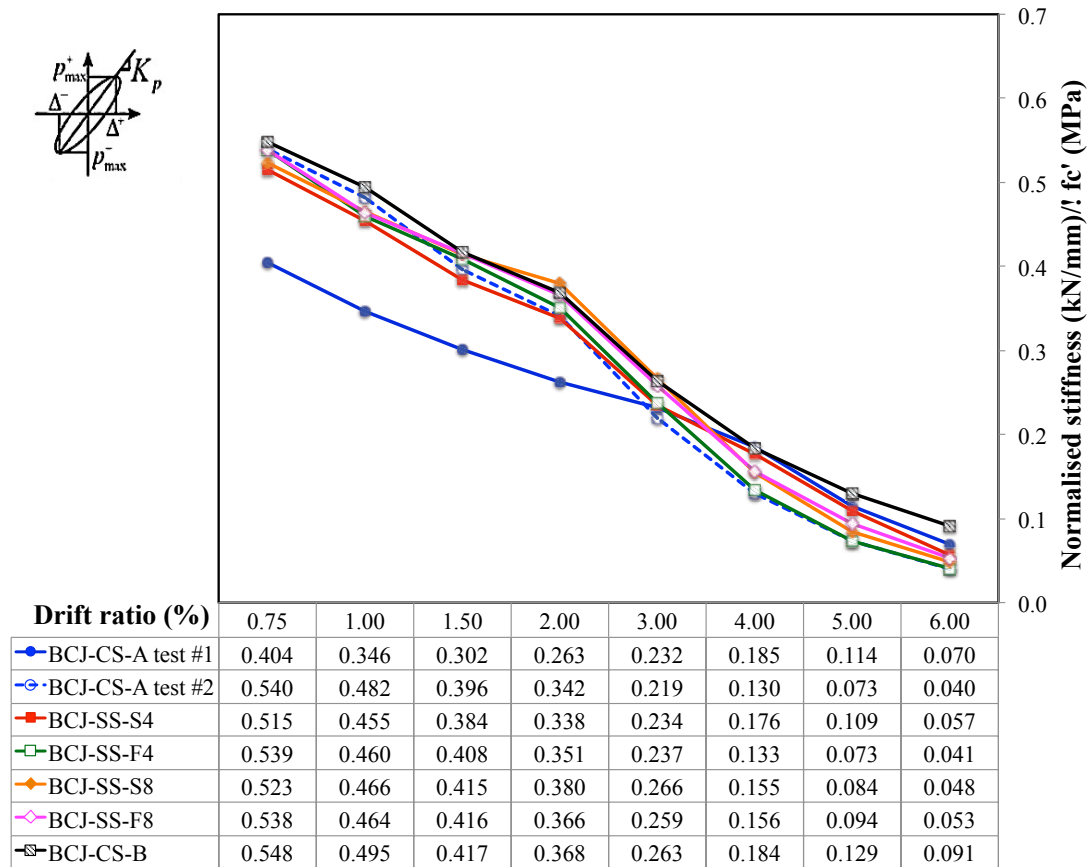


Figure 4.22. Comparison of normalized peak-to-peak stiffness

An examination of the stiffness degradation of the specimens reveals that a) the control specimen (BCJ-CS-A Test #2) experienced more stiffness degradation at 1.00% drift ratio; b) the strengthened specimens started to gain a higher level of stiffness at the loading of 1.00% drift ratio. As mentioned in the previous section, between drift ratio of 0.75 and 1.00%, the specimens experienced the joints' shear cracking and severe joint damage was observed beyond 3.00% drift ratio. At this point the joint shear stresses were fully transferred to the embedded bars in the strengthened joints before the embedded bars experienced a loss of bond.

Figure 4.22 shows that at 1.50% drift ratio, the normalized peak-to-peak stiffness for BCJ-SS-S8 and BCJ-SS-F8 was +4% and +6% compared to that of the duplicate control specimen, respectively. Comparing to the adequately designed joint specimen, the normalized peak-to-peak stiffness for the strengthened specimens was unremarkable. For example, the normalized peak-to-peak stiffness for specimens BJC-SS-S4, BCJ-SS-F4, BCJ-SS-S8 and BCJ-SS-F8 at 1.5% drift ratio were -2%, -6%, -2%, and -2% against that of BCJ-CS-B.

As depicted in Figure 4.23, the energy dissipation levels achieved by the strengthened specimens were generally higher than those achieved by the control specimens, especially at drift levels of 1.00% or more. For example, the energy absorbed by the strengthened specimens at 2.00% drift ratio was 4080 kN-mm (BCJ-SS-S4); 3543 kN-mm (BCJ-SS-F4); 3203 kN-mm (BCJ-SS-S8); and 3333 kN-mm (BCJ-SS-F8); representing increases of 31%, 14%, 3% and 7%, respectively, over the corresponding values for the duplicate control specimen (BCJ-CS-A Test #2). Moreover, the energy dissipation levels of the strengthened specimens up to 4% drift ratio were comparable to that of the BCJ-CS-B; except for the BCJ-SS-S8. Figure 4.23 shows that the energy absorbed by the strengthened specimens at 1% drift ratio was 1096 kN-mm (BCJ-SS-F4) and 1055 kN-mm (BCJ-SS-F8); while the corresponding energy for the BCJ-CS-B was 1047 kN-mm. In addition, the concrete strength significantly affected the dissipated energy of the beam-column joint specimens. The energy absorbed by the BCJ-SS-S4 at drift ratios of 1.00%, 2.00% and 3.00% was 1336 kN-mm, 4080 kN-mm and 8372 kN-mm, respectively. While the dissipated energy of the adequately designed joint (BCJ-CS-B) at the corresponding drift ratios was 1047 kN-mm, 3408 kN-mm and 6839 kN-mm, respectively.

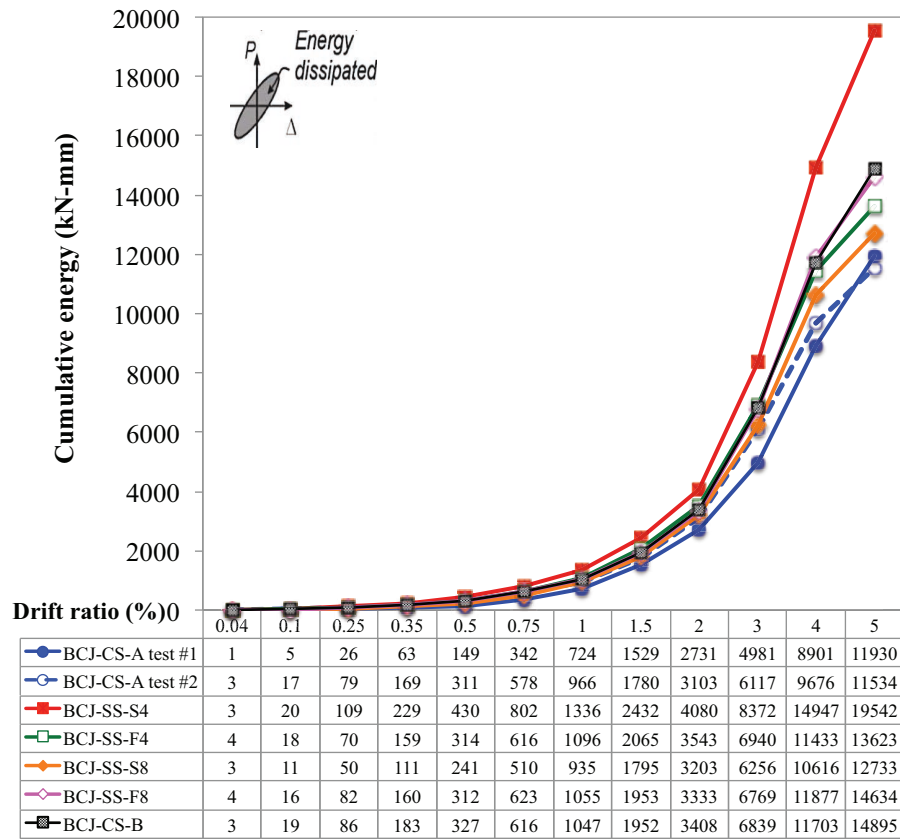


Figure 4.23. Comparison of energy dissipation

4.3.4. Beam Fixed-end Rotation

Figure 4.24 presents the envelope curves of the normalized load-fixed-end beam rotation relationships for the tested specimens. Both control specimens show limited rotation, while the specimens strengthened with embedded steel bars show more enhanced fixed-end beam rotation than specimens strengthened with embedded CFRP bars. Figure 4.24 confirms the effectiveness of the strengthening scheme employed in this study.

The beam rotation of both the control specimens was much smaller, indicating the absence of the plastic hinge in the specimens. The beam rotations of the BCJ-CS-A Test #1 and BCJ-CS-A Test #2 at the maximum load were 0.0040 and 0.0066 radians, respectively. While the beam rotations of the strengthened specimens at the maximum load were 0.012 radians (BCJ-

SS-S4); 0.009 radians (BCJ-SS-F4); 0.010 radians (BCJ-SS-S8); and 0.0074 radians (BCJ-SS-F8). It can also be seen that the specimens BCJ-SS-S4 and BCJ-SS-S8 exhibited 40% and 30% larger plastic deformations than the BCJ-SS-F4 and BCJ-SS-F8. Moreover, the maximum rotation of the BCJ-SS-S4 and BCJ-SS-S8 was comparable to that of specimen BCJ-CS-B, extending to around 0.03 radians at failure.

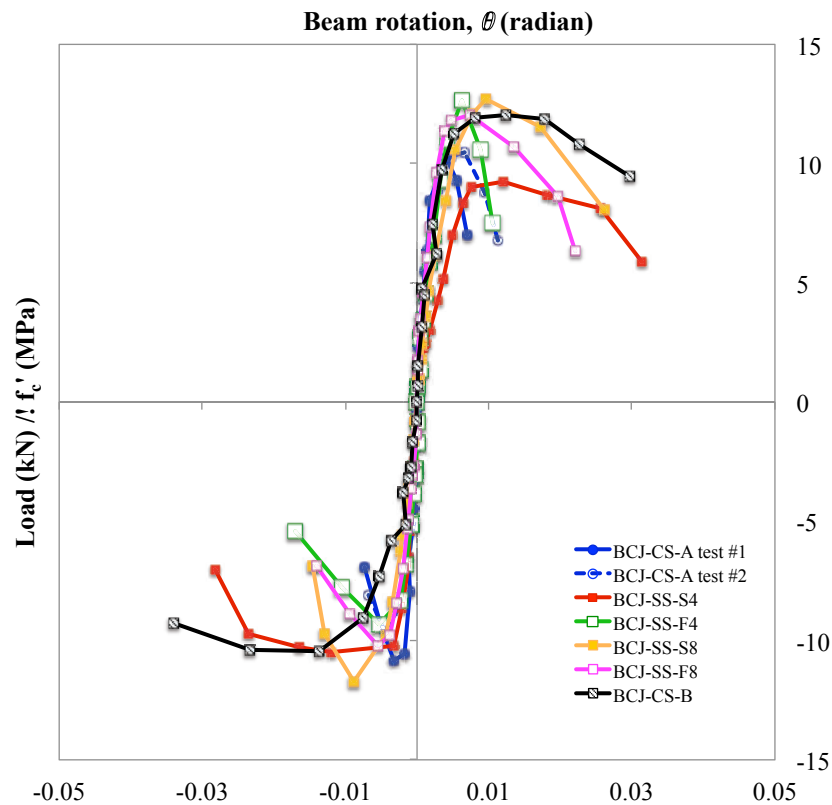


Figure 4.24. Envelope curves of normalized load-beam fixed-end rotation

4.3.5. Strain Measurements

The investigation conducted on the strain readings to the reinforcement bars within the joint area helps to provide useful information on the application of the DE strengthening method. Reinforcement bar strains are measured using strain gauges attached to the reinforcement bars located on critical regions within the joint.

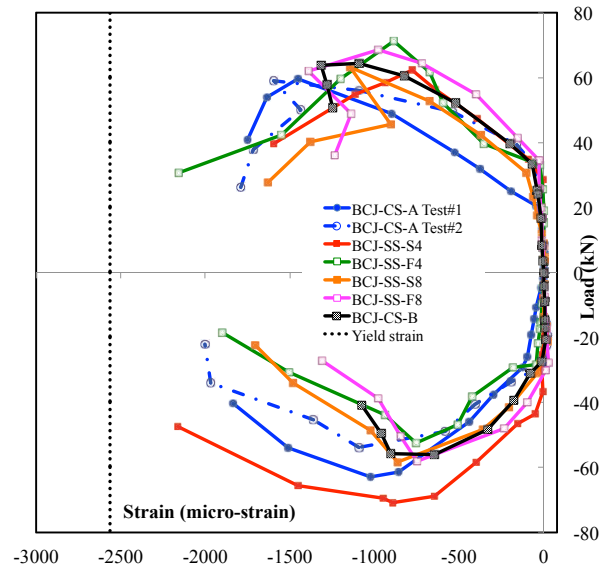


Figure 4.25. Envelope curves of load-strain for column reinforcement

Figure 4.25 depicts the envelope curves load-strain of the column reinforcement bar for the tested specimens. In general, the measured strains on the column main bars remained in the elastic range until the end of the test. After a 3% drift ratio, the joint area was heavily damaged and there was a local slippage between the concrete and some reinforcement bars, which stopped the load from increasing further. In detail, the strain reading on the column reinforcement bar for each specimen was as follows:

- For BCJ-SS-S4, the strain of the column reinforcement bar at maximum load was approximately 35% of the yield strain; while the strain readings for BCJ-SS-S8 at the peak load position of upward and downward loading directions, were 44.5% and 33.74% of the yield strain, respectively.
- For BCJ-SS-F8, the column reinforcement strain at 3% drift ratio of upward and downward loading directions was 976.43 and 748.55 micro-strain respectively; representing 38% and 29% to the corresponding values of the yield strain.

- The strain reading of BC-CS-B at the maximum load of upward and downward directions was approximately 42.5% and 25% of that of the yield strain, respectively.

Figure 4.26 depicts the envelope curves of the load-strain of the top and bottom beam reinforcement bar for the tested specimens. In general, the strain readings on those bars were in the elastic range until the 3% drift ratio. In detail, the strain reading on the beam reinforcement bars for each specimen can be described as follows:

- The bottom beam reinforcement bar on BCJ-CS-A Test #1 was first observed to start yielding during an upward loading direction of 4% drift ratio. At this point, the strain reading on the bottom beam reinforcement was 2870.559 micro-strains at the peak load of 59.70 kN. Reversing the load to the downward loading direction at the same drift ratio initiated the yielding of the top beam reinforcement at the load of 57.68 kN. Afterwards, the strain readings on the bottom reinforcement bar decreased until the end of the test. While for BCJ-CS-A Test #2, the yielding of the top reinforcement bar was observed at a downward loading of 3% drift ratio. At this point, the strain reading on the bottom beam reinforcement was 2677.6 micro-strains at the peak load of 53.80 kN. On the other hand, the bottom steel reinforcement yielded earlier at a 2% drift ratio of the upward loading direction (55.9 kN) with the measured strain of 2581.6 micro-strains. Joint cracking propagated on a 1.00% drift ratio reduced the joint's strength and transferred the stress to the beam steel reinforcement to carry the load.
- The top beam reinforcement on BCJ-SS-S4 reached its yield strain during a downward loading direction of 4% drift ratio at a maximum load of 69.4 kN. Further loading showed the strain reading on the top beam reinforcement bars decreased. it was due to the damage localization within the joint area and caused the strain gauges to detach

from the reinforcement bars. Compared to the top beam reinforcement bar, the bottom reinforcement bars yielded earlier at 3% drift ratio of the upward loading direction. At this point, the strain was 2764.56 micro-strains at the load of 62.38 kN. With further upward loading direction at a 5% drift ratio, the strain reading on these bars reached 4871.94 micro-strains; approximately 1.9 times the yielding strain at the load of 54.78 kN. Afterwards, the joint collapsed and the strain gauge detached from the steel bars. Unfortunately, the strain readings from the top and bottom beam reinforcement bars of BCJ-SS-F4 were not recorded well from the 3% drift ratio onwards, so that the strains were only plotted until the 3% drift ratio. In fact, the strain data from both beam reinforcement bars showed that the beam bars had never reached their yield strength. For the top reinforcement bar, the yield strain on the maximum load was 61% of the yield strain; whereas the bottom reinforcement bars reached a lower strain, approximately 43% of the yield strain.

- For BCJ-SS-S8, the yielding of the beam reinforcement was initially developed on the bottom beam reinforcement during the upward loading direction of 3% drift ratio; whereas the top beam reinforcement yielded at the same drift ratio in a downward loading direction. At this point, yield strain of the bottom and the top beam reinforcement was 2877.84 and 2953.93 micro-strains respectively; and further loading showed that the steel bars maintained their yield strength until it decreased due to concrete cracking developing within the joint area. For BCJ-SS-F8, both top and bottom beam reinforcement yielded at the 3% drift ratio. The corresponding strain value for the top and the bottom beam reinforcement was 2973.99 micro-strains and 2615.299 micro-strains respectively. The strains on the beam reinforcement then

decreased as the further loading caused the joint area to become heavily damaged and this led to strength deterioration.

- Lastly, the yielding of the top and the bottom beam reinforcement of BCJ-CS-B was observed at a maximum load of 3% drift ratio. The corresponding strain value for the top beam reinforcement was 3111.28 micro-strains; whereas the strain value for the bottom beam reinforcement was 2592.97 micro-strains.

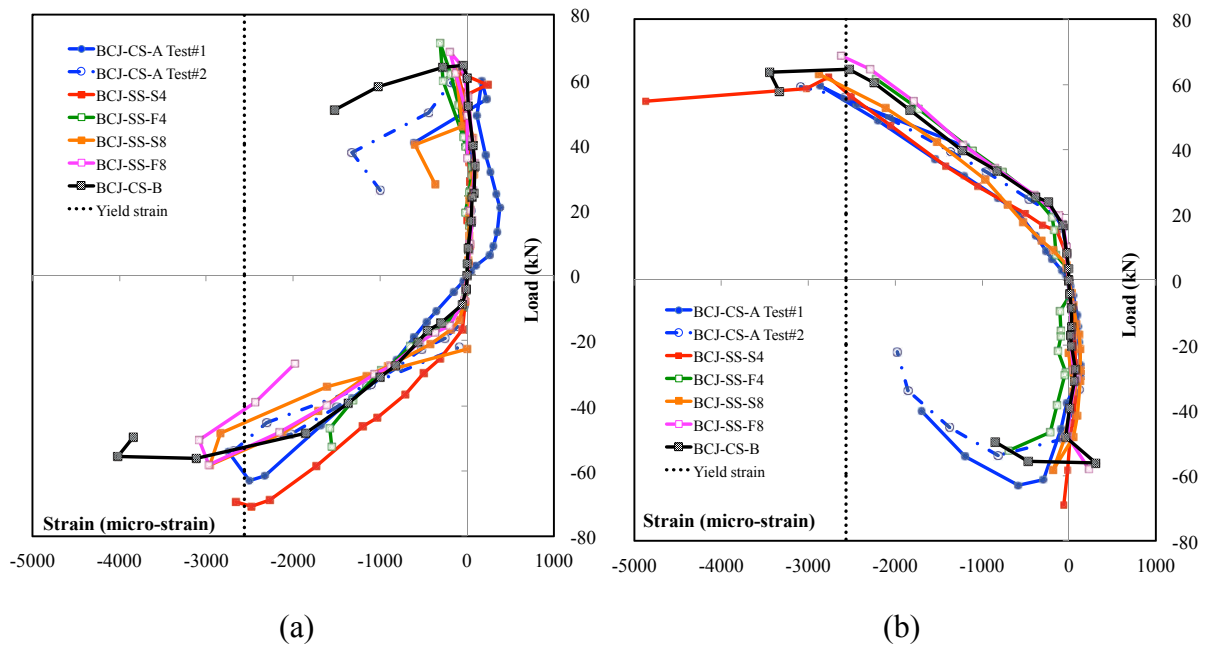


Figure 4.26. Envelope curves of load-strain: (a) Top beam reinforcement; (b) Bottom beam reinforcement

Figure 4.27 shows the envelope curves of the load-strain of the existing joint's shear reinforcement for the tested specimens. In detail, the strain reading on the existing joint's shear reinforcement for each specimen can be reported as follows:

- For both control specimens, the measured strains on the existing joint's shear reinforcement remained elastic until a 3% drift ratio.
- The strain readings on the joint's reinforcement for BCJ-SS-S4 remained in the elastic range until the end of the test; for the case of the upward loading direction, the strain

reading at the maximum load was only 43% of the yielding strain. While for BCJ-SS-F4, the strain readings at the upward and downward loading of 3.00% drift ratio were approximately 72% and 74% of the yield strength, respectively.

- For BCJ-SS-S8, the strain reading at the peak load for the upward loading direction was approximately 56% of the yield strain respectively; while for BCJ-SS-F8, at an upward loading direction of 3% drift ratio, the strain value was 2397.76 micro-strains. The corresponding value for the downward loading direction was 2174.99 micro-strains.
- Lastly, the existing shear joint reinforcements of BCJ-CS-B did not yield and shared the same amount of joint shear strain.

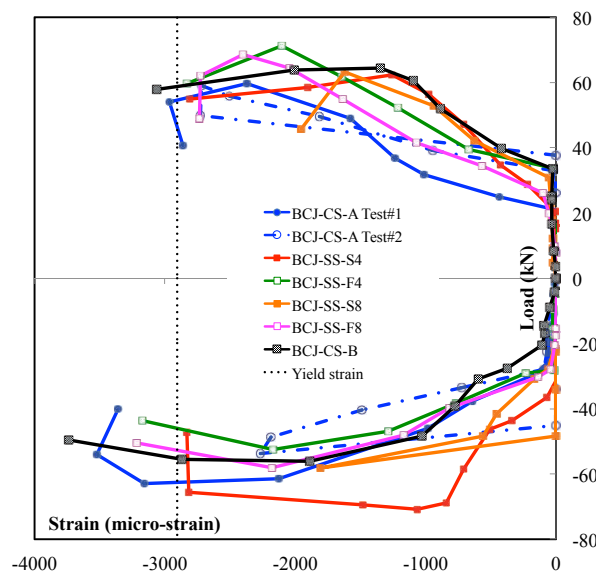


Figure 4.27. Envelope curves of load-strain for existing joints' shear reinforcement

Figure 4.28 depicts the envelope curves of the load-strain of the embedded bars for the strengthened specimens. In detail, the strain reading on the embedded bars for each specimen can be portrayed as follows:

- The embedded bar strain for BCJ-SS-S4 was still also in the elastic range; the strain of the first and the second rows of embedded bars was 40% and 72% of the yielding strain respectively. This suggested that the stress acting within the joint area was also distributed to the steel embedded bars and they helped to withstand the load as the stress transferred to the reinforcement bars after the concrete within the joint area started cracking. Moreover, the second row of embedded bars experienced a higher rate of strain compared to that of the joint's reinforcement bar and the first row of embedded bars. This was due to the fact that the joint was damaged during the upward loading of the 3% drift ratio and the joint could no longer withstand the loading in the reverse direction; also the tensile stress could no longer be transferred to the first row of embedded bars.
- For first and second rows of embedded FRP bars of BCJ-SS-F4, as expected, the strain reading was linear-elastic. At 3% drift ratio of an upward loading direction, the strain of the bars on the first and the second rows were 2467.93 micro-strains and 2846.04 micro-strains, respectively. Furthermore, these strains decreased on further loading, as the joint was heavily damaged. The strain values on the embedded FRP bars showed that they experienced deformations in the same order as the embedded steel bars (BCJ-SS-S4); which indicates that an FRP bar with large elastic deformation is capable of replacing the yielding of steel bars.
- The embedded steel bars for BCJ-SS-S8 also remained in the elastic range. The strain readings on the peak load of the upward direction for the first and the second rows of embedded steel bars were approximately 18% and 47% of the yield strain respectively. Moreover, the strain of the third and the fourth rows of the embedded steel bars was also still in the elastic range.

- Unfortunately, only the first row of the embedded FRP bar of BCJ-SS-F8 can be presented for this specimen, as the readings from other embedded bars were not recorded well. At a 3% drift ratio of the upward and downward loading directions, the strain of the first row was 948.42 micro-strains and 2086.53 micro-strains, respectively.

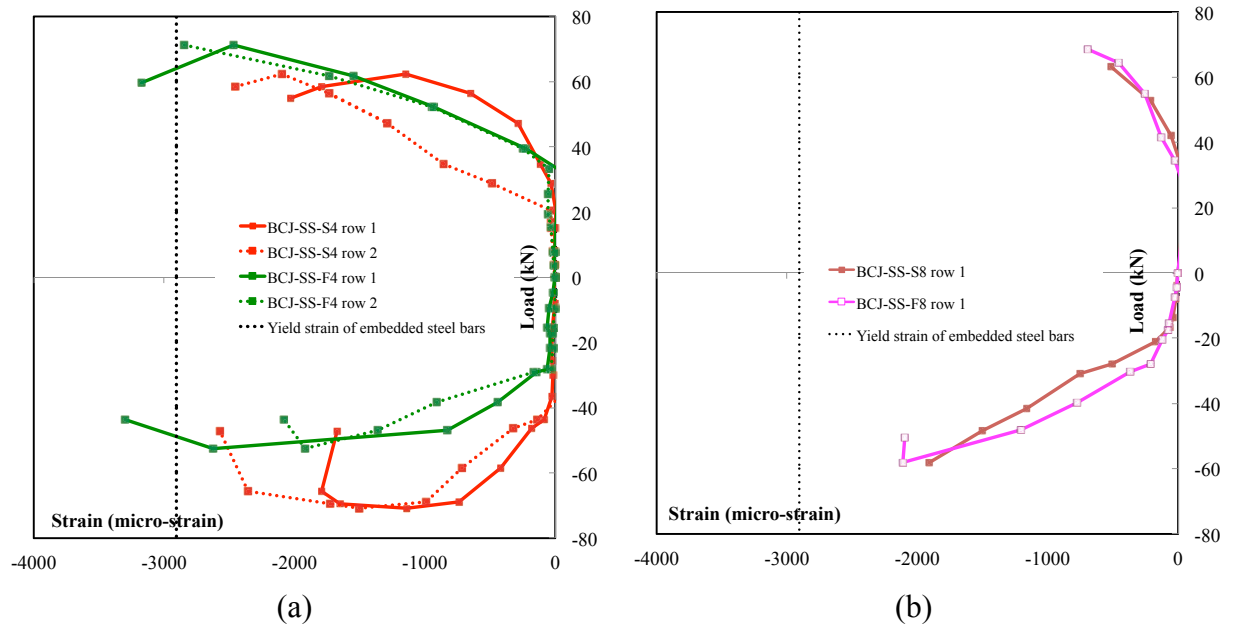


Figure 4.28. Envelope curves of load-strain for embedded bars for: (a) Group B specimen; (b) Group C specimen

4.4. EFFECT OF TEST PARAMETERS

The effect of the joints' shear reinforcement ratio and strengthening material on the behaviour of shear deficient exterior beam-column joints strengthened with embedded bars is investigated in this research. This is accomplished by employing two types of material (steel and CFRP bar) as the joints' shear reinforcement and two different amounts of embedded bars in each type of the material, as listed in Table 3.3. In the following section, the effect of the

joints' shear reinforcement ratio and strengthening material on the performance of the tested specimens is discussed and quantified.

4.4.1. Effect of Shear Reinforcement Ratio

The effect of the shear reinforcement ratio in the joint area on the global and local behaviour of the strengthened joints is presented in Figure 4.25 and Figure 4.26, respectively. In general, the strengthened specimens performed better in terms of the joints' shear strength under reversal cyclic load, compared to that of the duplicate control specimen (BCJ-CS-A Test #2). Moreover, specimens in Group C (with 8 embedded bars) achieved a higher maximum joint strength than the adequately designed joint (BCJ-CS-B).

Figure 4.29.(a) shows that the normalized load for specimen BCJ-SS-S8 increased by 34% and 36% compared to that of duplicate control specimen for the case of upward and downward loading, respectively. Moreover, a 13% (upward) and 19% (downward) increase in the normalized peak load of the BCJ-SS-S8 was observed compared to that of the BCJ-CS-B.

Figure 4.29.(b) shows that the normalized load of specimen BCJ-SS-F4 and BCJ-SS-F8 increased by 18.5% and 13%, respectively, compared to that of the duplicate control specimen for the case of upward loading. There was no enhancement observed for BCJ-SS-F4 for the case of downward loading due to damage accumulation in the joint during upward loading, which preceded downward loading. In addition, the corresponding enhancement for BCJ-SS-F8 was only 5% compared to that of the duplicate control specimen.

Figure 4.30.(a) shows that the normalized principal tensile stress of specimen BCJ-SS-S8 increased by 22% and 24% compared to that of the duplicate control specimen on upward and downward loading, respectively. Moreover, a 5% (upward) and 13% (downward) increase in the normalized principal tensile stress of the BCJ-SS-S8 was observed compared to that of BCJ-CS-B. For BCJ-SS-S4, a diagonal joint crack started to form during the download loading direction. There was no enhancement observed for BCJ-SS-S4 for the case of upward loading direction due to the damage accumulation in the joint during downward loading. However, the corresponding enhancement for the case of the downward loading was 16% compared to that of the duplicate control specimen; and the corresponding increase of BCJ-SS-S4 for the case of the downward loading was 5% to that of BCJ-CS-B.

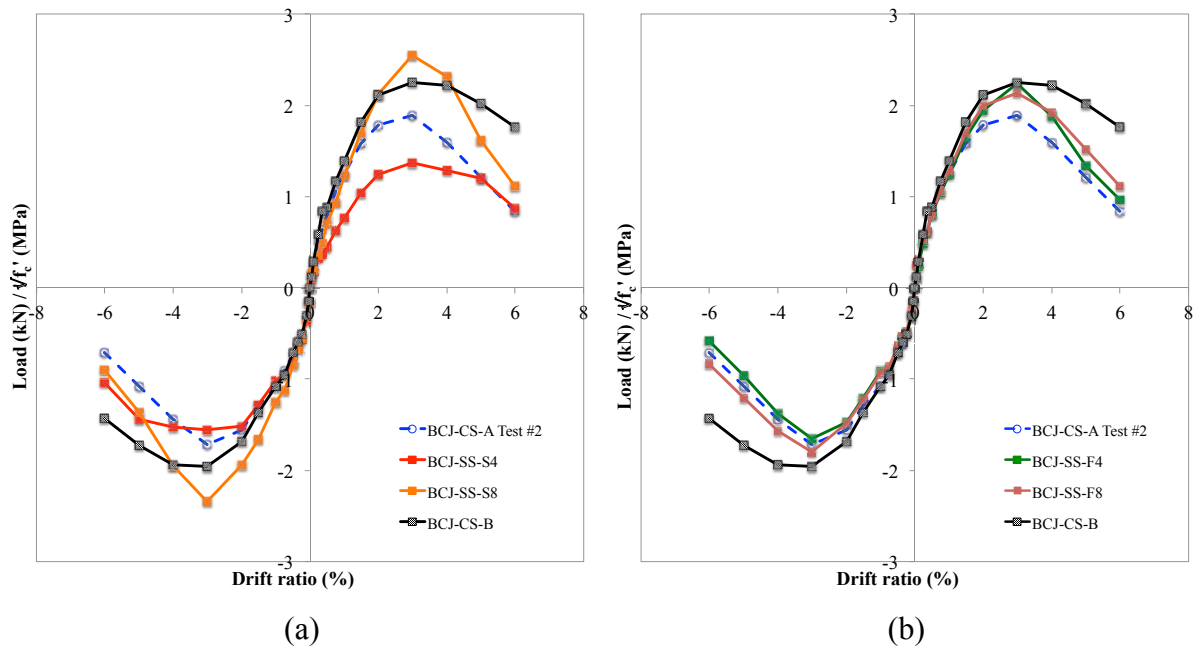


Figure 4.29. Enveloped curves of the normalized load-drift ratio of Group B and Group C: (a) Using steel bars; (b) Using CFRP bars

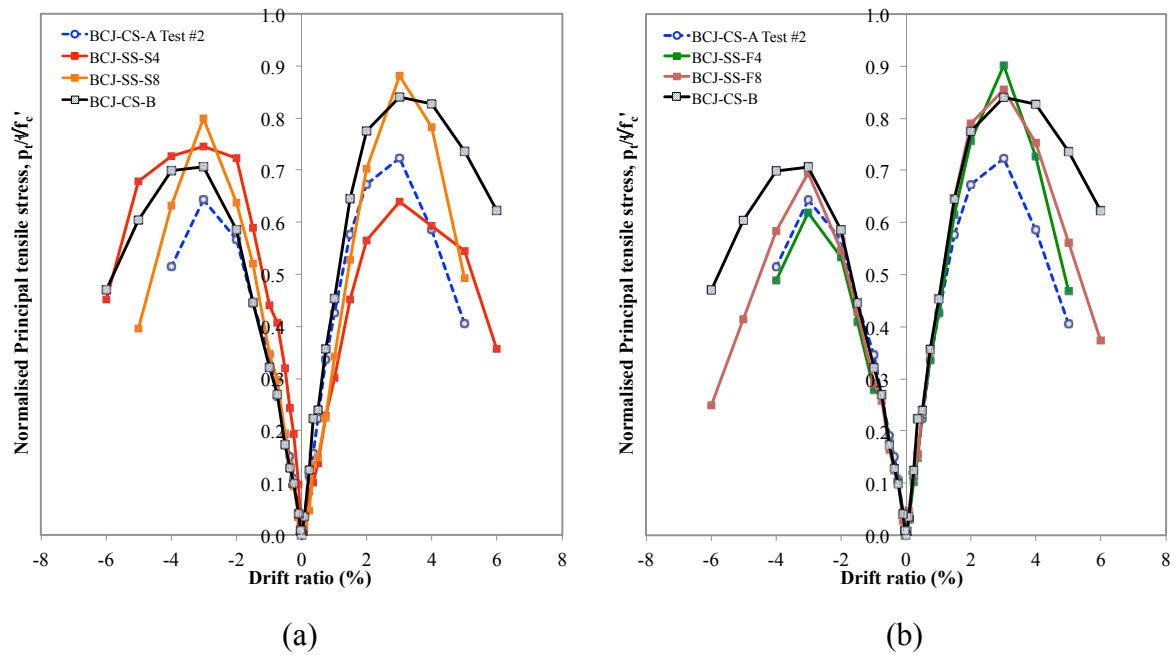


Figure 4.30. Envelope curves of the normalized principal tensile stress-drift ratio of Group B and Group C: (a) Using steel bars; (b) Using CFRP bars

Figure 4.30.(b) shows that the normalized principal tensile stress for specimen BCJ-SS-F4 and BCJ-SS-F8 increased by 25% and 18%, respectively, compared to that of the duplicate control specimen for the case of the upward loading. The corresponding enhancement for the case of the downward loading of BCJ-SS-F8 was 8% compared to that of the duplicate control specimen.

4.4.2. Effect of Strengthening Material

The effect of strengthening material on the global and local behaviour of the strengthened joint is presented in Figure 4.31 and Figure 4.32, respectively. In general, the strengthened specimens performed better in terms of the joint shears' strength under reversal cyclic load compared to that of the duplicate control specimen (BCJ-CS-A Test #2). Moreover, specimens strengthened with CFRP bars achieved higher joint shear strength than the adequately designed joint (BCJ-CS-B).

Figure 4.31.(a) shows that the normalized load of specimen BCJ-SS-F4 increased by 19% compared to that of the duplicate control specimen for the case of the upward loading. Both strengthened specimens depicted in Figure 4.31.(b) performed better for the cases of upward and downward loading than the duplicate control specimen. The normalized load of BCJ-SS-S8 and BCJ-SS-F8 at upward loading increased by about 35% and 13%, respectively, compared to that of the BCJ-CS-A Test #2. The corresponding increases for the case of the downward loading were 35% and 5%, respectively.

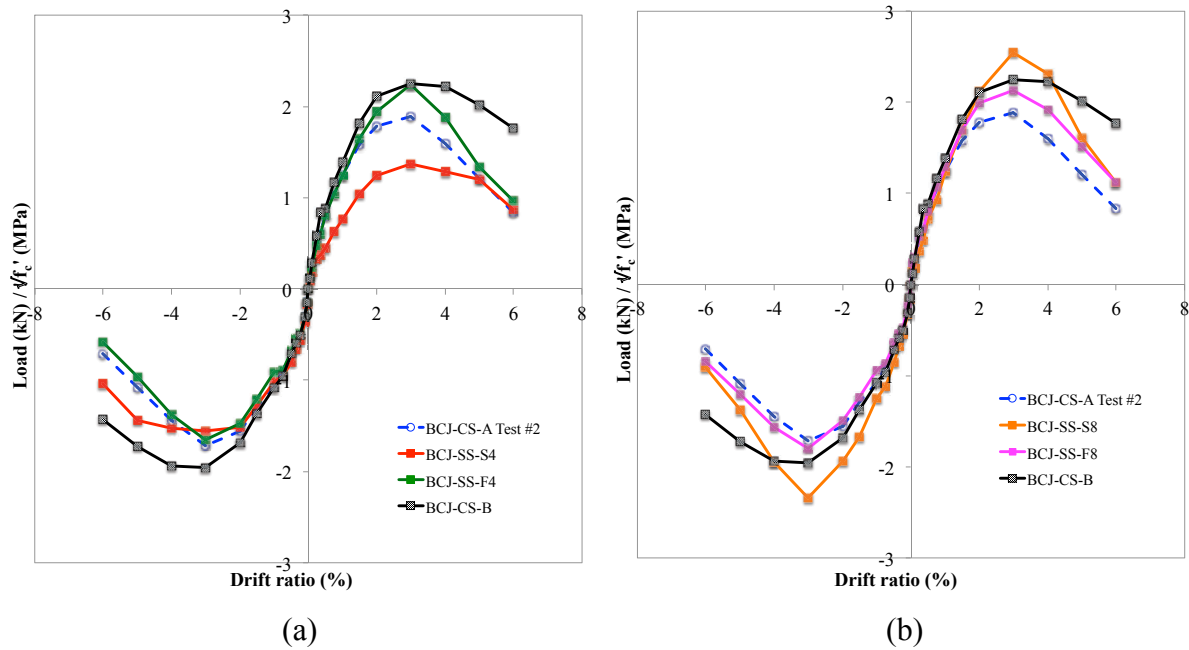


Figure 4.31. Envelope curves of the normalized load-drift ratio of the strengthened specimens:
(a) Using 4 embedded bars; (b) Using 8 embedded bars

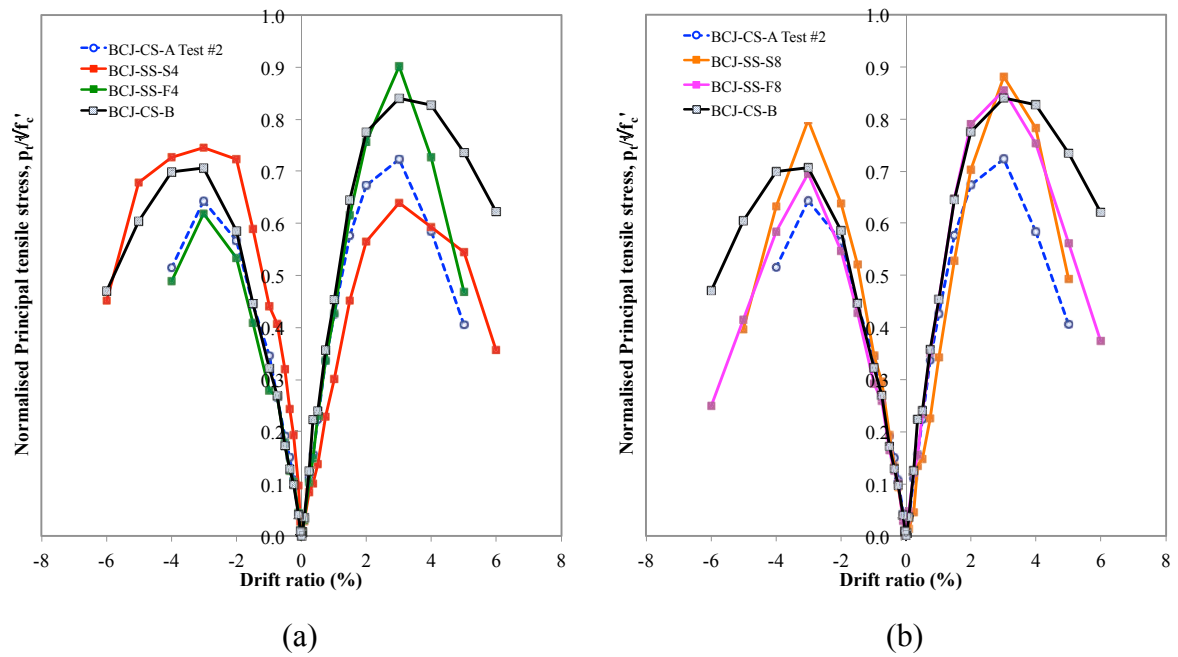


Figure 4.32. Envelope curves of the normalized principal tensile stress-drift ratio of the strengthened specimens: (a) Using 4 embedded bars; (b) Using 8 embedded bars

Figure 4.32.(a) depicts that the normalized principal tensile stress of the specimen strengthened with embedded CFRP bar (BCJ-SS-F4) was enhanced by about 25% compared to that of the duplicate control specimen for the case of the upward loading. Moreover, compared to that of the adequately designed joint (BCJ-CS-B), the normalized principal tensile stress of BCJ-SS-F4 increased by about 7% for the case of the upward loading. As explained previously, joint damage of BCJ-SS-S4 was accumulated during downward loading, which preceded upward loading; hence there was no enhancement in the joint shear strength at upward loading. On the other hand, the corresponding enhancement of specimen strengthened with embedded steel bar (BCJ-SS-S4) was 16% for the case of the downward loading. In addition, the corresponding increase of BCJ-SS-S4 was 5% compared to that of BCI-CS-B for the case of the downward loading.

Figure 4.32.(b) depicts that the normalized principal tensile stress of the specimens strengthened with embedded CFRP (BCJ-SS-F8) and steel (BCJ-SS-S8) bars was enhanced by about 18% and 22%, respectively, compared to that of the duplicate control specimen for the case of the upward loading. The corresponding enhancements for the case of the downward loading were 8% and 24% respectively. In addition, the normalized principal tensile stress of the BCJ-SS-F8 and BCJ-SS-S8 increased by about 2% and 5%, respectively, compared to that of the BCJ-CS-B for the case of the upward loading.

4.5. SUMMARY

In this chapter, the experimental findings of the unstrengthened and strengthened RC beam-column joints, as well as the adequately designed RC BC joint are presented. The benefit of the proposed strengthening scheme was investigated by means of global and local behaviour, failure modes, strength, stiffness and energy dissipation characteristics. The strain readings in the steel reinforcement within the joint area and the embedded bars were also analysed and discussed to compare the performance of the specimens. Based on the observed damages and hysteretic behaviour of the tested specimens of the experiment, the following conclusions can be drawn:

- 1) The test results of the unstrengthened specimens (BCJ-CS-A Test#1 and BCJ-CS-A Test #2) confirmed the structural deficiency of the poorly detailed beam-column joints designed according to the pre 1970s' specification. The specimens experienced hybrid local damage and a failure mechanism characterised by the joints' shear damage in the form of cross-diagonal cracks.
- 2) All strengthened specimens exhibited enhanced behaviour where damage occurred in the beam region at the early stages of loading; suggesting it was the outset of a beam hinge

(BH) mechanism, and then diagonal cracks were propagated in the joint after 1.00% drift ratio.

- 3) A substantial improvement in the global performance of BCJ-SS-S4 and BCJ-SS-F4 can be seen in the joints' shear strength, which for both specimens increased by 6% and 21% for the case of the upward loading; while both specimens BCJ-SS-S8 and BCJ-SS-F8 had increases of 7% and 16% in the joints' shear stress compared to that of the duplicate control specimen.
- 4) The specimens BCJ-SS-F4 and BCJ-SS-F8 had also significant enhancement in joint shear strength at the upward loading compared to that of BCJ-CS-B. The corresponding increases at the upward loading for specimens BCJ-SS-F4 and BCJ-SS-F8 were 11% and 7%, respectively.
- 5) A 39% (upward direction) and 93% (downward direction) increase in the displacement ductility of the BCJ-SS-S4 specimen was observed compared to that of BCJ-CS-A Test #2. The corresponding increases at the upward loading for specimens BCJ-SS-F4 and BCJ-SS-F8 were 6% and 22%, respectively. While the increases at the downward loading for specimens BCJ-SS-F4, BCJ-SS-S8 and BCJ-SS-F8 were 27%, 20% and 13%, respectively.
- 6) There was no displacement ductility enhancement observed for the upward loading of BCJ-SS-S8. After the specimen attained the peak load at 3.00% drift ratio, the load dropped significantly at the second cycle of 4.00% drift ratio. Damage accumulation in the joint during the peak load caused significant strength degradation, hence prevented the increase in the displacement ductility of BCJ-SS-S8.
- 7) The energy dissipation levels achieved by the strengthened specimens were generally higher than those achieved by the control specimens, especially at drift levels of 1.00% or

more. For example, the energy absorbed by the strengthened specimens at 2.00% drift ratio was 4080 kN-mm (BCJ-SS-S4); 3543 kN-mm (BCJ-SS-F4); 3203 kN-mm (BCJ-SS-S8); and 3333 kN-mm (BCJ-SS-F8); representing increases of 31%, 14%, 3% and 7%, respectively, over the corresponding values for the duplicate control specimen (BCJ-CS-A Test #2).

- 8) The energy dissipation levels of the strengthened specimens up to 4% drift ratio were comparable to that of the BCJ-CS-B, except for the BCJ-SS-S8. The energy absorbed by the strengthened specimens at a 1% drift ratio was 1096 kN-mm (BCJ-SS-F4) and 1055 kN-mm (BCJ-SS-F8); while the corresponding energy for the BCJ-CS-B was 1047 kN-mm.
- 9) Both the control specimens show limited rotation while the specimens strengthened with embedded steel bars show enhanced fixed-end beam rotation. The beam rotation of both the control specimens was much smaller indicating the absence of the plastic hinge in the specimens. The beam rotations of the BCJ-CS-A Test #1 and BCJ-CS-A Test #2 at the maximum load were 0.0040 and 0.0066 radians, respectively. While the beam rotations of the strengthened specimens at the maximum load were 0.012 radians (BCJ-SS-S4); 0.009 radians (BCJ-SS-F4); 0.010 radians (BCJ-SS-S8); and 0.0074 radians (BCJ-SS-F8). The specimens BCJ-SS-S4 and BCJ-SS-S8 exhibited 40% and 30% larger plastic deformations than the BCJ-SS-F4 and BCJ-SS-F8. Moreover, the maximum rotation of BCJ-SS-S4 and BCJ-SS-S8 specimens was comparable to that of specimen BCJ-CS-B, extending to around 0.03 radians at failure.
- 10) At the local level, the normalized principal tensile stress of specimen BCJ-SS-S8 increased by 22% and 24% compared to that of the duplicate control specimen in the upward and downward loading, respectively.

-
- 11) For BCJ-SS-S4, diagonal joint crack started to form during downward loading direction, hence there was no enhancement in the normalized principal tensile stress of BCJ-SS-S4 for the case of the upward loading due to the damage accumulation in the joint during the downward loading; but the corresponding enhancement for the case of the downward loading was 16% compared to that of the duplicate control specimen.
 - 12) A 5% (upward) and 13% (downward) increase in the normalized principal tensile stress of the BCJ-SS-S8 was observed compared to that of BCJ-CS-B; while the corresponding increase of BCJ-SS-S4 for the case of the downward loading was 5% compared to that of BCJ-CS-B.
 - 13) The normalized principal tensile stress of BCJ-SS-F4 and BCJ-SS-F8 was enhanced by about 25% and 18% respectively, compared to that of the BCJ-CS-A Test #2 for the case of the upward loading. Compared to the BCJ-CS-B, the corresponding increase of BCJ-SS-F4 and BCJ-SS-F8 were 7% and 2% respectively.
 - 14) On the basis of joint shear strength, the BCJ-SS-F4 proved more effective than BCJ-SS-S4. However, the specimen strengthened with embedded CFRP bars was 6.5 less ductile than the one strengthened with embedded steel bars.
 - 15) Increasing the amount of embedded bars was not significantly effective for the enhancement of the joint shear strength and ductility of the strengthened specimens.

CHAPTER 5

FINITE ELEMENT MODELLING OF EXTERIOR REINFORCED CONCRETE BEAM-COLUMN JOINTS

5.1. GENERAL

In this chapter, the development of nonlinear three-dimensional finite element (FE) models simulating the behaviour of exterior RC beam-column joints under cyclic loading is described in detail. The FE models were developed with the general purpose FE software ABAQUS and validated against the experimental results reported in the previous chapter. Upon validation of the models, parametric studies were conducted to investigate the effect of key parameters such as applied column compressive load, the concrete strength and the size of embedded bars on the response of unstrengthened and strengthened RC beam-column joints under cyclic load. The key response characteristics studied include the cumulative dissipative energy, the overall hysteresis curve and the joint deformation and crack pattern. Based on the experimental and numerical results, the effectiveness of strengthening RC beam-column joints with embedded bars is assessed in the following chapter.

5.2. GEOMETRIC MODELLING, ELEMENT TYPE AND MESH

In the developed 3D FE models, the concrete beam-column joint, the embedded longitudinal and shear reinforcement bars and the steel loading plates were explicitly modeled. As shown in Figure 5.1, the RC joint and loading plates were modelled as 3D geometric entities, whilst the embedded reinforcing bars were idealized as 1D entities.

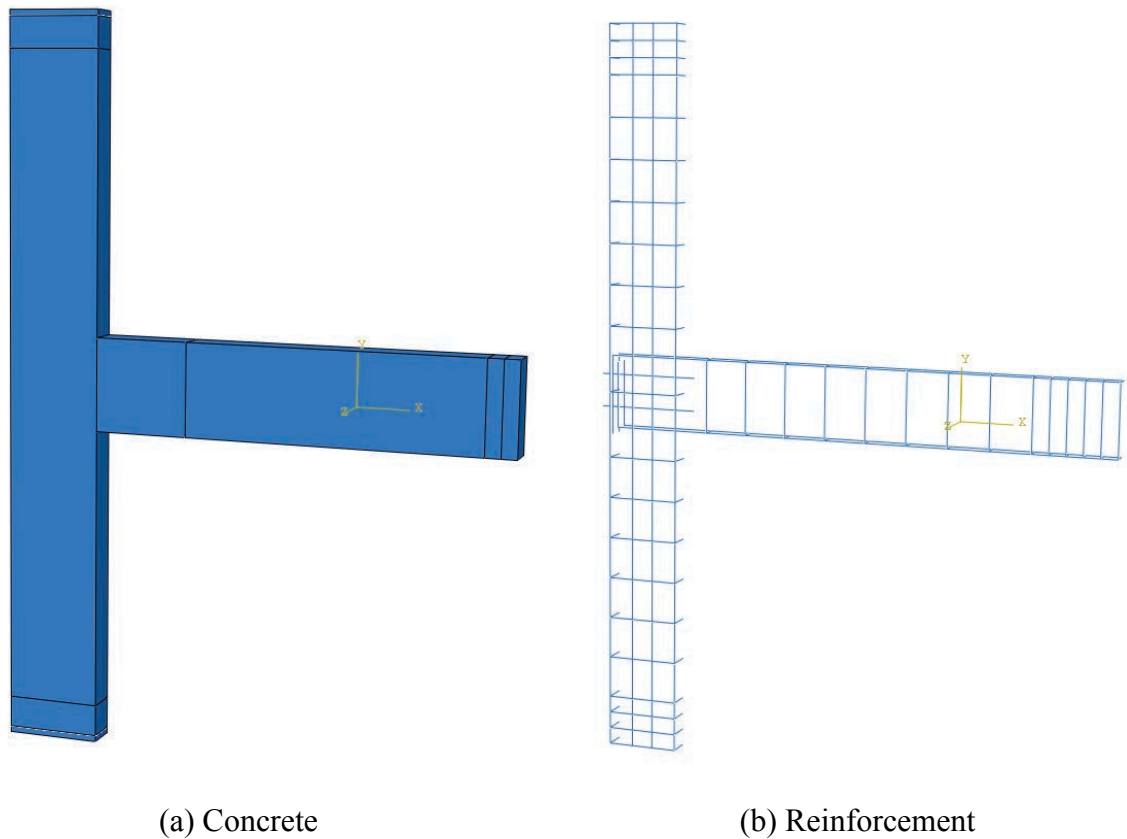


Figure 5.1. Geometric model of test specimen

5.2.1. Concrete Joint and Loading Plates

The 3D geometry of the concrete joint and the loading plates were discretized with continuum elements. The ABAQUS element library contains several types of 3D continuum elements, including linear and quadratic elements in hexahedral, tetrahedral or wedge geometries, which are capable of appropriately approximating the displacement field of the modeled component with various degrees of accuracy and varying computational costs. As will be discussed later, the use of explicit dynamic time integration in conjunction with slow loading rates (i.e. quasi-static analysis) was necessary to overcome the severe convergence difficulties associated with concrete cracking (or in fact any material model with a softening material response).

The use of explicit dynamics meant that only linear continuum elements could be employed. Among the available 3D linear elements, the linear tetrahedral elements (also known as a constant strain tetrahedral) cannot capture strain/stress gradient within the element, hence necessitating the use of very fine mesh and higher order elements. Therefore, linear tetrahedral elements are only used when geometric versatility is important, for example when a complex geometry needs to be discretized. Hence, the 8-node linear brick element with reduced integration (C3D8R) and hourglass control was chosen as the most appropriate one (Gebreyohannes, 2013). This element type was successfully implemented in modelling RC beam-column joint subjected to reversal cyclic loading in Danesh et al. (2008) and Abbas et al. (2014). These first order brick elements have three translational degrees of freedom at each node, as shown in Figure 5.2, and allow for trilinear stress variations. Moreover, the use of reduced integration mitigates the occurrence of shear and volumetric locking.

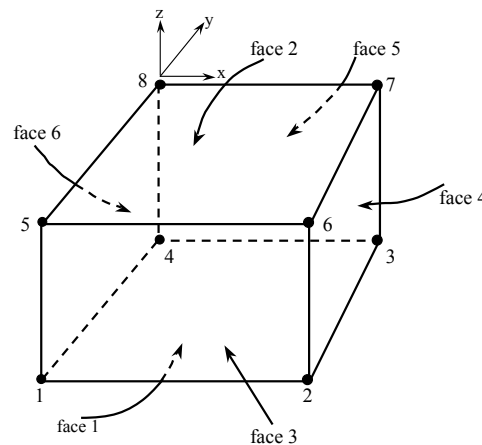


Figure 5.2. Eight-node brick element

5.2.2. Reinforcement Bars

Modelling reinforcement bars using one-dimensional element is appropriate, since the cross-sectional dimensions of the reinforcement bar are small compared to the length of bar

element. Several element types are available in ABAQUS and can be employed to model 1D reinforcement including truss elements (T3D2), linear beam elements (B31) and quadratic beam elements (B32). The two-node T3D2 element employs linear interpolation for position and displacement calculations: it allows only for constant axial stress along its length and has no stiffness when subjected to loading perpendicular to the axis of the element. On the other hand, beam elements B31 and B32 are Timoshenko beam elements possessing axial, shear and flexural stiffness. B32 uses quadratic interpolation functions for position and displacement (hence it can assume a curved form), whilst B31 is a 3D linear Timoshenko beam element. Figure 5.3 depicts the three elements mentioned, their associated nodes and geometry.

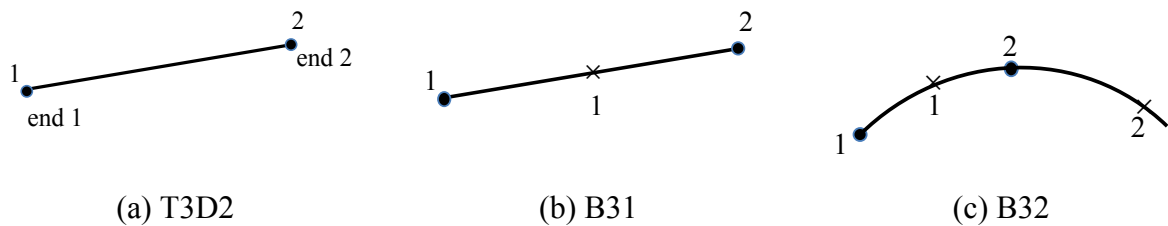


Figure 5.3. Elements to model reinforcement

A series of analysis has been conducted by Gebreyohaness (2013) to determine suitable element type to model reinforcing bars. The results showed that the three types of element mentioned above did not significantly affect the accuracy of the results, but the use of beam elements was associated with a higher computational cost compared to the truss elements. Moreover, it was shown that the use of B31 and B32 elements resulted in over-prediction of the post-peak stiffness and strength degradation, whilst T3D2 elements displayed a better agreement with experimental results at lower computational cost. Hence the T3D2 truss element is used to model reinforcement bar throughout this study.

5.2.3. Mesh

Structured meshing was adopted for all of the solid elements used in the models, as matrices based on structured meshing are simple and fast to assemble. In addition, the aspect ratios of solid elements were kept as close to one as practicable, as high aspect ratio elements would affect the accuracy of the analysis. Mesh convergence studies were conducted to determine the best balance between accuracy and computational cost. Three element sizes, namely 30 mm, 50 mm and 100 mm, were considered and a uniform element size of 30 mm was finally selected as stated in Section 5.5, where the validation of the model is discussed. The meshing adopted for all specimens is shown in Figure 5.4.

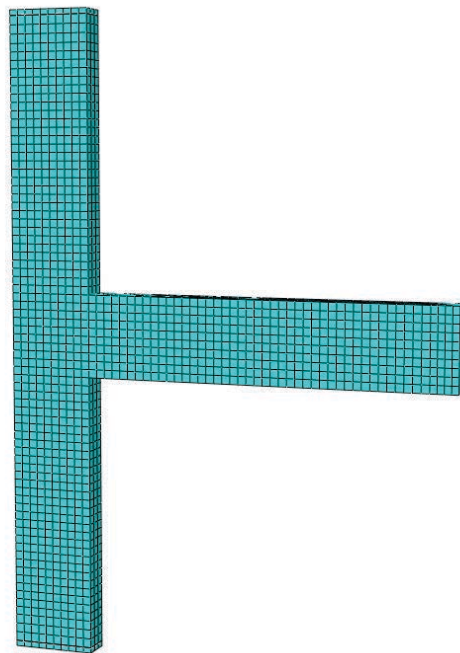


Figure 5.4. Finite element mesh for all models

5.3. MATERIAL BEHAVIOUR

5.3.1. Concrete

Several constitutive models are available in ABAQUS to describe the behaviour of plain concrete subjected to varying conditions of loading. These include the Smeared Crack model, the Brittle Cracking model and the Concrete Damage Plasticity (CDP) model. The smeared Crack model is usually employed when simulating the response of reinforced or unreinforced concrete under low confining pressure subjected to monotonic loading. The Brittle Crack model can only be used to simulate concrete when the compressive response can be assumed to remain elastic and the only source of material nonlinearity is tensile cracking. Finally the CDP model can simulate the cyclic response of concrete experiencing damage in both tension and compression and was therefore adopted in this study.

The CDP model is based on the yield functions proposed by Lubliner et al. (1989) and modified by Lee and Fenves (1998). It combines isotropic damage plasticity with hardening plasticity concepts. Two distinct material modes, namely concrete crushing and concrete cracking, are accounted for. The initiation of damage and its evolution (i.e. evolution of failure surface in the strain space) in this material model is traced by tensile and compressive equivalent plastic strains that are linked to tension and compression failure respectively. The CDP model is explained in detail in the ABAQUS Documentation.

The CDP model requires several input parameters to generalize concrete uniaxial stress-strain properties to the 3D stress space. These include:

- a. The uniaxial properties of concrete when subjected to tension and compression in terms of stress-strain;

- b. The dilatation angle that determines the direction of the plastic flow through the incremental plastic strain vector, ψ ;
- c. The flow potential eccentricity (the default value being 0.1);
- d. The ratio of initial equibiaxial compressive yield stress to initial uniaxial compressive stress, σ_{bo}/σ_{co} ; Lubliner et al. (1989) stated that this value ranges between 1.10 and 1.16, and the default value in ABAQUS is 1.16;
- e. The viscosity parameter, μ ;
- f. The ratio of the second stress invariant on the tensile meridian to that on the compressive meridian at initial yield for any given value of the pressure invariant such that the maximum principal stress is negative, K_c . The value of this parameter is between 0.5 and 1.0. When the ratio K_c is equal to 1, the stress becomes independent of the third deviatoric stress invariant. The default value of K_c in ABAQUS is 0.667.

Concrete in Compression

The stress-strain curve for concrete in uniaxial compression is defined in three different regions, namely elastic, hardening, and softening. When subjected to uniaxial compression, concrete responds initially in a linear-elastic manner, until the applied compressive stress reaches between 30-40% of its ultimate compressive strength. From this point, the hardening region of the stress-strain curve develops, in which the concrete stress increases until it reaches ultimate compressive strength and the tangential stiffness decreases from its initial value (given by concrete Young's modulus) to zero. After the ultimate compressive stress is reached, the softening region of the material response begins. This is the part of the stress-strain curve beyond the point of zero tangential stiffness where the strength of concrete degrades rapidly and concrete softens whilst losing its load carrying capacity.

The stress-strain relationship of concrete compressive load employed in this study is defined as shown in Figure 5.2. Part 1 in Figure 5.2 is the elastic linear part of the concrete stress-strain behaviour and is computed by using the expression in Equation (5-1):

$$\sigma_{c(1)} = E_c \times \varepsilon_c \quad (5-1)$$

where

$\sigma_{c(1)}$ is the concrete stress in elastic region, ε_c is the concrete strain in elastic region, and E_c is the concrete modulus of elasticity. In this study, the concrete modulus elasticity is calculated using the formula proposed by Carreira and Chu (1985):

$$E_c = 3320 \times (f_c)^{0.5} + 6900 \quad (5-2)$$

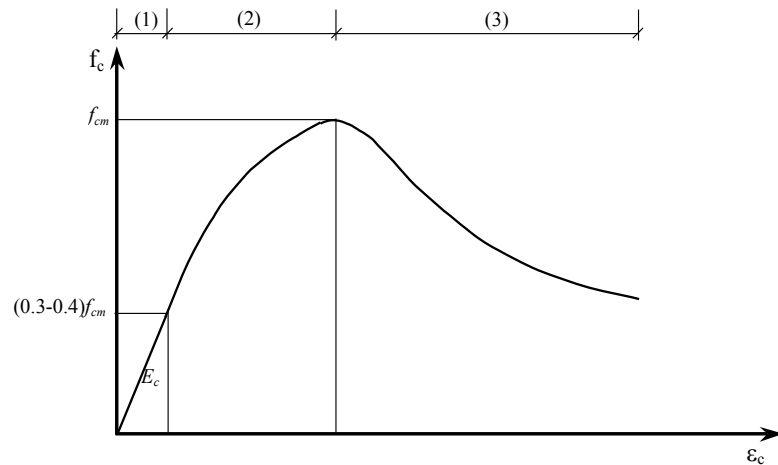


Figure 5.5. Assumed uniaxial stress-strain relation for concrete under compressive loading

Part 2 is the hardening region where the stress is still in the ascending branch up to the peak load of concrete strength f_{cm} at ε_{c1} . The stress-strain relationship of the concrete curve on this part is calculated by using the expression suggested in CEB-FIP Model Code 1990:

$$\sigma_{c(2)} = \frac{E_{ci} \frac{\varepsilon_c}{f_{cm}} - \left(\frac{\varepsilon_c}{\varepsilon_{ci}} - 1 \right) \frac{f_{cm}}{E_{ci}}}{1 + \left(\frac{\varepsilon_c}{\varepsilon_{ci}} - 2 \right) \frac{f_{cm}}{E_{ci}}} f_{cm} \quad (5-3)$$

where

$\sigma_{c(2)}$ is the concrete stress in region 2,

f_{cm} is the mean compressive strength,

ε_c is the concrete strain in elastic region,

ε_{ci} is the concrete strain at peak stress, and

E_{ci} is the secant modulus from the origin to the peak compressive stress. A formula suggested by Kratzig and Polling (2004) was used to calculate the secant modulus,

$$E_{ci} = \frac{1}{2} \frac{f_{cm}^2}{E_c \left(\frac{\varepsilon_c}{\varepsilon_{ci}} - 1 \right)} - \frac{f_{cm}}{\varepsilon_c} + \frac{3}{2} E_c \quad (5-4)$$

For the practical use, the concrete strain at peak stress ε_{ci} can be taken as 0.002 (Wight and MacGregor, 2009). In this study, this value was calculated using the formula proposed by Carreira and Chu (1985),

$$\varepsilon_{ci} = \frac{f_{cm}}{E_c} \left(\frac{r}{r-1} \right) \quad (5-5)$$

$$r = \frac{f_{cm}}{17} + 0.8 \quad (5-6)$$

Part 3 is the softening branch of the concrete stress-strain relationship. This part is characterized by the existence of damage localization when peak concrete compression strain is exceeded. The definition of the softening branch depends on the fracture energy dissipated through damage, the material parameters and characteristic length l_{eq} (Bažant and Oh, 1983)

of the concrete volume studied. The concept of fracture energy as a material parameter was initially accepted for tension cracks (Kratzig and Polling, 2004) and was introduced for softening under compression by Feenstra (1993). The fracture energy under compression is termed “crushing energy (G_{cl})” to distinguish it from the term of fracture energy under tension. Consequently, the following formula was used to calculate the stress-strain relationship on Part 3,

$$\sigma_{c(3)} = \left(\frac{2 + \gamma_c f_{cm} \varepsilon_{cl}}{2 f_{cm}} - \gamma_c \varepsilon_c + \frac{\gamma_c \varepsilon_c^2}{2 \varepsilon_{cl}} \right) \quad (5-7)$$

γ_c is the only parameter that controls the area under the stress-strain curve.

$$\gamma_c = \frac{\pi^2 f_{cm} \varepsilon_c}{\left(\frac{G_{cl}}{l_{eq}} - \frac{1}{2} f_{cm} \left(\varepsilon_{cl} (1-b) + b \frac{f_{cm}}{E_c} \right) \right)} \quad (5-8)$$

where:

G_{cl} is the localized crushing energy,

l_{eq} is the characteristic length of the respective FE integration point,

b is a material parameter with a value $0 < b \leq 1$, and is suggested to be 0.7 as it fits well with the experimental data of concrete under cyclic load test (Birtel and Mark, 2006).

Element character length should be limited to

$$l_{eq} \leq \frac{G_{cl}}{f_{cm} \left(\varepsilon_{cl} (1-b) + b \frac{f_{cm}}{E_c} \right)} \quad (5-9)$$

One of the key features of this concrete model is its capability to capture the response of concrete under cyclic loading, including stiffness degradation and stiffness recovery (i.e. when the cracks close, the concrete is assumed to regain its compressive stiffness) and

damage accumulation through successive cycles. To demonstrate this capability, the strain-strain curve model in Figure 5.6, which is developed using the above expressions, is used in FE analysis and the results were calibrated to the experimental results. Details of the results can be seen in the next section. l_{eq} was selected equal to the element size and the crushing energy G_{cl} was chosen such that the post-strength path is modelled with sufficient accuracy (i.e. sufficiently close to the experimental).

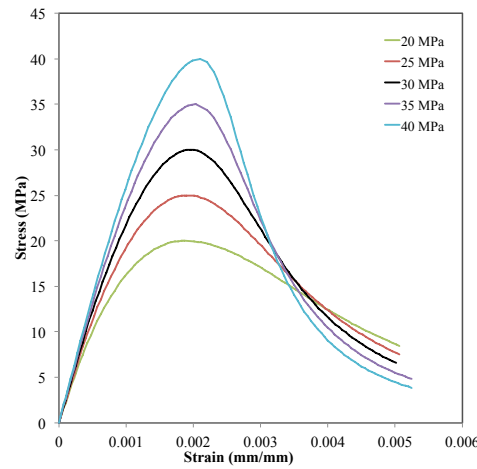


Figure 5.6. Compression concrete model plotted using Equations (5-1) to (5-9)

Concrete in Tension

The stress-strain curve of concrete subjected to uniaxial tension is also idealised in a similar manner to the compressive stress-strain curve. In this case, the stress-strain curve for concrete under tension displays two distinct regions, namely the elastic region and the softening region as shown in Figure 5.7.

The elastic region where the stress and strain relationship is linear is defined by Equation (5-10)

$$f_{ct} = E_c \epsilon_{cr} \quad (5-10)$$

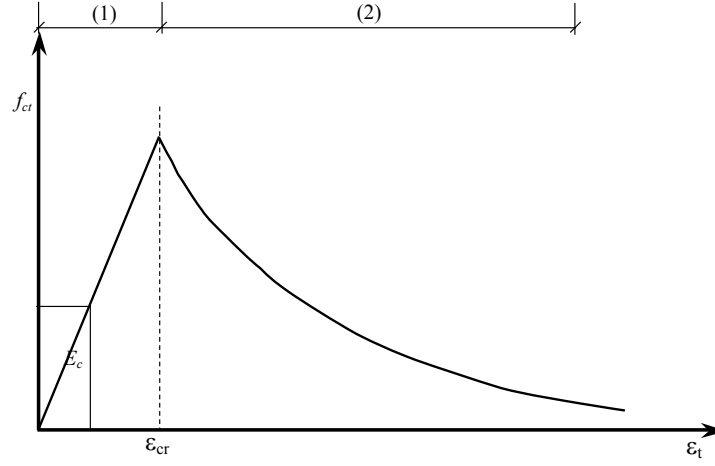


Figure 5.7. Uniaxial stress-strain response of concrete in tension

where

ε_{cr} is the cracking strain,

f_{ct} is the tensile strength of concrete.

In this study, the tensile strength of concrete is calculated using equation (5-11).

$$f_{ct} = 0.3 \times (f_{cm})^{\frac{2}{3}} \quad (5-11)$$

For the softening part of the response of concrete in tension initiates upon the attainment of the concrete tensile strength and it can be assumed to be linear or exponential. In this study, Equation (5-12) developed by Kratzig and Polling (2004) is used to define this region.

$$\sigma_{(\varepsilon)} = f_{ct} \times e^{\frac{(\varepsilon_{cr} - \varepsilon)}{\gamma_t}} \quad (5-12)$$

where

ε is concrete strain under tension and γ_t is the parameter that controls the area under stress-strain curve. The post-peak curve mainly depends on the fracture energy G_f , and the equivalent length l_{eq} .

$$\gamma_t = \frac{G_f}{l_{eq} f_{ct}} - \frac{1}{2} \frac{f_{ct}}{E_c} \quad (5-13)$$

where G_f is the fracture energy.

It should be noted that the fracture energy G_f is the most important aspect of tension stiffening and generally small differences are observed when using different expressions to describe the tension stiffening response.

Concrete under reversed cyclic load

The cyclic response of concrete is depicted in Figure 5.5. Under uniaxial tension, the stress-strain responds linearly up to the failure stress σ_{t0} , which represents the onset of micro-cracking in the concrete. Beyond the failure stress, the concrete responses follow the strain softening mechanism of the cracked concrete. On the other hand, under uniaxial compression, the concrete behaves linearly up to the initial yield value, σ_{c0} . In the plastic region, the response is typically characterized by the strain hardening followed by the strain softening beyond the ultimate stress, σ_{cu} .

During unloading and reloading, the elastic stiffness of concrete is damaged as the unloading response is weakened. The elastic stiffness degradation in ABAQUS is defined by two damage variables, d_t and d_c ($0 \leq d_t, d_c \leq 1$). The degradation mechanism under cyclic loading is complex, due to the opening and closing of previous micro-cracks and their interaction. The stiffness recovery effect, the recovery of some elastic stiffness as the load changes sign during cyclic loading, is considered. This recovery generally characterizes the amount of the tension damage d_t due to compressive loading. The reduction in the initial elastic stiffness E_0 is generally expressed by the following expression (Equation 5-14)

$$E = (1 - d_t) E_0 \quad (5-14)$$

The recovery factors, w_t and w_c , control the tensile and compression stiffness recovery upon load reversal, respectively. In ABAQUS, the default values for w_t and w_c are 1 and 0 which correspond to the full recovered compression stiffness and unrecovered tensile stiffness. However, slightly small or even no tensile stiffness recovery is expected due to the preformed developed cracks. The compression damage d_c is denoted by w_t . The compressive behaviour is defined by an input using the compression hardening data as a function of inelastic strain rate.

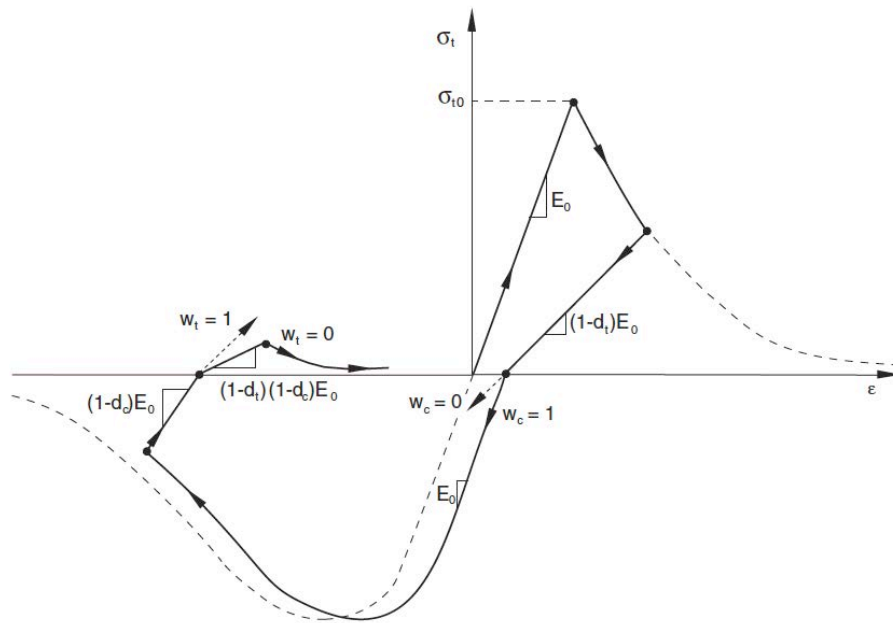


Figure 5.8. Concrete material model under cyclic loading, Abaqus and Inc (2008)

The evolution of concrete damage both for compression and tension was linked to the corresponding inelastic strain, using equation (5-15):

$$d = 1 - \frac{\sigma}{\sigma_{\max}} \quad (5-15)$$

where

d is the damage parameter, in compression (d_c) or tension (d_t). This value varies from 0 for no damage state to 1 to represent the concrete's complete failure;

\pm is the post-peak concrete strength corresponding to the inelastic strain, in compression or tension;

\pm_{max} is the concrete strength, in compression or tension.

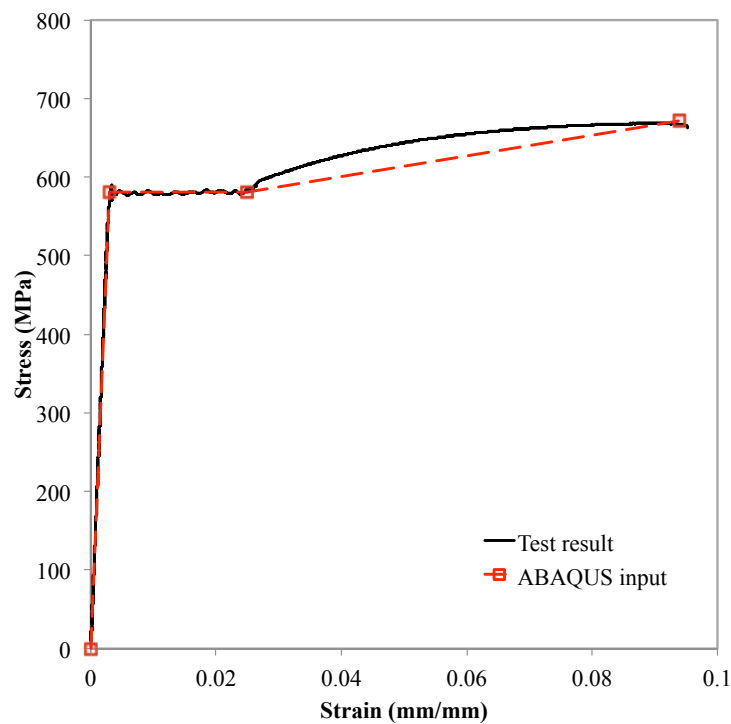


Figure 5.9. Material model for steel reinforcement bar

5.3.2. Steel Reinforcing Bars

The von Mises yield criterion in conjunction with isotropic hardening response was employed to describe the material response of reinforcing steel beyond its yield point. Up to yield, the steel was assumed linear elastic, with a Young's modulus equal to 200 GPa and a Poisson ration equal to 0.3. The reinforcement properties, namely yield stress, ultimate stress and

modulus of elasticity, were defined from tensile testing stress-strain data, and a trilinear elastic-plastic-linear hardening engineering stress-strain curve was defined as shown in Figure 5.9. The stress strain data were subsequently converted into true stress-logarithmic plastic strain format and input into ABAQUS.

5.4. BOUNDARY CONDITIONS, CONSTRAINTS, ANALYSIS TYPE AND LOADING

The tested specimens were symmetrical with respect to the vertical plane crossing through the beam/column width. In addition to geometric symmetry, the applied load and resulting failure modes were also symmetrical. Hence, the symmetry was exploited to reduce the computational cost by modeling only half the specimen and imposing appropriate symmetry boundary conditions, as shown in Figure 5.10. Tie constraints were employed to connect the degrees of freedom of the upper and lower loading plates to the corresponding degrees of freedom of the upper and lower column sections respectively. An additional constraint (i.e. EMBEDDED REGION) was employed to tie the degrees of freedom of the truss elements simulating the embedded reinforcing bars to the degrees of freedom of the brick elements of the surrounding concrete.

Boundary conditions replicating the ones applied on the specimen during testing were applied to the concrete sections at the top and bottom ends of the column. To this end, a reference point was defined at the top and bottom column ends, which was defined as the master node to which the degrees of freedom of the respective column sections were coupled by means of the distributing coupling constraint. Hence, the horizontal movement of the reference point at the top column end was restrained, thus simulating the horizontal restraint imposed during testing, whilst both the horizontal and vertical translation of the reference point, to which the

lower column end section was coupled, were restrained. A constant compressive force was applied at the top steel plate and cyclic loading in the form of a prescribing displacement history was imposed at the beam end.

Simulating concrete members under cyclic loading and particularly simulating tensile cracking (or any material with a softening stress-strain response) is a highly nonlinear problem and is known to cause convergence difficulties when the traditional implicit solver is employed. To overcome the convergence difficulties, which are particularly pronounced when concrete cracking is initiated, ABAQUS EXPLICIT was employed. ABAQUS EXPLICIT is an FE code that adopts an explicit time integration scheme to solve the equations of dynamic equilibrium of highly nonlinear problems. Instead of calculating the element matrices, assembling the global matrix of the structure, and solving a large system of equations by inverting the global matrix, ABAQUS EXPLICIT performs equilibrium calculations at each node. The out-of-balance nodal forces are divided by the respective nodal masses to yield the nodal accelerations, from which the nodal velocities and nodal displacements are obtained by means of explicit time integration. The explicit solver algorithm is conditionally stable, which means that the number of time increments employed is determined from the maximum stable time increment (i.e. the minimum time that a dilatational wave takes to move across any element of the model). Thus, the stable time increment depends upon the dilatational wave speed, which is generally a function of the material Young's modulus and density and the element size.

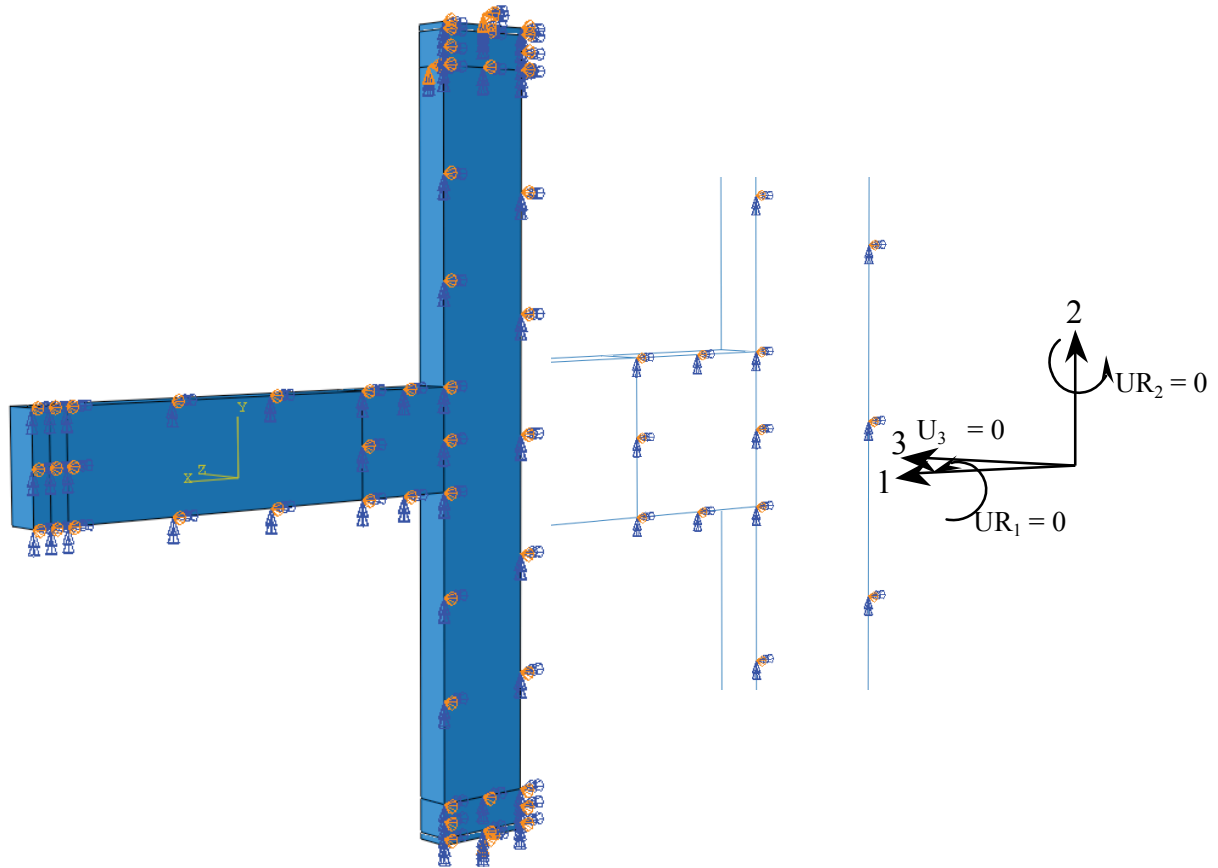


Figure 5.10. Symmetry boundary condition applied at mid-width of specimen

Even though ABAQUS EXPLICIT is a truly nonlinear solver, static behaviour can be simulated by imposing very slow loading conditions (i.e. simulating a procedure over a prolonged period of time), hence rendering the dynamic procedure quasi-static. As a rule of thumb, the time period over which an analysis is conducted is chosen to be at least equal to ten times the fundamental natural period of the structure simulated to ensure that inertia effects are negligible. Moreover, the SMOOTH AMPLITUDE feature of ABAQUS, a time history designed to minimize the dynamic effects of applied loads/displacements was utilized to mitigate sharp changes in inertia.

Given the maximum stable time increment and the relatively long time period that needs to be simulated, a very large number of computationally inexpensive time increments is employed to obtain the dynamic response of the structure. In order to reduce computational cost, a technique called mass scaling is employed, which artificially increases the density of some parts of the model, thereby locally reducing the dilatational wave speed and increasing the stable time increment and allowing fewer time increments to be employed. The increased density leads to increased inertia effects, which is clearly undesirable in a quasi-static analysis. In order to ensure that the inertia effects are negligible and that the response of the model is essentially static, the mass scaling factor is selected such that the kinetic energy of the model is a small fraction (smaller than 2%) of its internal energy throughout the analysis.

5.5. VALIDATION

5.5.1. Control Specimen, BCJ-CS-A Test #2

Mesh convergence studies were conducted to examine a suitable mesh size and the appropriate material parameters that lead to a close agreement with the experimentally observed response. Three element sizes, namely 100 mm, 50 mm and 30 mm, were initially adopted as a uniform mesh size; the results obtained for each mesh size are presented in Figure 5.11 in terms of the obtained load-displacement response of the duplicate control specimen (BCJ-CS-A Test #2). Figure 5.11 shows that the element size significantly affects the hysteresis curve behaviour. The results presented in Figure 5.11.c (using 30 mm element size) provided a closer agreement with the experimental results in terms of the peak load and stiffness at the peak load than those depicted in Figure 5.11.a and 5.11.b (using 100 mm and 50 mm element size, respectively). The similarity of the hysteresis curves suggested a

reasonably good agreement between the experimental observation and the prediction result gained from FE analysis using 30 mm element size.

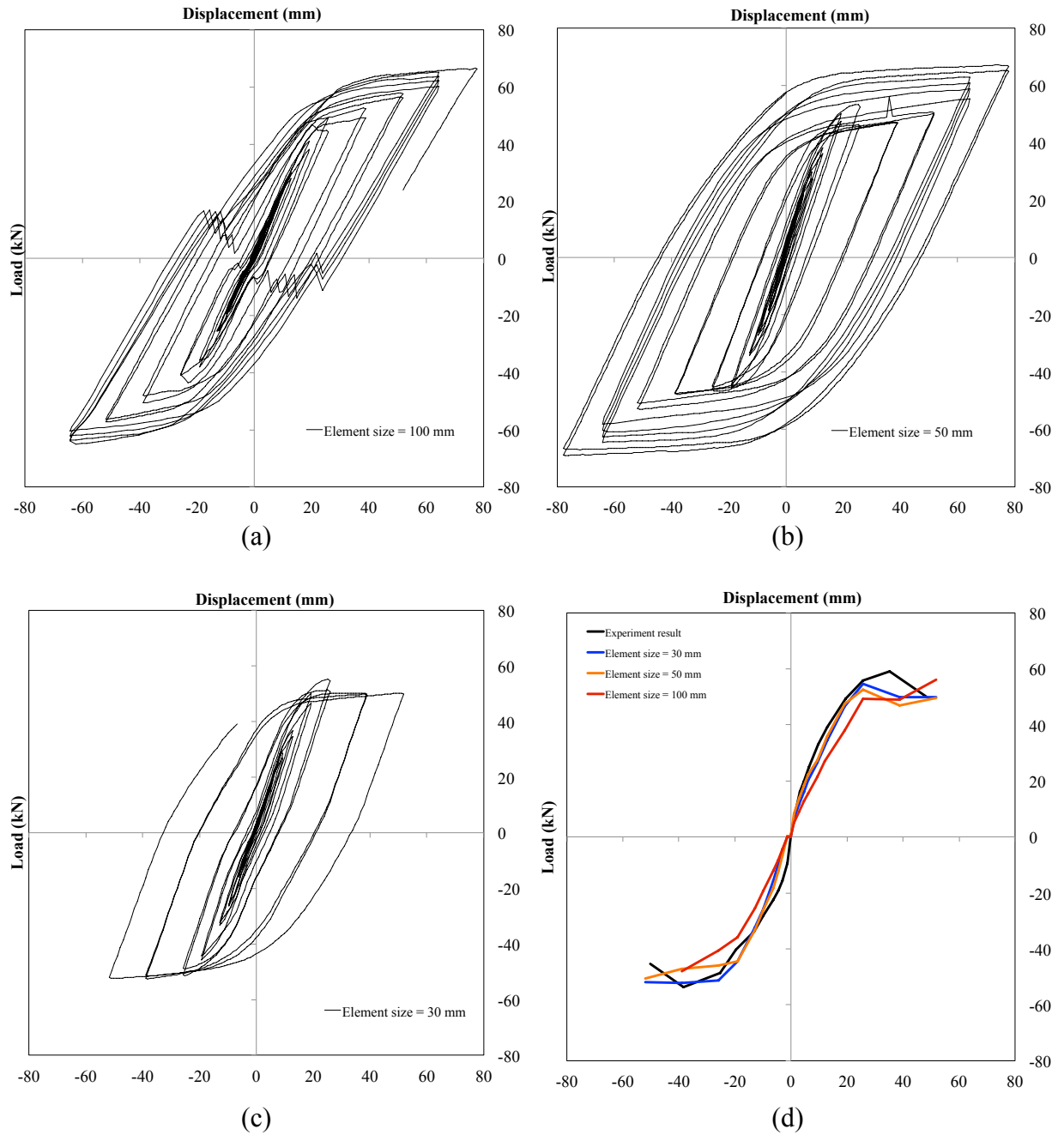


Figure 5.11. Load-displacement response for BCJ-CS-A Test #2: (a) 100 mm element size; (b) 50 mm element size; (c) 30 mm element size; (d) Envelope curves of FE analysis and experiment

The envelope curves of the load-displacement response from the FE analysis are compared to the respective experimental envelope curve in Figure 5.11.(d). Overall, load-displacement obtained from analysis using 30 mm element size showed better predictions than analysis using 100 mm and 50 mm element size for both loading directions as shown in Figure 5.11.(d). This is quantified in Table 5.1 where the mean value and coefficient of variation (CoV) of the numerical over experimental peak load ratio for each loading direction is reported for the specimen BCJ-CS-A Test #2.

Table 5.1. Comparison of numerical and experimental key results for BCJ-CS-A Test #2

Loading direction		FE/Test peak load			FE/Test stiffness at peak load		
		100 mm	50 mm	30 mm	100 mm	50 mm	30 mm
Upward	Average	0.88	0.95	0.96	0.87	0.94	0.96
	CoV	0.16	0.08	0.08	0.14	0.10	0.11
Downward	Average	0.88	1.01	1.05	0.89	1.02	1.05
	CoV	0.12	0.09	0.07	0.11	0.10	0.07

In the case of upward loading, the average load ratio of FE analysis to experimental work using a 30 mm element size was 0.96, while ratios using 50 mm and 100 mm element size were 0.95 and 0.88, respectively. On downward loading direction, the average load ratio using 30 mm, 50 mm and 100 mm element sizes were 1.05, 1.01 and 0.88, respectively. Table 5.1 shows that the FE analysis conducted on the 30 mm element size provided a very close agreement between the experiment and the numerical response of the stiffness and peak load. Based on these observations, further validation on the crack pattern and cumulative dissipation energy as well as the FE parametric study conducted on BCJ-CS-A Test #2, is based on the analysis using 30 mm element size.

The experimental and numerical hysteresis curves which were obtained up for a 3% drift ratio are presented in Figure 5.12.a, while the envelope curves for both results are shown in Figure 5.12.b. The comparison of average stiffness between predicted and observed response at upward loading direction was 0.96, with a coefficient variation of 0.11, while at downward loading direction, the comparison of average stiffness between predicted and observed response showed a lower value of 1.05 with a coefficient variation of 0.07.

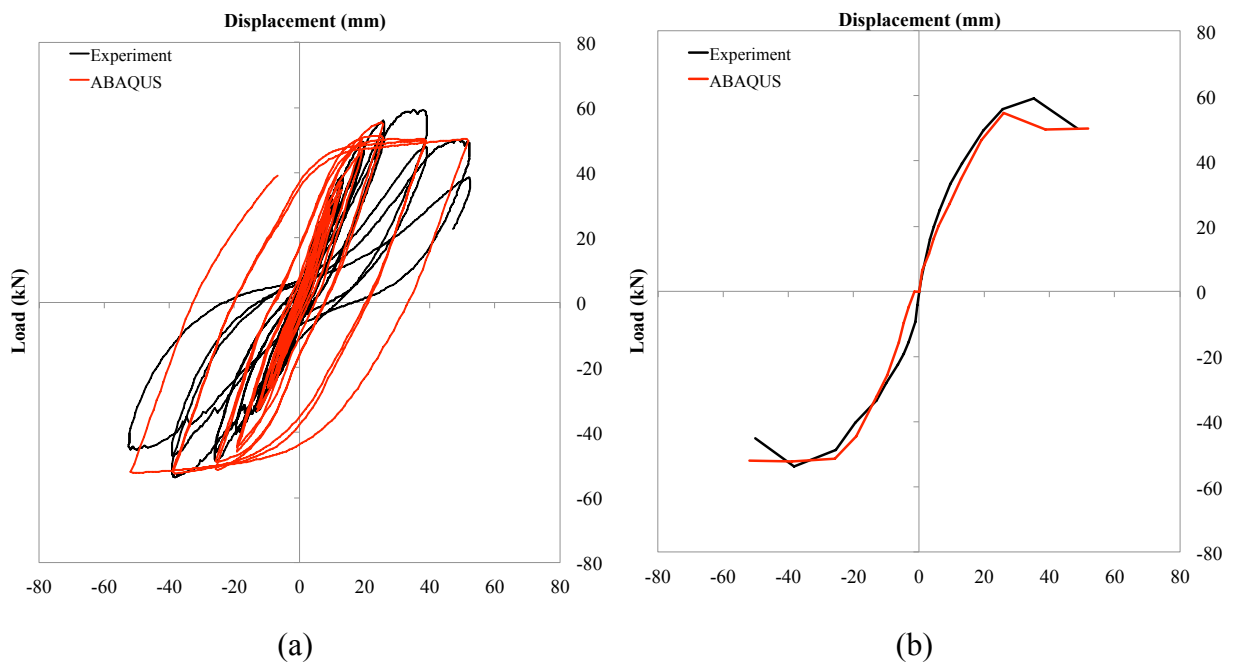


Figure 5.12. Load-displacement response of the experiment and ABAQUS for BCJ-CS-A Test #2: (a) Hysteresis curves; (b) Envelope curves

Figure 5.13 presents the dissipated energy obtained from the experiment and the finite element analysis. The cumulative dissipated energy of the experimental result calculated up to a 2% drift ratio was 2503.38 kN-mm, whilst the corresponding energy calculated from FE analysis was 2708.18 kN-mm, representing a difference of 8.18%, thus verifying the ability of the numerical model to replicate the experimental response.

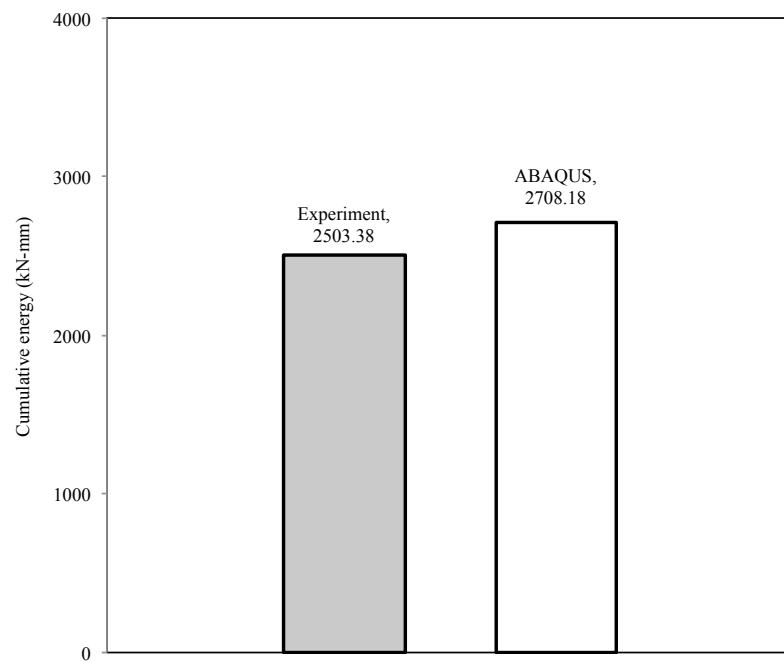
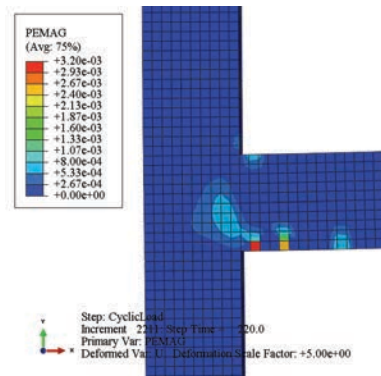


Figure 5.13. Cumulative energy comparison

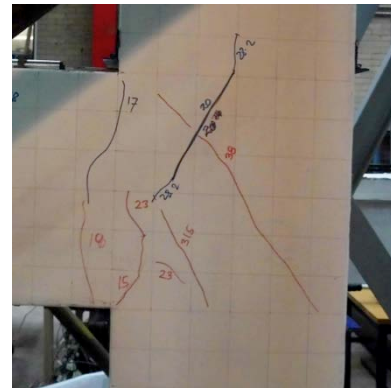
The FE analysis results for the formation of cracks under cyclic loading at 1%, 2% and 3% drift ratios are compared to those of the experiment in Figure 5.14. During the experiment, diagonal joint cracks were observed at a load of 31.5 kN (0.75% drift ratio). At 2.00% drift ratio (54.0 kN), cracks in the joint area continued and propagated towards the column back face, and the joint failed in shear at 3.00% drift ratio (59.0 kN).

For the CDP concrete material model adopted in the FE analysis, cracking propagation can be visualized by plotting the plastic strain (PE) in the first principal direction (i.e. corresponding to tensile plastic strain). Figure 5.14.a shows that, at the upward loading of 1.00% drift ratio (34.58 kN) of FE analysis, cracks formed at the lower corner of the beam-column joint. At 2.00% drift ratio (54.78 kN), joint cracks continued to form and propagated to the lower part of the column back face. Finally at 3.00% drift ratio (49.83 kN), cracks were concentrated in the joint area and at the beam-column interface.



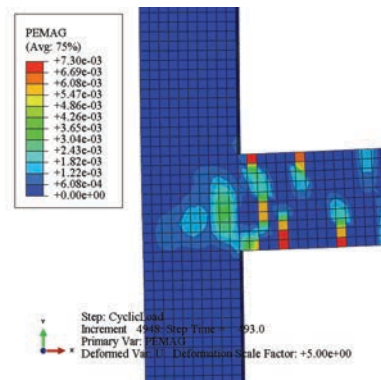
(a) 1% drift ratio of FE analysis

34.6 kN



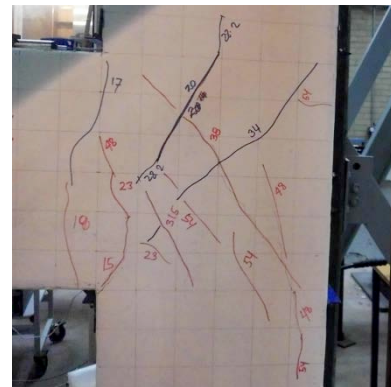
(b) 1% drift ratio of experiment

38.0 kN



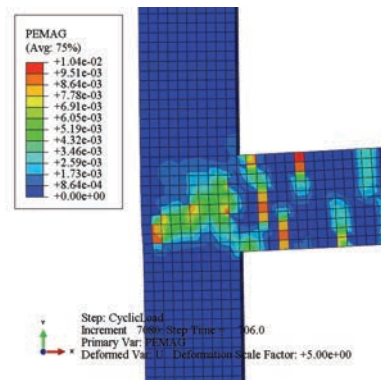
(c) 2% drift ratio of FE analysis

54.8 kN



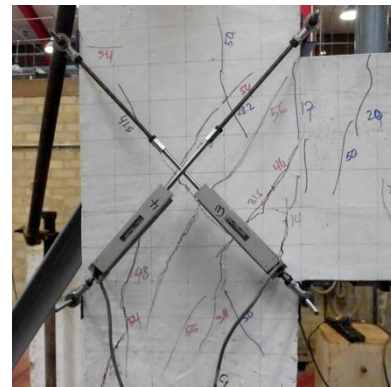
(d) 2% drift ratio of experiment

54.0 kN



(e) 3% drift ratio of FE analysis

49.8 kN



(f) 3% drift ratio of experiment

56.0 kN

Figure 5.14. Comparison of crack propagation of BCJ-CS-A Test #2

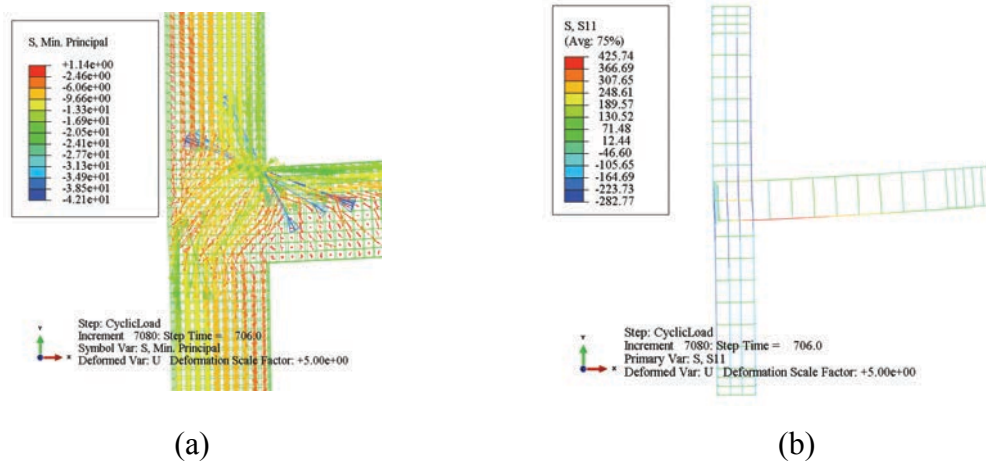


Figure 5.15. (a) Principal compressive stress in concrete; (b) Tensile stress in reinforcement for BCJ-CS-A Test #2

Examination of Figure 5.14 explains that the damage mechanism results in the FE analysis are basically formed in the joint region and identified as shear cracking since most concrete principal tensile strain was concentrated in the joint area. Overall, it is concluded that the model developed using the ABAQUS software predicted the failure mode successfully as it matched the failure mode given by the experimental result. By referring to Table 5.2, the load ratios extracted from FE analysis compared to the experimental results on 1%, 2% and 3% drift level were 0.91, 1.01 and 0.89 respectively.

The FE analysis was also able to capture the stress profile of the specimen appropriately. Figure 5.15.(a) shows that the concrete compressive stress occurs within the joint body, whilst Figure 5.15.(b) shows that the maximum stress of the bottom beam reinforcement on upward loading direction is localized within the beam-column face.

Table 5.2. Experiment and FE peak load comparison for BCJ-CS-A Test #2

Drift ratio (%)	Experiment (kN)	FE (kN)	FE/Test
1	38.0	34.6	0.91
2	54.0	54.8	1.01
3	56.0	49.8	0.89

5.5.2. Strengthened Specimen, BCJ-SS-S4

Figure 5.16 depicts the load-displacement response of the modelled specimen BCJ-SS-S4 in the mesh convergence test of three element sizes (30 mm, 50 mm and 100 mm). It is evident from Figure 5.16 that the element size significantly affects the hysteresis curve behaviour. The results presented in Figure 5.16.(c) (using 30 mm element size) provided a closer agreement with the experimental results than those depicted in Figure 5.16.(a) and 5.16.(b) (using 100 mm and 50 mm element sizes, respectively). Compared to the hysteresis curves obtained from 100 mm and 50 mm element sizes, the results for the 30 mm element size gave a better prediction. The similarity of the hysteresis curve results in FE analysis using the 30 mm element size compared to that gained from the experiment suggested a reasonably good agreement between the experimental observation and the prediction result from the FE analysis.

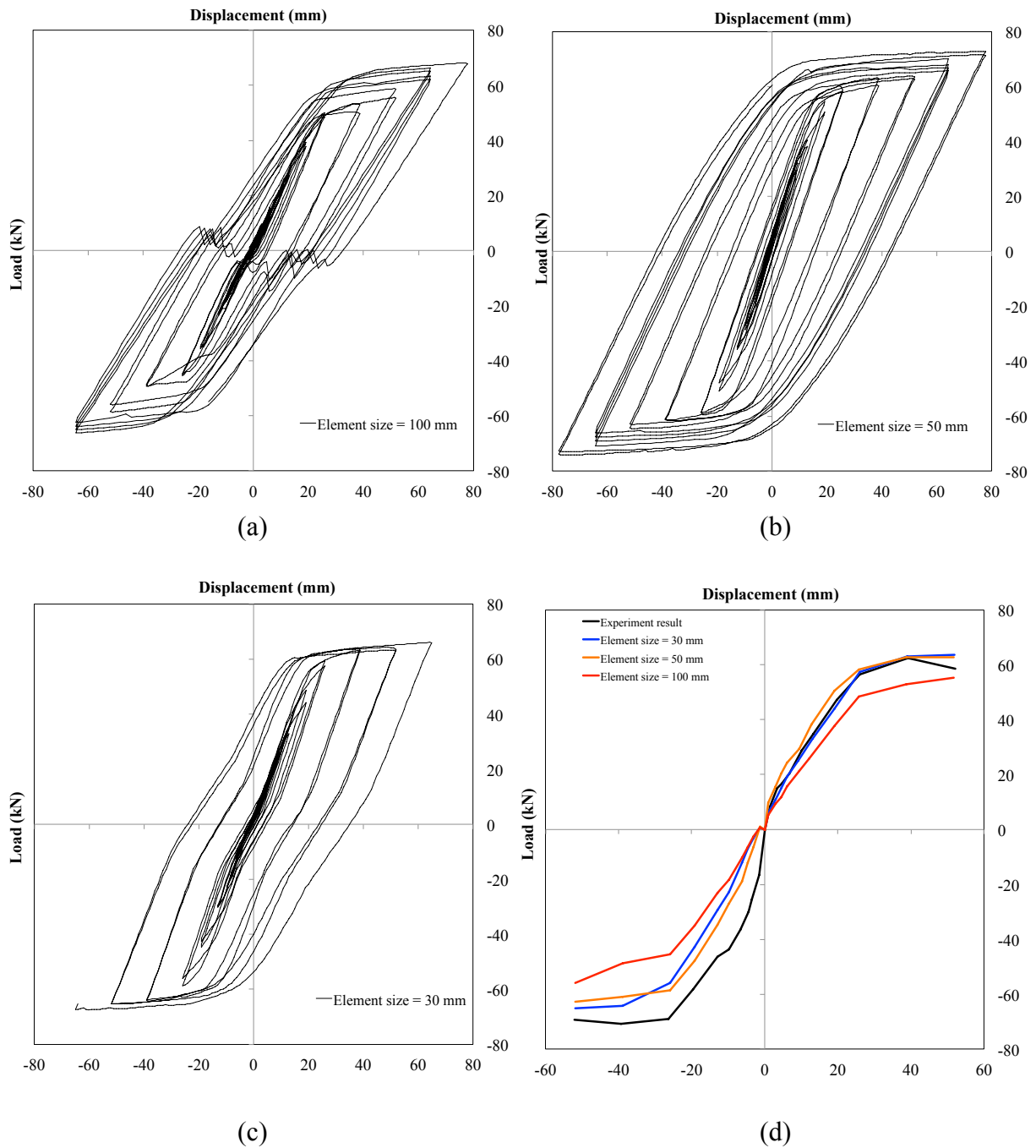


Figure 5.16. Load-displacement response for BCCJ-SS-S4: (a) 100 mm element size; (b) 50 mm element size; (c) 30 mm element size; (d) Envelope curves FE analysis and experiment

The envelope curves of the load-displacement response from the FE analysis are compared to the respective experimental envelope curve in Figure 5.16.d. Overall, better predictions were

obtained for the upward loading direction compared to those of the downward loading direction, as shown in Figure 5.16.(d). This is quantified in Table 5.3 where the mean value and coefficient of variation (CoV) of the numerical over experimental peak load ratio for each loading direction is reported for specimen BCJ-SS-S4.

For the upward loading direction, the average load ratio of the FE analysis using 30 mm element size at upward loading direction compared to the experimental results was 1.04, while those ratios using 50 mm and 100 mm element size were 1.10 and 0.87, respectively. On downward loading direction, the average load ratio in the FE analysis using 30 mm, 50 mm and 100 mm element size were 0.83, 0.86 and 0.67 respectively. Table 5.3 shows that the FE analysis conducted on 30 mm element size provided a very close agreement between the experiment and the numerical response of the peak load and stiffness. Based on these observations, further validation on crack patterns and cumulative dissipation energy, as well as the FE parametric study conducted on BCJ-SS-S4, is based on the analysis using 30 mm element size.

Table 5.3. Comparison of numerical and experimental key results for BCJ-SS-S4

Loading direction		FE/Test peak load			FE/Test stiffness at peak load		
		100 mm	50 mm	30 mm	100 mm	50 mm	30 mm
Upward	Average	0.87	1.10	1.04	0.89	1.12	1.06
	CoV	0.09	0.07	0.06	0.08	0.07	0.06
Downward	Average	0.67	0.86	0.83	0.68	0.87	0.84
	CoV	0.18	0.08	0.15	0.18	0.08	0.15

A comparison of the hysteresis curve between the experimental and the FE analysis result for the 30 mm element size up to 3% drift ratio is given in Figure 5.17.(a), and the envelope curves for both experimental and FE results are presented in Figure 5.17.(b). The FE result

showed a very good correlation in terms of capturing the peak load-displacement response compared to the experiment, as can be seen in Figure 5.17.(b). Further more, comparison of average stiffness at peak load between the predicted and observed response at upward loading direction was 1.06 with a coefficient variation of 0.06, while the comparison at downward loading direction was 0.84 with a coefficient variation of 0.15. Table 5.4 shows that the load ratio extracted from experimental results compared with the results from FE analysis at 1, 2 and 3% drift ratios are 0.88, 0.98 and 0.99 respectively.

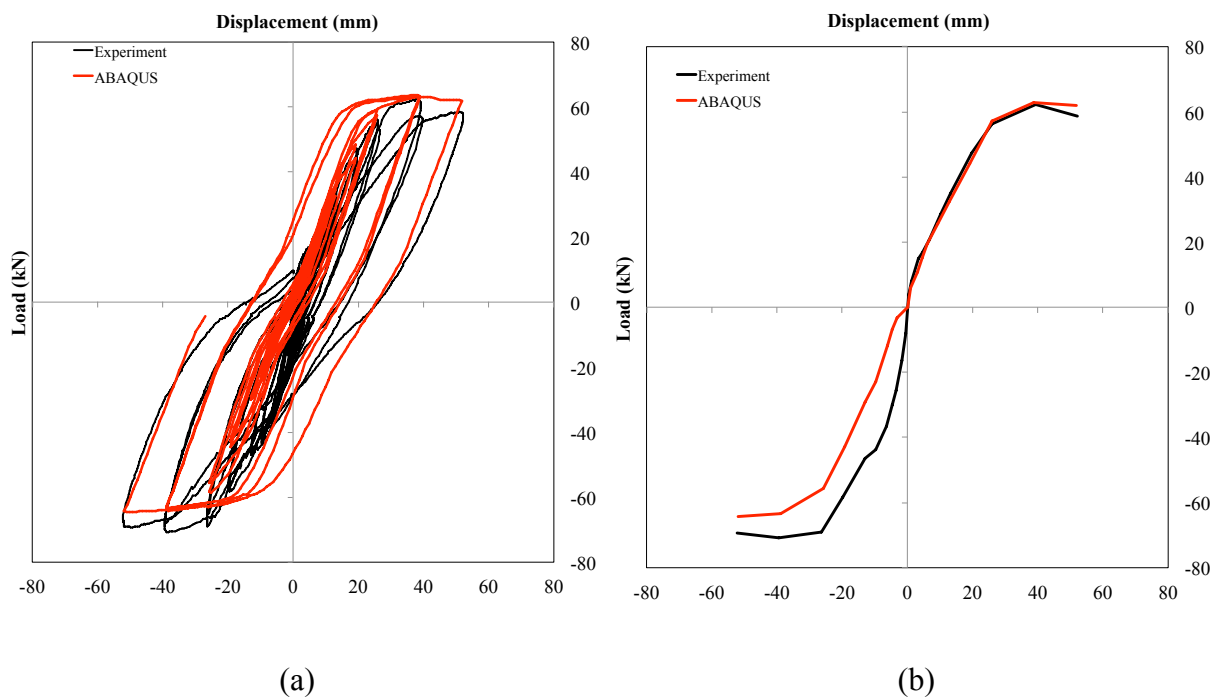


Figure 5.17. Load-displacement response of experiment and ABAQUS for BCJ-SS-S4; (a) hysteresis curves; (b) Envelope curves

Comparison of the dissipated energy result in the experiment and the FE analysis is presented in Figure 5.18. Cumulative dissipated energy of the experiment calculated up to 3% drift ratio was 8369 kN-mm, while the corresponding energy calculated from the FE analysis was

7964.28 kN-mm; represents a difference of 4.84% over the corresponding value for the experimental result.

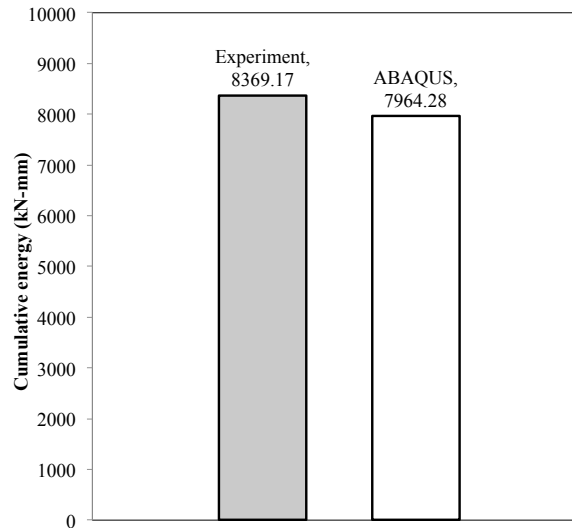
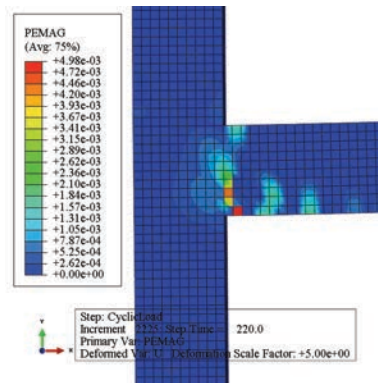
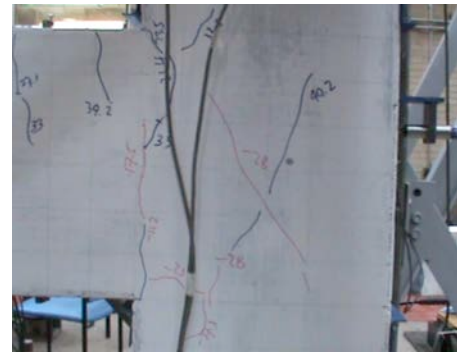


Figure 5.18. Cumulative energy comparison

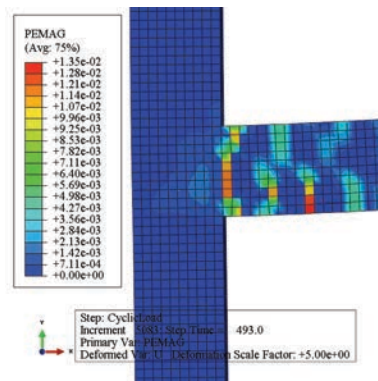
The FE analysis results for the formation of crack patterns under cyclic loading at 1%, 2% and 3% drift ratios are compared to those of the experimental results in Figure 5.19. During the experiment, a flexural crack appeared at the bottom of the beam-column interface at a drift ratio of 0.10%. With increased loading, this crack extended up to two-thirds of the beam depth. Diagonal cracks in the joint formed at a load of 28.72 kN (0.75% drift ratio). At 2.00% drift ratio (58.0 kN), further diagonal cracks formed at mid-depth of the joint area, and at 3.00% drift ratio (64.5 kN), diagonal cracks previously formed propagated to the column back face. At 3% drift ratio, several horizontal cracks also formed at the upper column adjacent to the joint area.



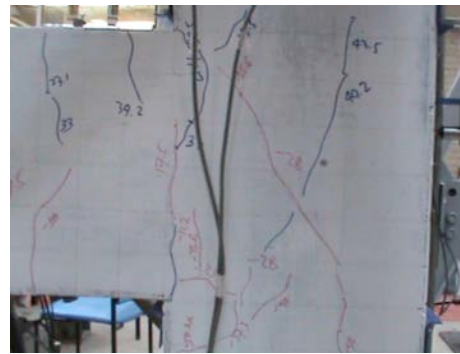
32.9 kN



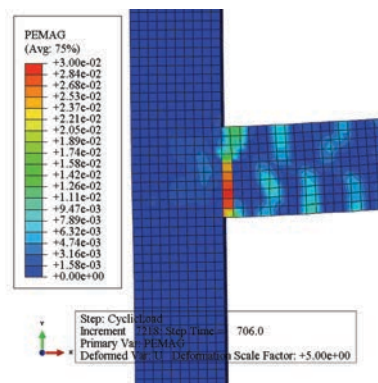
37.3 kN



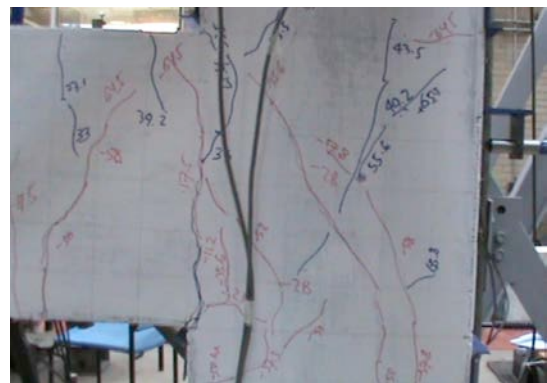
57.5 kN



58.0 kN



63.1 kN



64.5 kN

Figure 5.19. Comparison of crack propagation of BCJ-SS-S4

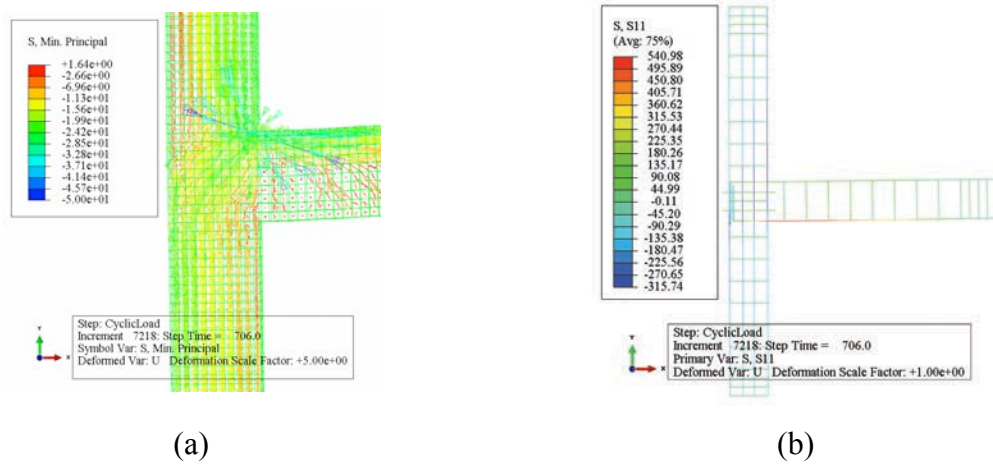


Figure 5.20. (a) Principal compressive stress in concrete; (b) Tensile stress in reinforcement at 3% drift ratio of the strengthened specimen BCJ-SS-S4

Table 5.4. Experiment and FE peak load at specific drift ratio

Drift ratio (%)	Experiment (kN)	FE (kN)	FE/Test
1	37.3	32.9	0.88
2	58.0	57.5	0.99
3	64.5	63.1	0.98

Concrete cracking pattern results in the FE analysis seen in Figure 5.19.a show that the model was capable of capturing the crack propagation of the specimen due to reversal load, specifically those within the joint area. Like the crack patterns produced in the experiment, the cracks in the FE analysis (as shown in Figures 5.19.(a), (c), and (e)) were shifted to the beam region, suggesting the benefit of embedded steel reinforcement in the joint area to achieve beam yielding mechanism. Figure 5.20 also shows that the stress profile constructed from the FE analysis agreed well with the results from the experiment. For example, Figure 5.20.(a) predicted that the concrete compressive stress concentrated within the joint body and diagonal shear cracks were also to be seen localized in the beam area. In addition, at this point

the beam bottom reinforcement had yielded during the upward loading direction (Figure 5.20.(b)).

5.5.3. Strengthened Specimen, BCJ-SS-F4

The load-displacement response of the modelled specimen BCJ-SS-F4 extracted from the mesh convergence test of three element sizes (30 mm, 50 mm and 100 mm) is presented in Figure 5.21. The result presented in Figure 5.21.(c) (using 30 mm element size) provided a closer agreement with the experimental results than those depicted in Figure 5.21.(a) and 5.21.(b) (using 100 mm and 50 mm element size, respectively). The envelope curves of the load-displacement response from the FE analysis are compared to the respective experimental envelope curve in Figure 5.11.(d). Overall, better predictions were obtained for the upward loading direction compared to those of the downward loading direction, as shown in Figure 5.11.(d). This is quantified in Table 5.5 where the mean value and coefficient of variation (CoV) of the numerical over experimental peak load ratio for each loading cycle is shown for specimen BCJ-SS-F4.

Table 5.5. Comparison of numerical and experimental key results for BCJ-SS-F4

Loading direction		FE/Test Load			FE/Test Stiffness at peak load		
		100 mm	50 mm	30 mm	100 mm	50 mm	30 mm
Upward	Average	0.94	0.79	0.98	0.96	0.80	1.00
	CoV	0.16	0.10	0.12	0.15	0.10	0.12
Downward	Average	1.23	1.04	1.29	1.18	1.00	1.24
	CoV	0.20	0.18	0.18	0.14	0.10	0.11

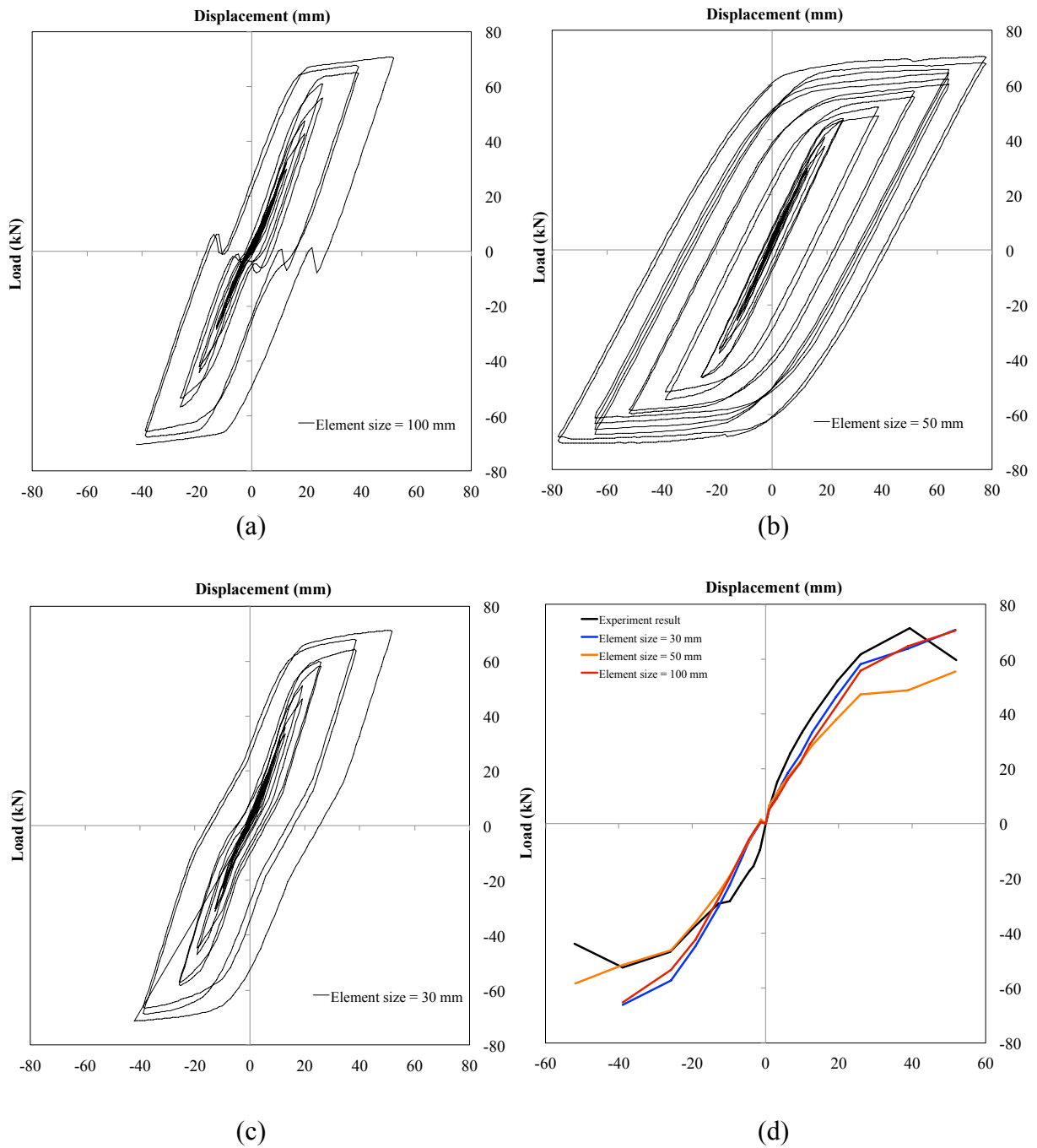


Figure 5.21. Load-displacement response for BCCJ-SS-F4: (a) 100 mm element size; (b) 50 mm element size; (c) 30 mm element size; (d) Envelope curves FE analysis and experiment

For the upward loading direction, the average load ratio of the FE analysis, using 30 mm element size at upward loading direction, to the experimental work was 0.98 while those

ratios using 50 mm and 100 mm element size were 0.79 and 0.94, respectively. On the downward loading direction, the average load ratio using 30 mm, 50 mm and 100 mm element size were 1.29, 1.04 and 1.23 respectively. Based on these observations, further validation on the crack patterns and cumulative dissipation energy, as well as the FE parametric study conducted on BCJ-SS-F4 is based on the analysis using 30 mm element size.

Comparison of the hysteresis curve extracted from the experiment and the FE analysis result for 30 mm element size until end of 3% drift ratio is shown in Figure 5.22.(a), and the envelope curves for both experiment and FE result are compared in Figure 5.22.(b). The FE result showed very good correlation in terms of capturing peak-to-peak load-displacement relationship compared to the experimental result, as depicted in Figure 5.22.(b). Comparison of the average stiffness at peak load between the prediction on observed response at upward loading direction was 1.00, with a coefficient variation of 0.12, while the comparison at downward loading was 1.24 with a coefficient variation of 0.11. Table 5.6 shows that the load ratio extracted from experimental results compared to those of the FE analysis at 1, 2, and 3% drift ratios are 0.85, 0.94 and 0.89 respectively.

Dissipated energy comparison between the experimental and the FE analysis is presented in Figure 5.23. Cumulative dissipated energy of the experimental result calculated up to 3% was 11036.84 kN-mm, while the corresponding energy calculated from FE analysis was 9436.96 kN-mm, representing a difference of 14.50% over the corresponding value for the experimental result.

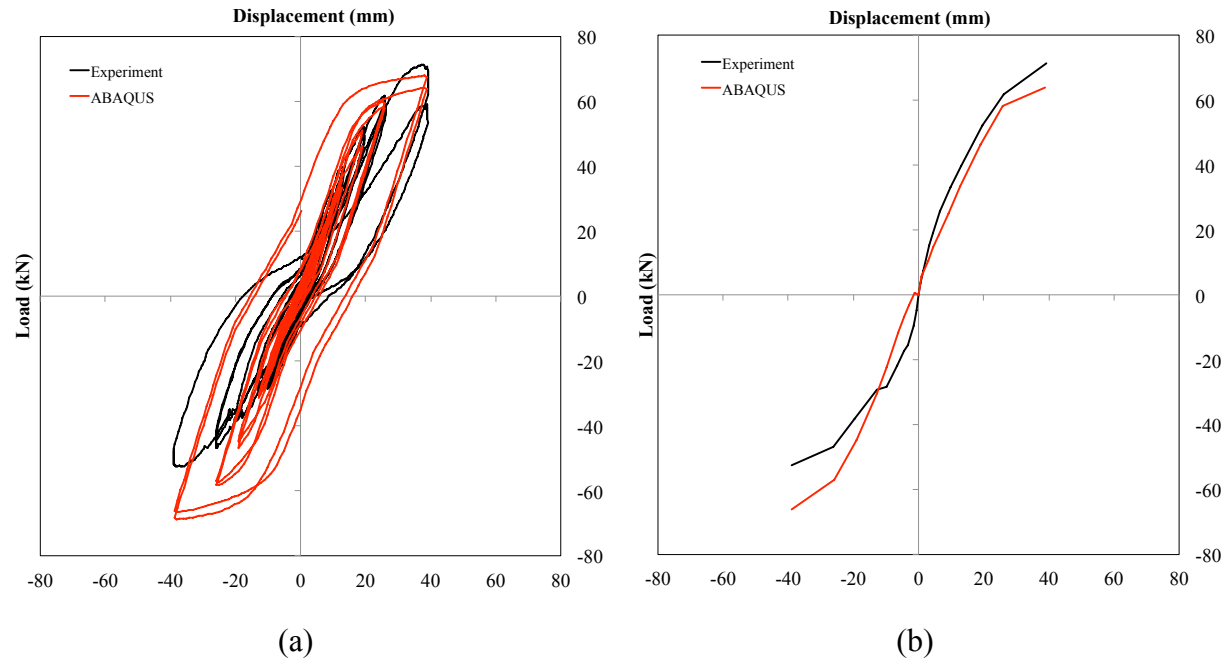


Figure 5.22. Load-displacement comparison between experiment and ABAQUS for control specimen: BCJ-SS-F4 (a) Hysteresis loops; (b) Peak-to-peak

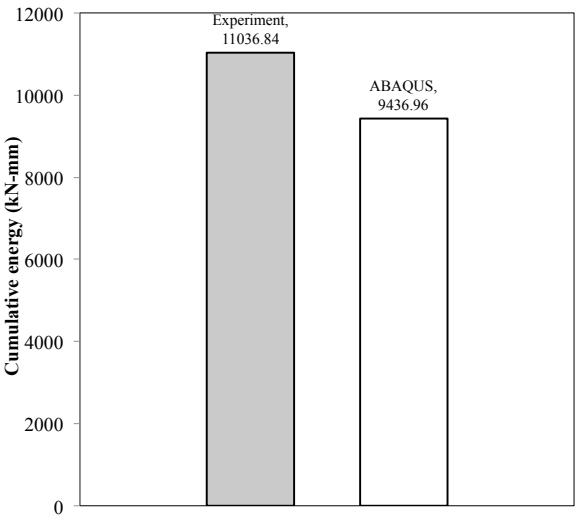


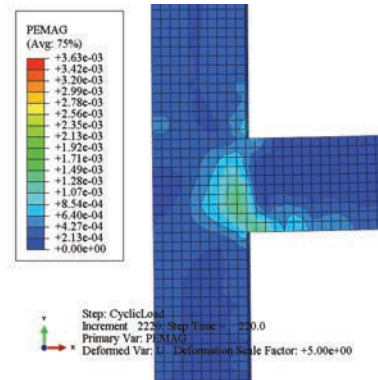
Figure 5.23. Cumulative energy comparison

Table 5.6. Experiment and FE peak load at specific drift ratio

Drift ratio (%)	Experiment (kN)	FE (kN)	FE/Experiment
1	36.0	33.5	0.93
2	58.0	58.0	1.00
3	66.0	63.7	0.96

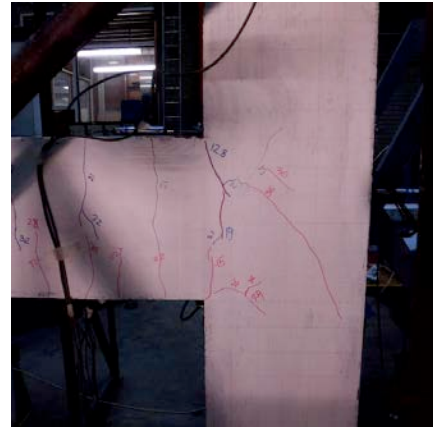
FE results for the formation of cracks up to 3% drift ratio compared to the experimental results are presented in Figure 5.24. In the experiment, the first flexural crack was reported at 0.35% drift ratio (21 kN) and joint shear cracking was observed at the end of 1.00% drift ratio (36 kN). Between 1.5 and 2.00% drift ratio, diagonal cracks developed within the joint area in an X-pattern and spread to the perimeter of the joint. Vertical hairline cracks and diagonal cracks in the beam were reported at upward loading corresponding to 3.00% drift ratio (66 kN).

According to the crack formation result in FE analysis, the shear crack in the joint and the flexural cracks at the beam-column interface were observed to be similar to experimental results at 1.00% drift ratio. Later at 2.00% drift ratio, FE analysis results showed the formation of joint diagonal cracks in an X-pattern and the propagation of the flexural cracks in the beam, as shown in Figure 5.24.(c). At 3.00% drift ratio in the FE analysis, vertical cracks also formed in the lower part of the beam-column joint.



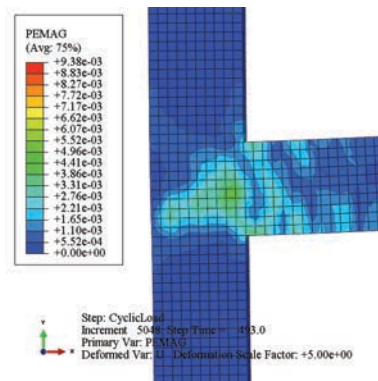
(a) 1% drift ratio of FE analysis

33.5 kN



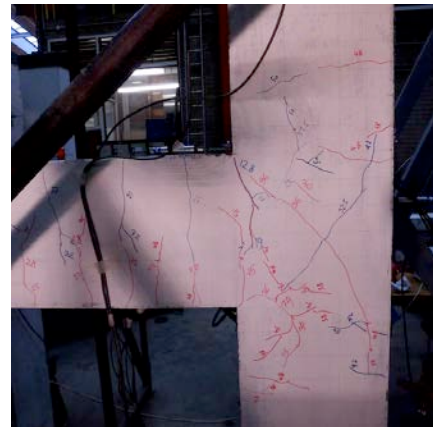
(b) 1% drift ratio of experiment

36 kN



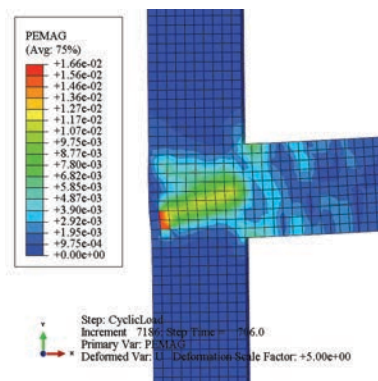
(c) 2% drift ratio of FE analysis

58.0 kN



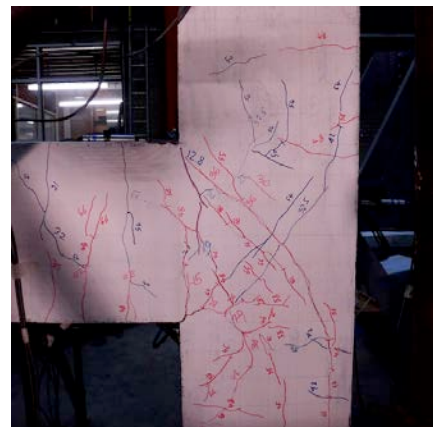
(d) 2% drift ratio of experiment

58 kN



(e) 3% drift ratio of FE analysis

63.7 kN



(f) 3% drift ratio of experiment

66 kN

Figure 5.24. Comparison of crack propagation of BCJ-SS-F4

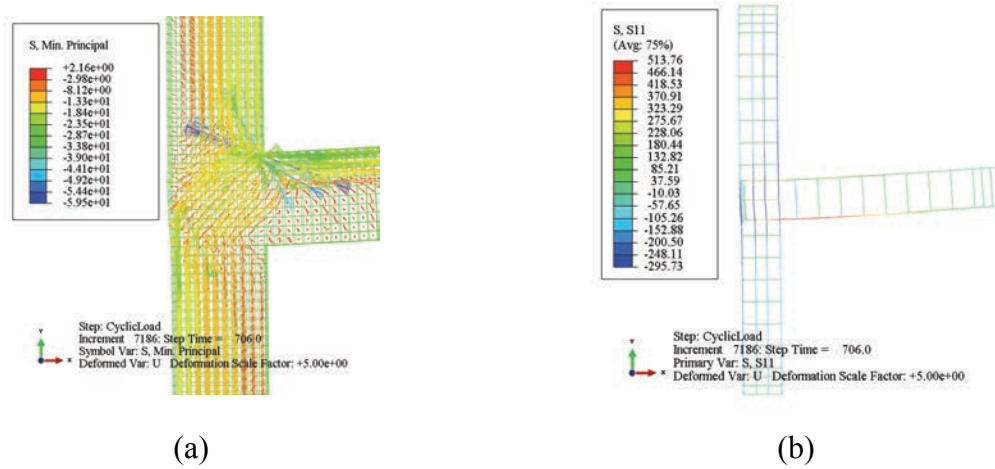


Figure 5.25. (a) Principal compressive stress in concrete; (b) Tensile stress in reinforcement at 3% drift ratio of the strengthened specimen BCJ-SS-F4

Furthermore, Figure 5.25 also shows that the stress profile constructed from FE analysis agreed well with results from the experiment. For example, Figure 5.25.(a) predicted that the concrete compressive stress concentrated within the joint body and diagonal shear cracks were also to be seen localized in the beam area at the end of the 3.00% drift ratio. In addition, at this point the beam bottom reinforcement had yielded during upward loading direction (Figure 5.20.(b)).

Concrete cracking pattern results from the FE analysis, as seen in Figure 5.24 and Figure 5.25, show that the model was capable of capturing the stress profile of the specimen, specifically those within the joint area. Comparison of the results for this specimen suggest a reasonably good correlation between the experiment and the FE analysis.

5.6. PARAMETRIC STUDY

In this section, the effect of three key parameters on the structural response of unstrengthened and strengthened joints is investigated. The key parameters considered include concrete compressive strength, column axial load and embedded bar size; their effect is considered in the remainder of this chapter.

5.6.1. Effect of concrete compressive strength

The variation of concrete compressive strength (f_c) implies the variation of other concrete properties, such as concrete tensile strength (f_{ct}) and Young's modulus (E_c), all of which are linked to concrete compressive strength. In this parametric study, a variation of concrete strength ranging from 20 to 55 MPa was chosen to cover the concrete strength found in existing pre-1970s structures, and also to anticipate the use of higher concrete strength in modern concrete buildings.

The effects of variation of concrete compressive strength, f_c , on the duplicate control specimen (BCJ-CS-A Test #2) and strengthened specimens (BCJ-SS-S4 and BCJ-SS-F4) are presented in Figures 5.26.a, 5.26.b and 5.26.c, respectively, in the form of normalized joint principal tensile stress, p_t/f_c . Two key points (Point A and Point C), corresponding to the first joint crack and the maximum joint shear strength respectively, were observed in the finite element analysis.

Figure 5.26.a shows that the predicted normalized principal tensile stress, p_t/f_c , in the event of first joint shear crack (Point A) at lower concrete strength ($f_c = 20$ and $f_c = 25$ MPa) was underestimated. For the rest of the variation of the concrete compressive strength f_c , the normalized principal tensile stress varied with the increase of the concrete strength, but less

significantly. On average, the normalized principal tensile stress on the joint first cracking in the FE analysis of the duplicate control specimen was $0.27 \sqrt{f_c}$. Figure 5.26.(b) shows that the normalized principal tensile stress, $p_t \sqrt{f_c}$ in the event of first joint shear crack (Point A) of BCJ-SS-S4 decreased slightly at $f_c \approx 50$ and $f_c \approx 55$ MPa. For BCJ-SS-S4, the average normalized principal tensile stress on the first joint cracking in the FE analysis was $0.29 \sqrt{f_c}$. Figure 5.26.(c) also shows that the normalized principal tensile stress in the event of first joint shear crack of BCJ-SS-F4 decreased slightly with the increase of the concrete strength. On average, the normalized principal tensile stress on first joint cracking was $0.31 \sqrt{f_c}$.

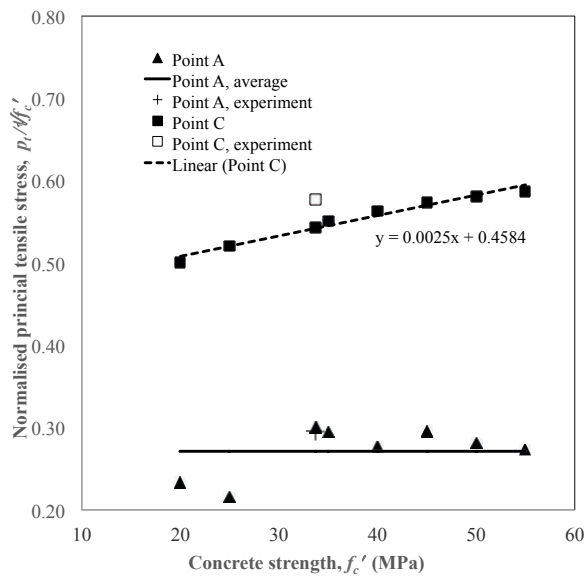
Based on these results, the first joint shear crack (Point A) can be simply defined by the function of a constant, k_a , and the normalized concrete strength, $\sqrt{f_c} [k_a \sqrt{f_c}]$. In this case, the normalized joint shear stress factors, k_a at first joint crack for BCJ-CS-A, BCJ-SS-S4 and BCJ-SS-F4, were 0.27, 0.29 and 0.31 respectively. The results also show that the embedded steel bars on BCJ-SS-S4 and CFRP bars on BCJ-SS-F4 enhanced the joint shear stress in the event of first joint cracking by 7% and 15%, respectively compared to that of the duplicate control specimen.

The default CDP concrete model available in ABAQUS and employed in this FE study was unable to capture strength and stiffness degradation behaviour; the analysis stopped after 3.00% drift ratio (the convergence problem appeared when applying large displacement). As a result, the maximum joint shear stress was not able to be clearly defined by observing only the load-joint shear deformation response, as explained in Section 4.3.(2). In order to define the maximum principal tensile stress, the maximum tensile stress in concrete joint at both loading directions was defined by limiting the joint principal tensile stress to the value of

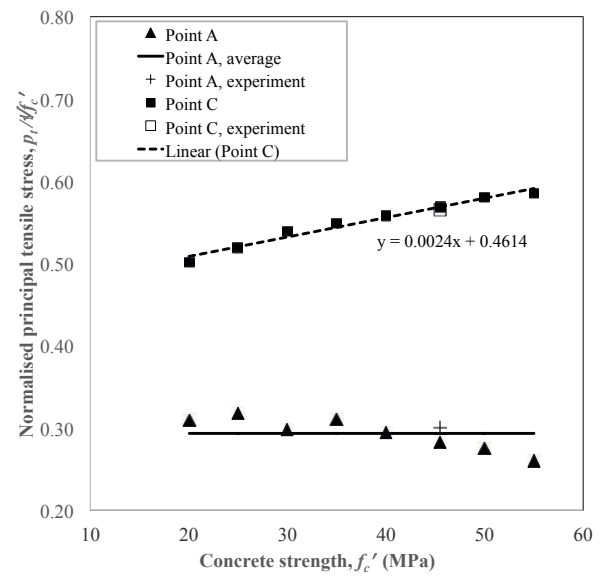
concrete tensile strength. This method was successfully able to determine the maximum joint shear strength. For example, the predicted maximum normalized joint shear stress (Point C) of BCJ-CS-A Test #2, BCJ-SS-S4 and BCJ-SS-F4 were $0.54\sqrt{f_c}$, $0.57\sqrt{f_c}$ and $0.55\sqrt{f_c}$ respectively, while the corresponding values that resulted in the experiment were $0.58\sqrt{f_c}$, $0.57\sqrt{f_c}$ and $0.53\sqrt{f_c}$ respectively.

Furthermore, Figure 5.26 shows that the maximum normalized principal tensile stress (Point C) in the joint was greatly influenced by the variation of the concrete strength. For the duplicate control specimen (BCJ-CS-A Test #2), this value increased linearly in the form of k_c , $0.0025f_c \pm 0.4584$. This finding gave a close approximation to the value of $(0.002f_c \pm 0.473)$ suggested in the parametric study conducted by Genesio (2012). For the strengthened specimens BCJ-SS-S4 and BCJ-SS-F4, the normalized principal tensile stresses at Point C were defined as a function of $(0.0024f_c \pm 0.4614)$ and $(0.0024f_c \pm 0.462)$ respectively.

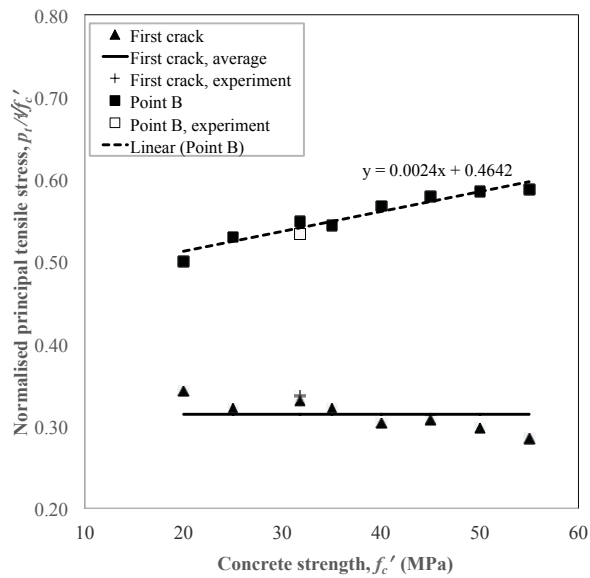
Concrete compressive strength is the common influence parameter for joint shear stress at the yielding of beam reinforcement (Point B) and at maximum joint shear stress (Point C) (Kim and LaFave, 2007). It was reported that joint shear stresses were proportional to the square root of concrete compressive strength at Point B and C. The finding of this parametric study is that joint strength (represented by the maximum normalized principal tensile stress, Point C) changes with the variation of concrete compressive strength. For example, for BCJ-CS-A Test #2 with a concrete strength (f_c) of 30 MPa, the maximum principal tensile stress was $0.54\sqrt{f_c}$ and for the $f_c = 40$ MPa, the maximum principal tensile stress was $0.56\sqrt{f_c}$. This is an increase of 4% for the same specimen with higher concrete strength.



(a) BCJ-CS-A Test #2



(b) BCJ-SS-S4



(c) BCJ-SS-F4

Figure 5.26. Effect of concrete compressive strength on the normalized joint principal tensile stress at Points A and C for: (a) Duplicate control specimen, BCJ-CS-A; (b) BCJ-SS-S4; (c) BCJ-SS-F4

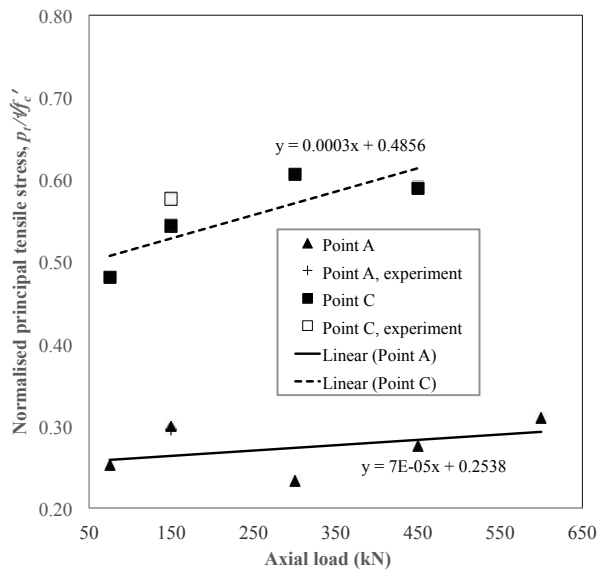
5.6.2. Effect of column axial load

Effect of axial load at column on the joints shear strength is controversial according to the surveyed literature. For loading cases including only vertical loads, it was suggested to assume that the axial load level acting on the column is less than 15% to 20% of the column compressive ultimate strength, while for building under lateral loading, 10% to 15% of the column ultimate strength should be considered as an upper limit of the applied column axial load (Genesio, 2012). In this study, five different axial load levels (75, 150, 300, 450 and 600 kN) are examined.

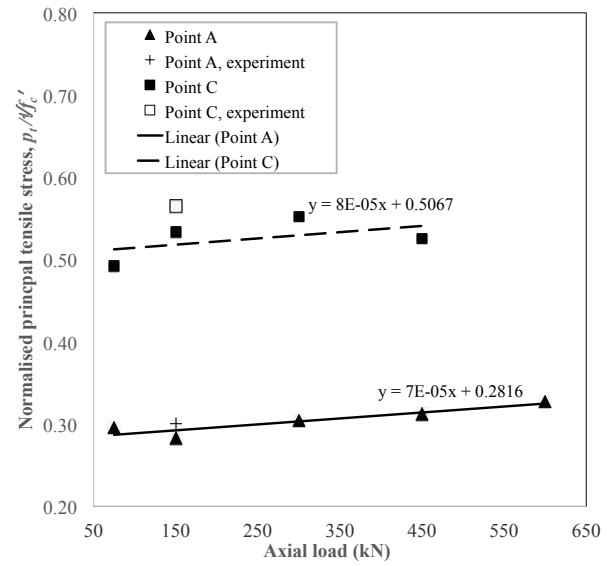
The effects of column axial load on normalized principal tensile stresses at joints on the duplicate control specimen (BCJ-CS-A Test #2) and strengthened specimens (BCJ-SS-S4 and BCJ-SS-F4) are depicted in Figures 5.27.(a), 5.27.(b) and 5.27.(c), respectively. Figure 5.27.(a) shows that the normalized principal tensile stress ($p_t/\sqrt{f_c}$) of BCJ-CS-A Test#2 at joint first crack (Point A) in the experiment (with a column axial load of 150 kN) was $0.295\sqrt{f_c}$ while the corresponding value in the FE analysis was $0.3\sqrt{f_c}$ showing the high accuracy of the predicted-to-observed value. Moreover, the normalized principal tensile stress of BCJ-CS-A Test #2, at maximum joint shear strength taken from the FE analysis, was $0.543\sqrt{f_c}$ while the corresponding stress result in the experiment was $0.577\sqrt{f_c}$. The FE results in Figure 6.27.(a) show that the axial load had a favorable effect on the joint shear stress at both joint first crack and maximum joint shear stress. In the case of the first crack at the joint, joint shear stress was enhanced with the increase of axial load (P in kN), $7 \times 10^{-5}P + 0.2538$. The corresponding enhancement at maximum joint shear stress was $0.003P + 0.4856$.

Figure 5.27.(b) shows that the normalized principal tensile stress (p_t/f_c) at joint first crack and normalized principal tensile stress at maximum joint shear stress of BCJ-SS-S4 were $0.300 f_c$ and $0.565 f_c$ respectively, while the corresponding values in the FE analysis were $0.283 f_c$ and $0.533 f_c$ respectively. The effect of increasing axial column load was significant to the increase of joint strength; thus it can be concluded that the principal tensile stress of BCJ-SS-S4 at joint first crack was enhanced linearly $7 \times 10^{-5}P + 0.2816$, while the corresponding enhancement in the event of maximum joint shear stress was $8 \times 10^{-5}P + 0.5067$.

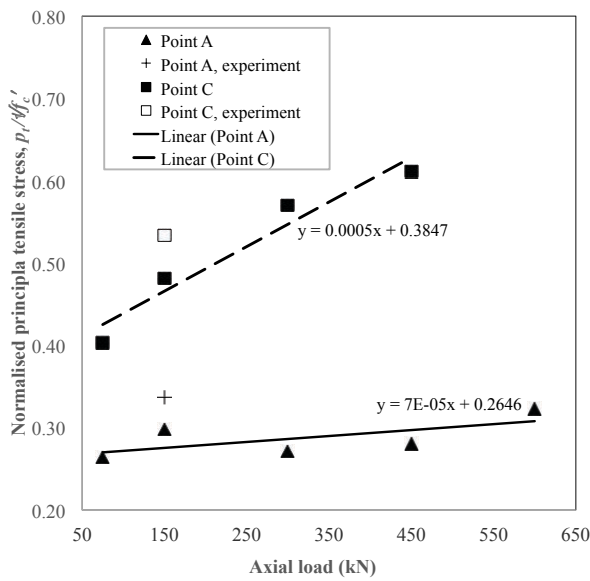
Figure 5.27.(c) shows that the normalized principal tensile stress (p_t/f_c) at joint first crack and the normalized principal tensile stress at maximum joint shear stress of BCJ-SS-F4 were $0.337 f_c$ and $0.534 f_c$ respectively, while the corresponding values in the FE analysis were $0.298 f_c$ and $0.482 f_c$ respectively. The effect of increasing the axial column load was significant to the increase of the joint strength; thus, it can be concluded that the principal tensile stress of BCJ-SS-F4 at joint first crack was enhanced linearly $7 \times 10^{-5}P + 0.2646$, while the corresponding enhancement in the event of maximum joint shear stress was $0.0005 P + 0.3847$.



(a) BCJ-CS-A Test #2



(b) BCJ-SS-S4



(c) BCJ-SS-F4

Figure 5.27. Effect of axial load on the normalized joint principal tensile stress at Points A and C

One main finding of this parametric study is that joint strength (represented by the maximum normalized principal tensile stress, point C) changes with the variation of column axial load.

For example, for BCJ-CS-A Test #2 with an axial load of 150 kN ($0.07f_c'A_g$), the maximum

principal tensile stress was $0.54\sqrt{f_c}$ and for column axial load of 300 kN ($0.07f_cA_g$), the maximum principal tensile stress was $0.61\sqrt{f_c}$. This is an increase of 13% for the same specimen with a higher axial column load. Experimental work conducted by Pantelides et al. (2002) reported that there was an increase of 15% joint shear strength for the specimen with the higher axial column load ($0.25f_cA_g$ compared to that of $0.1f_cA_g$).

5.6.3. Effect of embedded bar sizes

The effects of embedded bars on joint shear strength of strengthened specimens are presented in Figures 5.28.(a) and 5.28.(b). Overall, the normalized principal tensile stresses at first joint crack and at maximum joint shear for both strengthened specimens were enhanced with the increase of embedded bar sizes.

Figure 5.28.(a) shows that normalized principal tensile stress ($p_t/\sqrt{f_c}$) at joint first crack and normalized principal tensile stress at maximum joint shear stress of BCJ-SS-S4 were $0.3\sqrt{f_c}$ and $0.565\sqrt{f_c}$ respectively, while the corresponding values in the FE analysis were $0.283\sqrt{f_c}$ and $0.568\sqrt{f_c}$ respectively. Even though the enhancement was not too significant, it can still be concluded that the principal tensile stress of BCJ-SS-S4 at joint first crack increased linearly by $0.0006D+0.2774$, while the corresponding enhancement in the event of maximum joint shear stress was $0.0008D+0.562$, where D is the diameter of the embedded bar.

Figure 5.28.(b) shows normalized principal tensile stress ($p_t/\sqrt{f_c}$) at joint first crack and normalized principal tensile stress at maximum joint shear stress of BCJ-SS-F4 were $0.337\sqrt{f_c}$ and $0.534\sqrt{f_c}$ respectively, while the corresponding values in the FE analysis were $0.330\sqrt{f_c}$ and $0.548\sqrt{f_c}$ respectively. The effect of increasing embedded bar size was not too significant to the increase of joint strength, but it can be concluded that the principal tensile

stress of BCJ-SS-F4 at joint first crack was enhanced linearly by $0.00009D+0.3298$, while the corresponding enhancement in the event of maximum joint shear stress was $0.0009D+0.5421$.

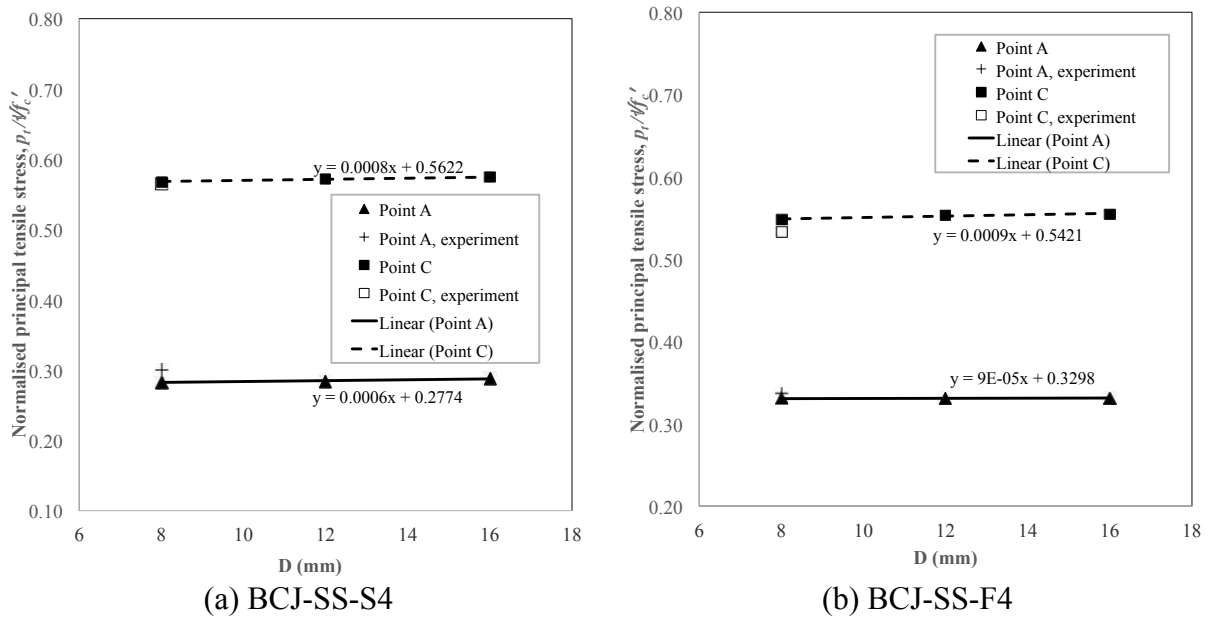


Figure 5.28. Effect of embedded bar sizes on the normalized joint principal tensile stress at Points A and C

The finding of this parametric study is that the principal tensile stress at first crack (Point A) and at maximum joint strength (Point C) does not change significantly with the variation of embedded bar size for the two strengthened specimens, BCJ-SS-S4 and BCJ-SS-F4. For example, for BCJ-SS-S4 with an embedded bar size of 8 mm, the maximum principal tensile stress was $0.568f_c'$, while with an embedded bar size of 12 mm, the maximum principal tensile stress was $0.571f_c'$. There is only an increase of 1% for the same specimen with a larger area of steel embedded bar.

5.7. SUMMARY

Three-dimensional numerical models were developed using FE software ABAQUS to study the behaviour of unstrengthened and strengthened exterior RC beam-column joints subjected to earthquake-type loading. The concrete damage plasticity (CDP) model was implemented and the default values of parameters from ABAQUS were used, as variation of these parameters did not affect the analysis of the specimens that were subjected to in-plane load only. Based on the FE results, the following conclusion can be drawn:

- 1) The stress-strain curve for concrete in uniaxial compression was defined in three different regions: elastic, hardening and softening. For concrete in tension, the stress-strain curve was also idealized in a similar manner to the compressive stress-strain curve. In this case, the stress-strain curve for concrete under tension was defined in the elastic and softening region. The corresponding equations used to develop stress-strain curve of concrete under compression and tension for each regions were discussed and employed in the FE analysis.
- 2) The von Mises yield criterion was employed to describe the material response of reinforcing steel. The reinforcement properties (yield stress, ultimate stress and modulus of elasticity) were defined from tensile testing stress-strain data. A trilinear elastic-plastic-linear hardening curve was defined as an input in ABAQUS.
- 3) The 8-node linear brick element with reduced integration (C3D8R) was chosen to model the concrete element and steel loading plates. These first order brick elements have three translational degrees of freedom at each node and allow for trilinear stress variations. Steel reinforcement and the embedded bars (steel and CFRP) were modelled as a one-dimensional truss element, T3D2. The two-node T3D2 element employs linear interpolation for position and displacement calculations.

- 4) Tie constraints were employed to connect the degrees of freedom of the upper and lower loading plates to the corresponding degrees of freedom of the upper and lower column sections respectively. In addition, the EMBEDDED REGION constraint was employed to tie the degrees of freedom of the truss elements simulating the embedded reinforcing bars to the degrees of freedom of the brick elements of the surrounding concrete.
- 5) Mesh convergence studies were conducted to examine a suitable mesh size and the appropriate material parameters that lead to a close agreement with the experimentally observed response. Three element sizes, 100 mm, 50 mm and 30 mm, were initially adopted as a uniform mesh size. The results showed that the element size significantly affects the hysteresis curve behaviour. In this study, FE analysis results for 30 mm element size gave a better prediction. The similarity of the hysteresis curve in the FE analysis using the 30 mm element size, compared to that gained by experiment, suggested a reasonably good agreement between the experimental observation and the prediction result from the FE analysis.
- 6) The FE models developed using ABAQUS were able to predict the failure mode, the overall response throughout the entire loading history and the dissipated energy successfully as they closely matched the respective experimental results.
- 7) The FE models showed a good prediction of load-displacement envelope curves but did not predict well the stiffness degradation under cyclic loading. Further investigation on this issue is needed.
- 8) The effect of three key parameters on the structural response of unstrengthened and strengthened joints is investigated. The key parameters considered include concrete compressive strength, column axial load and embedded bar size, and their effect on joint shear strength was also considered

-
- 9) Concrete compressive strength is the common influence parameter for joint shear stress at the yielding of the beam reinforcement (Point B) and at maximum joint shear stress (Point C). It was reported that joint shear stresses were proportional to the square root of the concrete compressive strength at Point B and C. In this parametric study, joint strength (represented by the maximum normalized principal tensile stress, Point C) changes with the variation of concrete compressive strength.
- 10) Parametric study also showed that joint strength (represented by the maximum normalized principal tensile stress, point C) changes with the variation of column axial load. There was an increase of 13% for specimen BCJ-CS-A Test #2 with higher axial column load.
- 11) The principal tensile stress at first crack (Point A) and at maximum joint strength (Point C) does not change significantly with the variation of embedded bar size for the two strengthened specimens, BCJ-SS-S4 and BCJ-SS-F4. For example, for BCJ-SS-S4 with an embedded bar size of 8 mm, the maximum principal tensile stress was $0.568 \sqrt{f_c}$ and for embedded bar size of 12 mm, the maximum principal tensile stress was $0.571 \sqrt{f_c}$. Thus, in the case of BCJ-SS-S4, there was only an increase of 1% by using a larger area of steel embedded bar.

CHAPTER 6

SHEAR CAPACITY EVALUATION OF BEAM-COLUMN JOINTS STRENGTHENED WITH EMBEDDED BARS

6.1. GENERAL

In this chapter, analytical models for the shear capacity evaluation of unstrengthened and strengthened beam-column joints with embedded bars are developed. The analytical models present equations of stresses and strains for several stages of response (before and after the yielding of the beam and column's reinforcement) until the ultimate capacity is obtained; this is defined by the crushing of the concrete or the failure of the embedded bars due to debonding. The accuracy of the analytical models is validated with: a) experimental results of the shear deficient RC beam-column joints available in the literature and the unstrengthened joint tested in this study and b) the joints strengthened with embedded bars tested in this study.

6.2. MECHANICS OF REINFORCED CONCRETE JOINTS STRENGTHENED WITH EMBEDDED FRP BARS

A beam-column joint is idealised as a plane frame element with dimensions h_c (width of column), w_b (width of beam) and h_b (height of beam). The idealisation of a typical exterior beam-column joint is presented in Figure 6.1 and the associated average stresses in the joint are shown in Figure 6.2. Shear stresses are introduced by direct member action and by the bond that develops between the reinforcement within the joint area (beam reinforcement, column reinforcement and the embedded steel or CFRP bars) and the joint core concrete. For

clarity, the shear stress, v , is assumed to be uniformly distributed over the boundaries of the joint. It is also assumed that in a practical situation, where the beam-column joints are being retrofitted with embedded bars, a set of initial normal strain in the transverse direction (ε_{0t}) and initial shear strain (γ_0) has developed because the structure has been loaded by its self-weight and this causes a small deformation in the steel bars (Antonopoulos and Triantafillou, 2002).

The principal strains, ε_1 and ε_2 , are linked to the principal strains in the longitudinal and transverse directions, ε_l and ε_t , through the Equations (6-1) to (6-4):

$$\tan^2 \theta = \frac{\varepsilon_1 - \varepsilon_t}{\varepsilon_1 - \varepsilon_l} = \frac{\varepsilon_2 - \varepsilon_l}{\varepsilon_2 - \varepsilon_t} \quad (6-1)$$

where,

θ is the inclination (from the t -axis) of the maximum principal strain ε_1 .

By assuming that: (1) the maximum principal stress in the concrete (σ_l) cannot exceed its tensile capacity, which is simply taken to be zero; and (2) the direction of principal strains and stresses coincide (when the reinforcement has not yielded), the following can be written:

$$\sigma_t = -v \tan \theta \quad (6-2)$$

$$\sigma_l = \frac{-v}{\tan \theta} \quad (6-3)$$

where,

σ_t and σ_l are the average compressive stress in the concrete in the transverse (t) and longitudinal (l) directions, respectively.

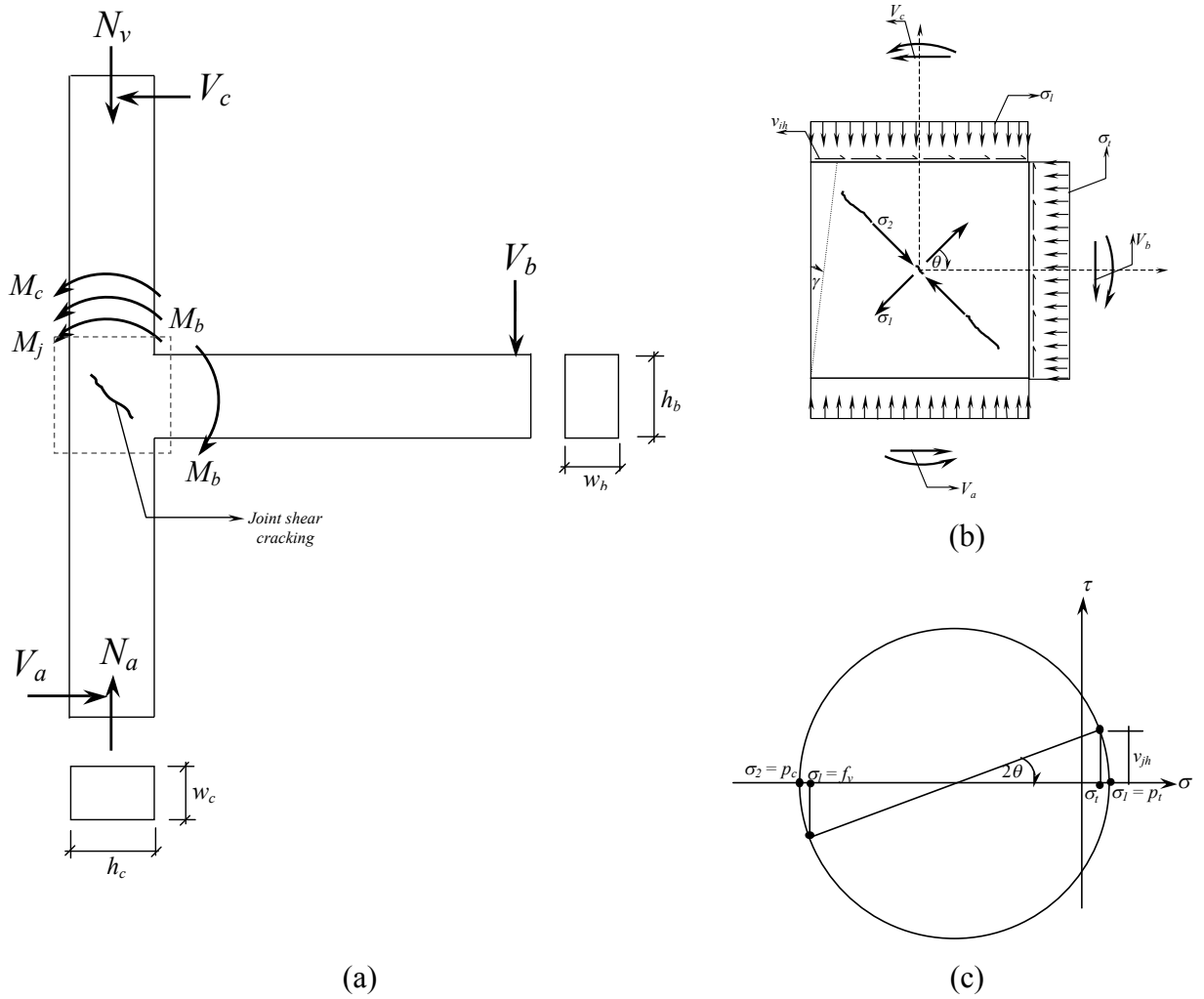


Figure 6.1. Idealisation of external beam-column joint, modified after Akguzel (2011): (a) Moments and shear forces acting on the boundaries of the plane frame element; (b) Kinematics and compatibility condition in joint region; (c) Mohr's circle for average stresses

Finally, with $\sigma_t = 0$, the stress invariant condition states give minimum principal stress in the concrete:

$$\sigma_2 = \sigma_t + \sigma_l \quad (6-4)$$

where,

σ_2 is the minimum principal stress of the concrete.

Equations (6-1) to (6-4) were derived and employed in the work of Pantazopoulou and Bonacci (1992).

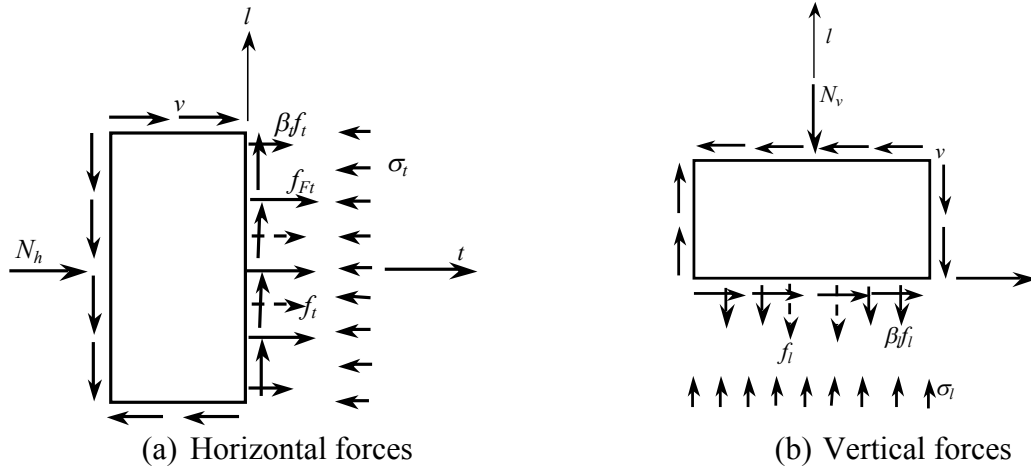


Figure 6.2. Joint stress equilibrium on joint with embedded bars, modified after Antonopoulos and Triantafillou (2002)

6.2.1. Equilibrium Considerations

The main point assumed in this section is that the strengthening of the joint is carried out through the use of a deep embedment method, where the steel or CFRP bars are inserted into the joint core in the horizontal direction only. Horizontal force equilibrium requires that the average concrete compressive stress in the transverse direction (σ_t) in Figure 6.2.(a), should meet the expression in Equation (6-5):

$$\sigma_t = -(\rho_s + \beta_t \rho_b) f_t - \rho_{Ft} f_{Ft} - \frac{N_h}{w_b h_b} \quad (6-5)$$

where,

- f_t = Average stress in the horizontal stirrups (at mid-width of the joint)
- ρ_s = Stirrup reinforcement ratio
- ρ_b = Total main beam reinforcement ratio

- β_t = Factor to account for the bond conditions along the main beam reinforcement
 f_{Ft} = Average normal stress in the embedded bars (steel or CFRP) at mid-width of the joint
 ρ_{Ft} = Steel or CFRP embedded reinforcement ratio in the transverse direction
 N_h = Compressive axial force of the beam (if any), usually $N_h = 0$
 w_b = Width of the beam
 h_b = Height of the beam

In a similar manner, vertical force equilibrium requires that the average concrete compressive stress in the longitudinal direction (σ_l) in Figure 6.2.(b), is given by:

$$\sigma_l = -(\rho_{c,in} + \beta_l \rho_c) f_l - \frac{N_v}{h_c w_c} \quad (6-6)$$

where

- f_l = Average stress in the longitudinal reinforcement (at mid-width of the joint)
 ρ_c = Total main column reinforcement ratio at the boundaries of the joint core
 $\rho_{c,in}$ = Total main column reinforcement ratio inside the joint core
 β_l = Factor to account for the bond conditions along the main column reinforcement at the boundaries of the joint core
 N_v = Compressive axial force at the column
 w_c = Width of the column
 h_c = Depth of the column

The bond condition between the reinforcement bar and the concrete is expressed by β . For a perfect bond condition, β is set to zero; while for negligible bond resistance β is set to 1. In an actual condition, the magnitude of the bond condition could be between these two numbers (Pantazopoulou and Bonacci, 1992).

Simplifications are made to reduce the number of variables in the problem,

$$\rho_t = \rho_s + \beta_t \rho_b \quad (6-7.a)$$

and

$$\rho_l = \rho_{c,in} + \beta_l \rho_c \quad (6-7.b)$$

where,

ρ_t and ρ_l are the effective transverse and longitudinal reinforcement ratio, respectively.

6.2.2. Analytical Evaluation of Joint Shear Capacity Strengthened with Deep Embedment Method

The development of the formulations to determine the joint shear capacity of the strengthened beam-column joint based on the analytical model is explained in this section. The analytical model in this study is proposed by considering the basic formulation developed by Pantazopoulou and Bonacci (1992) and Antonopoulos and Triantafillou (2002). Four steps of analysis based on the state of the stresses on the main reinforcements are considered, namely: a) before the yielding of the transverse and longitudinal reinforcement; b) after the yielding of the transverse reinforcement and before the yielding of the longitudinal reinforcement; c) after the yielding of both transverse and longitudinal reinforcements; and d) after the yielding of the longitudinal reinforcement and before the yielding of the transverse reinforcement.

a) Before the yielding of the transverse and longitudinal reinforcements

The material constitutive law in Equation (6-1) is rewritten in another form by substituting ε_2 with σ_2/E_c , where E_c is the secant modulus of concrete.

$$\tan^2 \theta = \frac{\varepsilon_2 - \varepsilon_l}{\varepsilon_2 - \varepsilon_t} \quad (6-8.a)$$

$$\tan^2 \theta = \frac{\varepsilon_2 - \varepsilon_l}{\varepsilon_2 - \varepsilon_t} = \left(\frac{\sigma_2}{E_c} - \varepsilon_l \right) \times \left(\frac{\sigma_2}{E_c} - \varepsilon_t \right)^{-1} \quad (6-8.b)$$

$$\tan^2 \theta = \left(\frac{\sigma_2 - E_c \varepsilon_l}{\sigma_2 - E_c \varepsilon_t} \right) \quad (6-8.c)$$

Substituting σ_t in Equation (6-2) and σ_l in Equation (6-3) into Equation (6-4) will yield:

$$\begin{aligned} \sigma_2 &= -\nu \tan \theta - \frac{\nu}{\tan \theta} \\ &= -\nu \left(\tan \theta + \frac{1}{\tan \theta} \right) \\ &= -\nu \left(\frac{\tan^2 \theta + 1}{\tan \theta} \right) \end{aligned} \quad (6-9)$$

The minimum principal tensile stress in concrete (σ_2), the principal strains in the longitudinal (ε_l) and transverse (ε_t) directions are written in form of average joint shear stress (ν) and $\tan \theta$ using Equations (6-2)-(6-6), with f_l , f_t and f_{Ft} defined as:

f_l is the average normal stress in the reinforcement along the longitudinal direction (at mid-width of the joint) within the elastic range ($f_l = E_s \varepsilon_l$)

f_t is the average stress in the horizontal stirrups (at mid-width of the joint) within the elastic range ($f_t = E_s \varepsilon_t$)

f_{Ft} is the average normal stress in the embedded bars along the transverse direction (at mid-width of the joint) ($f_{Ft} = E_s (\varepsilon_t - \varepsilon_{0t})$), where E_s and E_F is the elastic modulus of the steel

reinforcement and embedded bars (steel or CFRP) in the principal direction, respectively.

Next, v is replaced by $-\sigma_t/\tan\theta$, where σ_t is given by Equation (6-5). The result is:

$$v = \frac{1}{\tan\theta} (\rho_t E_s \varepsilon_t + \rho_{Ft} E_f \varepsilon_t - \rho_{Ft} E_F \varepsilon_{0t}) \quad (6-10)$$

The procedure described above will lead to a quadratic polynomial of $\tan^2\theta$:

$$(n_{sc} \rho_l \psi + K) \tan^4 \theta + e_v \tan^2 \theta - \psi (n_{sc} \rho_l + 1) = 0 \quad (6-11.a)$$

In short, Equation (6-11.a) can be rewritten in a simple form as

$$A \tan^4 \theta + B \tan^2 \theta + C = 0 \quad (6-11.b)$$

where

$$A = (n_{sc} \rho_l \psi + K), \quad B = e_v \quad \text{and} \quad C = -\psi (n_{sc} \rho_l + 1) \quad (6-11.c)$$

$$n_{sc} = \frac{E_s}{E_c}; \quad n_{Fs} = \frac{E_F}{E_s}; \quad e_v = \frac{N_v}{h_c w_c E_s}; \quad \psi = \rho_t \varepsilon_t + \rho_{Ft} n_{Fs} \varepsilon_t - \rho_{Ft} n_{Fs} \varepsilon_{0t} \quad (6-11.d)$$

$$K = \left(\frac{\rho_l E_s \varepsilon_t}{\rho_t E_s + \rho_{Ft} E_F} \rho_t + \frac{\rho_l E_s \varepsilon_t}{\rho_t E_s + \rho_{Ft} E_F} \rho_{Ft} n_{Fs} \right) \quad (6-11.e)$$

b) After the yielding of the transverse reinforcement and before the yielding of the longitudinal reinforcement

The analysis is conducted in a similar manner to step a), but in this case f_t is replaced with f_{yt} because the transverse reinforcement is assumed to have its yield strength. The shear stress v

is defined with Equation (6-10); and by replacing $E_s \varepsilon_t$ with f_{yt} , the polynomial of $\tan\theta$ can be written as:

$$\left(H + \frac{1}{n_{sc}} \varepsilon_t \right) \tan^4 \theta + \frac{1}{n_{sc} \rho_l} e_v \tan^2 \theta - H \left(\frac{1}{n_{sc} \rho_l} - 1 \right) = 0 \quad (6-12)$$

where

$$H = \rho_t \frac{f_{yt}}{E_s} + \rho_{Ft} n_{Fs} \varepsilon_t - \rho_{Ft} n_{Fs} \varepsilon_{0t} \quad (6-13)$$

c) Analysis after the yielding of the longitudinal and transverse reinforcements

The analysis is conducted in a similar manner to step a), by considering that both the longitudinal and transverse reinforcements have yielded, where f_t and f_l is replaced with f_{yt} and f_{yl} , respectively. The shear stress v is defined with Equation (6-10); and by replacing $E_s \varepsilon_t$ with f_{yt} and $E_s \varepsilon_l$ with f_{yl} , the polynomial of $\tan\theta$ can be written as

$$\left(H + \frac{1}{n_{sc}} \varepsilon_t \right) \tan^4 \theta - \frac{1}{n_{sc}} \frac{f_{yl}}{E_s} \tan^2 \theta - (H) = 0 \quad (6-14)$$

where H is the expression as written in Equation (6-13).

d) Analysis after the yielding of the longitudinal reinforcement and before the yielding of the transverse reinforcement

The analysis is conducted in a similar manner to step a), where f_l is replaced with f_{yl} . The shear stress v is defined with Equation (6-10); and by replacing $E_s \varepsilon_l$ with f_{yl} , the polynomial of $\tan\theta$ can be written as:

$$\left(T + \frac{1}{\rho_t E_s + \rho_{Ft} E_F} E_c \rho_t \varepsilon_t + \frac{1}{\rho_t E_s + \rho_{Ft} E_F} E_c \rho_{Ft} n_{Fs} \varepsilon_t \right) \tan^4 \theta - \frac{1}{n_{sc}} \left(\frac{f_{yl}}{E_s} \right) \tan^2 \theta - (T) = 0$$

(6-15)

where

$$T = \rho_t \varepsilon_t + \rho_{Ft} n_{Fs} \varepsilon_t - \rho_{Ft} n_{Fs} \varepsilon_{0t} \quad (6-16)$$

The derivation of the above equations in detail is given in Appendix A.3.

6.3. NUMERICAL SOLUTION AND VALIDATION

An analytical formulation to determine the shear capacity of the exterior RC beam-column joint strengthened with embedded bars has been proposed in the previous section. To begin the calculation, a series of inputs were given to trace the state of stresses and strains in the joint until failure. The inputs can be classified into: (a) the geometric variables (beam and column cross section, effective width and depth of the joint, horizontal and vertical reinforcement ratio, as well as existing and embedded joint reinforcement ratio); (b) variables of bond condition on the horizontal (β_l) and vertical direction (β_t); (c) the material properties (the concrete strength, yield strength of the beam, column and joint reinforcement) and (d) the normalized axial forces acting on the column.

The procedure is initiated by incrementing the transverse strain, ε_t . For each value of ε_t , Equation (6-11.b) is solved for $\tan\theta$ so that the shear stress in the joint area can be calculated by using Equation (6-10). At each step of the calculation, the stress on both transverse (beam and joint) and longitudinal (column) reinforcement is checked against their yield strength. When the first yield of the steel reinforcement occurs, the procedure should continue with step b), c), or d). The value of $\tan\theta$ is obtained by solving the equations corresponding to the active step on each iteration. Next, the normal stress in the embedded bars, along the

transverse direction at the mid-height of the joint, can be evaluated. At the end of each step of the iteration, the stress was checked against two conditions: a) concrete compressive crushing and b) failure of the embedded bars, (i.e. bond strength on the embedded bars at maximum slip).

Concrete compressive crushing occurs when the principal compressive stress, σ_2 , reaches the concrete strength, f_c^{max} as defined in Equation (6-17.a) (Pantazopoulou and Bonacci, 1992).

$$\sigma_2 = f_c^{max} \left\{ 2 \frac{\varepsilon_2}{\varepsilon_{max}} - \left(\frac{\varepsilon_2}{\varepsilon_{max}} \right)^2 \right\} \quad (6-17.a)$$

$$\left\{ \begin{array}{l} f_c^{max} = \lambda f_c \\ \varepsilon_{max} = \lambda \varepsilon_0 \\ \lambda = \frac{1 + \rho_{sv} |f_{ys}/f_c|}{0.8 - 0.34(\varepsilon_1/\varepsilon_0)} \end{array} \right. \quad (6-17.b)$$

On the other hand, the failure of the embedded bars is governed by the state of the stress when the maximum bond strength between the concrete and the embedded bars is exceeded. In the absence of average bond strength model, the average bond strength for DE CFRP bars is limited to a lower limit of 8.4 MPa (Mofidi et al., 2012); whilst the average bond strength for DE steel bars is taken as 20 MPa (Valerio et al. 2009).

In order to validate the proposed analytical model, the procedure to calculate the joint shear strength of exterior RC beam-column joints is presented. In this example, specimen S6 from

a series of beam-columns joint tested by Tsonos et al. (1992) was analyzed. The properties of the S6 specimen are:

Beam section: $w_b = 200 \text{ mm}$, $h_b = 300 \text{ mm}$

Column section: $h_c = 200 \text{ mm}$, $w_c = 200 \text{ mm}$

Joint section: $h_j = 200 \text{ mm}$, $w_j = 200 \text{ mm}$

Column axial load $N_v = 171800 \text{ N}$

Concrete compressive strength, $f_c = 28.98 \text{ MPa}$,

Concrete modulus of elasticity, $E_c = 4700 \times \sqrt{28.98}$
 $= 25301.5 \text{ MPa}$

The yield strength of the column, beam and joint reinforcements are:

$f_{yt} = 485 \text{ MPa}$, $f_{yl} = 465 \text{ MPa}$, $f_{ys} = 495 \text{ MPa}$

Modulus of elasticity of the steel reinforcement, $E_s = 200000 \text{ MPa}$,

Modulus of elasticity of the embedded bar, $E_F = 0 \text{ MPa}$ (no CFRP and steel embedded bars applied on this specimen)

Elastic modular ratio, $n_{sc} = 7.9$, $n_{Fs} = 0$ (See Equation (6.11.d))

$\varepsilon_0 = 0.002$

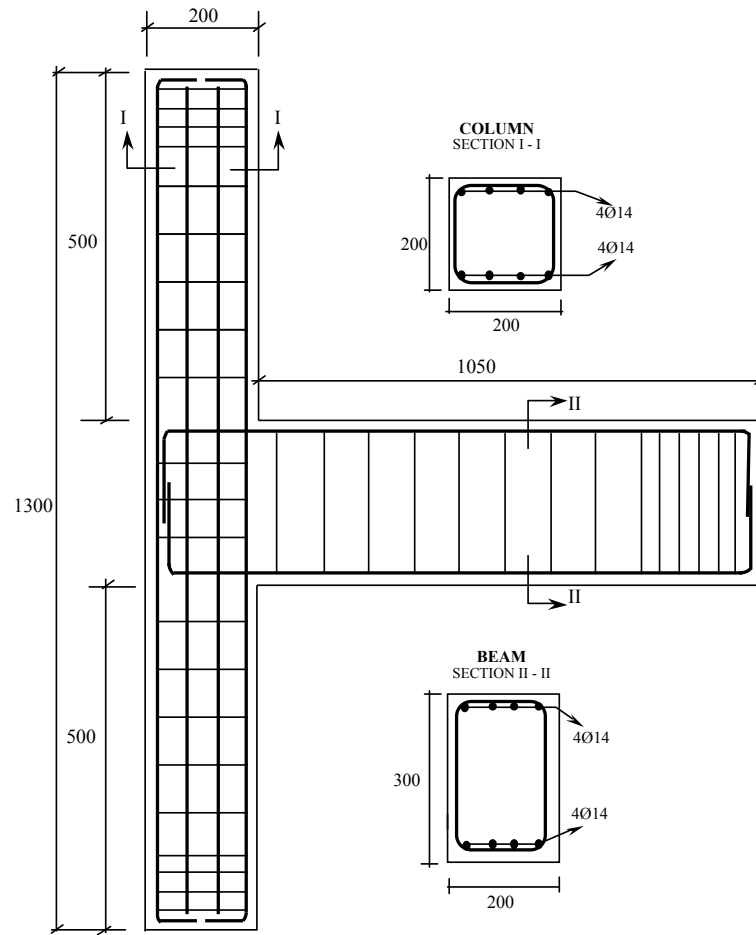


Figure 6.3. Reinforcement detail for beam-column joint specimen, Tsonos et al. (1992)

- Compute existing joint reinforcement ratio, e_v

$$e_v = 0.0000215$$

- Compute existing joint reinforcement ratio, ρ_s

$$\rho_s = 302/(200 \times 200)$$

$$= 0.0075$$

- Compute beam reinforcement ratio, ρ_b

$$\rho_b = 1232/(200 \times 300)$$

$$= 0.0205$$

- Compute column reinforcement ratio inside the joint core, $\rho_{c,in}$

$$\begin{aligned}\rho_{c,in} &= 616/(200 \times 200) \\ &= 0.0154\end{aligned}$$

- Column reinforcement ratio outside the joint core, ρ_c

$$\begin{aligned}\rho_c &= 616/(200 \times 200) \\ &= 0.0154\end{aligned}$$

- Compute the effective transverse and longitudinal reinforcement ratios by referring to Equation (6-7.a) and (6-7.b)

$$\begin{aligned}\rho_t &= 0.0240 \text{ and } \rho_l = 0.0277 \\ \rho_{sv} &= 0.0075, \rho_{Ft} = 0\end{aligned}$$

The following procedure is summarised in section 6.3; initially, assume there is no yielding on the beam, column and joint reinforcement.

Step 1 – choose $\varepsilon_t = 0.00085$ (note that any $\varepsilon_t \leq \varepsilon_{yt}$ can be chosen for consideration)

Step 2 – solve ψ using Equation (6-11.d) and K using Equation (6-11.e)

$$\begin{aligned}\psi &= \rho_t \varepsilon_t + \rho_{Ft} n_{Fs} \varepsilon_t - \rho_{Ft} n_{Fs} \varepsilon_{0t} \\ &= (0.024 \times 0.00085) + 0 - 0 \\ &= 0.0000204\end{aligned}$$

$$\begin{aligned}K &= \frac{\rho_l E_s \varepsilon_t}{\rho_t E_s + \rho_{Ft} E_F} \rho_t + \frac{\rho_l E_s \varepsilon_t}{\rho_t E_s + \rho_{Ft} E_F} \rho_{Ft} n_{Fs} \\ &= \left(\frac{0.0277 \times 200000 \times 0.00085}{(0.0240 \times 200000) + 0} \right) 0.0240 + 0\end{aligned}$$

$$= 0.0000236$$

Step 3 – solve angle to principal plane, θ , using Equation (6-11.a)

$$\begin{aligned} & (n_{sc}\rho_l\psi + K)\tan^4\theta + e_v\tan^2\theta - \psi(n_{sc}\rho_l + 1) = 0 \\ & ((7.9 \times 0.0277 \times 0.0000204) + 0.0000236)\tan^4\theta \\ & + 0.0000215\tan^2\theta - 0.0000204 \times ((7.9 \times 0.0277) + 1) = 0 \\ & 0.0000281\tan^4\theta + 0.0000215\tan^2\theta - 0.0000249 = 0 \\ & \tan\theta = 0.7957 ; \theta = 38.51^\circ \end{aligned}$$

Step 4 – solve joint shear stress, v , using Equation (6-10)

$$\begin{aligned} v &= \frac{1}{\tan\theta} (\rho_t E_s \varepsilon_t + \rho_{Ft} E_F \varepsilon_t - \rho_{Ft} E_F \varepsilon_{0t}) \\ &= \frac{1}{0.7957} ((0.0240 \times 200000 \times 0.00085) + 0 - 0) \\ &= 5.12 \text{ MPa.} \end{aligned}$$

Step 5 – solve the minimum concrete principal stress, σ_2 , using Equation (6-9)

$$\begin{aligned} \sigma_2 &= -v \left(\frac{\tan^2\theta + 1}{\tan\theta} \right) \\ &= -5.12 \times \left(\frac{0.7957^2 + 1}{0.7957} \right) \\ &= -10.51 \text{ MPa} \end{aligned}$$

This value is checked against the allowed minimum principal stress in the concrete. Using Equation (6-17.a)

$$\lambda = \frac{1 + \rho_{sv} |f_{ys}/f_c|}{0.8 - 0.34(\varepsilon_1/\varepsilon_0)}$$

$$\begin{aligned}\varepsilon_l &= \frac{1}{\rho_l E_s} \left(\frac{V}{h \tan \theta} - \frac{N_v}{h_c w_c} \right) \\ &= \frac{1}{(0.0277 \times 200000)} \left(\frac{5.12}{0.7957} - \frac{171800}{200 \times 200} \right) \\ &= 0.000386\end{aligned}$$

From Equation (6-1) we will have

$$\begin{aligned}\varepsilon_1 &= \frac{\varepsilon_t - (\varepsilon_l \times \tan^2 \theta)}{1 - \tan^2 \theta} \\ &= \frac{0.00085 - (0.000386 \times 0.7957^2)}{1 - 0.7957^2} \\ &= 0.001651\end{aligned}$$

$$\begin{aligned}\varepsilon_2 &= \varepsilon_t + \varepsilon_l - \varepsilon_1 \\ &= 0.00085 + 0.000386 - 0.001651 \\ &= -0.000415\end{aligned}$$

$$\begin{aligned}\lambda &= \frac{1 + \rho_{sv} |f_{ys} / f_c|}{0.8 - 0.34 (\varepsilon_1 / \varepsilon_0)} \\ &= 0.8062\end{aligned}$$

$$\begin{aligned}f_c^{\max} &= \lambda f_c \\ &= 0.8062 \times -28.98 \\ &= -23.36 \text{ MPa}\end{aligned}$$

$$\begin{aligned}\varepsilon_{\max} &= \lambda \varepsilon_0 \\ &= 0.8062 \times -0.002 \\ &= -0.0016\end{aligned}$$

$$\begin{aligned}
\sigma_2 &= f_c^{\max} \left(2 \frac{\varepsilon_2}{\varepsilon_{\max}} - \left(\frac{\varepsilon_2}{\varepsilon_{\max}} \right)^2 \right) \\
&= -23.36 \times \left(2 \frac{-0.000415}{-0.0016} - \left(\frac{-0.000415}{-0.0016} \right)^2 \right) \\
&= (-)10.48 \text{ MPa} < (-)10.51 \text{ MPa}
\end{aligned}$$

With the current strain state ($\varepsilon_t = 0.00085$), the joint fails when there is concrete crushing, with a calculated joint shear stress of 5.12 MPa. The analytical procedure for the rest of the beam-column joint database is presented in Appendix A.4, along with the design parameters for each test.

Table 6.1 and Table 6.2 present the comparison between the joint's shear strength calculated using the formulation proposed in this study (see section 6.2.2) and the experimental results of the exterior RC beam-column joints extracted from the selected database. The joint's shear strength for the control and strengthened specimens resulting from the tests conducted in this study was also examined using the proposed formula and the results are compared in Table 6.3.

Overall, a good agreement between the analytical prediction and the experimental results was found within 38 beam-column joint tests extracted from the selected database. For example, the ratio between the joint strength of the beam-column joints predicted using the analytical models proposed in this study and the experimental results of Ehsani and Wight (1985) in Table 6.1 was 1.04 with the coefficient of variation of 2.04%. High accuracy was also observed for the rest of the beam-column joint database in Table 6.1 and Table 6.2.

Table 6.1. Comparison of analytical model predictions with the experimental results from several researchers

No.	First author	Specimen ID	f_c □ (MPa)	Joint shear strength (MPa)		Ratio (f)/(e)
				Experimental	Analytical	
(a)	(b)	(c)	(d)	(e)	(f)	(g)
1	Ehsani	1B	33.60	6.83	6.93	1.01
2		2B	34.98	6.97	7.07	1.01
3		3B	40.92	6.79	7.08	1.04
4		4B	44.64	6.93	7.32	1.06
5		6B	39.81	4.61	4.87	1.06
					Average	1.04
					CoV (%)	2.04
6	Tsonos ^a	S6	32.98	4.69	5.37	1.14
7		S6a	28.98	5.04	5.12	1.02
					Average	1.08
					CoV (%)	8.45
8	Tsonos ^b	M1	34.02	4.74	5.56	1.17
9		M2	33.53	7.21	6.77	0.94
					Average	1.06
					CoV (%)	15.67
10	Clyde	Test #2	46.20	6.80	7.09	1.04
11		Test #6	40.10	6.70	7.51	1.12
12		Test #4	41.00	7.10	7.79	1.10
13		Test #5	37.00	6.80	7.52	1.11
					Average	1.09
					CoV (%)	3.19
14	El-Amoury	TS1	30.80	5.55	5.88	1.06
15	Wong	JA-NN03	44.80	3.41	3.57	1.05
16		JA-NN15	46.00	3.59	4.09	1.14
17		JB-NN03	47.40	3.51	3.69	1.05
18		JA-NY03	34.90	3.37	3.54	1.05

19		JA-NY15	38.50	3.60	3.91	1.09
20		JB-NY03	34.20	3.63	3.90	1.07
					Average	1.07
					CoV (%)	3.28
21	Tsonos ^c	A1	35.00	4.31	4.70	1.09
22		E2	35.00	4.10	5.13	1.25
					Average	1.17
					CoV (%)	9.271

Note:

Ehsani = Ehsani and Wight (1985); Tsonos^a = Tsonos et al. (1992); Tsonos^b = Tsonos (1999); Clyde = Clyde et al. (2000); El-Amoury = El-Amoury (2004); Wong = Wong (2005); Tsonos^c = Tsonos (2007).

Table 6.2. Comparison of analytical model predictions with the experimental results from Kaku and Asakusa (1991)

No.	First author	Specimen ID	f_c (MPa)	Joint shear strength (MPa)		Ratio (f)/(e)
				Experimental	Analytical	
(a)	(b)	(c)	(d)	(e)	(f)	(g)
1	Kaku	1	31.10	5.03	5.14	1.02
2		2	41.70	4.90	5.32	1.09
3		3	41.70	4.43	4.68	1.06
4		4	44.70	4.50	4.70	1.04
5		5	36.70	4.20	4.37	1.04
6		6	40.40	4.41	4.88	1.11
					Average	1.06
					CoV (%)	2.71
7		7	32.20	4.76	5.15	1.08
8		8	41.20	4.74	4.91	1.04

9		9	40.60	4.40	4.98	1.13
10		10	44.40	4.62	5.24	1.13
11		11	41.90	4.55	5.21	1.15
12		12	35.10	4.40	4.55	1.03
13		13	46.40	4.47	4.73	1.06
					Average	1.09
					CoV (%)	4.41
14		14	41.00	4.44	4.60	1.04
15		15	39.70	4.12	4.40	1.07
					Average	1.05
					CoV (%)	2.15
16		16	37.40	4.76	5.27	1.11

Table 6.3. Comparison of analytical model predictions with experimental results from this experiment

No.	First author	Specimen ID	f_c □ (MPa)	Joint shear strength (MPa)		Ratio (f)/(e)
				Experimental	Analytical	
(a)	(b)	(c)	(d)	(e)	(f)	(g)
1	Ridwan	BCJ-CS-A Test #1	33.71	5.199	5.32	1.02
2		BCJ-CS-A Test #2	31.31	5.144	5.18	1.01
3		BCJ-CS-B	28.68	5.613	6.20	1.11
					Average	1.05
					CoV (%)	5.03
4		BCJ-SS-S4	45.52	5.427	5.59	1.03
5		BCJ-SS-S8	24.88	5.509	5.89	1.07
					Average	1.05
					CoV (%)	2.63
6		BCJ-SS-F4	31.80	6.207	6.48	1.04
7		BCJ-SS-F8	32.29	5.977	6.11	1.02
					Average	1.03
					CoV (%)	1.48

The analytical models developed in section 6.2.2. were also employed to predict the joints' shear strength of the beam-column joint tests of this study and the results are presented in Table 6.3. On average, the joints' strength ratio between the analytical and the experiment results of the unstrengthened joints and the adequately designed joint was 1.11 with the coefficient of variation of 1.05. The analytical prediction of the beam-column joints strengthened with steel (BCJ-SS-S4 and BCJ-SS-S8) and CFRP (BCJ-SS-F4 and BCJ-SS-F8) embedded bars was also in good agreement with the experimental results. The corresponding ratio between the analytical model and the experiment was 1.05 and 1.03 with the coefficient of variation of 2.63% and 1.48%, respectively.

6.4. EXAMPLE FOR A JOINT

In this section, the steps in determining the amount of embedded joint shear reinforcement are presented. The material properties of the concrete and steel reinforcement used in this example are as follows:

Concrete strength, $f_c = 30$ MPa

Beam section : $w_b = 200$ mm $h_b = 300$ mm

Column section: $h_c = 300$ mm $w_c = 200$ mm

Joint section : $h_c = 300$ mm $w_c = 200$ mm

Reinforcement :

D-16, Diameter = 16 mm; $A_s = 603.2$ mm²; $F_y = 512.3$ MPa; $E_s = 200000$ MPa

D-08 steel, Diameter = 8 mm; $A_s = 50.3$ mm²; $F_y = 580.5$ MPa; $E_s = 198672$ MPa

D-08 CFRP, Diameter = 7.5 mm; $A_s = 44.2$ mm²; $E_s = 130000$ MPa

Axial load = 150 kN

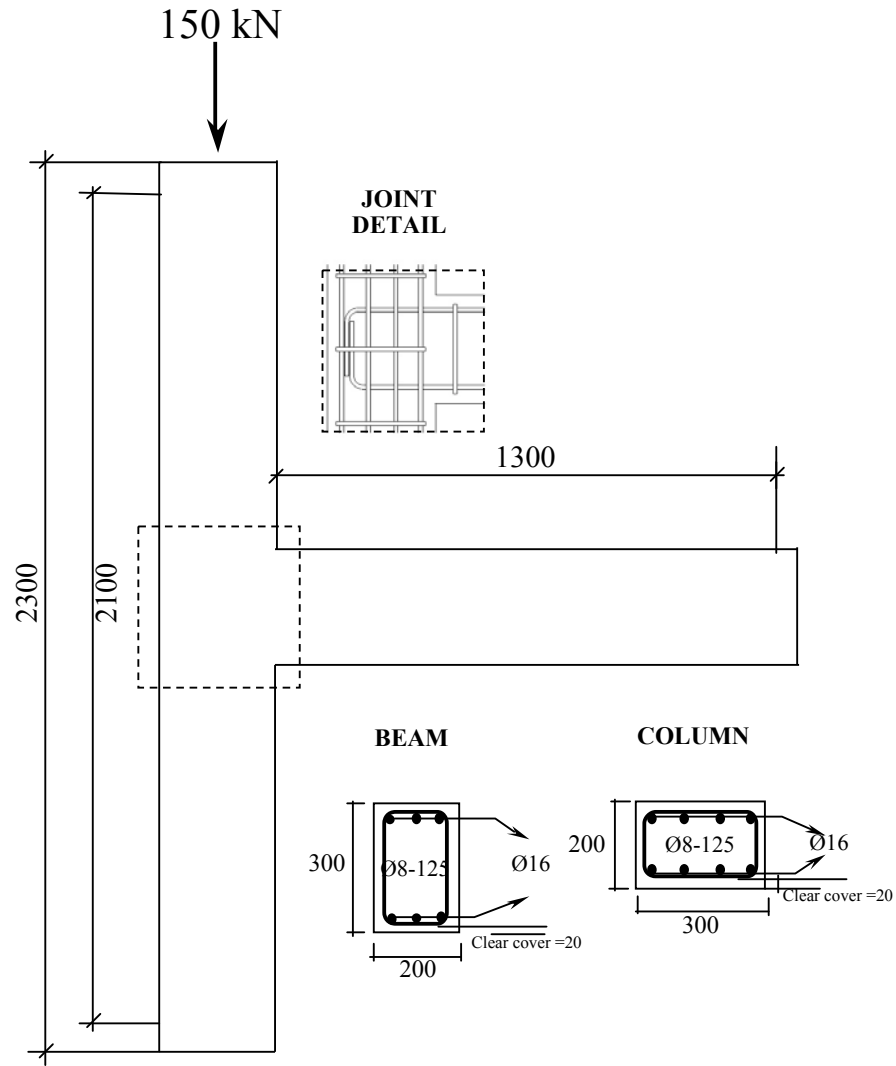


Figure 6.4. Joint dimensions and details used in the design example, unit in mm

- Calculate the shear force developed in the joint, V_u

$$V_u = T_u - V_{col}$$

where

V_u is the developed joint shear force, T_u is tensile force acting on the top steel reinforcement; and V_{col} is the shear force in the column.

$$V_{col} = \frac{\alpha M_{n,beam}}{2.1}$$

$$V_{col} = \frac{1.25 \times 72.02}{2.1}$$

$$= 42.87 \text{ kN}$$

$$T_u = A_s \times \alpha \times F_y$$

$$= 603.2 \times 1.25 \times 512.3$$

$$= 386274.2 \text{ N}$$

$$V_u = 386274.2 - 42870$$

$$= 343404.2 \text{ N}$$

- Calculate joint's shear resistance, V_j

The total shear resistance of the joint consists of the concrete's resistance V_c , the resistance of the existing joint's reinforcement V_s and the resistance provided by the embedded bars V_{EB} .

$$V_j = V_c + V_s + V_{EB}$$

The concrete shear resistance is calculated using ACI 318-14 (22.5.6.1) provision,

$$V_c = 2 \left(1 + \frac{N_u}{2000 A_g} \right) \sqrt{f'_c b_w d} \text{ in US customary units or,}$$

$$V_c = 0.17 \left(1 + \frac{N_u}{14 A_g} \right) \sqrt{f'_c b_w d} \text{ in SI units.}$$

where

N_u is column axial load; f'_c is the concrete strength; and b_w and d is column width and column depth respectively.

$$V_c = 0.17 \left(1 + \frac{150000}{14 \times 200 \times 300} \right) \sqrt{30 \times 200 \times 300}$$

$$= 269.12 \text{ N}$$

The resistance of the existing joint's reinforcement in the joint is calculated using:

$$V_s = \frac{A_s f_y d_j}{s}$$

$$V_s = \frac{100.6 \times 580.5 \times 300}{200}$$

$$= 87597.45 \text{ N}$$

The contribution of the embedded bars in resisting the joint's shear stress V_{EB} can be estimated as:

$$V_{EB} = V_j - V_c - V_s$$

$$= 343404.2 - 269.12 - 87597.45$$

$$= 255537.63 \text{ N}$$

Using the conventional truss model, the area of the embedded bars required to resist the shear force of V_{EB} is:

$$A_{EB} = \frac{V_{EB}}{\epsilon_{EB} E_{EB}}$$

a) For the case of steel reinforcement used as embedded bars;

$$A_{EB} = \frac{255537.63}{580.5}$$

$$= 440.20 \text{ mm}^2$$

b) For the case of CFRP used as embedded bars;

To control the shear crack width, ACI 440 (2006) section 9.2 suggested that the stress level of FRP shear reinforcement should be limited by $f_{fv} = 0.004E_f \leq f_{fb}$. Even though El-Amoury (2004) found that the effective FRP strain would vary from 1/4 to 1/3 of the ultimate FRP strain, in this example, the effective FRP strain is limited at a value of 0.004.

$$\begin{aligned} A_{EB} &= \frac{255537.63}{0.004 \times 130000} \\ &= 491.4 \text{ mm}^2 \end{aligned}$$

6.5. SUMMARY

In this chapter, analytical models to evaluate the joints' shear capacity of the unstrengthened and strengthened beam-column joints with embedded bars are developed. The equations to determine the stresses and strains for several stages of response (i.e. before and after the yielding of the steel reinforcement until the joint's ultimate capacity is reached) are also provided. Based on the results, the following conclusions can be drawn:

- 1) The analytical model in this study is proposed by considering the basic formulation developed by Pantazopoulou and Bonacci (1992) and Antonopoulos and Triantafillou (2002).
- 2) Four steps of analysis based on the state of the stresses on the main reinforcements are considered, namely: a) before the yielding of the transverse and longitudinal reinforcements; b) after the yielding of the transverse reinforcement and before the yielding of the longitudinal reinforcement; c) after the yielding of both transverse and longitudinal reinforcements; and d) after the yielding of the longitudinal reinforcement and before the yielding of the transverse reinforcement.
- 3) A good agreement between the analytical prediction and the experimental results was found within 38 beam-column joint tests extracted from the selected database.
- 4) The ratio between the joints' strength of the beam-column joints predicted using the analytical models proposed in this study and the experimental results of Ehsani and Wight

(1985) was 1.04 with the coefficient of variation of 2.04%. High accuracy was also observed for the rest of the beam-column joint database.

- 5) On average, the joints' strength ratio between the analytical and the experiment results of the unstrengthened joints and the adequately designed joint was 1.11 with the coefficient of variation of 1.05%. The analytical prediction of the beam-column joints strengthened with steel (BCJ-SS-S4 and BCJ-SS-S8) and CFRP (BCJ-SS-F4 and BCJ-SS-F8) embedded bars was also in good agreement with the experimental results. The corresponding ratio between the analytical model and the experiment was 1.05 and 1.03, respectively.

CHAPTER 7

CONCLUSIONS AND RECOMMENDATIONS

7.1. GENERAL

This research aimed to provide a fundamental understanding of the seismic response of shear critical exterior RC beam-column joints strengthened using the deep embedment (DE) method. One of the main objectives of this research was to propose the DE strengthening technique for the shear deficient exterior RC beam-column joints. In order to meet the aim and objectives, two approaches were conducted: experimental and finite element investigations.

The experimental study contained the fabrication and testing of seven exterior RC beam-column joints. All specimens had the same dimensions and reinforcement configurations. One of the specimens was adequately designed according to the ACI 352R-02 code; whilst the rest were designed in accordance with the pre-1970 code provisions to represent joint shear strength deficiency. Two types of load were applied during the test. The first load was a constant axial load, acting on the upper part of the column and the second load was a reversal quasi-static load applied at the beam end. Variables considered during this experimental study were: the type of material used for the embedded joint reinforcement (steel and CFRP bar); and the ratio of the embedded joint reinforcement bar.

The finite element study included the construction of a finite element model for beam-column joints using ABAQUS software to simulate the behaviour of the tested specimens. The results

from this model were validated against the results from the experimental study. Then the validated models were used to conduct a parametric study to assess the effect of the column axial load level, concrete compressive strength and embedded bar size on the joints' shear strength.

The results of this research have provided understanding of the behaviour of shear deficient exterior RC beam-column joints, subjected to reversal cyclic loading and the behaviour of strengthened beam-column joints using the deep embedment method. For each task, the important findings and conclusions are summarised and recommendations for future work are also suggested.

7.2. CONCLUSIONS

7.2.1. Conclusions from the Literature Review

Based on the reviewed literature on the seismic performance of deficient exterior RC beam-column joints and the review on the FRP strengthening of beam-column joints presented in Chapter 2, the following conclusions can be drawn:

1. RC beam-column joints of buildings constructed prior to the 1970s are prone to sustain shear failure in the joint under seismic excitations. This is based on findings from beam-column joint tests and post-earthquake reconnaissance reports.
2. The major drawbacks of pre-1970s' RC structures have been classified as column, beam, and frame deficiencies. In addition, the most common type of deficiency is the lack of confinement due to the absence of transverse reinforcement in the joint area.

3. A number of key parameters affect the behaviour of exterior RC beam-column joints; such as the ratio of the column axial load, the concrete compressive strength and the confinement of the joint reinforcement.
4. Numerous rehabilitation techniques have been investigated and adopted to enhance the seismic performance of exterior RC beam-column joints; such as epoxy repair, partial removal and replacement of the concrete of the damaged elements, RC and steel jacketing. Those techniques are referred to as conventional techniques and are associated with various difficulties in practical applications.
5. Recent efforts have focused on the use of FRPs for upgrading the existing beam-column joints in various ways; such as epoxy-bonded and near surface mounted rods.
6. The FRP strengthening techniques were shown to provide significant benefits and advantages over the conventional techniques, e.g. high strength-to-weight ratio, high corrosion resistance, light unit weight and high durability.
7. Experimental research into beam-column joints strengthened using externally bonded FRPs also showed that debonding of the FRPs was followed by the rupture of the fracture of FRPs at subsequent loading stages. In terms of practical applications of the FRPs, surface preparation of the concrete substrate is required and the adhesive material needs to be applied by skilled workers.
8. The DE technique was developed for the strengthening of shear deficient concrete beams by Valerio et al. (2009) and Chaallal et al. (2011). Their test results showed that the DE technique is more effective compared to the conventional EB and NSM techniques, because this technique relies on the concrete core to transfer stresses between the concrete and the FRP reinforcement. Moreover, surface preparation and protection against fire and vandalism are not required.

7.2.2. Conclusions from the Experiments

Based on the results of the experimental study conducted on seven RC beam-column joints, the following conclusions can be drawn:

- 1) The test results of the unstrengthened specimens (BCJ-CS-A Test#1 and BCJ-CS-A Test #2) confirmed the structural deficiency of the poorly detailed beam-column joints designed according to the pre 1970s' specification. The specimens experienced hybrid local damage and a failure mechanism. This mechanism was characterised by the joints' shear damage in the form of cross-diagonal cracks.
- 2) All the strengthened specimens exhibited more enhanced behaviour where damage occurred in the beam region at the early stages of loading, suggesting the outset of a beam hinge (BH) mechanism and then diagonal cracks propagated in the joint after 1.00% drift ratio.
- 3) A substantial improvement in the global performance of BCJ-SS-S4 and BCJ-SS-F4 can be seen in the joints' shear stress which for both specimens increased by 6% and 21% for the case of upward loading; while both specimens BCJ-SS-S8 and BCJ-SS-F8 had an increase of 7% and 16% in the joints' shear strength, compared to that of the duplicate control specimen (BCJ-CS-A Test #2).
- 4) The specimens BCJ-SS-F4 and BCJ-SS-F8 also had significant enhancement in the joints' shear stress with the upward loading, compared to that of the adequately designed specimen (BCJ-CS-B). The corresponding increases with the upward loading for specimens BCJ-SS-F4 and BCJ-SS-F8 were 11% and 7%, respectively.
- 5) A 39% (upward direction) and 93% (downward direction) increase in the displacement ductility of the BCJ-SS-S4 specimen was observed compared to that of BCJ-CS-A Test #2. The corresponding increases with the upward loading for specimens BCJ-SS-F4 and

BCJ-SS-F8 were 6% and 22%, respectively. While the increases with the downward loading for specimens BCJ-SS-F4, BCJ-SS-S8 and BCJ-SS-F8 were 27%, 20% and 13%, respectively.

- 6) There was no displacement ductility enhancement observed for the case of upward loading for BCJ-SS-S8. After the specimen reached its peak load at 3.00% drift ratio, the load dropped significantly at the second cycle of 4.00% drift ratio. Damage accumulation in the joint during the peak load caused significant strength degradation; and hence prevented the increase in the displacement ductility of BCJ-SS-S8.
- 7) The energy dissipation levels achieved by the strengthened specimens were generally higher than those achieved by the control specimens, especially at drift levels of 1.00% or more. For example, the energy absorbed by the strengthened specimens at 2.00% drift ratio was 4080 kN-mm (BCJ-SS-S4); 3543 kN-mm (BCJ-SS-F4); 3203 kN-mm (BCJ-SS-S8); and 3333 kN-mm (BCJ-SS-F8); representing increases of 31%, 14%, 3% and 7%, respectively, over the corresponding values for the BCJ-CS-A Test #2.
- 8) The energy dissipation levels of the strengthened specimens up to 4% drift ratio were comparable to that of the BCJ-CS-B, except for the BCJ-SS-S8 where the concrete strength was lower. For example, the energy absorbed by the strengthened specimens at 1% drift ratio were 1096 kN-mm (BCJ-SS-F4) and 1055 kN-mm (BCJ-SS-F8), while the corresponding energy for the BCJ-CS-B was 1047 kN-mm.
- 9) Both the control specimens showed limited fixed-end beam rotation; while the specimens strengthened with embedded steel bars showed enhanced fixed-end beam rotation. The beam rotation of both the control specimens was much smaller, indicating the absence of the plastic hinge at the beam-column joint. The beam rotations of the BCJ-CS-A Test #1 and BCJ-CS-A Test #2 at the maximum load were 0.0040 and 0.0066 radians,

respectively. While the beam rotations of the strengthened specimens at the maximum load were 0.012 radians (BCJ-SS-S4); 0.009 radians (BCJ-SS-F4); 0.010 radians (BCJ-SS-S8); and 0.0074 radians (BCJ-SS-F8).

- 10) The specimens BCJ-SS-S4 and BCJ-SS-S8 exhibited 40% and 30% larger plastic deformations than BCJ-SS-F4 and BCJ-SS-F8. Moreover, the maximum rotation of BCJ-SS-S4 and BCJ-SS-S8 specimens was comparable to that of specimen BCJ-CS-B, extending to around 0.03 radians at failure.
- 11) At the local level, the normalized principal tensile stress of specimen BCJ-SS-S8 increased by 22% and 24% compared to that of the BCJ-CS-A Test #2 with upward and downward loading, respectively. For BCJ-SS-S4, a diagonal joint crack started to form during downward loading, hence there was no enhancement in the normalized principal tensile stress of BCJ-SS-S4 for the case of upward loading due to the damage accumulation in the joint during downward loading; but the corresponding enhancement for the case of downward loading was 16% compared to that of the BCJ-CS-A Test #2.
- 12) A 5% (upward) and 13% (downward) increase in the normalized principal tensile stress of BCJ-SS-S8 was observed compared to that of BCJ-CS-B; while the corresponding increase of BCJ-SS-S4 for the case of downward loading was 5% compared to that of BCJ-CS-B.
- 13) The normalized principal tensile stress of BCJ-SS-F4 and BCJ-SS-F8 was enhanced by about 25% and 18% respectively compared to that of BCJ-CS-A Test #2 for the case of upward loading. Compared to BCJ-CS-B, the corresponding increases of BCJ-SS-F4 and BCJ-SS-F8 were 7% and 2% respectively.

- 14) On the basis of joint shear strength, the BCJ-SS-F4 proved more effective than BCJ-SS-S4. However, the specimen strengthened with embedded CFRP bars was 6.5 less ductile than the one strengthened with embedded steel bars.
- 15) Increasing the amount of embedded bars was not significantly effective for the enhancement of the joint shear strength and ductility of the strengthened specimens.

7.2.3. Conclusions from the Finite Element Analysis

Based on the results of the finite element study conducted using ABAQUS software, the following conclusions can be drawn:

1. Mesh convergence studies were conducted to determine a suitable mesh size that would lead to a close agreement with the experimentally observed response. Three sizes of element, namely 100 mm, 50 mm and 30 mm were initially adopted as a uniform mesh size. The results showed that the element's size significantly affects the hysteresis curve behaviour. In this study, FE analysis results for the 30 mm element's size gave a better prediction. The similarity of the hysteresis curve resulted in the FE analysis using the 30 mm element's size compared to that gained from the experiment; this suggested a reasonably good agreement between the experimental observation and the prediction result from the FE analysis.
2. The FE models developed using ABAQUS were able to predict the failure mode, the overall response throughout the entire loading history and the dissipated energy successfully, as they closely matched the respective experimental result.
3. The FE models showed a good prediction of load-displacement envelope curves but did not predict well the stiffness degradation under cyclic loading.

4. The effect of three key parameters on the structural response of unstrengthened and strengthened joints was investigated. The key parameters considered were the concrete's compressive strength, the column's axial load and the embedded bar sizes; their effect on the joints' shear strength was also considered.
5. Based on the FE study, the first joint's shear crack (Point A) can be simply defined by the function of a constant k_a and the normalized concrete strength, $\sqrt{f_c} \square (k_a \sqrt{f_c})$. In this case, the normalized joint's shear stress factor, k_a at the first joint crack for BCJ-CS-A Test #2, BCJ-SS-S4 and BCJ-SS-F4 were 0.27, 0.29 and 0.31, respectively.
6. The joint's strength (represented by the maximum normalized principal tensile stress, Point C) changes with the variation of the concrete compressive strength. For the BCJ-CS-A Test #2, this value increased linearly in the form of k_c , $0.0025f_c \square 0.4584$. This finding gave a close approximation to the value of $(0.002f_c \square 0.473)$ suggested in the parametric study conducted by Genesio (2012). For the strengthened specimens BCJ-SS-S4 and BCJ-SS-F4, the normalized principal tensile stresses at Point C were defined as a function of $(0.0024f_c \square 0.4614)$ and $(0.0024f_c \square 0.462)$, respectively.
7. The joint's strength changes with the variation of the column's axial load. For example, for BCJ-CS-A Test #2 with an axial load of 150 kN ($0.07f_c A_g$), the maximum principal tensile stress was $0.54 \sqrt{f_c}$ and for the column axial load of 300 kN ($0.07f_c A_g$), the maximum principal tensile stress was $0.61 \sqrt{f_c}$. This is an increase of 13% for the same specimen with a higher axial column load.
8. The axial load had a favourable effect on both the joints' first crack and maximum joint shear stress. For example, for the case of the first crack at the joint of BCJ-CS-A Test #2, the joint's shear stress was enhanced with the increase of an axial load of

$(7 \times 10^{-5}P + 0.2538)$ (P is axial load in kN). The corresponding enhancement at the maximum joint shear stress was $0.003P + 0.4856$.

9. The principal tensile stress at the first crack (Point A) and at the maximum joint strength (Point C) only changes insignificantly with the variation of embedded bar size for the two strengthened specimens, BCJ-SS-S4 and BCJ-SS-F4. For example, for BCJ-SS-S4 with the embedded bar size of 8 mm, the maximum principal tensile stress was $0.568 \sqrt{f_c}$ and for embedded bar size of 12 mm, the maximum principal tensile stress was $0.571 \sqrt{f_c}$. There was only an increase of 1% for the case of BCJ-SS-S4 by using the larger area of steel embedded bar.

7.2.4. Conclusions from the Analytical Model

Based on an evaluation of the joint shear capacity of the unstrengthened and strengthened beam-column joints, the following conclusions can be drawn:

1. The analytical model in this study is proposed by considering the basic formulation developed by Pantazopoulou and Bonacci (1992) and Antonopoulos and Triantafillou (2002).
2. Four steps of analysis based on the state of the stresses on the main reinforcements are considered, namely: a) before the yielding of the transverse and longitudinal reinforcement; b) after the yielding of the transverse reinforcement and before the yielding of the longitudinal reinforcement; c) after the yielding of both transverse and longitudinal reinforcements; and d) after the yielding of the longitudinal reinforcement and before the yielding of the transverse reinforcement.
3. A good agreement between the analytical prediction and the experimental results was found within 38 beam-column joint tests extracted from the selected database. For example, the ratio between joints' strength of the beam-column joints predicted using

the analytical models proposed in this study and the experimental results of Ehsani and Wight (1985) was 1.04, with the coefficient of variation of 2.04%. High accuracy was also observed for the rest of the beam-column joint database.

4. On average, the joints' strength ratio between the analytical and the experiment results of the unstrengthened joints and the adequately designed joint conducted in this study was 1.11 with the coefficient of variation of 1.05%. The analytical prediction of the beam-column joints strengthened with steel (BCJ-SS-S4 and BCJ-SS-S8) and CFRP (BCJ-SS-F4 and BCJ-SS-F8) embedded bars was also in good agreement with the experimental results. The corresponding ratio between the analytical model and the experiment was 1.05 and 1.03, respectively.

7.3. RECOMMENDATIONS FOR FUTURE WORK

Based on the work conducted in this research, the following can be recommended for future work:

1. Further experimental research is necessary to investigate the performance of strengthening shear deficient exterior beam-column joints involving variables, e.g. embedded bar size and embedded bar positioned in the centre of the joint's core.
2. Further experimental research is required to develop a deep embedment method with a mechanical anchorage system at both ends of the embedded bar to prevent bond failure between the bar and concrete in the joint's core.
3. Experimental investigations are needed to study the possibility of using a self-drilling anchor system (available commercially, i.e. SupAnchor®) as embedded bars to strengthen shear deficient exterior beam-column joints.

4. This study has focused on the strengthening of exterior beam-column joints. Experimental investigations are needed to extend the possibility of the use the deep embedment method to strengthen interior reinforced concrete beam-column joints; where the presence of the edge beams and slabs make it difficult to insert the bars horizontally into the joint's core.
5. Further FE investigations are called for to predict the behaviour of current strengthened beam-column joints, by adopting bond slip models and employing the pinching of the hysteretic response.

REFERENCES

- Abaqus (2008) **ABAQUS analysis : user's manual**. Providence, Rhode Island: ABAQUS Inc.
- Abbas, A.A., Mohsin, S.M.S. and Cotsovos, D.M. (2014) Seismic response of steel fibre reinforced concrete beam-column joints. **Engineering Structures**, 59: 261-283.
- ACI 318 (2014) **Building code requirements for structural concrete (ACI 318-14) : an ACI standard : commentary on building code requirements for structural concrete (ACI 318R-14), an ACI report**.
- ACI 374 (2013) **374.2R-13 Guide for Testing Reinforced Concrete Structural Elements under Slowly Applied Simulated Seismic Loads**. Detroit, Mich.: American Concrete Institute.
- ACI 440 (2006) **Guide for the Design and Construction of Structural Concrete Reinforced with FRP Bars : ACI 440.1R-06**. Detroit: American Concrete Institute.
- Akguzel, U. (2011) **Seismic Performance of FRP Retrofitted Exterior RC Beam-Column Joints Under Varying Axial and Bidirectional Loading**. University of Canterbury.
- Alsayed, S.H., Al-Salloum, Y.A., Almusallam, T.H., et al. (2010) Seismic Response of FRP- Upgraded Exterior RC Beam-Column Joints. **Journal of Composites for Construction**, 14: (2): 195-208.
- Antonopoulos, C.P. and Triantafillou, T.C. (2002) Analysis of FRP-Strengthened RC Beam-Column Joints. **Journal of Composites for Construction**, 6: (1): 41-51.
- Antonopoulos, C.P. and Triantafillou, T.C. (2003) Experimental Investigation of FRP-Strengthened RC Beam-Column Joints. **Journal of Composites for Construction**, 7: (1): 39-49.

- Bakis, C.E., Bank, L.C., Brown, V.L., et al. (2002) Fiber-Reinforced Polymer Composites for Construction-State-of-the-Art Review. **Journal of Composites for Construction**, 6: (2): 73-87.
- Bayasi, Z. and Gebman, M. (2002) Reduction of lateral reinforcement in seismic beam-column connection via application of steel fibers. **Aci Structural Journal**, 99: (6): 772-780.
- Bažant, Z. and Oh, B.H. (1983) Crack band theory for fracture of concrete. **Matériaux et Construction**, 16: (3): 155-177.
- Béton, C.E.-I.d. (1993) **CEB-FIP Model Code 1990**. London: Thomas Telford Services, Ltd.
- Birtel, V. and Mark, P.(2006) **Proceedings of the 19th Annual International ABAQUS Users' Conference. Boston:[sn]**
- Carreira, D., J and Chu, K.-H. (1985) Stress-Strain Relationship for Plain Concrete in Compression. **Journal Proceedings**, 82: (6).
- Chaallal, O., Mofidi, A., Benmokrane, B., et al. (2011) Embedded Through-Section FRP Rod Method for Shear Strengthening of RC Beams: Performance and Comparison with Existing Techniques. **Journal of Composites for Construction**, 15: (3): 374-383.
- Clyde, C., Pantelides, C.P. and Reaveley, L.D. (2000) "Performance-Based Evaluation of Exterior Reinforced Concrete Building Joints for Seismic Excitation". Pacific Earthquake Engineering Research Center.
- Danesh, F., Esmaeeli, E. and Alam, M.F. (2008) Shear Strengthening of 3D RC Beam-Column Connection Using GFRP: FEM Study. **Asian Journal of Applied Sciences**, 1: 217-227.
- Dirar, S., Lees, J. and Morley, C. (2012) Precracked Reinforced Concrete T-Beams Repaired in Shear with Bonded Carbon Fiber-Reinforced Polymer Sheets. **Aci Structural Journal**, 109: (2): 215-223.

- Dirar, S., Lees, J.M. and Morley, C.T. (2013) Precracked Reinforced Concrete T-Beams Repaired in Shear with Prestressed Carbon Fiber-Reinforced Polymer Straps. **Aci Structural Journal**, 110: (5): 855-865.
- Dritsos, S.E. (2005) Seismic Retrofit of Buildings a Greek Perspective. **Bulletin of the New Zealand Society for Earthquake Engineering**, 38: (3): 165-181.
- Ehsani, M.R. and Wight, J.K. (1985) Exterior Reinforced Concrete Beam-to-Column Connections Subjected to Earthquake-Type Loading. **Journal of the American Concrete Institute**, 82: (4): 492-499.
- El-Amoury, T. and Ghobarah, A. (2002) Seismic Rehabilitation of Beam-Column Joint using GFRP Sheets. **Engineering Structures**, 24: (11): 1397-1407.
- El-Amoury, T.A. (2004) **Seismic rehabilitation of concrete frame beam-column joints**. McMaster University.
- Engindeniz, M., Kahn, L.F. and Zureick, A.H. (2005) Repair and Strengthening of Reinforced Concrete Beam-Column Joints: State of the Art. **Aci Structural Journal**, 102: (2): 187-197.
- Faison, H., Comartin, C.D. and Elwood, K. (2004) "Reinforced Concrete Moment Frame Building without Seismic Details". USA, Encyclopedia of Housing Construction in Seismically Active Areas of the World.
- Feenstra, P.H. (1993) **Computational aspects of biaxial stress in plain and reinforced concrete**. Delft University Press.
- GangaRao, H.V.S., Taly, N. and Vijay, P.V. (2007) **Reinforced Concrete Design with FRP Composites**. Boca Raton: CRC Press.
- Gebreyohannes, A.S. (2013) **Seismic Assessment of Pre-1936 Dual RC Wall-Riveted Steel Frame Buildings**. University of Auckland.

-
- Genesio, G. (2012) **Seismic Assessment of RC Exterior Beam-Column Joints and Retrofit with Haunches using Post-Installed Anchors**. Universität Stuttgart.
- Ghobarah, A. and El-Amoury, T. (2005) Seismic Rehabilitation of Deficient Exterior Concrete Frame Joints. **Journal of Composites for Construction**, 9: (5): 408-416.
- Ghobarah, A. and Said, A. (2002) Shear Strengthening of Beam-Column Joints. **Engineering Structures**, 24: (7): 881-888.
- Griffith, M.C., Ingham, J.M. and Weller, R. (2010) Earthquake Reconnaissance: Forensic Engineering on an Urban Scale. **Australian Journal of Structural Engineering**, 11: (1): 63-74.
- Guadagnini, M., Pilakoutas, K. and Waldron, P. (2003) Shear performance of FRP reinforced concrete beams. **Journal of Reinforced Plastics and Composites**, 22: (15): 1389-1407.
- Hakuto, S., Park, R. and Tanaka, H. (2000) Seismic Load Tests on Interior and Exterior Beam-Column Joints with Substandard Reinforcing Details. **Aci Structural Journal**, 97: (1): 11-25.
- Hassan, W.M. (2011) "Analytical and Experimental Assessment of Seismic Vulnerability of Beam-Column Joints without Transverse Reinforcement in Concrete Buildings". Berkeley, CA,.
- Hollaway, L.C. and Leeming, M.B. (1999) "Strengthening of Reinforced Concrete Structures - Using Externally-Bonded FRP Composites in Structural and Civil Engineering". Woodhead Publishing.
- Hwang, S.-J. and Lee, H.-J. (1999) Analytical Model for Predicting Shear Strengths of Exterior Reinforced Concrete Beam-Column Joints for Seismic Resistance. **Aci Structural Journal**, 96: (5): 846-857.

- Ilki, A., Bedirhanoglu, I. and Kumbasar, N. (2011) Behavior of FRP-Retrofitted Joints Built with Plain Bars and Low-Strength Concrete. **Journal of Composites for Construction**, 15: (3): 312-326.
- Kaku, T. and Asakusa, H. (1991) Ductility Estimation of Exterior Beam-Column Subassemblages in Reinforced Concrete frames. **Special Publication**, 123.
- Kam, W.S. (2014) **Cyclic behaviour of wide beam-column joints : computational simulations**. M.Phil., Hong Kong University of Science and Technology.
- Karayannis, C.G. and Sirkelis, G.M. (2008) Strengthening and Rehabilitation of RC Beam-Column Joints using Carbon-FRP Jacketing and Epoxy Resin Injection. **Earthquake Engineering & Structural Dynamics**, 37: (5): 769-790.
- Kim, J. and LaFave, J.A. (2007) Key Influence Parameters for The Joint Shear Behaviour of Reinforced Concrete (RC) Beam-Column Connections. **Engineering Structures**, 29: (10): 2523-2539.
- Kotsovos, M.D. and Pavlović, M.N. (1995) **Structural concrete: Finite-element analysis for limit-state design**. London: Thomas Telford.
- Kratzig, W.B. and Polling, R. (2004) An elasto-plastic damage model for reinforced concrete with minimum number of material parameters. **Computers & Structures**, 82: (15-16): 1201-1215.
- Lee, J.H. and Fenves, G.L. (1998) Plastic-Damage Model for Cyclic Loading of Concrete Structures. **Journal of Engineering Mechanics-Asce**, 124: (8): 892-900.
- Lubliner, J., Oliver, J., Oller, S., et al. (1989) A Plastic-Damage Model for Concrete. **International Journal of Solids and Structures**, 25: (3): 299-326.

-
- Mofidi, A. and Chaallal, O. (2011) Shear Strengthening of RC Beams with EB FRP: Influencing Factors and Conceptual Debonding Model. **Journal of Composites for Construction**, 15: (1): 62-74.
- Mofidi, A., Chaallal, O., Benmokrane, B., et al. (2012) Experimental Tests and Design Model for RC Beams Strengthened in Shear Using the Embedded Through-Section FRP Method. **Journal of Composites for Construction**, 16: (5): 540-550.
- Pampanin, S., Calvi, G. and Moratti, M. (2002) "Seismic Behavior of RC Beam-Column Joints Designed for Gravity Only". **12th European Conference on Earthquake Engineering**. London, Elsevier Science Ltd.
- Pantazopoulou, S. and Bonacci, J. (1992) Consideration of Questions about Beam-Column Joints. **Aci Structural Journal**, 89: (1): 27-36.
- Pantelides, C.P., Hansen, J., Nadauld, J., et al. (2002) **Assessment of reinforced concrete building exterior joints with substandard details**. Berkeley: Pacific Earthquake Engineering Research Center.
- Park, R. (1989) Evaluation of Ductility of Structures and Structural Assemblages from Laboratory Testing. **Bulletin of the New Zealand National Society for Earthquake Engineering**, 22: (3): 155-166.
- Park, R. and Paulay, T. (1975) **Reinforced Concrete Structures**. New York: John Wiley & Sons, Inc.
- Parvin, A., Altay, S., Yalcin, C., et al. (2010) CFRP Rehabilitation of Concrete Frame Joints with Inadequate Shear and Anchorage Details. **Journal of Composites for Construction**, 14: (1): 72-82.
- Paulay, T., Park, R. and Priestley, M.J.N. (1978) Reinforced-Concrete Beam-Column Joints under Seismic Actions. **Journal of the American Concrete Institute**, 75: (11): 585-593.

-
- Paulay, T. and Priestley, M.J.N. (1992) **Seismic Design of Reinforced Concrete and Masonry Buildings**. New York: Wiley.
- Priestley, M.J.N. (1997) Displacement-based Seismic Assessment of Reinforced Concrete Buildings. **Journal of Earthquake Engineering**, 1: (1): 157-192.
- Sezen, H. (2012) Repair and Strengthening of Reinforced Concrete Beam-Column Joints with Fiber-Reinforced Polymer Composites. **Journal of Composites for Construction**, 16: (5): 499-506.
- Sezen, H., Whittaker, A.S., Elwood, K.J., et al. (2003) Performance of Reinforced Concrete Buildings During the August 17, 1999 Kocaeli, Turkey Earthquake, and Seismic Design and Construction Practise in Turkey. **Engineering Structures**, 25: (1): 103-114.
- Thermou, G.E. and Elnashai, A.S. (2006) Seismic Retrofit Schemes for RC Structures and Local-Global Consequences. **Progress in Structural Engineering and Materials**, 8: (1): 1-15.
- Tsonos, A.G. (1999) Lateral Load Response of Strengthened Reinforced Concrete Beam-to-Column Joints. **Aci Structural Journal**, 96: (1): 46-56.
- Tsonos, A.G. (2007) Cyclic Load Behavior of Reinforced Concrete Beam-Column Subassemblages of Modern Structures. **Aci Structural Journal**, 104: (4): 468-478.
- Tsonos, A.G. (2008) Effectiveness of CFRP-Jackets and RC-Jackets in Post-Earthquake and Pre-Earthquake Retrofitting of Beam-Column Subassemblages. **Engineering Structures**, 30: (3): 777-793.
- Tsonos, A.G., Tegos, I.A. and Penelis, G.G. (1992) Seismic Resistance of Type 2 Exterior Beam-Column Joints Reinforced With Inclined Bars. **Aci Structural Journal**, 89: (1).

Valerio, P., Ibell, T.J. and Darby, A.P. (2009) Deep Embedment of FRP for Concrete Shear Strengthening. **Proceedings of the Institution of Civil Engineers-Structures and Buildings**, 162: (5): 311-321.

Wight, J.K. and MacGregor, J.G. (2009) **Reinforced Concrete: Mechanics and Design**. Pearson Prentice Hall.

Wong, H.F. (2005) **Shear Strength and Seismic Performance of Non-Seismically Designed Reinforced Concrete Beam-Column Joints**. Hong Kong University of Science and Technology.

APPENDIX 1
MATERIAL PROPERTIES:
CFRP BARS
REINFORCEMENT
CONCRETE

CFRP BARS


CFRP CARBOPREE product specification

Sireg SpA - Geotechnics & Civil Engineering

Via del Bruno, 12 - 20862 Arcore (MB) – Italy - Tel. (+39) 039 627021 - Fax (+39) 039 615996

web: www.sireg.it - e-mail: info@sireg.it

	Product	DURGLASS	GLASS PREE	CARBO PREE	ARAP REE	STEEL EN 15630
Specification	Application	Temporary	Permanent	Permanent	Permanent	Temporary/ Permanent
Minimum diameter bar	(mm)	1	1	3	5.5	
Maximum diameter bar	(mm)	40	40	14	12.5	
Flat bar		YES	YES	YES	YES	
Y Shape		YES	YES	YES	YES	
Self-drilling		YES	YES	-	-	
Hollow bar- pipes		YES	YES	-	-	
Tensile strength	(MPa)	800-1000	800- 1000	2300- 3000	1400	550
Strain- ultimate- limit	(mm)	2.0-2.5	2.0-2.5	1.4-2.2	2.3	7
E-Modulus	(GPa)	40	40	135-200	60	200
Density	(g/cm ³)	1.9	1.9	1.6	1.3	7.85
Thermal Conductivity	(W/mK)	0.3	0.3	YES	YES	60
Electrical Conductivity		-	-	YES	-	YES
Magnetic Conductivity		-	-	YES	-	YES

CARBOPREE®	Bars				
	SIREG Code	Diameter (mm)	E-Modulus (GPa)	Tensile strength (kN)	
	HS5,5	5.5	130	2300	High strength
	HS7,5	7.5	130	2300	High strength
	HS10	10	130	2300	High strength
	HS12	12	130	2300	High strength
	HS12,5	12.5	130	2300	High strength
	HM7	7	200	2750	High modulus
	HM10	10	200	2750	High modulus
	LM10	10	130	1400	High strength
	LM12,5	12.5	130	1400	High strength
	LM13,5	13.5	130	1400	High strength
	LM14	14	130	1400	High strength
	LM16	16	130	1400	High strength
	LM20	20	130	1400	High strength

CONCRETE TEST RESULTS

Control specimen, BCJ-CS-A Test #1

Cube compressive test (BS EN 12390-3:2009)

Casting date : 4/24/2014

Test : 5/22/2014

Age: 28 days

Specimen ID	A	B	C
Weight (gr)	2237.2	2219.9	2230.0
Width (mm)	100.1	100.3	99.9
Height (mm)	100.9	100.0	100.6
Thick (mm)	100.1	100.2	100.2
Density (kg/m ³)	2213.0	2209.7	2213.8
Load (kN)	358.60	353.70	389.70
f_{cu} (MPa)	35.51	35.27	38.76
$f_{c\square}$ (MPa)	27.27	27.09	29.77
$f_{c\square}$ average (MPa)	28.04		

Casting date : 4/24/2014

Test : 7/17/2014

Age: 84 days

Specimen ID	A	B	C
Weight (gr)	2259.5	2243.0	2193.0
Width (mm)	100.00	100.00	100.00
Height (mm)	101.00	100.00	100.00
Thick (mm)	100.00	100.00	100.00
Density (kg/m ³)	2237.1	2243.0	2193.0
Load (kN)	461.00	454.70	405.50
f_{cu} (MPa)	45.64	45.47	40.55
$f_{c\square}$ (MPa)	35.05	34.92	31.14
$f_{c\square}$ average (MPa)	33.71		

Cylinder split tests (BS EN 12390-6:2000)

Casting date : 4/24/2014

Test : 7/17/2014

Age: 84 days

Specimen ID	A	B	C
Diameter (mm)	100.00	100.00	100.00
Height (mm)	200.00	200.00	200.00
Load (kN)	95.60	112.90	90.70
Splitting strength (MPa)	3.04	3.59	2.89
Splitting strength, average (MPa)	3.17		

Strengthened specimen, BCJ-SS-S4

Cube compressive test (BS EN 12390-3:2009)

Casting date : 9/16/2014

Test : 10/14/2014

Age: 28 days

Specimen ID	A	B	C
Weight (gr)	2370.9	2389.5	2375.7
Width (mm)	101.00	101.00	101.00
Height (mm)	100.00	100.00	100.00
Thick (mm)	100.00	100.00	100.00
Density (kg/m ³)	2347.4	2365.8	2352.2
Load (kN)	495.50	536.00	581.00
f_{cu} (MPa)	49.06	53.07	57.52
$f_{c\Box}$ (MPa)	37.68	40.76	44.18
$f_{c\Box}$ average (MPa)	40.87		

Casting date : 9/16/2014

Test : 11/4/2014

Age: 49 days

Specimen ID	A	B	C
Weight (gr)	2361.3	2381.1	2369.4
Width (mm)	100.00	100.00	100.00
Height (mm)	101.00	102.00	102.00
Thick (mm)	100.00	101.00	101.00
Density (kg/m ³)	2337.9	2311.3	2299.9
Load (kN)	594.00	609.00	605.00
f_{cu} (MPa)	58.81	59.71	59.31
$f_{c\Box}$ (MPa)	45.17	45.85	45.55
$f_{c\Box}$ average (MPa)	45.52		

Cylinder split tests (BS EN 12390-6:2000)

Casting date : 9/16/2014

Test : 11/4/2014

Age: 49 days

Specimen ID	A	B	C
Diameter (mm)	100.00	100.00	100.00
Height (mm)	200.00	200.00	200.00
Load (kN)	122.10	106.10	115.70
Splitting strength (MPa)	3.89	3.38	3.68
Splitting strength, average (MPa)	3.65		

Strengthened specimen, BCJ-SS-F4

Cube compressive test (BS EN 12390-3:2009)

Casting date : 10/22/2014

Test : 11/20/2014

Age: 29 days

Specimen ID	A	B	C
Weight (gr)	2338.1	2455.2	2473.5
Width (mm)	100.00	102.00	102.00
Height (mm)	100.00	102.00	102.00
Thick (mm)	100.00	102.00	101.00
Density (kg/m ³)	2338.1	2313.6	2353.9
Load (kN)	412.80	405.60	408.30
f_{cu} (MPa)	41.28	38.99	39.24
$f_{c\Box}$ (MPa)	31.70	29.94	30.14
$f_{c\Box}$ average (MPa)	30.59		

Casting date : 10/22/2014

Test : 11/26/2014

Age: 35 days

Specimen ID	A	B	C
Weight (gr)	2355.9	2350.1	2315.3
Width (mm)	100.00	100.00	101.00
Height (mm)	101.00	100.00	100.00
Thick (mm)	100.00	100.00	100.00
Density (kg/m ³)	2332.6	2350.1	2292.4
Load (kN)	417.90	415.40	417.00
f_{cu} (MPa)	41.38	41.54	41.29
$f_{c\Box}$ (MPa)	31.78	31.90	31.71
$f_{c\Box}$ average (MPa)	31.80		

Cylinder split tests (BS EN 12390-6:2000)

Casting date : 10/22/2014

Test : 11/26/2014

Age: 35 days

Specimen ID	A	B	C
Diameter (mm)	100.00	100.00	100.00
Height (mm)	200.00	200.00	200.00
Load (kN)	103.30	107.70	98.70
Splitting strength (MPa)	3.29	3.43	3.14
Splitting strength, average (MPa)	3.29		

Strengthened specimen, BCJ-SS-S8

Cube compressive test (BS EN 12390-3:2009)

Casting date : 12/4/2014

Test : 2/12/2015

Age: 70 days

Specimen ID	A	B	C
Weight (gr)	2223.7	2241.2	2295.6
Width (mm)	100.00	100.00	102.00
Height (mm)	100.00	102.00	101.00
Thick (mm)	100.00	100.00	100.00
Density (kg/m ³)	2223.7	2197.3	2228.3
Load (kN)	321.40	322.90	343.80
f_{cu} (MPa)	32.14	31.66	33.37
$f_{c\perp}$ (MPa)	24.68	24.31	25.63
$f_{c\perp}$ average (MPa)	24.88		

Cylinder split tests (BS EN 12390-6:2000)

Casting date : 12/4/2014

Test : 2/12/2015

Age: 70 days

Specimen ID	A	B	C
Diameter (mm)	100.00	100.00	100.00
Height (mm)	200.00	200.00	200.00
Load (kN)	77.10	69.40	63.10
Splitting strength (MPa)	2.45	2.21	2.01
Splitting strength, average (MPa)	2.22		

Strengthened specimen, BCJ-SS-F8

Cube compressive test (BS EN 12390-3:2009)

Casting date : 3/5/2015

Test : 4/2/2015

Age: 28 days

Specimen ID	A	B	C
Weight (gr)	2355.8	2322.6	2358.5
Width (mm)	100.00	100.00	100.00
Height (mm)	100.00	100.00	100.00
Thick (mm)	101.00	101.00	100.00
Density (kg/m ³)	2332.5	2299.6	2358.5
Load (kN)	360.60	371.30	368.10
f_{cu} (MPa)	36.06	37.13	36.81
$f_{c\perp}$ (MPa)	27.69	28.52	28.27
$f_{c\perp}$ average (MPa)	28.16		

Casting date : 3/5/2015

Test : 4/16/2015

Age: 42 days

Specimen ID	A	B	C
Weight (gr)	2316.6	2359.7	2313.1
Width (mm)	100.00	100.00	100.00
Height (mm)	100.00	100.00	100.00
Thick (mm)	100.00	100.00	100.00
Density (kg/m ³)	2316.6	2359.7	2313.1
Load (kN)	418.20	431.80	411.50
f_{cu} (MPa)	41.82	43.18	41.15
$f_{c\perp}$ (MPa)	32.12	33.16	31.60
$f_{c\perp}$ average (MPa)	32.29		

Cylinder split tests (BS EN 12390-6:2000)

Casting date : 3/5/2015

Test : 4/16/2015

Age: 42 days

Specimen ID	A	B	C
Diameter (mm)	100.00	100.00	100.00
Height (mm)	200.00	200.00	200.00
Load (kN)	104.8	107.6	103.7
Splitting strength (MPa)	3.34	3.43	3.30
Splitting strength, average (MPa)	3.35		

Duplicate control specimen, BCJ-CS-A Test #2

Cube compressive test (BS EN 12390-3:2009)

Casting date : 3/26/2015

Test : 4/23/2015

Age: 28 days

Specimen ID	A	B	C
Weight (gr)	2314.9	2334.0	2344.1
Width (mm)	100.00	100.00	100.00
Height (mm)	101.00	100.00	101.00
Thick (mm)	100.00	100.00	100.00
Density (kg/m ³)	2292.0	2334.0	2320.9
Load (kN)	337.50	341.10	340.90
f_{cu} (MPa)	33.42	34.11	33.75
$f_{c\square}$ (MPa)	25.66	26.20	25.92
$f_{c\square}$ average (MPa)	25.93		

Casting date : 3/26/2015

Test : 5/14/2015

Age: 49 days

Specimen ID	A	B	C
Weight (gr)	2352.5	2327.9	2310.5
Width (mm)	100.00	100.00	100.00
Height (mm)	100.00	100.00	100.00
Thick (mm)	100.00	100.00	100.00
Density (kg/m ³)	2352.5	2327.9	2310.5
Load (kN)	410.00	406.90	406.20
f_{cu} (MPa)	41.00	40.69	40.62
$f_{c\square}$ (MPa)	31.49	31.25	31.20
$f_{c\square}$ average (MPa)	31.31		

Cylinder split tests (BS EN 12390-6:2000)

Casting date : 3/26/2015

Test : 5/14/2015

Age:

Specimen ID	A	B	C
Diameter (mm)	100.00	100.00	100.00
Height (mm)	200.00	200.00	200.00
Load (kN)	89.20	105.30	99.90
Splitting strength (MPa)	2.84	3.35	3.18
Splitting strength, average (MPa)	3.12		

Adequately designed control specimen, BCJ-CS-B

Cube compressive test (BS EN 12390-3:2009)

Casting date : 5/18/2015

Test : 6/16/2015

Age: 29 days

Specimen ID	A	B	C
Weight (gr)	2307.9	2312.2	2336.3
Width (mm)	100.00	100.00	100.00
Height (mm)	100.00	100.00	100.00
Thick (mm)	100.00	100.00	100.00
Density (kg/m ³)	2307.9	2312.2	2336.3
Load (kN)	348.80	368.50	369.90
f_{cu} (MPa)	34.88	36.85	36.99
$f_{c\Box}$ (MPa)	26.79	28.30	28.41
$f_{c\Box}$ average (MPa)	27.83		

Casting date : 5/18/2015

Test : 6/18/2015

Age: 31 days

Specimen ID	A	B	C
Weight (gr)	2329.9	2323.6	2310.9
Width (mm)	100.00	100.00	100.00
Height (mm)	100.00	100.00	100.00
Thick (mm)	100.00	100.00	100.00
Density (kg/m ³)	2329.9	2323.6	2310.9
Load (kN)	377.80	370.60	371.60
f_{cu} (MPa)	37.78	37.06	37.16
$f_{c\Box}$ (MPa)	29.02	28.46	28.54
$f_{c\Box}$ average (MPa)	28.68		

Cylinder split tests (BS EN 12390-6:2000)

Casting date : 5/18/2015

Test : 6/18/2015

Age: 31 days

Specimen ID	A	B	C
Diameter (mm)	100.00	100.00	100.00
Height (mm)	200.00	200.00	200.00
Load (kN)	78.10	83.50	81.00
Splitting strength (MPa)	2.49	2.66	2.58
Splitting strength, average (MPa)	2.57		



a)



b)

Figure A.1.1. Concrete material properties: a) Cube compressive test; b) Cylinder split test

REINFORCEMENT TENSILE TESTS

Main reinforcement properties

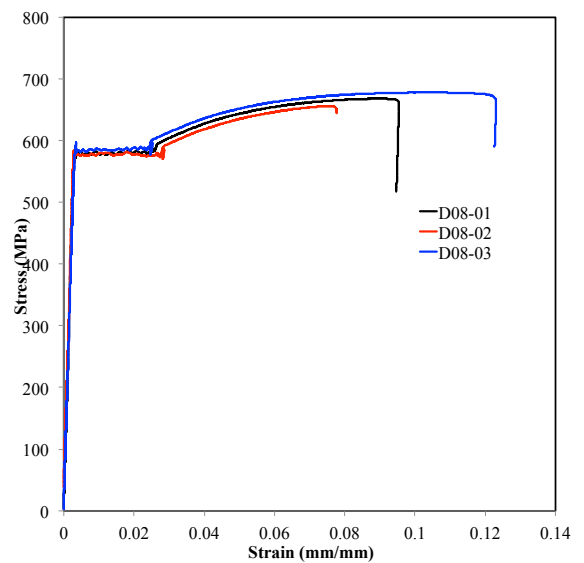
Bar size (mm)	f_y (MPa)	$\epsilon_s (\times 10^{-3})$	f_u (MPa)	E_s (GPa)
16	518	2.62	676	198.0
	510	2.53	675	201.5
	508	2.53	662	200.5
Average	512	2.56	671	200

Transverse reinforcement properties

Bar size (mm)	f_y (MPa)	$\epsilon_s (\times 10^{-3})$	f_u (MPa)	E_s (GPa)
8	580	2.94	669	197.4
	575	2.75	669	208.8
	587	3.09	679	189.8
Average	581	2.92	672	198.7



a)



b)

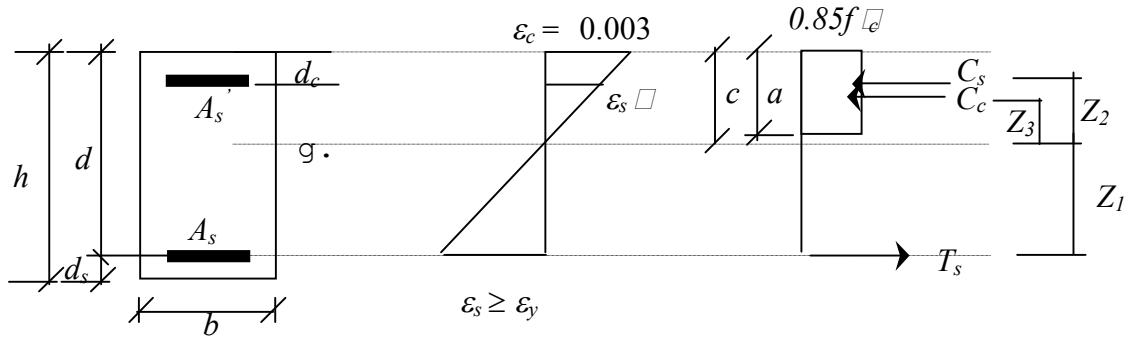
Figure A.1.2. Tensile test: a) Specimen during tensile test; b) Stress-strain curves

APPENDIX 2

BEAM AND COLUMN FLEXURAL STRENGTH

JOINT SHEAR STRENGTH

BEAM-COLUMN JOINT HIERARCHY ANALYSIS

A. Analysis of beam nominal moment strength, $M_{n,b}$ (ACI 318-14)

$$\begin{aligned}
 A_s &= 603.2 & \text{mm}^2 \\
 A_s' &= 603.2 & \text{mm}^2 \\
 b &= 200 & \text{mm} \\
 h &= 300 & \text{mm} \\
 d_s &= 40 & \text{mm} \\
 d_c &= 40 & \text{mm}
 \end{aligned}$$

$$\begin{aligned}
 f_c' &= 30.0 & \text{MPa} \\
 f_y &= 512.3 & \text{MPa} \\
 E_s &= 200000 & \text{MPa}
 \end{aligned}$$

From Table 22.2.2.4.3 ACI 318M-14, $\beta_1 = 0.85 - 0.05 \left(\frac{f_c' - 28}{7} \right) = 0.8357$

Iterative procedure was used to establish section equilibrium and find the depth to the neutral axis, c . Assume the tension steel is yielding ($\epsilon_s \geq \epsilon_y$) and the compression steel is still in elastic range ($\epsilon_s < \epsilon_y$).

a. Find Concrete compression force, C_c

$$\begin{aligned}
 C_c &= 0.85 f_c' b a \\
 a &= \beta_1 c \\
 C_c &= 0.85 \times 30 \times 200 \times 0.8357 \times c = 4262.1c \text{ N}
 \end{aligned}$$

b. Find force in compression reinforcement, C_s

$$\begin{aligned}
 C_s &= A_s' f_s \\
 C_s &= 603.2 \times 200000 \times 0.003 \times \left(\frac{c - 40}{c} \right) \\
 C_s &= 361920 \times \left(\frac{c - 40}{c} \right) \text{ N}
 \end{aligned}$$

c. Find force in tension reinforcement, T_s

$$\begin{aligned}
 T_s &= A_s f_y \\
 T_s &= 603.2 \times 512.3 = 309019.4 \text{ N}
 \end{aligned}$$

d. Section equilibrium, $C_c + C_s = T_s$

$$4262.1c + 361920 \times \left(\frac{c-40}{52.4} \right) = 309019.4$$

$$4262.1c^2 + 361920 \times (c-40) = 309019.4c$$

$$4262.1c^2 + 52900.6c - 14476800 = 0$$

$$c = 52.4 \text{ mm}$$

e. Confirm that the tension steel is yielding and the compression steel is elastic

$$\varepsilon_y = 2.5615 \times 10^{-3}$$

$$\varepsilon_s' = \frac{c-d_c}{c} \varepsilon_{cu}$$

$$\varepsilon_s' = \frac{52.4-40}{52.4} \times 0.003$$

$$= 7.1 \times 10^{-4} < \varepsilon_y$$

$$\varepsilon_s = \frac{d-c}{c} \varepsilon_{cu}$$

$$\varepsilon_s = \frac{260-52.4}{52.4} \times 0.003$$

$$= 0.012 > \varepsilon_y$$

f. Calculate the nominal moment strength, M_n

$$C_c = 4262.1 \times 52.4$$

$$= 223334 \text{ N}$$

$$C_s = 361920 \times \left(\frac{52.4-40}{52.4} \right)$$

$$= 85645.2 \text{ N}$$

$$T_s = 309019.4 \text{ N}$$

$$z_3 = c - \frac{a}{2}$$

$$z_3 = 52.4 - (0.5 \times 0.8357 \times 52.4)$$

$$= 30.5 \text{ mm}$$

$$z_2 = c - d_c = 52.4 - 40$$

$$= 12.4 \text{ mm}$$

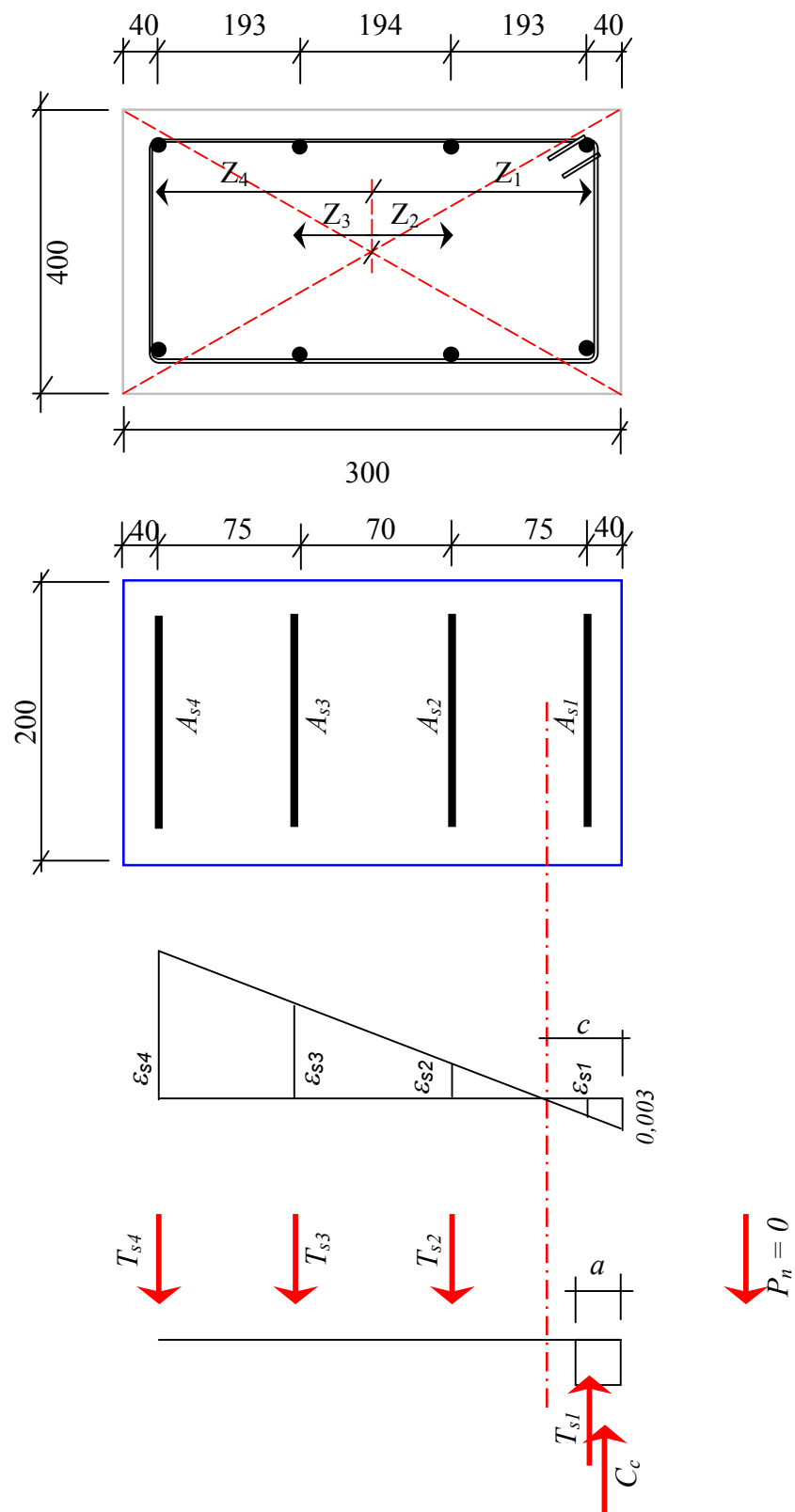
$$z_1 = d - c = 260 - 52.4$$

$$= 207.6 \text{ mm}$$

$$M_n = C_c z_3 + C_s z_2 + T_s z_1$$

$$= (223334 \times 30.5) + (85645.2 \times 12.4) + (309019.4 \times 207.6) \text{ N-mm}$$

$$= 72 \text{ kN-m}$$

B. Analysis of column nominal moment strength, $M_{n,c}$ 

$$A_{s1} = A_{s2} = A_{s3} = A_{s4} = 402 \text{ mm}^2$$

Iterative procedure was used to establish section equilibrium and find the depth to the neutral axis, c . Assume column steel reinforcement on rows 3 and 4 (T_{s3} and T_{s4}) are yielding ($\epsilon_s \geq \epsilon_y$) and steel reinforcement on rows 1 and 2 (T_{s1} and T_{s2}) are still in elastic range ($\epsilon_s < \epsilon_y$).

- a. Compute force in column steel reinforcement on row 1, 2, 3 and 4

$$\begin{aligned} T_{s1} &= A_{s1} \times f_s \\ &= A_{s1} \times \epsilon_{s1} \times E_s = 402 \times \frac{c-40}{c} \times 0.003 \times 200000 = 241200 \times \frac{c-40}{c} \text{ N} \\ T_{s2} &= A_{s2} \times f_s \\ &= A_{s2} \times \epsilon_{s2} \times E_s = 402 \times \frac{115-c}{c} \times 0.003 \times 200000 = 241200 \times \frac{115-c}{c} \text{ N} \\ T_{s3} &= A_{s3} \times f_y \\ &= 402 \times 512.3 = 205944.6 \text{ N} \\ T_{s4} &= A_{s4} \times f_y \\ &= 402 \times 512.3 = 205944.6 \text{ N} \end{aligned}$$

- b. Compute concrete compression force

$$\begin{aligned} C_c &= 0.85 f_c \beta_1 a b \\ &= 0.85 f_c \beta_1 \times c \times b \\ &= 0.85 \times 30 \times 0.8357 \times c \times 200 = 4262c \text{ N} \end{aligned}$$

- c. Section equilibrium, $\Sigma H = 0$

$$\begin{aligned} P_n + T_{s2} + T_{s3} + T_{s4} &= T_{s1} + C_c \\ P_n &= 0 \\ 205944.6 + 205944.6 + 241200 \times \frac{115-c}{c} &= 241200 \times \frac{c-40}{c} + 4262c \\ (411889.2 + 241200 \times \frac{115-c}{c} &= 241200 \times \frac{c-40}{c} + 4262c) \times c \\ 411889.2c + 241200 \times (115-c) &= 241200 \times (c-40) + 4262c^2 \\ 241200c - 9648000 + 4262c^2 - 27738000 + 241200c - 411889.2c &= 0 \\ 4262c^2 + 70510.8c - 37386000 &= 0 \\ c &= 86 \text{ mm} \end{aligned}$$

The depth of the compression stress block, $a = 0.8357 \times 86 = 72 \text{ mm}$

- d. Confirm the state of stress for each rows of column steel reinforcement

$$\begin{aligned} \epsilon_{s1} &= \frac{c-40}{c} \times 0.003 = \frac{86-40}{86} \times 0.003 \\ &= 1.6 \times 10^{-3} < \epsilon_y = 2.56 \times 10^{-3} \\ \epsilon_{s2} &= \frac{115-c}{c} \times 0.003 = \frac{115-86}{86} \times 0.003 \\ &= 1.0 \times 10^{-3} < \epsilon_y \end{aligned}$$

$$\varepsilon_{s3} = \frac{185 - c}{c} \times 0.003 = \frac{185 - 86}{86} \times 0.003$$

$$= 3.4 \times 10^{-3} > \varepsilon_y$$

- e. Compute force for each column steel reinforcement

$$T_{s1} = A_{s1} \times f_s$$

$$= A_{s1} \times \varepsilon_{s1} \times E_s = 402 \times 1.6 \times 10^{-3} \times 200000 = 128640 \text{ N}$$

$$T_{s2} = A_{s2} \times f_s$$

$$= A_{s2} \times \varepsilon_{s2} \times E_s = 402 \times 1.0 \times 10^{-3} \times 200000 = 80400 \text{ N}$$

$$T_{s3} = A_{s3} \times f_y$$

$$= 402 \times 512.3 = 205944.6 \text{ N}$$

$$T_{s4} = A_{s4} \times f_y$$

$$= 402 \times 512.3 = 205944.6 \text{ N}$$

- f. Compute force in concrete compression

$$C_c = 0.85 f_c' \times \beta_1 \times c \times b$$

$$= 366532 \text{ N}$$

Calculate the nominal moment strength, M_n

$$M_n = [C_c (\frac{1}{2} h - \frac{1}{2} a)] + (T_{s1} \times z_1) + (T_{s2} \times z_2) + (T_{s3} \times z_3) + (T_{s4} \times z_4)$$

$$= (366532 \times 114) + (128640 \times 110) + (80400 \times 35) + (205944.6 \times 35) + (205944.6 \times 110)$$

$$= 88.6 \text{ kNm}$$

C. Stirrups design

$$f'_c = 33.71 \text{ MPa} = 33.71 \times 145 \text{ psi} = 4887.95 \text{ psi}$$

$$b_w = 200 \text{ mm} = 200/25.4 = 7.9 \text{ inch}$$

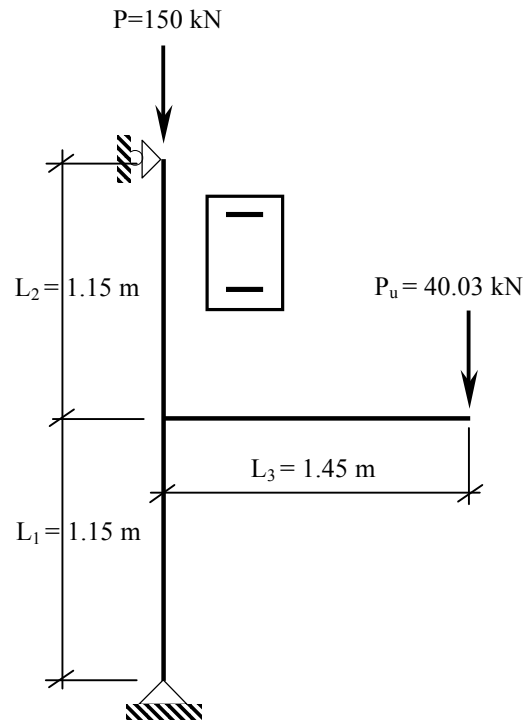
$$d = 10.4 \text{ inch}$$

$$\phi = 0.8$$

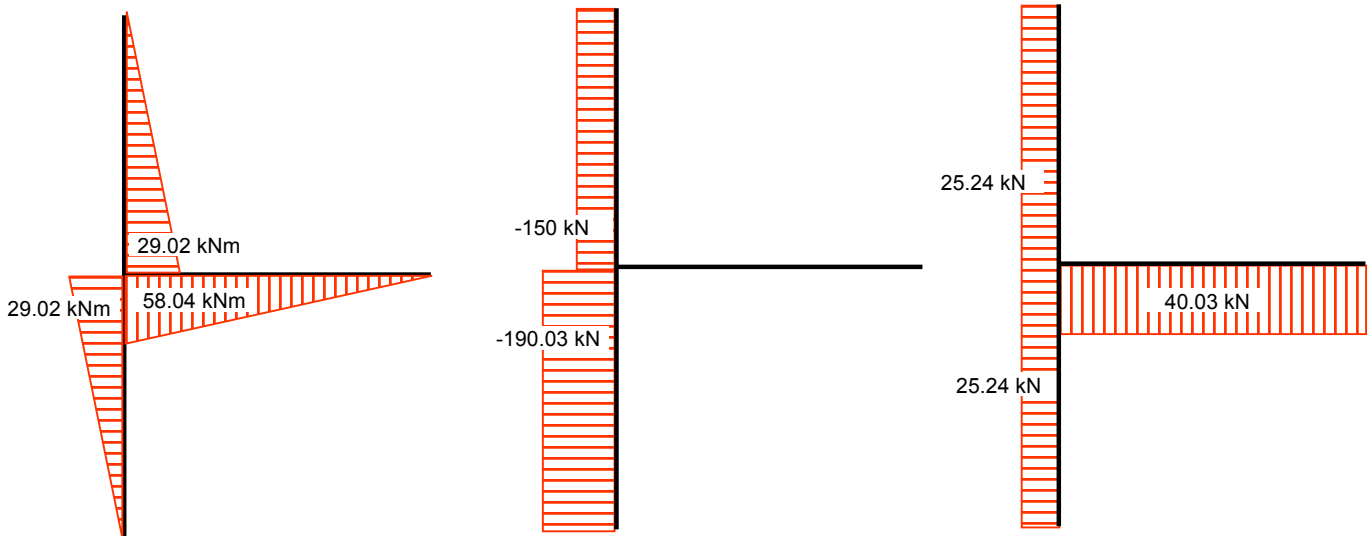
$$M_n = \frac{M_u}{\phi}$$

$$M_u = \phi \times M_n = 0.8 \times 72.56 = 58.05 \text{ kN}$$

$$P_u = \frac{M_u}{L_3} = \frac{58.05}{1.45} = 40.03 \text{ kN}$$



Bending Moment Diagram



Beam

$$V_c = 2 \times \lambda \times \sqrt{f'_c} \times b_w \times d$$

$$\lambda = 1.0$$

$$V_c = 2 \times 1.0 \times \sqrt{4887.95} \times 7.9 \times 10.4$$

$$= 11488.25 \text{ lbs (11.48 kips)}$$

$$0.5V_c = 5.74 \text{ kips}$$

$$V_u = 40.03 \text{ kN}$$

$$\text{conversion } 1 \text{ lb} = 0.004448 \text{ kN}$$

$$= 40.03 \times 224.8 \text{ lb}$$

$$= 8998.74 \text{ lbs} = 8.99 \text{ kips}$$

$$V_n = \frac{V_u}{\phi} = \frac{8.99}{0.75} = 11.9 \text{ kips} > 0.5V_c = 5.74 \text{ kips} \dots \text{Stirrups are required}$$

$$V_s = V_n - V_c$$

$$= 11.9 - 11.48 = 0.42 \text{ kips}$$

$$(V_u/\phi)_{\max} = 5 \times V_c = 5 \times 11.48 = 57.4 \text{ kips}$$

$$V_u/\phi < (V_u/\phi)_{\max} \dots \text{section is large enough}$$

$$A_v = 0.14 \text{ in}^2$$

$$s = \frac{A_v \times f_y \times d}{V_s} = \frac{0.14 \times 72500 \times 10.4}{0.42 \times 1000} = 14.1 \text{ inch} \approx 358.1 \text{ mm}$$

$$\text{Max spacing is } 0.5d = 0.5 \times 10.4 = 5.2 \text{ inch} = 132.1 \text{ mm}$$

$$6 \times \sqrt{f_c'} \times b_w \times d = 6 \times \sqrt{4350} \times 7.9 \times 10.4 = 32513 \text{ lbs} = 32.50 \text{ kips}$$

$$V_u/\phi = 12.9 \text{ kips} < 32.50 \text{ kips, maximum stirrup spacing is } 0.5d \text{ (5.2 inch)}$$

Use D8-125

Shear Capacity

$$V_n = V_c + V_s$$

$$V_c = 10.8 \text{ kips}$$

$$V_s = \frac{A_v \times f_y \times d}{s} = \frac{0.14 \times 72500 \times 10.4}{4.9}$$

$$= 21542.8 \text{ lbs} \approx 21.5 \text{ kips}$$

$$V_n = 10.8 + 21.5 = 32.3 \text{ kips}$$

$$V_u = 0.75 \times 32.3 = 24.225 \text{ kips}$$

Column

$$N = 190.3 \text{ kN, } V = 25.24 \text{ kN, } M = 29.02 \text{ kNm}$$

$$N_u = 190.3 \times \frac{224.8}{1000} = 42.78 \text{ kips}$$

$$V_u = 25.24 \times \frac{224.8}{1000} = 5.7 \text{ kips}$$

$$M_u = 29.02 \times \frac{224.8}{1000} = 6.5 \text{ kips-m}$$

$$= 6.5 \times \frac{1000}{25.4} = 255.9 \text{ kips-in}$$

$$\begin{aligned}
 V_c &= 2 \times \left(1 + \frac{N_u}{2000 A_g} \right) \times \lambda \times \sqrt{f'_c} \times b_w \times d \\
 &= 2 \times \left(1 + \frac{42.78 \times 1000}{2000 \times 93.22} \right) \times 1.0 \times \sqrt{4887.95} \times 7.9 \times 10.4 \\
 &= 14124.31 \text{ lbs} = 14.12 \text{ kips} \\
 0.5V_c &= 7.06 \text{ kips}
 \end{aligned}$$

$$V_n = \frac{V_u}{\phi} = \frac{5.7}{0.75} = 7.6 \text{ kips} > 0.5V_c = 7.06 \text{ kips} \dots \text{Stirrups are required}$$

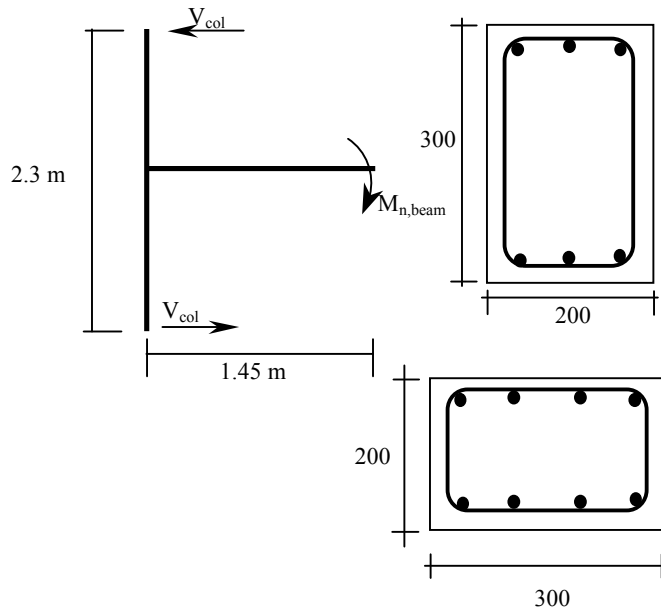
$$\begin{aligned}
 (V_u/\phi)_{\max} &= 5 \times V_c = 5 \times 14.12 = 70.6 \text{ kips} \\
 V_u/\phi &< (V_u/\phi)_{\max} \dots \text{section is large enough}
 \end{aligned}$$

$$\begin{aligned}
 V_c + \left(4 \times \sqrt{f'_c} \times b_w \times d \right) &= 14.12 + \left(\frac{4 \times \sqrt{4887.95} \times 7.9 \times 10.4}{1000} \right) \\
 &= 37.10 \text{ kips}
 \end{aligned}$$

$$V_u/\phi = 7.6 \text{ kips} < 37.1 \text{ kips, maximum stirrup spacing is } 0.5d \text{ (5.2 inch)}$$

Use D8-125

D. Joint shear stress, ACI 352R-02



Dimension :

$$f_c' = 30 \text{ MPa}$$

$$= 30 \times 145 \text{ psi} = 4350 \text{ psi}$$

Joint exterior type 2 $\alpha=1.25$, $\gamma=12$

$$V_{col} = \frac{\alpha M_{n,beam}}{2.3} = \frac{1.25 \times 72}{2.3} = 39.1 \text{ kN} = 39100 \text{ N}$$

$$T_u = A_s \times \alpha \times f_y$$

$$= 603.2 \times 1.25 \times 512.3 = 386274.20 \text{ N}$$

$$V_u = T_u - V_{col} = 386274.20 - 39100 = 347174.20 \text{ N}$$

$$V_u \approx 347174.20 / (4.54 \times 1000) \text{ kips} = 76.50 \text{ kips}$$

Joint type, exterior type 2 $\gamma = 12$

$$b_j = \frac{b_c + b_b}{2} = \frac{200 + 200}{2} = 200 \text{ mm} \approx 7.87 \text{ inch}$$

Joint shear strength

$$V_n = \gamma \sqrt{f_c'} \times b_j \times h_c$$

$$= 12 \sqrt{4350} \times 7.87 \times 11.8 = 73499.2 \text{ lbs} = 73.5 \text{ kips}$$

$$\phi V_n = 0.85 \times 73.5 = 62.5 \text{ kips} < V_u = 76.50 \text{ kips} \gg \text{joint deficient in shear}$$

Joint shear stress

$$= \frac{V_u}{b_j \times h_c} = \frac{76.50}{7.87 \times 11.8} = 0.82 \text{ ksi} = 820 \text{ psi} > 12 \sqrt{f_c'} = 12 \sqrt{4350} = 791 \text{ psi}$$

E. Hierarchy of Strength

A simple procedure to evaluate internal hierarchy of strength and sequence of events developed by Pampanin (2007) was held. The capacities of elements within the beam-column joint subassembly was evaluated relating to specific limit state and written in term of equivalent moment (M_c) and the given axial load (N_c) in the column referring to the occurrence of that limit state.

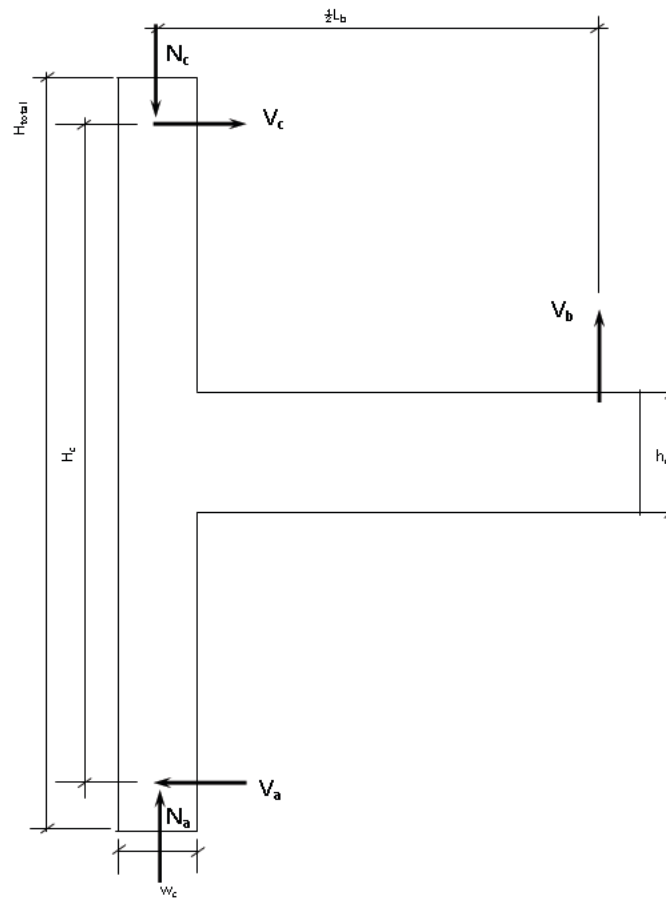


Figure A.2.1. External actions in 2D exterior beam-column joint

Table 2.1. Geometry of the specimen

Beam		Column		Joint	
$L_b/2$	1450 mm	$H_c =$	2300 mm	$w_j =$	300 mm
$h_b =$	300 mm	$h_c =$	200 mm	$h_j =$	200 mm
$w_b =$	200 mm	$w_c =$	300 mm	$A_s =$	50.3 mm ²
Long reinf.	3D16	Long reinf.	4D16	Anchorage	Type 1
$A_s =$	603.19 mm ²	$A_s =$	804.25 mm ²		
Shear reinf.	D8-125	Shear reinf.	D8-125	$c =$	34 mm

Table 2.2. Material properties of the specimen

Concrete		Reinforcement		
f_c	30 MPa	D16	f_y	512.3 MPa
			E_s	200000 MPa
		D8	f_y	580.5 MPa
			E_s	198672 MPa

The calculation explained below is based on work of Pampanin (2007) and step by step calculation is explained briefly by Genesio (2012). By using equation (1) to (13), the calculation is tabulated and listed in Table D.2, Figure 3 and Figure 4 respectively.

Beam and column flexural strength

$$M_{c,beam-hinge} = A_s \times f_y \times j_b \frac{L_b(H_c - h_b)}{H_c(L_b - h_c)} \quad (D.1)$$

Beam and column shear strength

$$M_{c,beam-shear} = \frac{H_c}{L_b} (H_c - h_b) \times V_{R,c,beam} \quad (D.2)$$

with :

$$V_{R,c,beam} = \left[0.1 \times \eta_1 \times K \times (100 \times \rho_b \times f_c)^{\frac{1}{3}} - 0.12 \times f_{a,b} \right] \times w_b \times (h_b - c) \quad (D.3)$$

$$K = 1 + \sqrt{200 / (h_b - c)} \quad (D.4)$$

$\eta_1 = 1.0$ for normal concrete

$f_{a,b}$ = axial stress in the beam, equal to zero

$$M_{c,column-shear} = \frac{(H_c - h_b)}{2} V_{R,c,column} \quad (D.5)$$

$\eta_1 = 1.0$ for normal concrete

$$V_{R,c,column} = \left[0.1 \times \eta_1 \times K \times (100 \times \rho_c \times f_c)^{\frac{1}{3}} - 0.12 \times f_{a,c} \right] \times w_c \times (h_c - c) \quad (D.6)$$

Joint shear strength, without joint reinforcement

$$M_{c,joint-shear} = \frac{V_{jh}(H_c - h_b)/2}{\left(\frac{H_c}{j_b} \left[1 - \frac{h_c}{L_b} \right] - 1 \right)} \quad (D.7)$$

with

$$V_{jh} = w_j \times h_j \times \sqrt{P_t^2 - P_t \times f_{a,c} + 2f_{a,c}} \quad (D.8)$$

$$P_t = \alpha_{setup} \times k \times \sqrt{f_c} = k_0 + k_1 \left(\frac{h_b}{h_c} \right) \times \sqrt{f_c} \quad (D.9)$$

$$\alpha_{setup} = 0.85$$

for joint type 1 $k_0 = 0.15$, $k_1 = 0.3$

Joint shear strength, with joint reinforcement (Pantazopoulou and Bonacci, 1992)

Case 1, yielding of joint reinforcement

$$v_n = \sqrt{\left(\rho_t \times f_y + \frac{N_h}{b \times h} \right) \times \left(\rho_l \times f_y + \frac{N_v}{b \times d_w} \right)} \quad (D.10)$$

$$\rho_t = \rho_s + \rho_b$$

ρ_s = ratios of horizontal stirrups

ρ_b = ratios of total longitudinal beam reinforcement

N_h = beam axial force = 0

ρ_l = ratios of total column reinforcement

N_v = compressive axial force of the column

b = width of beam

h = height of beam

d_w = width of column

$$M_{c,joint-shear} = \frac{V_{jh}(H_c - h_b)/2}{\left(\frac{H_c}{j_b} \left[1 - \frac{h_c}{L_b} \right] - 1 \right)} \quad (D.11)$$

with

$$V_{jh} = w_j \times h_j \times v_n$$

case 2, compressive crushing of concrete in joint core

$$v_n = \sqrt{\left(\frac{\#}{\%} f_c^{\max} \right) - \rho_t \times f_y - \frac{N_h}{b \times h} \left(\times \frac{\#}{\%} \rho_t \times f_y + \frac{N_h}{b \times h} \right)} \quad (\text{D.12})$$

$$f_c^{\max} = \lambda \times f_c'$$

$$\lambda = \frac{1 + \rho_{sv} |f_{ys}/f_c|}{0.8 - 0.34(\varepsilon_1/\varepsilon_0)} \quad (13)$$

ρ_{sv} = ratios of horizontal stirrups

$$\varepsilon_0 = -0.002$$

Table 5. Predicted load for each failure mode

Column axial load	Beam shear cracking	Column shear cracking	Beam flexural yield	Joint shear cracking, case 1	Joint shear cracking, case 2
(kN)	(kN)	(kN)	(kN)	(kN)	(kN)
150	34.86	35.81	46.58	20.86	28.49

Table 6. Failure mode based on sequence of event

Axial load	Failure mode							
	1 st		2 nd		3 rd		4 th	
150	Joint cracking	shear	Column cracking	shear	Beam cracking	shear	Beam yield	flexural

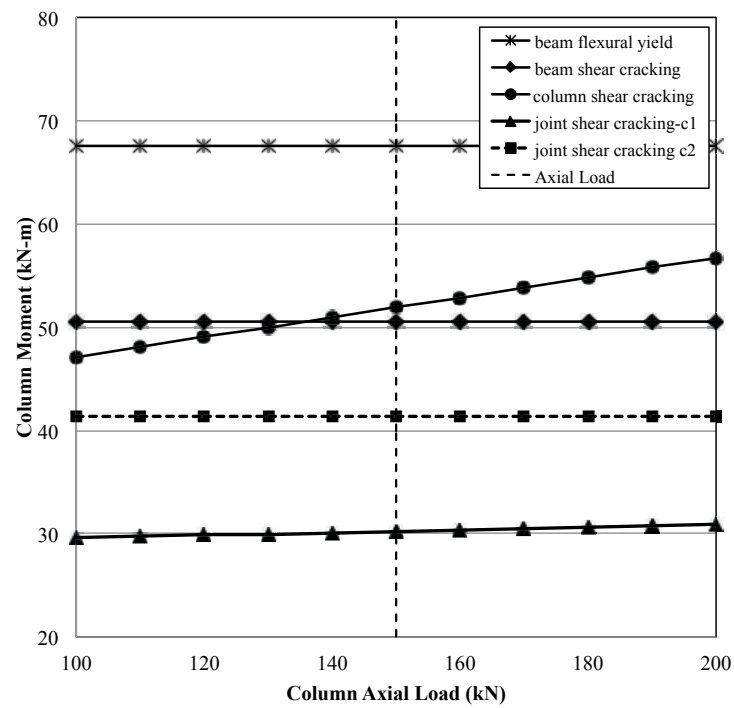


Figure A.2.2. The hierarchy of strength and sequences of events for constant axial load of 150kN

APPENDIX 3
DERIVATION OF THE QUADRATIC POLYNOMIAL
EQUATIONS

A. Analysis before yielding of steel reinforcement

Using Mohr's circle, the definition of the average direction of the principal stresses, $\tan \theta$ can be evaluated as

$$\begin{aligned} \tan^2 \theta &= \frac{\varepsilon_2 - \varepsilon_l}{\varepsilon_2 - \varepsilon_t} \\ &= \left(\frac{\sigma_2}{E_c} - \varepsilon_l \right) \times \left(\frac{\sigma_2}{E_c} - \varepsilon_t \right) \end{aligned} \quad (1)$$

As a result, $\tan^2 \theta$ can be written as

$$\tan^2 \theta = \left(\frac{\sigma_2 - E_c \varepsilon_l}{\sigma_2 - E_c \varepsilon_t} \right)$$

The average of compressive stress in the concrete in the transverse (t) and longitudinal (l) directions are defined as σ_t and σ_l :

$$\sigma_t = -v \tan \theta \quad (2)$$

$$\sigma_l = \frac{-v}{\tan \theta} \quad (3)$$

By assuming the maximum tensile stress in the concrete (σ_l) is zero, we can state the minimum principal tensile stress in the concrete as:

$$\sigma_2 = \sigma_t + \sigma_l \quad (4)$$

Substituting σ_t and σ_l from Eq.2 and Eq.3 into Eq.4, we can define the minimum concrete principal tensile stress (σ_2) in the form of joint shear stress:

$$\begin{aligned} \sigma_2 &= -v \tan \theta - \frac{v}{\tan \theta} \\ &= -v \left(\tan \theta + \frac{1}{\tan \theta} \right) \\ &= -v \left(\frac{\tan^2 \theta + 1}{\tan \theta} \right) \end{aligned}$$

And next, σ_2 resulted from Eq.4 is substituted back into Eq. 1

$$\tan^2 \theta = \left(\frac{-v \left(\frac{\tan^2 \theta + 1}{\tan \theta} \right) - E_c \varepsilon_l}{-v \left(\frac{\tan^2 \theta + 1}{\tan \theta} \right) - E_c \varepsilon_t} \right)$$

$$\tan^2 \theta \times \left(\frac{\nu}{\tan \theta} \right) \left(\frac{\tan^2 \theta + 1}{\tan \theta} \right) (-E_c \varepsilon_t) = -\nu \left(\frac{\tan^2 \theta + 1}{\tan \theta} \right) (-E_c \varepsilon_t)$$

$$\tan^2 \theta \times \left(\frac{\nu}{\tan \theta} \right) \left(\frac{\tan^2 \theta + 1}{\tan \theta} \right) (-\tan^2 \theta \times (E_c \varepsilon_t)) = -\nu \left(\frac{\tan^2 \theta + 1}{\tan \theta} \right) (-E_c \varepsilon_t)$$

Multiplication both sides with $\tan \theta$ gives

$$\left\{ \tan^2 \theta \times \left(\frac{\nu}{\tan \theta} \right) \left(\frac{\tan^2 \theta + 1}{\tan \theta} \right) (-\tan^2 \theta \times (E_c \varepsilon_t)) = -\nu \left(\frac{\tan^2 \theta + 1}{\tan \theta} \right) (-E_c \varepsilon_t) \right\} \times \tan \theta$$

$$-\nu (\tan^2 \theta + 1) \tan^2 \theta - (E_c \varepsilon_t) \tan^3 \theta = -\nu (\tan^2 \theta + 1) - E_c \varepsilon_t \tan \theta$$

Rearranging the above equation will yield

$$-\nu (\tan^2 \theta + 1) \tan^2 \theta - (E_c \varepsilon_t) \tan^3 \theta = -\nu (\tan^2 \theta + 1) - E_c \varepsilon_t \tan \theta$$

$$-\nu \tan^4 \theta - \nu \tan^2 \theta - (E_c \varepsilon_t) \tan^3 \theta = -\nu \tan^2 \theta - \nu - E_c \varepsilon_t \tan \theta$$

$$(-\nu) \tan^4 \theta - (E_c \varepsilon_t) \tan^3 \theta + (E_c \varepsilon_t) \tan \theta + \nu = 0$$

$$(-\nu) \tan^4 \theta - (E_c \varepsilon_t) \tan^3 \theta + (E_c \varepsilon_t) \tan \theta + \nu = 0 \quad (5)$$

Equilibrium of vertical forces require that the average longitudinal compressive stress in the concrete (σ_l) should satisfy the following expression

$$\sigma_l = -\rho_l f_l - \frac{N_v}{h_c w_c} \quad (6-a)$$

For the case of lateral reinforcement within the elastic range:

$$\sigma_l = -\frac{\nu}{\tan \theta} \quad f_l = E_s \varepsilon_l$$

$$-\rho_l f_l - \frac{N_v}{h_c w_c} = -\frac{\nu}{\tan \theta}$$

$$\rho_l E_s \varepsilon_l + \frac{N_v}{h_c w_c} = \frac{\nu}{\tan \theta}$$

$$\varepsilon_l = \frac{1}{\rho_l E_s} \left(\frac{\nu}{\tan \theta} - \frac{N_v}{h_c w_c} \right) \quad (6-b)$$

Similarly, equilibrium of horizontal forces requires that the average transversal compressive stress in the concrete (σ_t) should satisfy the following expression:

$$\sigma_t = -\rho_t f_t - \rho_{Ft} f_{Ft} \quad \sigma_t = -\nu \tan \theta \quad (7-a)$$

For the case of transversal reinforcement within the elastic range:

$$f_t = E_s \varepsilon_t \quad f_{Ft} = E_F (\varepsilon_t - \varepsilon_{0t})$$

$$-\rho_t f_t - \rho_{Ft} f_{Ft} = -v \tan \theta$$

$$\rho_t E_s \varepsilon_t + \rho_{Ft} (E_F (\varepsilon_t - \varepsilon_{0t})) = v \tan \theta$$

$$\rho_t E_s \varepsilon_t + \rho_{Ft} E_F \varepsilon_t - \rho_{Ft} E_F \varepsilon_{0t} = v \tan \theta$$

The magnitude of joint shear stress is related to the strain on the horizontal reinforcement:

$$\varepsilon_t = \frac{1}{\rho_t E_s + \rho_{Ft} E_F} (v \tan \theta + \rho_{Ft} E_F \varepsilon_{0t}) \quad (7-b)$$

Hence,

$$v = \frac{1}{\tan \theta} (\rho_t E_s \varepsilon_t + \rho_{Ft} E_F \varepsilon_t - \rho_{Ft} E_F \varepsilon_{0t}) \quad (8)$$

Substitute E.q.6-b, Eq. 7-b and Eq. 8 into Eq. 5

$$A = (-v) \tan^4 \theta$$

$$v = \frac{1}{\tan \theta} (\rho_t E_s \varepsilon_t + \rho_{Ft} E_F \varepsilon_t - \rho_{Ft} E_F \varepsilon_{0t})$$

$$A = - \left(\frac{1}{\tan \theta} (\rho_t E_s \varepsilon_t + \rho_{Ft} E_F \varepsilon_t - \rho_{Ft} E_F \varepsilon_{0t}) \right) \tan^4 \theta$$

$$= -\rho_t E_s \varepsilon_t \tan^3 \theta - \rho_{Ft} E_F \varepsilon_t \tan^3 \theta + \rho_{Ft} E_F \varepsilon_{0t} \tan^3 \theta$$

$$B = -(E_c \varepsilon_t) \tan^3 \theta$$

$$\varepsilon_t = \frac{1}{\rho_t E_s + \rho_{Ft} E_F} (v \tan \theta + \rho_{Ft} E_F \varepsilon_{0t})$$

$$B = -\frac{E_c}{\rho_t E_s + \rho_{Ft} E_F} (v \tan^4 \theta + \rho_{Ft} E_F \varepsilon_{0t} \tan^3 \theta)$$

$$B = -\frac{E_c}{\rho_t E_s + \rho_{Ft} E_F} v \tan^4 \theta - \frac{E_c}{\rho_t E_s + \rho_{Ft} E_F} \rho_{Ft} E_F \varepsilon_{0t} \tan^3 \theta$$

$$B = -\frac{E_c \varepsilon_t}{\rho_t E_s + \rho_{Ft} E_F} (\rho_t E_s + \rho_{Ft} E_F) \tan^3 \theta$$

$$C = (E_c \varepsilon_t) \tan \theta$$

$$\varepsilon_t = \frac{1}{\rho_t E_s} \left(\frac{v}{\tan \theta} - \frac{N_v}{h_c w_c} \right)$$

$$C = \frac{E_c}{\rho_t E_s} \left(\frac{v}{\tan \theta} - \frac{N_v}{h_c w_c} \right) \tan \theta$$

$$C = \frac{E_c}{\rho_l E_s} v - \frac{E_c \tan \theta}{\rho_l E_s} \frac{N_v}{h_c w_c}$$

$$C = \frac{E_c}{\rho_l E_s} \frac{1}{\tan \theta} \rho_t E_s \varepsilon_t + \frac{E_c}{\rho_l E_s} \frac{1}{\tan \theta} \rho_{Ft} E_F \varepsilon_t - \frac{E_c}{\rho_l E_s} \frac{1}{\tan \theta} \rho_{Ft} E_F \varepsilon_{0t} - \frac{E_c \tan \theta}{\rho_l E_s} \frac{N_v}{h_c w_c}$$

$$D = \frac{1}{\tan \theta} (\rho_t E_s \varepsilon_t + \rho_{Ft} E_F \varepsilon_t - \rho_{Ft} E_F \varepsilon_{0t})$$

$$\begin{aligned}
&= -\rho_t E_s \varepsilon_t \tan^3 \theta - \rho_{Ft} E_F \varepsilon_t \tan^3 \theta + \rho_{Ft} E_F \varepsilon_{0t} \tan^3 \theta - \frac{E_c \varepsilon_t}{\rho_t E_s + \rho_{Ft} E_F} (\rho_t E_s + \rho_{Ft} E_F) \tan^3 \theta \\
&+ \frac{E_c}{\rho_l E_s} \frac{1}{\tan \theta} \rho_t E_s \varepsilon_t + \frac{E_c}{\rho_l E_s} \frac{1}{\tan \theta} \rho_{Ft} E_F \varepsilon_t - \frac{E_c}{\rho_l E_s} \frac{1}{\tan \theta} \rho_{Ft} E_F \varepsilon_{0t} - \frac{E_c \tan \theta}{\rho_l E_s} \frac{N_v}{h_c w_c} \\
&\frac{1}{\tan \theta} (\rho_t E_s \varepsilon_t + \rho_{Ft} E_F \varepsilon_t - \rho_{Ft} E_F \varepsilon_{0t}) = 0
\end{aligned}$$

Multiplying above expression with $\tan \theta$

$$\begin{aligned}
&-\rho_t E_s \varepsilon_t \tan^4 \theta - \rho_{Ft} E_F \varepsilon_t \tan^4 \theta + \rho_{Ft} E_F \varepsilon_{0t} \tan^4 \theta - \frac{E_c \varepsilon_t}{\rho_t E_s + \rho_{Ft} E_F} (\rho_t E_s + \rho_{Ft} E_F) \tan^4 \theta \\
&-\frac{E_c \tan^2 \theta}{\rho_l E_s} \frac{N_v}{h_c w_c} + \frac{E_c}{\rho_l E_s} \rho_t E_s \varepsilon_t \\
&+ \frac{E_c}{\rho_l E_s} \rho_{Ft} E_F \varepsilon_t - \frac{E_c}{\rho_l E_s} \rho_{Ft} E_F \varepsilon_{0t} + (\rho_t E_s \varepsilon_t + \rho_{Ft} E_F \varepsilon_t - \rho_{Ft} E_F \varepsilon_{0t}) = 0
\end{aligned}$$

Introducing;

$$n_{sc} = \frac{E_s}{E_c}; \quad n_{sc} = \frac{E_s}{E_c}; \quad e_v = \frac{N_v}{h_c w_c E_s} \quad (9)$$

Divided by E_s

$$\begin{aligned}
 & -\rho_t \varepsilon_t \tan^4 \theta - \rho_{Ft} n_{Fs} \varepsilon_t \tan^4 \theta + \rho_{Ft} n_{Fs} \varepsilon_{0t} \tan^4 \theta - \frac{E_c \varepsilon_t}{\rho_t E_s + \rho_{Ft} E_F} (\rho_t + \rho_{Ft} n_{Fs}) \tan^4 \theta \\
 & - \frac{E_c}{\rho_l E_s} e_v \tan^2 \theta + \frac{E_c}{\rho_l E_s} \rho_t \varepsilon_t \\
 & + \frac{E_c}{\rho_l E_s} \rho_{Ft} n_{Fs} \varepsilon_t - \frac{E_c}{\rho_l E_s} \rho_{Ft} n_{Fs} \varepsilon_{0t} + (\rho_t \varepsilon_t + \rho_{Ft} n_{Fs} \varepsilon_t - \rho_{Ft} n_{Fs} \varepsilon_{0t}) = 0
 \end{aligned}$$

multiply with -1

$$\begin{aligned}
 & \rho_t \varepsilon_t \tan^4 \theta + \rho_{Ft} n_{Fs} \varepsilon_t \tan^4 \theta - \rho_{Ft} n_{Fs} \varepsilon_{0t} \tan^4 \theta + \left(\frac{E_c \varepsilon_t}{\rho_t E_s + \rho_{Ft} E_F} \rho_t \tan^4 \theta + \frac{E_c \varepsilon_t}{\rho_t E_s + \rho_{Ft} E_F} \rho_{Ft} n_{Fs} \tan^4 \theta \right) \\
 & + \frac{1}{\rho_l n_{sc}} e_v \tan^2 \theta \\
 & - \frac{1}{\rho_l n_{sc}} (\rho_t \varepsilon_t + \rho_{Ft} n_{Fs} \varepsilon_t - \rho_{Ft} n_{Fs} \varepsilon_{0t}) - (\rho_t \varepsilon_t + \rho_{Ft} n_{Fs} \varepsilon_t - \rho_{Ft} n_{Fs} \varepsilon_{0t}) = 0
 \end{aligned}$$

multiply with n_{sc} and ρ_l

$$\begin{aligned}
& n_{sc} \rho_l \rho_t \varepsilon_t \tan^4 \theta + n_{sc} \rho_l \rho_{Ft} n_{Fs} \varepsilon_t \tan^4 \theta - n_{sc} \rho_l \rho_{Ft} n_{Fs} \varepsilon_{0t} \tan^4 \theta + \left(\frac{\rho_l E_s \varepsilon_t}{\rho_t E_s + \rho_{Ft} E_F} \rho_t \tan^4 \theta + \frac{\rho_l E_s \varepsilon_t}{\rho_t E_s + \rho_{Ft} E_F} \rho_{Ft} n_{Fs} \tan^4 \theta \right) \\
& + e_v \tan^2 \theta \\
& - n_{sc} \rho_l (\rho_t \varepsilon_t + \rho_{Ft} n_{Fs} \varepsilon_t - \rho_{Ft} n_{Fs} \varepsilon_{0t}) - (\rho_t \varepsilon_t + \rho_{Ft} n_{Fs} \varepsilon_t - \rho_{Ft} n_{Fs} \varepsilon_{0t}) = 0
\end{aligned}$$

$$\psi = \rho_t \varepsilon_t + \rho_{Ft} n_{Fs} \varepsilon_t - \rho_{Ft} n_{Fs} \varepsilon_{0t} \quad (10)$$

$$\begin{aligned}
K &= \left(\frac{\rho_l E_s \varepsilon_t}{\rho_t E_s + \rho_{Ft} E_F} \rho_t + \frac{\rho_l E_s \varepsilon_t}{\rho_t E_s + \rho_{Ft} E_F} \rho_{Ft} n_{Fs} \right) \\
& (n_{sc} \rho_l \psi + K) \tan^4 \theta + e_v \tan^2 \theta - \psi (n_{sc} \rho_l + 1) = 0 \quad (11)
\end{aligned}$$

$$A \tan^4 \theta + B \tan^2 \theta + C = 0$$

$$A = (n_{sc} \rho_l \psi + K)$$

$$B = e_v$$

$$C = -\psi (n_{sc} \rho_l + 1)$$

B. Analysis after yielding of effective horizontal reinforcement and before yielding of effective vertical reinforcement

The analysis is carried out as in previous step with $f_t = f_{yt}$. The shear stress ν is given by Eq. 8 with the product of $E_s \varepsilon_t$ replaced by f_{yt} , and the polynomial of $\tan \theta$ becomes:

$$\left(H + \frac{1}{n_{sc}} \varepsilon_t \right) \tan^4 \theta + \frac{1}{n_{sc} \rho_l} e_v \tan^2 \theta - H \left(\frac{1}{n_{sc} \rho_l} - 1 \right) = 0 \quad (12)$$

$$A \tan^4 \theta + B \tan^2 \theta + C = 0$$

$$A = \left(H + \frac{1}{n_{sc}} \varepsilon_t \right)$$

$$B = \frac{1}{n_{sc} \rho_l} e_v$$

$$C = -H \left(\frac{1}{n_{sc} \rho_l} - 1 \right)$$

$$H = \rho_t \frac{f_{yt}}{E_s} + \rho_{Ft} n_{Fs} \varepsilon_t - \rho_{Ft} n_{Fs} \varepsilon_{0t}$$

C. Analysis after Yielding both Effective Horizontal and Vertical Reinforcement

The analysis is carried out as in previous step with $f_t = f_{yt}$, $f_l = f_{yl}$. The shear stress ν is given by Eq. 8 with the product of $E_s \varepsilon_t$ replaced by f_{yl} , and the polynomial of $\tan \theta$ becomes:

$$\left(H + \frac{1}{n_{sc}} \varepsilon_t \right) \tan^4 \theta - \frac{1}{n_{sc}} \frac{f_{yl}}{E_s} \tan^2 \theta - (H) = 0 \quad (13)$$

$$A \tan^4 \theta + B \tan^2 \theta + C = 0$$

$$A = \left(H + \frac{1}{n_{sc}} \varepsilon_t \right)$$

$$B = -\frac{1}{n_{sc}} \frac{f_{yl}}{E_s}$$

$$C = -(H)$$

$$H = \rho_t \frac{f_{yt}}{E_s} + \rho_{Ft} n_{Fs} \varepsilon_t - \rho_{Ft} n_{Fs} \varepsilon_{0t}$$

D. Analysis after Yielding of effective vertical reinforcement before yielding of Effective Horizontal Reinforcement

The analysis is carried out as in previous step with $f_l = f_{yl}$. The shear stress ν is given by Eq. 8 with the product of $E_s \varepsilon_t$ replaced by f_{yl} , and the polynomial of $\tan \theta$ becomes:

$$\left(T + \frac{1}{\rho_t E_s + \rho_{Ft} E_F} E_c \rho_t \varepsilon_t + \frac{1}{\rho_t E_s + \rho_{Ft} E_F} E_c \rho_{Ft} n_{Fs} \varepsilon_t \right) \tan^4 \theta - \frac{1}{n_{sc}} \left(\frac{f_{yl}}{E_s} \right) \tan^2 \theta - (T) = 0 \quad (14)$$

$$A \tan^4 \theta + B \tan^2 \theta + C = 0$$

$$A = \left(T + \frac{1}{\rho_t E_s + \rho_{Ft} E_F} E_c \rho_t \varepsilon_t + \frac{1}{\rho_t E_s + \rho_{Ft} E_F} E_c \rho_{Ft} n_{Fs} \varepsilon_t \right)$$

$$B = -\frac{1}{n_{sc}} \left(\frac{f_{yl}}{E_s} \right)$$

$$C = -(T)$$

$$T = \rho_t \varepsilon_t + \rho_{Ft} n_{Fs} \varepsilon_t - \rho_{Ft} n_{Fs} \varepsilon_{0t}$$

APPENDIX 4

SHEAR CAPACITY EVALUATION
OF BEAM-COLUMN JOINT

Table 4.1 Summary of beam column joint parameters for case studies from several researchers

Author	Specimen ID	f_c' (Mpa)	Axial Load (kN)	ρ_b	$\rho_{c,in}$	$\rho_{c'}$	ρ_s	ρ_t	ρ_l	ρ_{Ft}
(1)	(2)	(3)	(4)	(5)	(6)	(7)	(8)	(9)	(10)	(11)
El-Amoury		30.80	600	0.0239	0.0040	0.0179	0.0000	0.0119	0.0130	0.0000
Ehsani	1	33.60	178	0.0325	0.0063	0.0190	0.0065	0.0228	0.0159	0.0000
	2	34.98	222	0.0355	0.0063	0.0254	0.0065	0.0172	0.0140	0.0000
	3	40.92	222	0.0325	0.0063	0.0190	0.0098	0.0147	0.0092	0.0000
	4	44.64	222	0.0355	0.0063	0.0254	0.0098	0.0151	0.0102	0.0000
	6	39.81	304	0.0241	0.0049	0.0148	0.0050	0.0086	0.0071	0.0000
Tsonos	6	32.98	184	0.0205	0.0000	0.0154	0.0075	0.0106	0.0023	0.0000
	6'	28.98	172	0.0205	0.0154	0.0154	0.0075	0.0240	0.0277	0.0000
Tsonos	M1	34.02	0	0.0128	0.0000	0.0079	0.0050	0.0178	0.0079	0.0000
	M2	33.53	150	0.0205	0.0000	0.0079	0.0050	0.0256	0.0079	0.0000
Clyde	2	46.20	689	0.0417	0.0056	0.0167	0.0000	0.0125	0.0106	0.0000
	6	40.10	559	0.0417	0.0056	0.0167	0.0000	0.0142	0.0112	0.0000
	4	41.00	1429	0.0417	0.0056	0.0167	0.0000	0.0104	0.0097	0.0000
	5	37.00	1289	0.0417	0.0056	0.0167	0.0000	0.0104	0.0097	0.0000
Wong	JA-NN03	44.80	121	0.0161	0.0000	0.0218	0.0000	0.0056	0.0076	0.0000
	JA-NN15	46.00	621	0.0161	0.0000	0.0218	0.0000	0.0040	0.0055	0.0000
	JB-NN03	47.40	128	0.0121	0.0000	0.0218	0.0000	0.0054	0.0098	0.0000
	JA-NY03	34.90	94	0.0161	0.0000	0.0218	0.0040	0.0072	0.0044	0.0000
	JA-NY15	38.50	520	0.0161	0.0000	0.0218	0.0040	0.0048	0.0011	0.0000
	JB-NY03	34.20	92	0.0121	0.0000	0.0218	0.0040	0.0058	0.0109	0.0000
Tsonos	A1	35.00	200	0.0105	0.0039	0.0118	0.0057	0.0067	0.0051	0.0000
	E2	35.00	200	0.0103	0.0077	0.0231	0.0071	0.0072	0.0079	0.0000

Table 4.2 Summary of beam column joint parameters for case studies from Kaku

Author	Specimen ID	f_c' (Mpa)	Axial Load (kN)	ρ_b	$\rho_{c,in}$	$\rho_{c'}$	ρ_s	ρ_t	ρ_l	ρ_{Ft}
(1)	(2)	(3)	(4)	(5)	(6)	(7)	(8)	(9)	(10)	(11)
Kaku	1	31.10	258	0.0302	0.0000	0.0166	0.0064	0.0110	0.0025	0.0000
	2	41.70	199	0.0302	0.0000	0.0166	0.0064	0.0131	0.0037	0.0000
	3	41.70	0	0.0302	0.0000	0.0166	0.0064	0.0155	0.0050	0.0000
	4	44.70	360	0.0302	0.0000	0.0166	0.0016	0.0076	0.0033	0.0000
	5	36.70	160	0.0302	0.0000	0.0166	0.0016	0.0107	0.0050	0.0000
	6	40.40	0	0.0302	0.0000	0.0166	0.0016	0.0182	0.0091	0.0000
	7	32.20	194	0.0302	0.0065	0.0130	0.0064	0.0103	0.0082	0.0000
	8	41.20	160	0.0302	0.0065	0.0130	0.0064	0.0103	0.0082	0.0000
	9	40.60	0	0.0302	0.0065	0.0130	0.0064	0.0155	0.0104	0.0000
	10	44.40	360	0.0302	0.0065	0.0130	0.0016	0.0076	0.0091	0.0000
	11	41.90	160	0.0302	0.0065	0.0130	0.0016	0.0107	0.0104	0.0000
	12	35.10	0	0.0302	0.0065	0.0130	0.0016	0.0122	0.0110	0.0000
	13	46.40	100	0.0302	0.0065	0.0130	0.0064	0.0110	0.0084	0.0000
	14	41.00	160	0.0302	0.0023	0.0133	0.0016	0.0107	0.0063	0.0000
	15	39.70	160	0.0302	0.0032	0.0142	0.0016	0.0091	0.0068	0.0000
	16	37.40	0	0.0302	0.0110	0.0219	0.0064	0.0122	0.0151	0.0000

Table 4.3 Summary of beam column joint parameters for case studies from Ridwan

Author	Specimen ID	f_c' (Mpa)	Axial Load (kN)	ρ_b	$\rho_{c,in}$	$\rho_{c'}$	ρ_s	ρ_t	ρ_l	ρ_{Ft}
(1)	(2)	(3)	(4)	(5)	(6)	(7)	(8)	(9)	(10)	(11)
Ridwan	CS-Test #1	33.71	150	0.0201	0.0134	0.0134	0.0017	0.0071	0.0170	0.0000
	CS-Test #2	31.31	150	0.0201	0.0134	0.0134	0.0017	0.0077	0.0174	0.0000
	CS-B	28.68	150	0.0201	0.0134	0.0134	0.0084	0.0154	0.0181	0.0000
	S4	45.52	150	0.0201	0.0134	0.0134	0.0017	0.0097	0.0188	0.0034
	S8	24.88	150	0.0201	0.0134	0.0134	0.0017	0.0067	0.0168	0.0067
	F4	31.80	150	0.0201	0.0134	0.0134	0.0017	0.0117	0.0201	0.0029
	F8	32.29	150	0.0201	0.0134	0.0134	0.0017	0.0218	0.0268	0.0059

Table 4.4 Analytical model prediction results for case studies from several researchers

Author	Specimen ID	ε_t (1)	$\tan \theta$ (2)	θ (3)	ν (4)	ε_t (5)	ε_l (6)	ε_l (7)	ε_2 (8)	σ_2 (9)	λ (10)	f_c max (11)	ε_{max} (12)	σ_2 (13)	Status 1 (14)	σ_t (15)	σ_l (16)	σ_2 (17)	σ_t (18)	σ_l (19)	f_t (20)	Status 2 (21)	f_l (22)	Status 3 (23)
El-amoury		0.00181	0.736	36.4	5.88	0.0018	0.0008	0.0030	-0.0005	-12.31	0.7588	-23.37	-0.0015	-12.27	Crushing	-4.32	-7.98	-12.31	-4.32	-7.98	362.0	Not Yield	152.8	Not Yield
Ehsani	1	0.00153	1.005	45.1	6.93	0.0015	0.0015	0.0036	-0.0005	-13.86	0.6490	-21.81	-0.0013	-13.75	Crushing	-6.96	-6.90	-13.86	-6.96	-6.90	306.0	Not Yield	309.9	Not Yield
	2	0.00197	0.957	43.7	7.07	0.0020	0.0018	0.0042	-0.0005	-14.15	0.6039	-21.13	-0.0012	-14.05	Crushing	-6.76	-7.39	-14.15	-6.76	-7.39	394.0	Not Yield	352.2	Not Yield
	3	0.00237	1.014	45.4	7.08	0.0024	0.0025	0.0054	-0.0006	-14.17	0.5209	-21.31	-0.0010	-17.16	No Crushing	-7.18	-6.98	-14.17	-7.18	-6.98	474.0	Not Yield	490.6	Yield
	4	0.00229	1.010	45.3	7.32	0.0023	0.0024	0.0053	-0.0007	-14.65	0.5289	-23.61	-0.0011	-21.01	No Crushing	-7.40	-7.25	-14.65	-7.40	-7.25	458.0	Not Yield	470.6	Yield
	6	0.00245	0.863	40.8	4.87	0.0025	0.0021	0.0034	0.0012	-9.85	0.6851	-27.28	-0.0014	65.62	No Crushing	-4.20	-5.65	-9.85	-4.20	-5.65	490.0	Yield	424.0	Not Yield
Tsonos	6	0.00241	0.955	43.7	5.36	0.0024	0.0022	0.0050	-0.0004	-10.73	0.5390	-17.78	-0.0011	-10.69	Crushing	-5.12	-5.61	-10.73	-5.12	-5.61	482.0	Not Yield	433.1	Not Yield
	6'	0.00085	0.796	38.5	5.12	0.0009	0.0004	0.0017	-0.0004	-10.51	0.8062	-23.36	-0.0016	-10.48	Crushing	-4.07	-6.43	-10.51	-4.07	-6.43	170.0	Not Yield	77.2	Not Yield
Tsonos	M1	0.00095	1.490	56.1	5.56	0.0010	0.0024	0.0035	-0.0002	-12.02	0.6607	-22.48	-0.0013	-6.84	Crushing	-8.29	-3.73	-12.02	-8.29	-3.73	190.0	Not Yield	475.3	Yield
	M2	0.00141	1.064	46.8	6.77	0.0014	0.0017	0.0036	-0.0005	-13.57	0.6579	-22.06	-0.0013	-13.55	Crushing	-7.21	-6.36	-13.57	-7.21	-6.36	282.0	Not Yield	332.6	Not Yield
Clyde	2	0.00227	0.801	38.7	7.09	0.0023	0.0018	0.0030	0.0011	-14.53	0.7604	-35.13	-0.0015	68.45	No Crushing	-5.68	-8.85	-14.53	-5.68	-8.85	454.4	Yield	369.7	Not Yield
	6	0.00227	0.856	40.6	7.52	0.0023	0.0021	0.0027	0.0017	-15.21	0.7952	-31.89	-0.0016	104.58	No Crushing	-6.44	-8.78	-15.21	-6.44	-8.78	454.4	Yield	423.9	Not Yield
	4	0.00228	0.607	31.3	7.79	0.0023	0.0013	0.0028	0.0008	-17.56	0.7805	-32.00	-0.0016	39.19	No Crushing	-4.73	-12.83	-17.56	-4.73	-12.83	455.0	Yield	264.7	Not Yield
	5	0.00227	0.629	32.2	7.52	0.0023	0.0014	0.0029	0.0008	-16.68	0.7780	-28.79	-0.0016	37.24	No Crushing	-4.73	-11.95	-16.68	-4.73	-11.95	454.4	Yield	276.7	Not Yield
Wong	JA-NN03	0.00260	0.821	39.4	3.57	0.0026	0.0020	0.0039	0.0007	-7.28	0.6828	-30.59	-0.0014	36.57	No Crushing	-2.93	-4.35	-7.28	-2.93	-4.35	520.0	Yield	393.5	Not Yield
	JA-NN15	0.00260	0.512	27.1	4.09	0.0026	0.0010	0.0032	0.0004	-10.07	0.7464	-34.33	-0.0015	21.46	No Crushing	-2.09	-7.97	-10.07	-2.09	-7.97	520.0	Yield	197.1	Not Yield
	JB-NN03	0.00260	0.765	37.4	3.69	0.0026	0.0017	0.0038	0.0005	-7.65	0.6896	-32.69	-0.0014	28.69	No Crushing	-2.83	-4.83	-7.65	-2.83	-4.83	520.0	Yield	346.9	Not Yield
	JA-NY03	0.00228	1.064	46.8	3.54	0.0023	0.0026	0.0051	-0.0002	-7.10	0.5640	-19.68	-0.0011	-7.16	No Crushing	-3.77	-3.33	-7.10	-3.77	-3.33	456.0	Not Yield	522.7	Yield
	JA-NY15	0.00260	0.642	32.7	3.91	0.0026	0.0015	0.0034	0.0007	-8.61	0.6874	-26.46	-0.0014	30.97	No Crushing	-2.51	-6.09	-8.61	-2.51	-6.09	520.0	Yield	290.9	Not Yield
	JB-NY03	0.00260	0.778	37.9	3.91	0.0026	0.0018	0.0038	0.0007	-8.06	0.6528	-22.32	-0.0013	28.12	No Crushing	-3.04	-5.02	-8.06	-3.04	-5.02	520.0	Yield	366.4	Not Yield
Tsonos	A1	0.00250	0.713	35.5	4.70	0.0025	0.0016	0.0035	0.0006	-9.95	0.6574	-23.01	-0.0013	26.12	No Crushing	-3.35	-6.60	-9.95	-3.35	-6.60	500.0	Yield	313.6	Not Yield
	E2	0.00248	0.692	34.7	5.13	0.0025	0.0015	0.0034	0.0006	-10.95	0.6492	-22.72	-0.0013	27.35	No Crushing	-3.55	-7.40	-10.95	-3.55	-7.40	496.0	Yield	303.3	Not Yield

Table 4.5 Analytical model prediction results for case studies from Kaku

Author	Specimen ID	ε_t (1)	$\tan \theta$ (2)	θ (3)	ν (4)	ε_t (5)	ε_l (6)	ε_l (7)	ε_2 (8)	σ_2 (9)	λ (10)	$f_c \max$ (11)	ε_{max} (12)	σ_2 (13)	Status 1 (14)	σ_t (15)	σ_l (16)	σ_2 (17)	σ_t (18)	σ_l (19)	f_t (20)	Status 2 (21)	f_l (22)	Status 3 (23)
Kaku	1	0.00196	0.832	39.8	5.14	0.0020	0.0017	0.0025	0.0011	-10.46	0.7708	-23.97	-0.0015	48.33	No Crushing	-4.28	-6.18	-10.46	-4.28	-6.18	392.0	Yield	341.3	Not Yield
	2	0.00198	0.961	43.8	5.32	0.0020	0.0019	0.0024	0.0016	-10.64	0.7986	-33.30	-0.0016	96.02	No Crushing	-5.11	-5.53	-10.64	-5.11	-5.53	396.0	Yield	389.4	Yield
	3	0.00101	1.293	52.3	4.68	0.0010	0.0036	0.0075	-0.0029	-9.67	0.4625	-19.29	-0.0009	67.17	No Crushing	-6.05	-3.62	-9.67	-6.05	-3.62	202.0	Not Yield	725.7	Yield
	4	0.00181	0.585	30.3	4.70	0.0018	0.0009	0.0023	0.0004	-10.79	0.8335	-37.26	-0.0017	21.95	No Crushing	-2.75	-8.04	-10.79	-2.75	-8.04	362.0	Yield	181.0	Not Yield
	5	0.00181	0.878	41.3	4.37	0.0018	0.0017	0.0023	0.0012	-8.81	0.8332	-30.58	-0.0017	60.99	No Crushing	-3.84	-4.98	-8.81	-3.84	-4.98	362.0	Yield	334.9	Not Yield
	6	0.001	1.343	53.3	4.88	0.0010	0.0020	0.0032	-0.0002	-10.19	0.7340	-29.65	-0.0015	-8.58	Crushing	-6.55	-3.63	-10.19	-6.55	-3.63	200.0	Not Yield	397.6	Yield
	7	0.00196	0.786	38.2	5.15	0.0020	0.0016	0.0026	0.0009	-10.59	0.7626	-24.56	-0.0015	36.93	No Crushing	-4.05	-6.54	-10.59	-4.05	-6.54	392.0	Yield	310.2	Not Yield
	8	0.00196	0.824	39.5	4.91	0.0020	0.0016	0.0027	0.0009	-10.00	0.7654	-31.53	-0.0015	47.97	No Crushing	-4.05	-5.96	-10.00	-4.05	-5.96	392.0	Yield	324.0	Not Yield
	9	0.001269	1.214	50.5	4.98	0.0013	0.0020	0.0035	-0.0002	-10.16	0.6912	-28.06	-0.0014	-8.32	Crushing	-6.05	-4.10	-10.16	-6.05	-4.10	253.8	Not Yield	395.3	Yield
	10	0.001987	0.570	29.7	5.24	0.0020	0.0010	0.0025	0.0005	-12.19	0.8107	-36.00	-0.0016	24.52	No Crushing	-2.99	-9.20	-12.19	-2.99	-9.20	397.4	Yield	194.0	Not Yield
	11	0.001955	0.799	38.6	5.21	0.0020	0.0016	0.0027	0.0008	-10.69	0.7889	-33.06	-0.0016	44.26	No Crushing	-4.17	-6.53	-10.69	-4.17	-6.53	391.0	Yield	310.0	Not Yield
	12	0.001785	1.045	46.2	4.55	0.0018	0.0020	0.0041	-0.0003	-9.12	0.6624	-23.25	-0.0013	-9.35	No Crushing	-4.76	-4.36	-9.12	-4.76	-4.36	357.0	Not Yield	395.0	Yield
	13	0.001955	0.905	42.1	4.73	0.0020	0.0019	0.0023	0.0015	-9.51	0.8080	-37.49	-0.0016	102.52	No Crushing	-4.28	-5.23	-9.51	-4.28	-5.23	391.0	Yield	374.8	Not Yield
	14	0.001785	0.905	42.1	4.61	0.0018	0.0014	0.0035	-0.0003	-9.26	0.7111	-29.16	-0.0014	-10.34	No Crushing	-4.17	-5.09	-9.26	-4.17	-5.09	357.0	Not Yield	282.0	Yield
	15	0.001955	0.813	39.1	4.40	0.0020	0.0016	0.0027	0.0008	-9.00	0.7815	-31.03	-0.0016	38.28	No Crushing	-3.58	-5.42	-9.00	-3.58	-5.42	391.0	Yield	310.7	Not Yield
	16	0.001955	0.902	42.1	5.27	0.0020	0.0019	0.0021	0.0018	-10.59	0.8310	-31.08	-0.0017	104.98	No Crushing	-4.75	-5.84	-10.59	-4.75	-5.84	391.0	Yield	385.8	Yield

Table 4.6 Analytical model prediction results for case studies from several researchers

Author	Specimen ID	ε_t (1)	$\tan \theta$ (2)	θ (3)	ν (4)	ε_t (5)	ε_l (6)	ε_l (7)	ε_2 (8)	σ_2 (9)	λ (10)	$f_c \max$ (11)	ε_{max} (12)	σ_2 (13)	Status 1 (14)	σ_t (15)	σ_l (16)	σ_2 (17)	σ_t (18)	σ_l (19)	f_t (20)	Status 2 (21)	f_l (22)	Status 3 (23)
Ridwan	CS-Test #1	0.00257	0.684	34.4	5.32	0.0026	0.0016	0.0035	0.0007	-11.42	0.6990	-23.56	-0.0014	27.15	No Crushing	-3.64	-7.78	-11.42	-3.64	-7.78	514.0	Yield	310.0	Not Yield
	CS-Test #2	0.00253	0.753	37.0	5.18	0.0025	0.0013	0.0042	-0.0004	-10.78	0.6402	-20.05	-0.0013	-10.78	Crushing	-3.90	-6.88	-10.78	-3.90	-6.88	506.0	Not Yield	251.3	Not Yield
	CS-B	0.00177	0.880	41.3	6.20	0.0018	0.0013	0.0035	-0.0005	-12.51	0.5935	-17.02	-0.0012	-11.27	Crushing	-5.46	-7.05	-12.51	-5.46	-7.05	354.0	Not Yield	251.5	Not Yield
	S4	0.00189	0.884	41.5	5.59	0.0019	0.0010	0.0050	-0.0021	-11.26	0.5917	-26.93	-0.0012	-10.16	Crushing	-4.94	-6.32	-11.26	-4.94	-6.32	378.0	Not Yield	203.4	Not Yield
	S8	0.002565	1.168	49.4	5.89	0.0026	0.0008	-0.0042	0.0075	-11.91	11.5642	-287.72	-0.0231	218.19	No Crushing	-6.87	-5.04	-11.91	-6.87	-5.04	513.0	Yield	151.7	Not Yield
	F4	0.00209	0.880	41.3	6.48	0.0021	0.0012	0.0051	-0.0018	-13.07	0.5808	-18.47	-0.0012	-12.67	Crushing	-5.70	-7.36	-13.07	-5.70	-7.36	418.0	Not Yield	241.9	Not Yield
	F8	0.00113	0.947	43.4	6.11	0.0011	0.0007	0.0046	-0.0027	-12.24	0.6159	-19.89	-0.0012	7.99	Crushing	-5.79	-6.45	-12.24	-5.79	-6.45	226.0	Not Yield	147.4	Not Yield

Note : Formula used on each column

$$(6) \nu = \frac{1}{\tan \theta} (\rho_l E_s \varepsilon_t + \rho_{Ft} E_F \varepsilon_t - \rho_{Ft} E_F \varepsilon_{0t})$$

$$(7) \varepsilon_t = \frac{1}{\rho_l E_s + \rho_{Ft} E_F} (\nu \tan \theta + \rho_{Ft} E_F \varepsilon_{0t})$$

$$(8) \varepsilon_l = \frac{1}{\rho_l E_s} \left(\frac{\nu}{\tan \theta} - \frac{N_v}{h_c w_c} \right)$$

$$(9) \varepsilon_1 = \frac{\varepsilon_t - (\varepsilon_l \times \tan^2 \theta)}{1 - \tan^2 \theta}$$

$$(10) \varepsilon_2 = \varepsilon_t + \varepsilon_l - \varepsilon_1$$

$$(11) \sigma_2 = -\nu \frac{(\tan^2 \theta + 1)}{\tan \theta}$$

$$(12) \lambda = \frac{1 + \rho_{sv} |f_{ys} / f_c|}{0.8 - 0.34 (\varepsilon_1 / \varepsilon_0)}$$

$$(13) f_c^{\max} = \lambda f_c$$

$$(14) \varepsilon_{\max} = \lambda \varepsilon_0$$

$$(15) \sigma_2 = f_c^{\max} \left(2 \frac{\varepsilon_2}{\varepsilon_{\max}} - \left(\frac{\varepsilon_2}{\varepsilon_{\max}} \right)^2 \right)$$

$$(17) \sigma_t = -\nu \tan \theta$$

$$(18) \sigma_l = \frac{-\nu}{\tan \theta}$$

$$(19) \sigma_2 = \sigma_t + \sigma_l$$

$$(20) \sigma_t = -(\rho_l E_s \varepsilon_t) - (\rho_{Ft} E_F \varepsilon_t)$$

$$(21) \sigma_l = -(\rho_l E_s \varepsilon_l) - \left(\frac{N_v}{h_c w_c} \right)$$

Table 4.7. Joint shear stress comparison between: FE analysis and Analytical model for BCJ-SS-S4

A. Concrete strength variation

Concrete cylinder strength (MPa)	20	25	30	35	40	45.52	50	55	
Normalised principal tensile stress	0.501	0.519	0.539	0.549	0.559	0.568	0.581	0.585	From FE in Chapter 5
Principal tensile stress, p_{tl} (MPa)	2.241	2.595	2.951	3.246	3.533	3.835	4.106	4.339	
Joint stress, v_{jh} (MPa)	3.260	3.636	4.010	4.319	4.616	4.929	5.208	5.448	
Joint stress, v_{jh} (MPa)	3.240	3.710	4.300	4.760	5.120	5.590	5.940	6.290	From formula in Chapter 6
Experiment >						5.427			

B. Axial load variation

Concrete cylinder strength (MPa)	75	150	300	450	600	
Normalised principal tensile stress	0.492	0.533	0.552	0.525	0.501	From Chapter 5
Principal tensile stress, p_{tl} (MPa)	3.318	3.595	3.723	3.540	3.377	
Joint stress, v_{jh} (MPa)	3.893	4.681	5.699	6.251	6.721	
Joint stress, v_{jh} (MPa)	5.297	5.590	5.670	6.690	7.150	From formula in Chapter 6
Experiment >		5.427				

C. Embedded bar size variation

Concrete cylinder strength (MPa)	8	12	16	
Normalised principal tensile stress	0.568	0.571	0.575	From Chapter 5
Principal tensile stress, p_{tl} (MPa)	3.835	3.855	3.876	
Joint stress, v_{jh} (MPa)	4.929	4.950	4.972	
Joint stress, v_{jh} (MPa)	5.590	7.720	9.420	From formula in Chapter 6
Experiment >		5.427		

Table 4.8. Joint shear stress comparison between: FE analysis and Analytical model for BCJ-SS-F4

A. Concrete strength variation

Concrete cylinder strength (MPa)	20	25	31.8	35	40	45	50	55	From Chapter 5
Normalised principal tensile stress	0.501	0.530	0.548	0.544	0.568	0.579	0.585	0.587	
Principal tensile stress, p_{tl} (MPa)	2.240	2.650	3.091	3.218	3.592	3.886	4.136	4.356	
Joint stress, v_{jh} (MPa)	3.259	3.695	4.157	4.289	4.678	4.982	5.239	5.464	From formula in Chapter 6
Joint stress, v_{jh} (MPa)	4.760	5.500	6.480	6.850	7.460	7.590	7.610	7.640	

Experiment

> 6.207

B. Axial load variation

Concrete cylinder strength (MPa)	75	150	300	450	600	From Chapter 5
Normalised principal tensile stress	0.403	0.482	0.570	0.611	N/A	
Principal tensile stress, p_{tl} (MPa)	2.274	2.718	3.213	3.448	N/A	
Joint stress, v_{jh} (MPa)	2.831	3.766	5.137	6.144	N/A	From formula in Chapter 6
Joint stress, v_{jh} (MPa)	5.270	6.480	7.430	7.570		

Experiment

> 6.207

C. Embedded bar size variation

Concrete cylinder strength (MPa)	8	12	16	From Chapter 5
Normalised principal tensile stress	0.548	0.554	0.555	
Principal tensile stress, p_{tl} (MPa)	3.091	3.123	3.129	
Joint stress, v_{jh} (MPa)	4.157	4.190	4.197	From formula in Chapter 6
Joint stress, v_{jh} (MPa)	6.480	7.990	8.990	

Experiment > 6.207

APPENDIX 5

TEST RESULTS

LOAD-DISPLACEMENT RESPONSE

JOINT SHEAR DEFORMATION

LOAD-DISPLACEMENT RESPONSE

Control specimen, BCJ-CS-A Test #1

Upward loading

Cycles	Load (kN)	Displacement (mm)
1	1.33	0.51
2	1.53	0.60
3	2.91	1.29
4	2.91	1.32
5	6.31	3.21
6	5.93	3.12
7	8.85	4.35
8	8.57	4.35
9	13.42	6.45
10	13.51	6.57
11	20.69	9.81
12	19.81	9.69
13	24.98	13.07
14	23.27	12.98
15	31.84	19.49
16	30.87	19.67
17	36.94	26.24
18	34.96	25.91
19	48.96	40.39
20	47.30	39.01
21	59.70	51.99
22	54.15	52.08
23	53.99	65.13
24	42.75	65.70
25	40.75	78.35
26	31.38	78.20

Downward loading

Cycles	Load (kN)	Displacement (mm)
1	-1.91	-0.51
2	-1.94	-0.51
3	-4.91	-1.56
4	-5.10	-1.53
5	-10.87	-3.30
6	-11.00	-3.30
7	-14.39	-4.41
8	-15.15	-4.68
9	-19.14	-6.66
10	-18.98	-6.48
11	-25.82	-9.99
12	-26.06	-9.87
13	-29.34	-13.13
14	-29.44	-13.22
15	-37.69	-19.52
16	-37.59	-19.43
17	-45.94	-26.06
18	-44.59	-26.24
19	-61.35	-39.04
20	-58.04	-39.07
21	-62.97	-52.24
22	-57.68	-52.21
23	-54.09	-65.31
24	-44.03	-65.16
25	-40.13	-78.38
26	-31.76	-78.26

Duplicate Control specimen, BCJ-CS-A Test #2

Upward loading

Cycles	Load (kN)	Displacement (mm)
1	3.88	0.63
2	3.70	0.57
3	8.00	1.44
4	8.36	1.47
5	16.04	3.27
6	15.16	3.21
7	19.80	4.56
8	19.60	4.65
9	24.92	6.42
10	24.64	6.63
11	33.08	9.75
12	32.34	9.90
13	39.24	13.11
14	37.58	13.05
15	49.46	19.62
16	47.26	19.59
17	55.92	25.74
18	52.26	25.71
19	59.16	35.25
20	48.00	39.01
21	49.98	48.61
22	38.40	52.15
23	37.80	62.41
24	28.08	64.63
25	26.12	77.74
26	19.06	77.95

Downward loading

Cycles	Load (kN)	Displacement (mm)
1	-4.36	-0.45
2	-4.16	-0.45
3	-9.36	-1.23
4	-10.10	-1.44
5	-15.70	-3.12
6	-15.74	-3.27
7	-19.24	-4.53
8	-18.10	-4.44
9	-22.50	-6.39
10	-22.60	-6.63
11	-28.04	-9.90
12	-27.30	-9.84
13	-33.64	-12.99
14	-33.10	-13.14
15	-40.44	-19.52
16	-39.30	-19.46
17	-48.74	-25.40
18	-46.12	-25.73
19	-53.82	-38.39
20	-47.38	-38.75
21	-45.24	-50.18
22	-36.14	-50.42
23	-33.94	-62.86
24	-24.68	-64.84
25	-22.08	-78.61
26	-15.84	-78.55

BCJ-SS-S4

Upward loading

Cycles	Load (kN)	Displacement (mm)
1	3.90	0.54
2	3.52	0.51
3	8.16	1.35
4	8.52	1.32
5	15.00	3.39
6	13.42	3.30
7	16.82	4.71
8	14.22	4.47
9	20.42	6.66
10	19.42	6.66
11	28.70	10.14
12	26.00	9.75
13	34.80	13.19
14	32.98	13.07
15	47.26	19.64
16	45.18	19.67
17	56.42	26.03
18	55.08	26.60
19	62.38	39.22
20	57.20	39.70
21	58.56	52.17
22	56.86	52.41
23	54.78	65.19
24	42.60	65.40
25	39.56	78.80
26	28.16	78.50

Downward loading

Cycles	Load (kN)	Displacement (mm)
1	-7.88	-0.57
2	-6.14	-0.48
3	-16.50	-1.56
4	-14.44	-1.26
5	-25.46	-3.45
6	-27.72	-4.08
7	-30.06	-4.53
8	-29.74	-4.53
9	-36.52	-6.57
10	-35.78	-6.51
11	-43.62	-9.83
12	-41.92	-9.80
13	-46.42	-12.95
14	-46.94	-12.98
15	-58.40	-19.72
16	-57.06	-19.75
17	-68.98	-26.38
18	-65.28	-26.20
19	-70.82	-39.42
20	-67.72	-39.27
21	-69.40	-52.16
22	-67.38	-52.07
23	-65.52	-65.71
24	-54.94	-66.91
25	-47.26	-79.71
26	-32.44	-79.56

BCJ-SS-F4

Upward loading

Cycles	Load (kN)	Displacement (mm)
1	3.58	0.66
2	3.54	0.57
3	7.60	1.35
4	8.58	1.44
5	15.34	3.21
6	14.62	3.24
7	19.18	4.50
8	20.10	4.83
9	25.52	6.68
10	24.96	6.65
11	33.24	9.92
12	31.78	9.83
13	39.60	12.95
14	39.38	13.25
15	52.30	19.63
16	50.00	19.63
17	61.78	26.01
18	58.84	26.16
19	71.34	39.35
20	59.04	39.14
21	59.72	52.05
22	44.78	52.14
23	42.44	65.60
24	31.94	65.27
25	30.60	78.21
26	24.56	77.94

Downward loading

Cycles	Load (kN)	Displacement (mm)
1	-4.72	-0.57
2	-5.60	-0.72
3	-9.62	-1.47
4	-9.14	-1.32
5	-15.54	-3.30
6	-15.04	-3.24
7	-17.22	-4.50
8	-17.62	-4.74
9	-21.68	-6.63
10	-21.04	-6.54
11	-28.32	-9.74
12	-28.16	-9.89
13	-29.10	-12.86
14	-29.18	-13.16
15	-38.28	-19.75
16	-26.60	-13.64
17	-46.84	-26.05
18	-44.34	-25.93
19	-52.58	-39.06
20	-45.64	-39.21
21	-43.72	-52.16
22	-33.74	-52.28
23	-30.68	-65.47
24	-21.68	-65.44
25	-18.44	-79.17
26	-11.36	-78.57

BCJ-SS-S8

Upward loading

Cycles	Load (kN)	Displacement (mm)
1	3.86	0.93
2	2.40	0.69
3	4.76	1.47
4	5.20	1.56
5	9.06	3.33
6	9.20	3.30
7	12.06	4.56
8	12.70	4.80
9	17.74	7.02
10	16.72	6.81
11	23.16	9.86
12	24.18	9.92
13	30.76	13.13
14	30.70	13.43
15	42.24	19.73
16	40.74	19.70
17	52.80	26.18
18	51.66	26.72
19	63.26	39.22
20	55.16	39.64
21	57.48	52.23
22	42.96	52.08
23	40.18	65.45
24	29.76	65.21
25	27.84	77.99
26	21.12	80.26

Downward loading

Cycles	Load (kN)	Displacement (mm)
1	-3.90	-0.63
2	-3.82	-0.60
3	-7.94	-1.53
4	-6.76	-1.29
5	-13.56	-3.24
6	-13.66	-3.39
7	-16.72	-4.56
8	-16.40	-4.56
9	-21.12	-6.72
10	-21.52	-6.75
11	-27.86	-10.14
12	-28.26	-10.17
13	-31.00	-13.13
14	-31.06	-13.16
15	-41.52	-19.82
16	-41.12	-19.88
17	-48.28	-26.12
18	-48.70	-26.18
19	-58.32	-39.43
20	-49.64	-39.22
21	-48.44	-52.35
22	-38.16	-53.01
23	-34.12	-66.66
24	-25.30	-65.52
25	-22.46	-78.62
26	-17.40	-79.52

BCJ-SS-F8

Upward loading

Cycles	Load (kN)	Displacement (mm)
1	7.84	1.11
2	4.22	0.54
3	9.84	1.50
4	8.76	1.29
5	17.02	3.39
6	17.10	3.51
7	19.84	4.47
8	19.62	4.59
9	26.04	6.51
10	25.58	6.57
11	34.44	9.69
12	32.80	9.78
13	41.56	13.05
14	39.90	13.02
15	54.80	19.37
16	53.34	19.49
17	64.48	25.94
18	60.82	25.82
19	68.72	39.02
20	61.36	38.39
21	61.94	52.27
22	49.52	51.22
23	49.04	64.18
24	38.50	64.78
25	36.06	77.59
26	27.72	78.64

Downward loading

Cycles	Load (kN)	Displacement (mm)
1	-4.34	-0.66
2	-4.60	-0.72
3	-7.50	-1.26
4	-8.30	-1.50
5	-15.30	-3.54
6	-13.14	-3.15
7	-17.40	-4.62
8	-16.72	-4.50
9	-20.58	-6.54
10	-20.28	-6.51
11	-27.78	-9.81
12	-27.32	-9.87
13	-30.22	-13.23
14	-29.22	-13.17
15	-39.82	-19.11
16	-39.26	-19.65
17	-48.04	-25.68
18	-46.88	-25.89
19	-58.08	-38.49
20	-52.60	-39.09
21	-50.48	-52.20
22	-41.64	-51.36
23	-38.86	-65.16
24	-30.68	-65.31
25	-27.14	-78.73
26	-19.82	-79.03

BCJ-CS-B

Upward loading

Cycles	Load (kN)	Displacement (mm)
1	3.50	0.51
2	3.78	0.48
3	8.26	1.41
4	8.88	1.47
5	16.72	3.27
6	16.60	3.30
7	24.08	5.55
8	18.24	4.50
9	25.38	6.42
10	25.02	6.60
11	33.44	9.75
12	31.94	9.72
13	39.78	12.84
14	39.16	13.20
15	52.08	19.65
16	49.60	19.56
17	60.42	25.95
18	58.36	26.67
19	64.52	38.88
20	58.76	38.88
21	63.72	51.18
22	54.82	51.48
23	57.90	63.99
24	48.92	64.98
25	50.64	76.98
26	42.60	78.37

Downward loading

Cycles	Load (kN)	Displacement (mm)
1	-4.12	-0.51
2	-4.66	-0.63
3	-8.84	-1.44
4	-8.72	-1.47
5	-14.50	-3.36
6	-13.86	-3.39
7	-17.02	-4.59
8	-16.60	-4.65
9	-20.44	-6.39
10	-19.96	-6.45
11	-27.48	-10.11
12	-25.20	-9.75
13	-31.02	-12.90
14	-30.36	-13.05
15	-39.28	-19.68
16	-37.78	-19.59
17	-48.32	-25.74
18	-45.22	-25.83
19	-56.12	-38.33
20	-50.52	-38.60
21	-55.60	-51.23
22	-46.74	-51.68
23	-49.58	-64.28
24	-41.06	-65.06
25	-40.92	-77.93
26	-33.26	-77.15

JOINT DEFORMATION RESPONSE

BCJ-CS-A Test #1

Upward loading

Cycles	$p_{ti}/\sqrt{f_c}$	γ (radians)
1	1.12E-03	-2.18E-06
2	1.48E-03	-8.73E-06
3	5.22E-03	-1.09E-05
4	5.22E-03	-1.31E-05
5	2.34E-02	-8.73E-06
6	2.09E-02	-1.53E-05
7	4.38E-02	1.31E-05
8	4.13E-02	1.53E-05
9	9.00E-02	5.68E-05
10	9.12E-02	6.77E-05
11	1.79E-01	1.86E-04
12	1.67E-01	2.01E-04
13	2.36E-01	5.98E-04
14	2.13E-01	6.09E-04
15	3.30E-01	9.93E-04
16	3.17E-01	1.02E-03
17	4.02E-01	1.31E-03
18	3.74E-01	1.39E-03
19	5.77E-01	2.39E-03
20	5.52E-01	2.78E-03
21	7.34E-01	4.49E-03
22	6.51E-01	5.67E-03
23	6.49E-01	7.40E-03
24	4.86E-01	7.13E-03
25	4.57E-01	9.63E-03
26	3.24E-01	1.09E-02

Downward loading

Cycles	$p_{ti}/\sqrt{f_c}$	γ (radians)
1	2.27E-03	-4.37E-06
2	2.34E-03	-8.73E-06
3	1.46E-02	-6.55E-06
4	1.55E-02	-1.75E-05
5	6.28E-02	-2.84E-05
6	6.41E-02	-3.27E-05
7	1.01E-01	-5.46E-05
8	1.10E-01	-6.77E-05
9	1.59E-01	-8.30E-05
10	1.57E-01	-7.20E-05
11	2.47E-01	-9.39E-05
12	2.50E-01	-6.22E-04
13	2.95E-01	-4.37E-06
14	2.97E-01	-6.33E-05
15	4.13E-01	-4.72E-04
16	4.11E-01	-5.74E-04
17	5.31E-01	-1.02E-03
18	5.12E-01	-1.26E-03
19	7.57E-01	-2.65E-03
20	7.08E-01	-2.77E-03
21	7.81E-01	-4.27E-03
22	7.03E-01	-5.09E-03
23	6.50E-01	-1.12E-02
24	5.04E-01	-1.43E-02
25	4.48E-01	-2.11E-02
26	3.29E-01	1.09E-02

BCJ-CS-A Test #2

Upward loading

Cycles	$p_{ti}/\sqrt{f_c}$	γ (radians)
1	7.92E-03	2.84E-06
2	7.21E-03	2.18E-06
3	3.21E-02	1.31E-06
4	3.49E-02	2.18E-07
5	1.11E-01	-2.18E-07
6	1.08E-01	-2.81E-05
7	1.57E-01	-2.86E-05
8	1.54E-01	-6.17E-05
9	2.23E-01	4.15E-06
10	2.20E-01	2.40E-05
11	3.37E-01	2.61E-04
12	3.27E-01	2.91E-04
13	4.26E-01	6.53E-04
14	4.02E-01	6.54E-04
15	5.77E-01	1.36E-03
16	5.44E-01	1.35E-03
17	6.73E-01	2.22E-03
18	6.18E-01	2.52E-03
19	7.23E-01	4.21E-03
20	5.55E-01	5.40E-03
21	5.85E-01	7.42E-03
22	4.14E-01	9.99E-03
23	4.05E-01	4.74E-03
24	0.00E+00	0.00E+00
25	0.00E+00	0.00E+00
26	0.00E+00	0.00E+00

Downward loading

Cycles	$p_{ti}/\sqrt{f_c}$	γ (radians)
1	1.01E-02	8.73E-07
2	9.26E-03	2.18E-07
3	4.32E-02	-2.40E-06
4	4.98E-02	-6.55E-07
5	1.08E-01	-2.75E-05
6	1.08E-01	-2.88E-05
7	1.50E-01	-6.46E-05
8	1.36E-01	-6.98E-05
9	1.92E-01	-1.05E-04
10	1.93E-01	-1.18E-04
11	2.67E-01	-1.54E-04
12	2.56E-01	-1.65E-04
13	3.45E-01	-2.45E-04
14	3.38E-01	-3.08E-04
15	4.44E-01	-7.57E-04
16	4.27E-01	-8.47E-04
17	5.66E-01	-1.47E-03
18	5.28E-01	-1.62E-03
19	6.43E-01	-3.99E-03
20	5.47E-01	-4.94E-03
21	5.15E-01	-9.43E-03
22	3.85E-01	-1.44E-02
23	0.00E+00	0.00E+00
24	0.00E+00	0.00E+00
25	0.00E+00	0.00E+00
26	0.00E+00	0.00E+00

BCJ-SS-S4

Upward loading

Cycles	$p_{tl}/\sqrt{f_c}$	γ (radians)
1	6.84E-03	-6.55E-07
2	5.54E-03	1.75E-06
3	2.79E-02	2.40E-06
4	3.02E-02	3.27E-06
5	8.29E-02	6.77E-06
6	6.84E-02	1.03E-05
7	1.00E-01	1.38E-05
8	7.55E-02	1.51E-05
9	1.37E-01	2.14E-05
10	1.26E-01	1.40E-05
11	2.29E-01	2.24E-04
12	1.98E-01	8.95E-05
13	3.00E-01	4.55E-04
14	2.79E-01	5.07E-04
15	4.52E-01	1.36E-03
16	4.26E-01	1.41E-03
17	5.65E-01	2.07E-03
18	5.49E-01	2.35E-03
19	6.40E-01	2.84E-03
20	5.75E-01	3.15E-03
21	5.92E-01	3.72E-03
22	5.71E-01	4.70E-03
23	5.45E-01	5.59E-03
24	3.95E-01	4.84E-03
25	3.58E-01	5.21E-03
26	0.00E+00	0.00E+00

Downward loading

Cycles	$p_{tl}/\sqrt{f_c}$	γ (radians)
1	2.59E-02	-2.18E-07
2	1.62E-02	4.37E-07
3	9.66E-02	-8.73E-07
4	7.72E-02	2.18E-06
5	1.94E-01	1.09E-06
6	2.17E-01	5.46E-06
7	2.44E-01	1.03E-05
8	2.40E-01	8.08E-06
9	3.20E-01	-8.66E-05
10	3.11E-01	-1.38E-04
11	4.07E-01	-2.91E-04
12	3.86E-01	-3.28E-04
13	4.41E-01	-4.83E-04
14	4.47E-01	-5.76E-04
15	5.89E-01	-1.12E-03
16	5.73E-01	-1.15E-03
17	7.23E-01	-1.68E-03
18	6.76E-01	-1.77E-03
19	7.45E-01	-2.30E-03
20	7.07E-01	-2.62E-03
21	7.27E-01	-3.37E-03
22	7.03E-01	-4.20E-03
23	6.79E-01	-6.49E-03
24	5.47E-01	-7.09E-03
25	4.52E-01	-1.16E-02
26	0.00E+00	0.00E+00

BCJ-SS-F4

Upward loading

Cycles	$p_{ti}/\sqrt{f_c}$	γ (radians)
1	3.60E+00	6.16E-06
2	3.56E+00	8.58E-06
3	7.62E+00	2.71E-05
4	8.58E+00	2.00E-05
5	1.53E+01	3.23E-05
6	1.46E+01	-2.86E-06
7	1.92E+01	1.19E-05
8	2.01E+01	1.83E-05
9	2.55E+01	6.64E-05
10	2.50E+01	6.51E-05
11	3.32E+01	1.79E-04
12	3.18E+01	1.20E-04
13	3.96E+01	4.51E-04
14	3.94E+01	5.10E-04
15	5.23E+01	1.24E-03
16	5.00E+01	1.31E-03
17	6.18E+01	2.14E-03
18	5.88E+01	2.35E-03
19	7.14E+01	4.24E-03
20	5.90E+01	4.57E-03
21	5.97E+01	5.53E-03
22	4.48E+01	7.55E-03
23	4.24E+01	1.16E-02
24	3.19E+01	1.12E-02
25	3.06E+01	8.83E-03
26	2.46E+01	2.00E-03

Downward loading

Cycles	$p_{ti}/\sqrt{f_c}$	γ (radians)
1	-4.72E+00	8.80E-06
2	-5.60E+00	8.80E-06
3	-9.62E+00	1.94E-05
4	-9.12E+00	2.66E-05
5	-1.55E+01	-1.87E-05
6	-1.50E+01	-1.54E-05
7	-1.72E+01	-1.83E-05
8	-1.76E+01	-2.20E-05
9	-2.17E+01	-5.81E-05
10	-2.10E+01	-6.38E-05
11	-2.83E+01	-2.67E-04
12	-2.81E+01	-3.08E-04
13	-2.91E+01	-3.54E-04
14	-2.92E+01	-3.95E-04
15	-3.83E+01	-9.00E-04
16	-2.66E+01	-6.94E-04
17	-4.68E+01	-1.58E-03
18	-4.43E+01	-1.67E-03
19	-5.26E+01	-4.86E-03
20	-4.56E+01	-5.50E-03
21	-4.37E+01	-1.19E-02
22	-3.37E+01	-1.51E-02
23	-3.07E+01	-2.41E-02
24	-2.17E+01	-2.89E-02
25	-1.84E+01	-4.02E-02
26	-1.14E+01	-5.08E-02

BCJ-SS-S8

Upward loading

Cycles	$p_{ti}/\sqrt{f_c}$	γ (radians)
1	1.21E-02	1.51E-06
2	3.47E-03	2.37E-06
3	1.35E-02	8.63E-07
4	2.63E-02	3.45E-06
5	4.58E-02	2.37E-06
6	9.51E-02	2.37E-06
7	1.34E-01	1.08E-06
8	8.43E-02	8.63E-07
9	1.48E-01	3.45E-06
10	1.34E-01	8.63E-07
11	2.25E-01	8.20E-06
12	2.40E-01	-9.49E-06
13	3.42E-01	1.34E-05
14	3.38E-01	-3.60E-05
15	5.27E-01	3.21E-04
16	5.03E-01	4.96E-04
17	7.03E-01	1.56E-03
18	6.84E-01	1.86E-03
19	8.82E-01	3.49E-03
20	7.46E-01	3.72E-03
21	7.83E-01	5.60E-03
22	5.40E-01	6.59E-03
23	4.93E-01	1.39E-02
24	0.00E+00	0.00E+00
25	0.00E+00	0.00E+00
26	0.00E+00	0.00E+00

Downward loading

Cycles	$p_{ti}/\sqrt{f_c}$	γ (radians)
1	9.15E-03	6.47E-07
2	8.79E-03	0.00E+00
3	3.57E-02	-8.63E-07
4	2.63E-02	1.51E-06
5	9.39E-02	-1.29E-06
6	9.51E-02	-2.16E-07
7	1.34E-01	-4.10E-06
8	1.30E-01	-3.02E-06
9	1.95E-01	1.29E-06
10	2.01E-01	-5.18E-06
11	2.97E-01	-2.09E-05
12	3.03E-01	-2.59E-05
13	3.47E-01	-7.51E-05
14	3.46E-01	-8.59E-05
15	5.20E-01	-7.04E-04
16	5.10E-01	-1.09E-03
17	6.37E-01	-1.66E-03
18	6.35E-01	-2.02E-03
19	7.98E-01	-5.56E-03
20	6.51E-01	-6.29E-03
21	6.31E-01	-1.17E-02
22	4.64E-01	-1.40E-02
23	3.96E-01	-1.84E-02
24	0.00E+00	0.00E+00
25	0.00E+00	0.00E+00
26	0.00E+00	0.00E+00

BCJ-SS-F8

Upward loading

Cycles	$p_{tl}/\sqrt{f_c}$	γ (radians)
1	3.06E-02	2.40E-06
2	9.37E-03	4.36E-07
3	4.66E-02	1.94E-05
4	3.78E-02	4.80E-06
5	1.21E-01	1.03E-05
6	1.22E-01	-6.55E-06
7	1.55E-01	2.18E-07
8	1.52E-01	7.86E-06
9	2.36E-01	6.68E-05
10	2.29E-01	7.57E-05
11	3.52E-01	2.29E-04
12	3.28E-01	3.22E-04
13	4.53E-01	5.80E-04
14	4.29E-01	6.07E-04
15	6.47E-01	1.28E-03
16	6.26E-01	1.38E-03
17	7.91E-01	2.11E-03
18	7.37E-01	2.23E-03
19	8.55E-01	3.04E-03
20	7.44E-01	3.30E-03
21	7.54E-01	4.00E-03
22	5.69E-01	3.63E-03
23	5.62E-01	5.58E-03
24	4.09E-01	9.14E-03
25	3.74E-01	1.45E-02
26	2.58E-01	1.90E-02

Downward loading

Cycles	$p_{tl}/\sqrt{f_c}$	γ (radians)
1	9.72E-03	-1.53E-06
2	1.09E-02	-8.73E-07
3	2.80E-02	-1.03E-05
4	3.39E-02	-1.29E-05
5	1.01E-01	-4.52E-05
6	7.79E-02	-4.17E-05
7	1.25E-01	-6.55E-05
8	1.17E-01	-6.63E-05
9	1.64E-01	-8.60E-05
10	1.60E-01	-9.01E-05
11	2.58E-01	-1.28E-04
12	2.53E-01	-1.38E-04
13	2.92E-01	-1.56E-04
14	2.78E-01	-1.73E-04
15	4.27E-01	-4.49E-04
16	4.20E-01	-5.35E-04
17	5.47E-01	-1.14E-03
18	5.31E-01	-1.30E-03
19	6.96E-01	-4.19E-03
20	6.14E-01	-5.01E-03
21	5.83E-01	-8.84E-03
22	4.54E-01	-9.67E-03
23	4.14E-01	-1.31E-02
24	2.99E-01	-1.33E-02
25	2.50E-01	-1.65E-02
26	1.55E-01	-1.97E-02

BCJ-CS-B

Upward loading

Cycles	$p_{ti}/\sqrt{f_c}$	γ (radians)
1	6.90E-03	-8.73E-07
2	7.94E-03	-5.02E-06
3	3.60E-02	-8.95E-06
4	4.11E-02	-2.34E-05
5	1.25E-01	-2.49E-05
6	1.23E-01	-6.94E-05
7	2.23E-01	1.09E-06
8	1.44E-01	-1.99E-05
9	2.40E-01	5.55E-05
10	2.35E-01	2.23E-05
11	3.58E-01	3.02E-04
12	3.36E-01	3.52E-04
13	4.54E-01	7.89E-04
14	4.44E-01	9.08E-04
15	6.44E-01	1.86E-03
16	6.05E-01	1.97E-03
17	7.75E-01	2.97E-03
18	7.42E-01	3.37E-03
19	8.40E-01	4.54E-03
20	7.49E-01	5.12E-03
21	8.27E-01	6.77E-03
22	6.87E-01	7.37E-03
23	7.35E-01	8.91E-03
24	5.95E-01	1.05E-02
25	6.22E-01	1.29E-02
26	4.97E-01	1.56E-02

Downward loading

Cycles	$p_{ti}/\sqrt{f_c}$	γ (radians)
1	9.40E-03	-2.62E-06
2	1.19E-02	-8.51E-06
3	4.06E-02	-1.75E-05
4	3.94E-02	-2.38E-05
5	9.82E-02	-6.62E-05
6	9.06E-02	-6.33E-05
7	1.28E-01	-2.42E-05
8	1.23E-01	-2.05E-05
9	1.72E-01	-2.31E-05
10	1.66E-01	-8.21E-05
11	2.70E-01	-1.16E-04
12	2.38E-01	-1.03E-04
13	3.22E-01	-2.58E-04
14	3.12E-01	-2.72E-04
15	4.46E-01	-6.17E-04
16	4.23E-01	-6.52E-04
17	5.86E-01	-1.14E-03
18	5.37E-01	-1.25E-03
19	7.07E-01	-3.52E-03
20	6.19E-01	-3.46E-03
21	6.99E-01	-6.98E-03
22	5.60E-01	-7.66E-03
23	6.05E-01	-1.05E-02
24	4.73E-01	-1.09E-02
25	4.71E-01	-1.48E-02
26	3.55E-01	-1.76E-02

APPLIED LOAD/STRESS RESPONSE IN THE JOINT

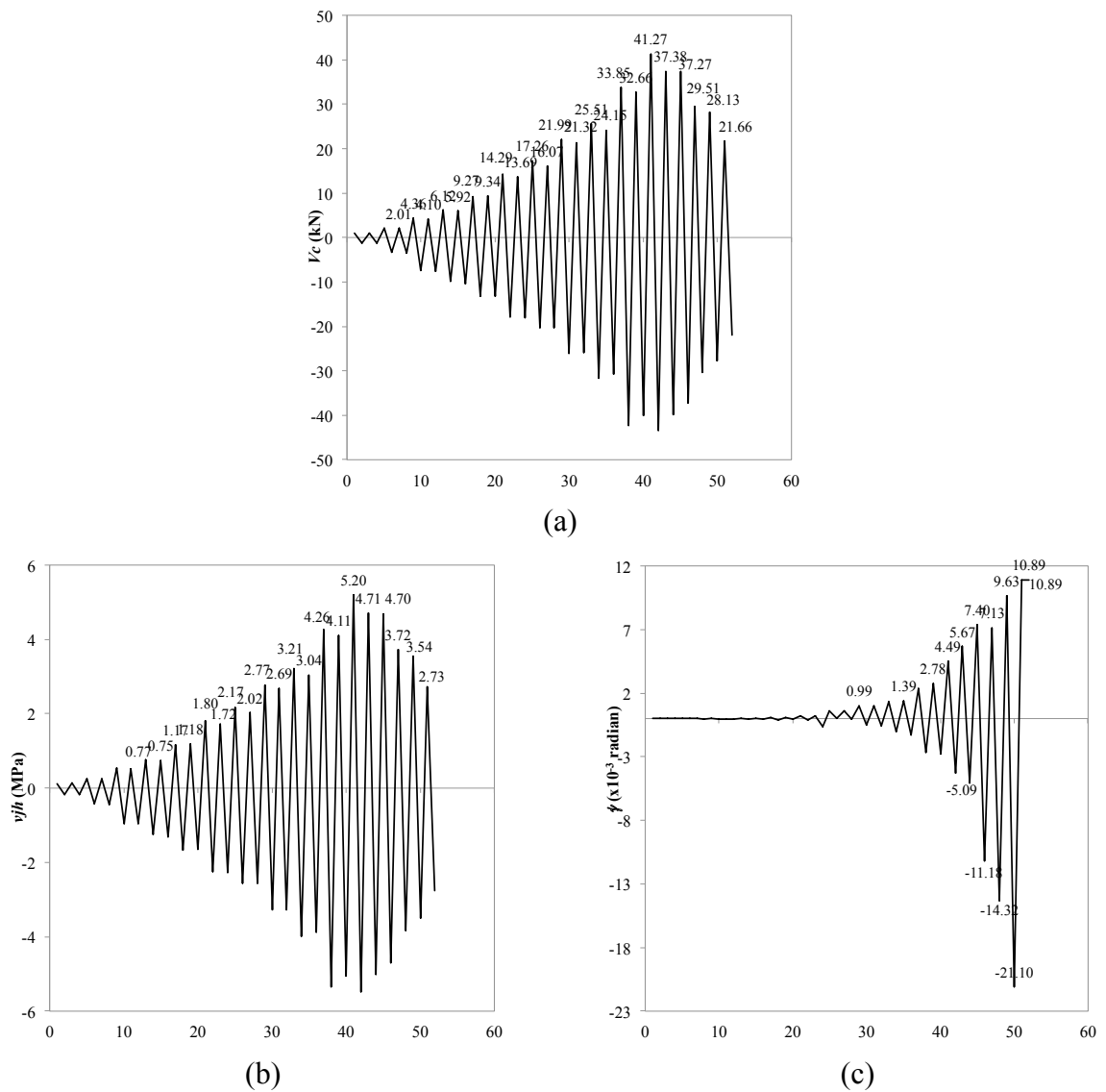
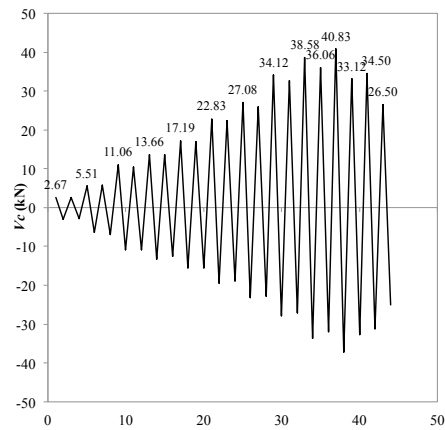
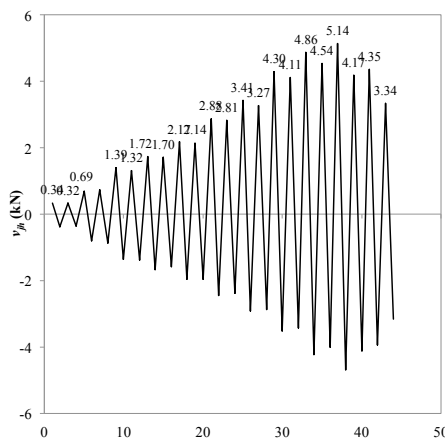


Figure A.5.1. Responses of BCJ-CS-A Test #1 : (a) Story column shear; (b) Horizontal shear stress at joint; (c) Shear deformation at joint

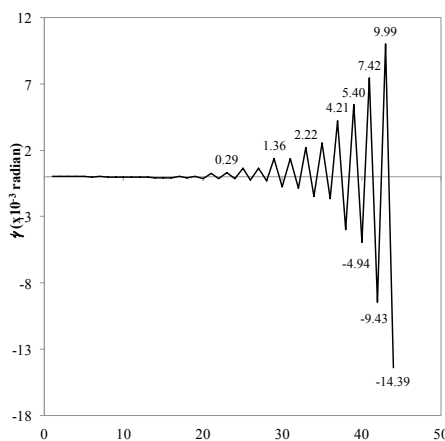
BCJ-CS-A Test #2



(a)



(b)

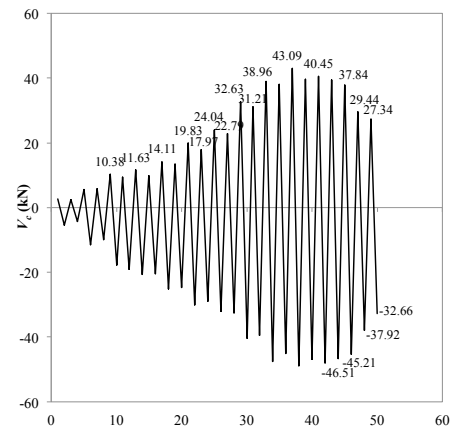


(c)

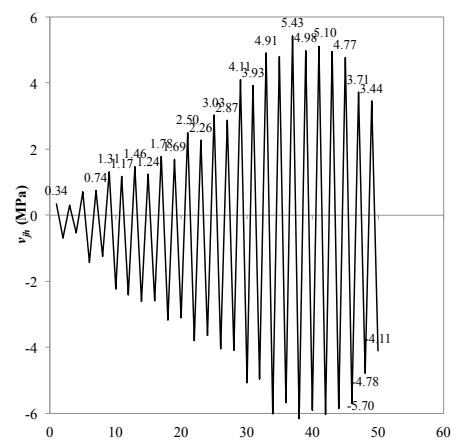
Figure A.5.2. Responses of BCJ-CS-A Test #2 : (a) Story column shear; (b)

Horizontal shear stress at joint; (c) Shear deformation at joint

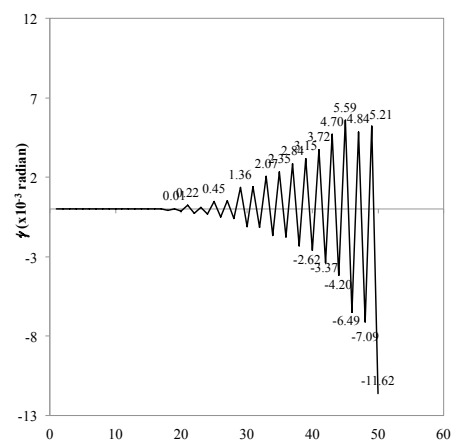
BCJ-SS-S4



(a)



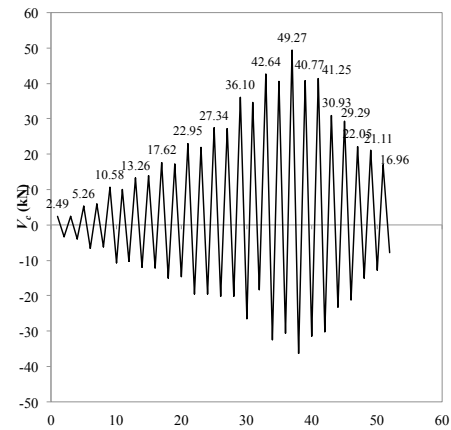
(b)



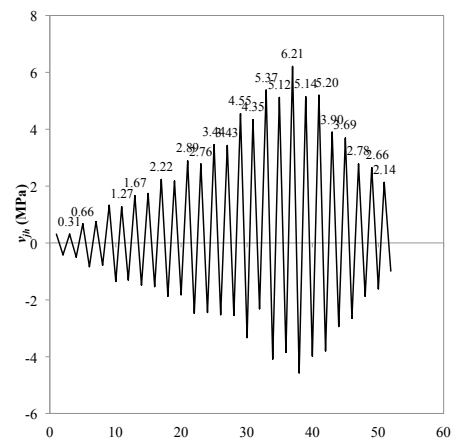
(c)

Figure A.5.3. Responses of BCJ-SS-S4 : (a) Story column shear; (b) Horizontal shear stress at joint; (c) Shear deformation at joint

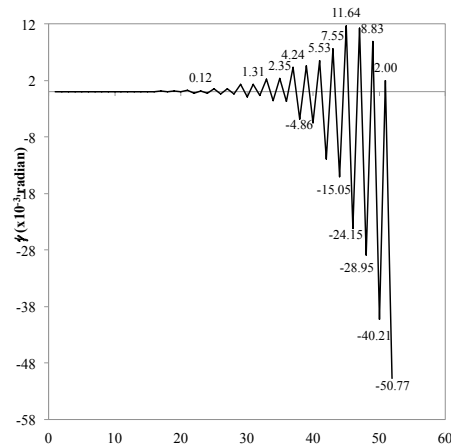
BCJ-SS-F4



(a)



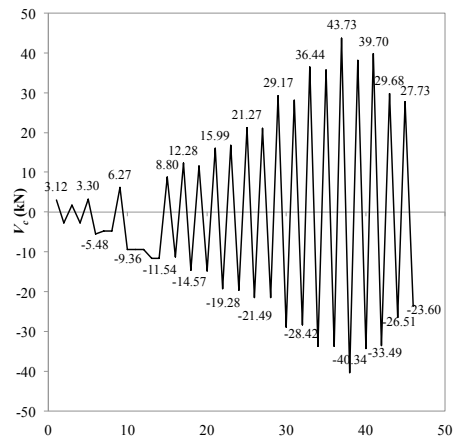
(b)



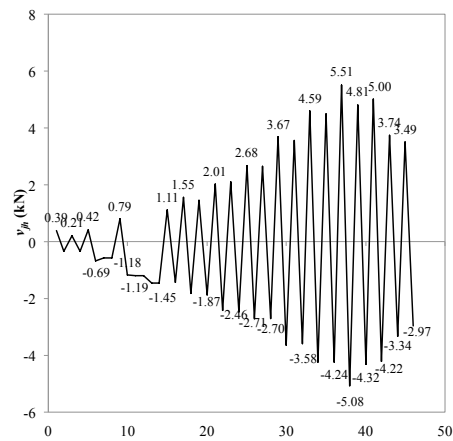
(c)

Figure A.5.4. Responses of BCJ-SS-F4 : (a) Story column shear; (b) Horizontal shear stress at joint; (c) Shear deformation at joint

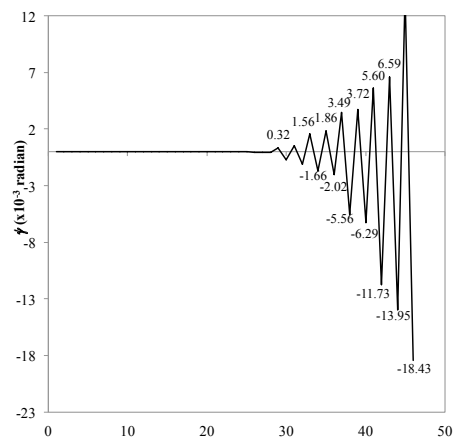
BCJ-SS-S8



(a)



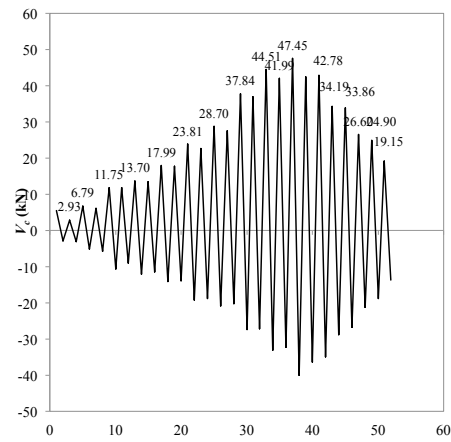
(b)



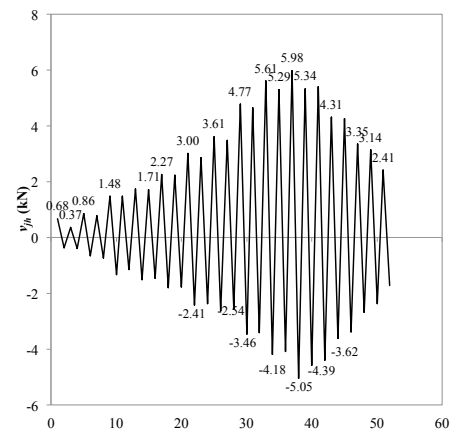
(c)

Figure A.5.5. Responses of BCJ-SS-S8 : (a) Story column shear; (b) Horizontal shear stress at joint; (c) Shear deformation at joint

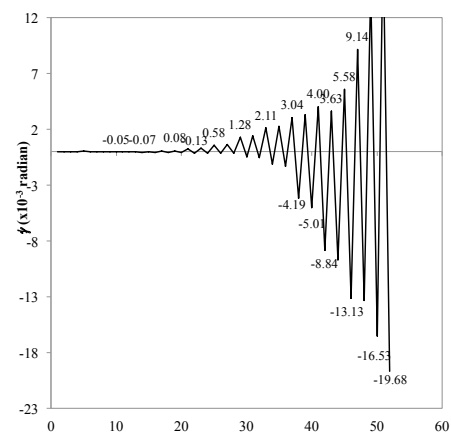
BCJ-SS-F8



(a)



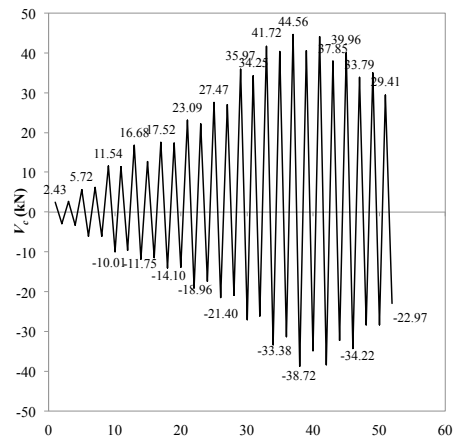
(b)



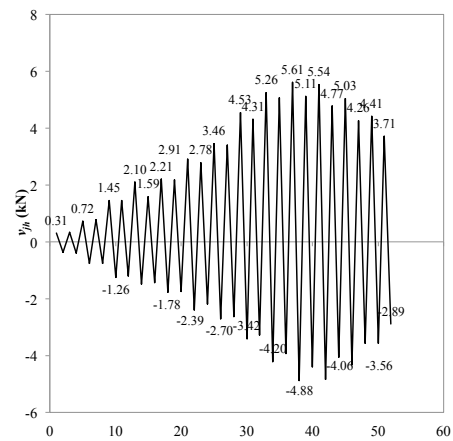
(c)

Figure A.5.6. Responses of BCJ-SS-F8 : (a) Story column shear; (b) Horizontal shear stress at joint; (c) Shear deformation at joint

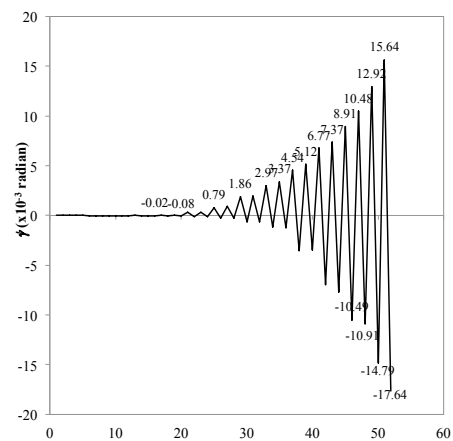
BCJ-CS-B



(a)



(b)

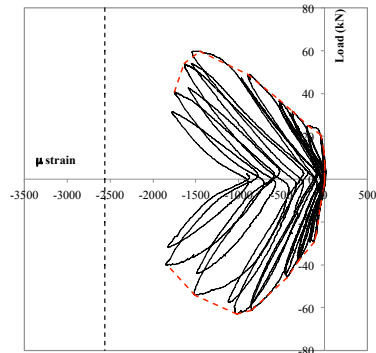


(c)

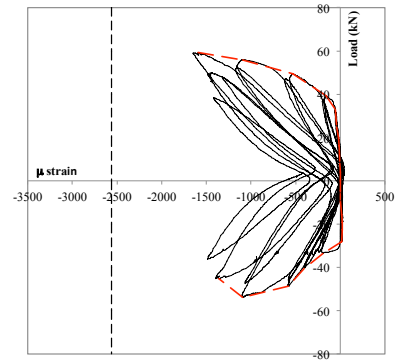
Figure A.5.7. Responses of BCJ-CS-B : (a) Story column shear; (b) Horizontal shear stress at joint; (c) Shear deformation at joint

LOAD-STRAIN RESPONSE

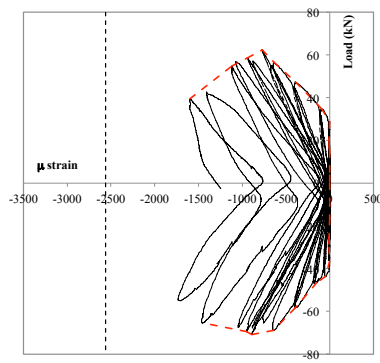
Strain Reading on column



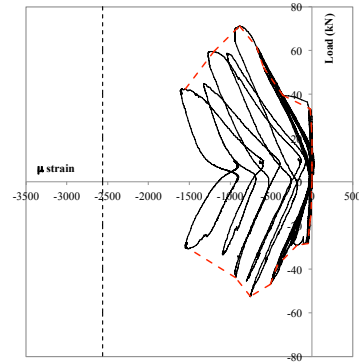
(a) BCJ-CS-A Test #1



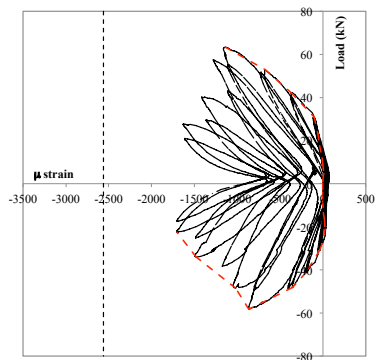
(b) BCJ-CS-A Test #2



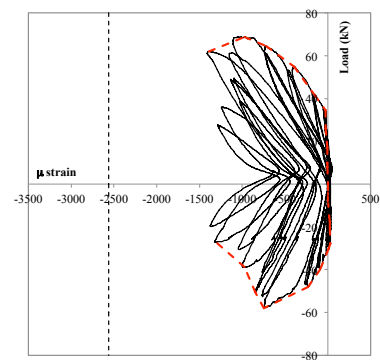
(c) BCJ-SS-S4



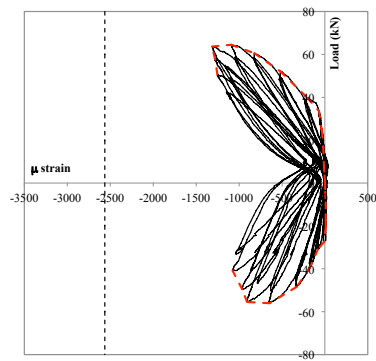
(d) BCJ-SS-F4



(e) BCJ-SS-S8

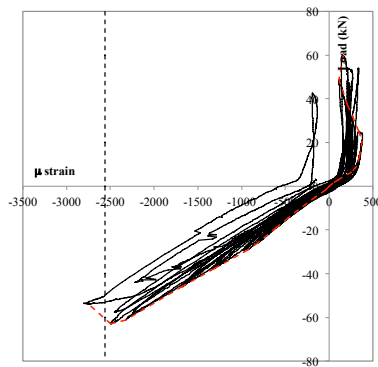


(f) BCJ-SS-F8

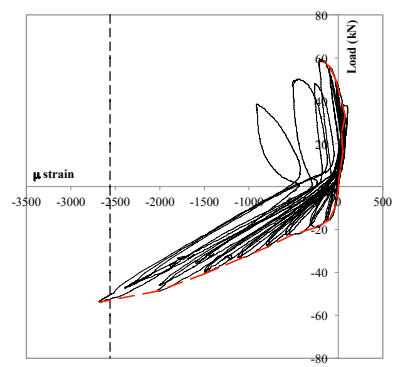


(g) BCJ-CS-B

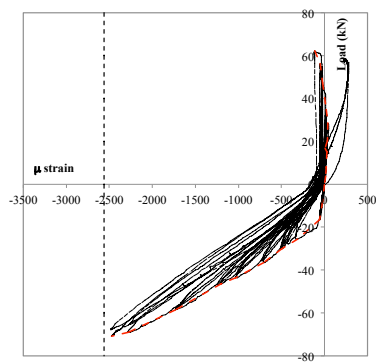
Strain Reading on top beam reinforcement



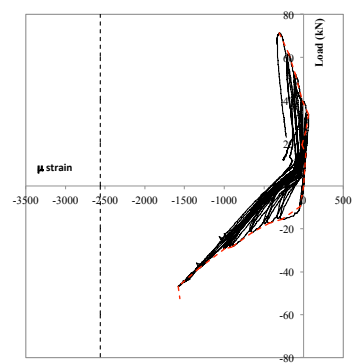
(a) BCJ-CS-A Test #1



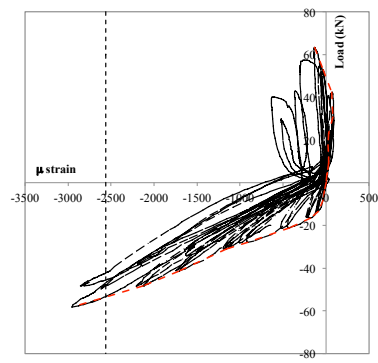
(b) BCJ-CS-A Test #2



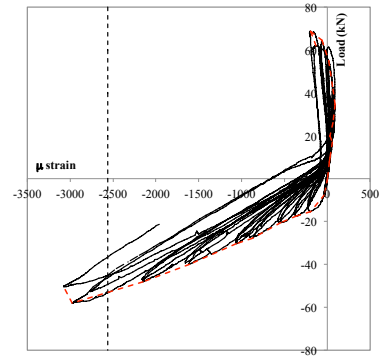
(c) BCJ-SS-S4



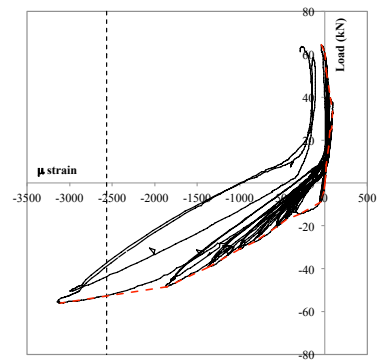
(d) BCJ-SS-F4



(e) BCJ-SS-S8

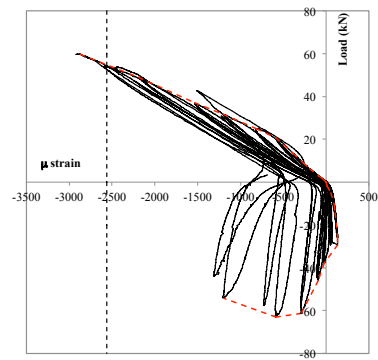


(f) BCJ-SS-F8

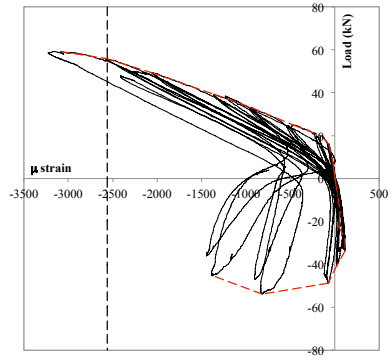


(g) BCJ-CS-B

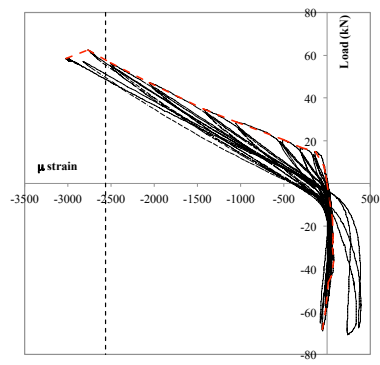
Strain Reading on bottom beam reinforcement



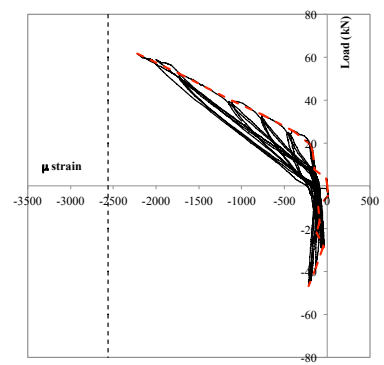
(a) BCJ-CS-A Test #1



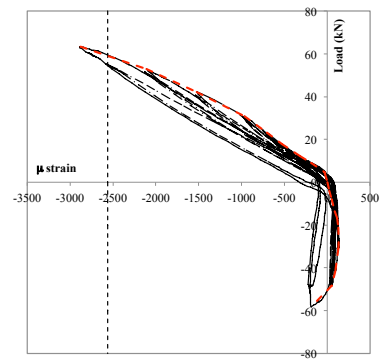
(b) BCJ-CS-A Test #2



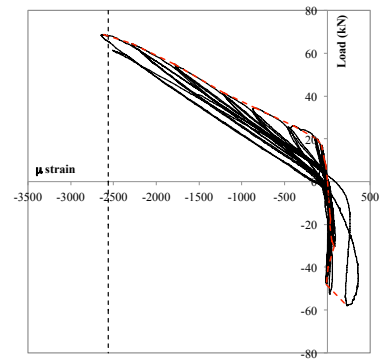
(c) BCJ-SS-S4



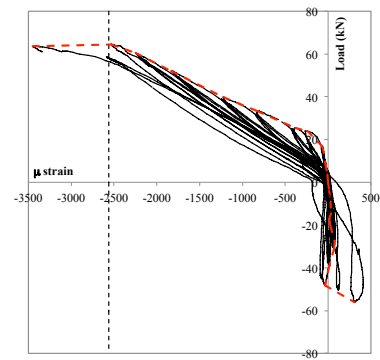
(d) BCJ-SS-F4



(e) BCJ-SS-S8

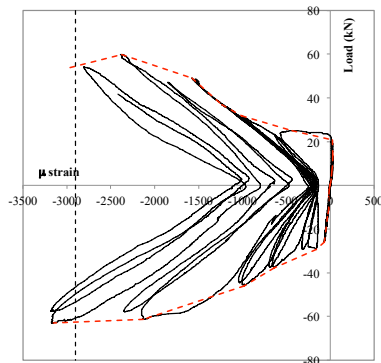


(f) BCJ-SS-F8

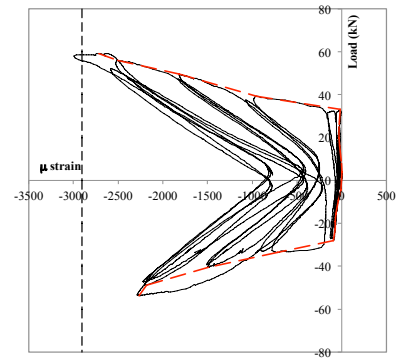


(g) BCJ-CS-B

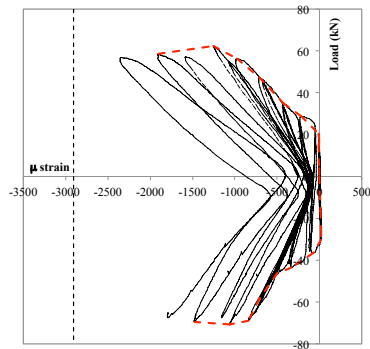
Strain Reading on joint shear reinforcement



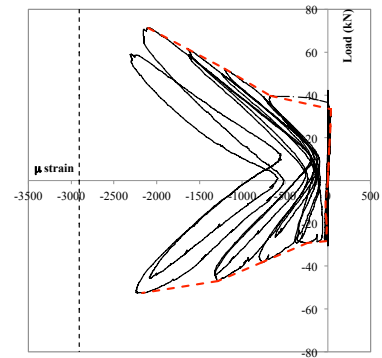
(a) BCJ-CS-A Test #1



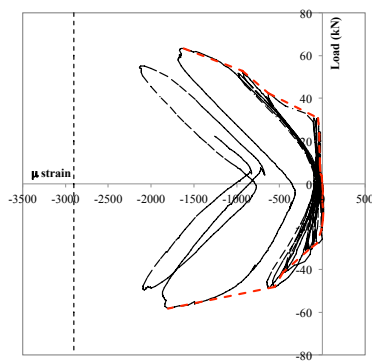
(b) BCJ-CS-A Test #2



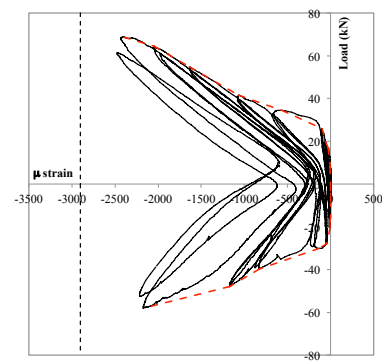
(c) BCJ-SS-S4



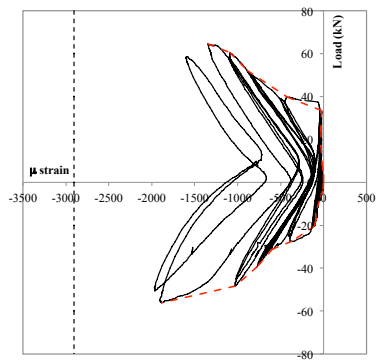
(d) BCJ-SS-F4



(e) BCJ-SS-S8

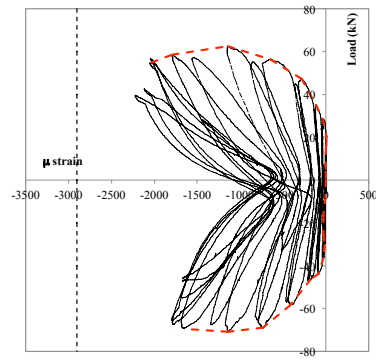


(f) BCJ-SS-F8

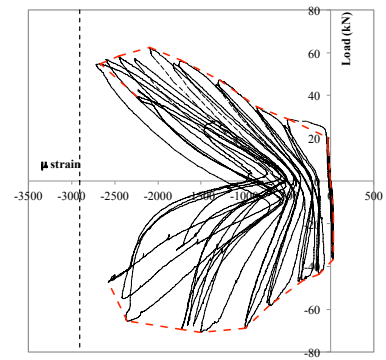


(g) BCJ-CS-B

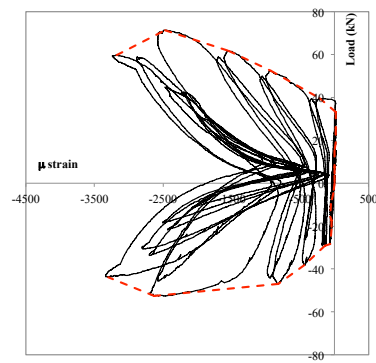
Strain Reading on embedded bars



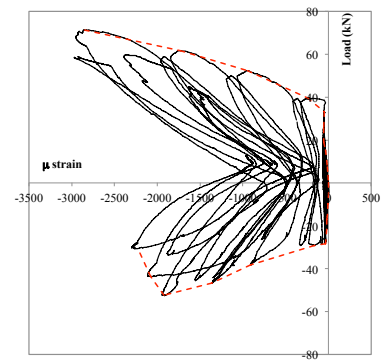
(c) BCJ-SS-S4 row 1



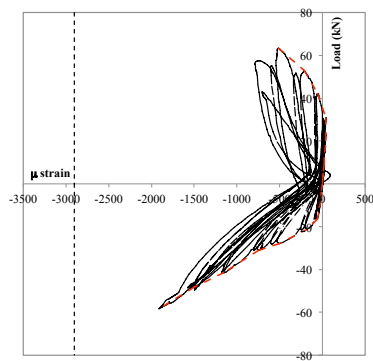
(d) BCJ-SS-S4 row 2



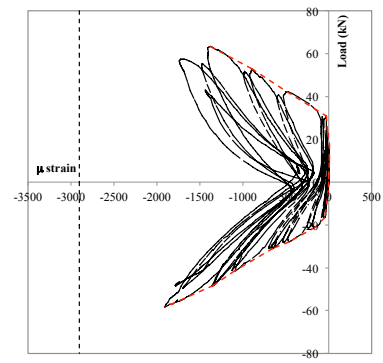
(e) BCJ-SS-F4 row 1



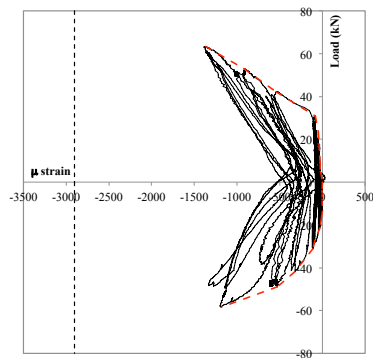
(f) BCJ-SS-F4 row 2



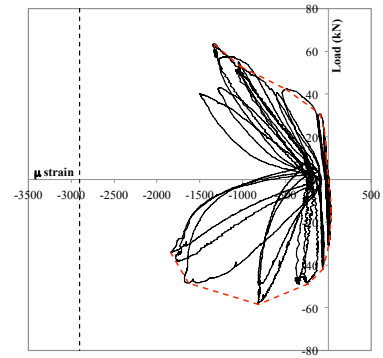
(g) BCJ-SS-S8 row 1



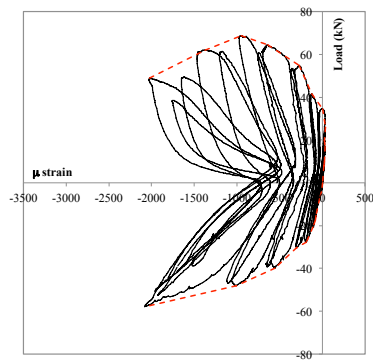
(h) BCJ-SS-S8 row 2



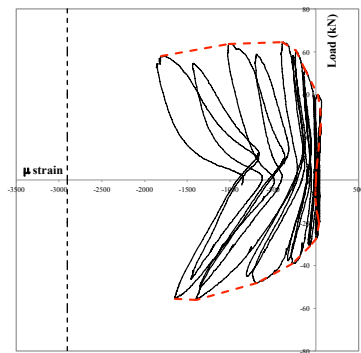
(i) BCJ-SS-S8 row 3



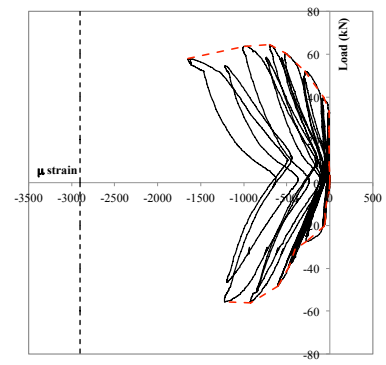
(j) BCJ-SS-S8 row 4



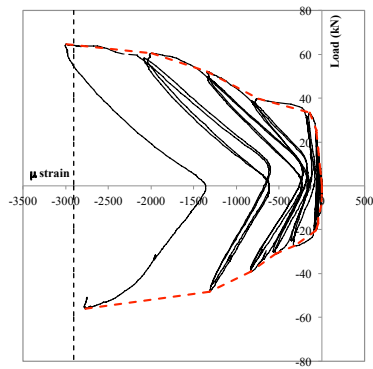
(k) BCJ-SS-F8 row 1



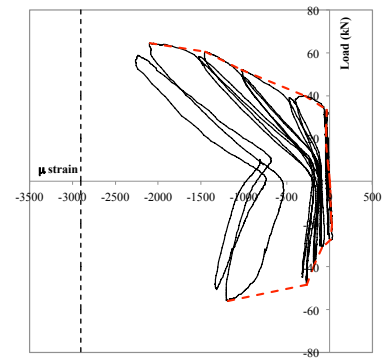
(a) BCJ-CS-B row 1



(b) BCJ-CS-B row 2



(c) BCJ-CS-B row 3



(d) BCJ-CS-B row 4